Quantum chemical and analytical investigations of radionuclide adsorption

Daniel Walsh

Thesis submitted for

MSc (By Research)

March 2021

Lancaster University

Department of Chemistry

Supervisors:

Dr Andrew Kerridge

Dr John Griffin

Declaration

I, Daniel Walsh, confirm that the work presented in this thesis is my own work, and has not been submitted for the award of a higher degree elsewhere. Where information has been derived from other sources, I confirm that this has been indicated in the thesis. In addition, I confirm that this thesis does not exceed the permitted maximum length.

Abstract

Generating electricity by the combustion of fossil fuels is one of the largest contributors to worldwide greenhouse gas emissions. To combat climate change, alternative ways of producing and using energy is essential. Nuclear power is one of the lowest carbon-producing technologies for generating electricity and is considered a viable alternative to conventional power stations for the purpose of meeting typical energy demands. Increased utilisation of nuclear power will result in an increased production of nuclear waste. Management, storage and reprocessing of nuclear wastes create radioactive effluent. There are various methods for the treatment of radioactive effluent, however radionuclide adsorption has distinct advantages in comparison to alternative treatment methods. Graphene oxide has the potential to be an exceptional radionuclide adsorbent for the treatment of radioactive effluent.

This research is comprised of computational simulations and analytical studies which aim to elucidate the mechanisms of radionuclide adsorption on various graphene oxide surfaces. The computational component involves the creation of models including graphene oxide, reduced graphene oxide and modified analogues of both. The models are based on structures adapted from current scientific literature and theoretical idealised concepts. The models are modified to improve their adsorption affinity and capacity for the selected radioisotopes ^{137}Cs and ^{90}Sr. Ab initio molecular dynamic simulations are performed to observe the interaction between the models and Cs$^+$ and Sr^{2+} ions in solution. Visualisation of simulated ion trajectories allows for the identification of the location of adsorption of the ions on the model surfaces.

The analytical component of this research involves both material characterisation and adsorption experiments. Graphene oxide is prepared via the Hummer's method and subsequently reduced. These were characterised along with externally sourced equivalents. Analytical characterisation was performed using FTIR, Raman spectroscopy, SEM, EDS, and solid-state NMR.

Adsorption experiments were conducted by filtering Cs and Sr solutions through each variant of graphene oxide and a standard molecular sieve for comparison. Quantitative analysis to determine adsorption capacities for each material was performed. The identification of the location of ion adsorption on the surface of the externally sourced graphene variants is attempted using solid state NMR.

Movement of a Cs^+ towards a fluorine functionalised graphene oxide surface in an AIMD simulation suggests potential attraction of a Cs^+ to fluorinated functional groups on the modified graphene oxide surface. Carboxyl group instability shown in AIMD simulations on the basal plane of all carboxyl functionalised graphene oxides suggests that carboxyl groups may only occur on the edges of graphene sheets. The removal of carboxyl groups from the surface of all carboxyl functionalised graphene oxide variants and the absence of attraction between Cs^+ and Sr^{2+} to these variants suggests that stable carboxyl functionalisation is a requirement to provide adequate attractive forces for cation adsorption on graphene oxide.

Acknowledgements

Contents

List of Figures

List of Tables

Chapter 1: Introduction

1.1 - Nuclear power

The scientific field of radiochemistry has been in development since the late 19th century. Originating from the discovery of radioactivity by Henri Becquerel in 1898 the study of the fundamental laws and behaviour of radioactive compounds continued into the middle of the 20th century. The ambition of harnessing nuclear energy began shortly after nuclear fission was firstly achieved by the Italian physicist Enrico Fermi in 1934. Commercial exploitation of nuclear energy began with the start-up of the first nuclear power plant in 1954. According to the International Atomic Energy Agency there are currently 454 nuclear power plants in operation world-wide with a further 54 under construction. Nuclear power is considered an important component of global energy security and provides a significant proportion of the world's electricity, approximately 11 % as of 2018. [1] There are various types of commercial nuclear reactors which operate in different ways, but all have the same purpose. This is to produce and control the energy released from nuclear fission. The energy released from nuclear fission is harnessed to produce steam which is used to generate electricity by driving turbines. Generating electricity by conventional means such as the combustion of fossil fuels is one of the largest contributors to worldwide greenhouse gas emissions. [2] In order to combat climate change, huge changes are required in how energy is produced and used. The successful phasing out of carbon rich fuels will require a variety of low carbon electricity generation sources capable of producing a stable quantity of energy for an ever-increasing global demand. Carbon reduction commitments are increasingly becoming components of many of the worlds' government's energy policies and some are looking to nuclear power to

meet emission targets whilst securing and improving the security of their electricity supply. [3] Nuclear power is already considered to be one of the lowest carbon technologies for generating electricity producing comparatively little carbon dioxide during their working lifetime. Countries are set to become more reliant on nuclear power to bridge the gap between conventional power stations and renewable energy sources as currently available renewable technologies do not meet typical energy demand. [4] An increased reliance on nuclear power will result in an increased production of nuclear waste.

1.2 - Nuclear waste management

During the mid to late 20th century, studies relating to the chemical properties of the artificial chemical elements generated through nuclear fission were conducted alongside the creation of technologies to treat spent nuclear fuel and the development of methodologies to mitigate the problems arising from active nuclear waste management. The discarding of large quantities of hazardous radionuclides into the environment coincided with the growth of the nuclear power industry. [5]

The ecological problems associated with historical radioactive pollution and environmental protection mechanisms to deal with generated radioactive wastes are currently of major concern. Historic wastes generated from the nuclear fuel cycle (NFC) including contaminated materials, corroded fuel cladding, old tools, and equipment were mixed and poorly characterised, occasionally stored under water and as a result degraded overtime forming complex sludges and supernatant liquids. [6] The main source of nuclear waste is produced from the NFC. The basic fuel of nuclear reactors is uranium, typically uranium oxide in the form of pellets which are stacked into long thin tubes to form fuel rods. The fissile component of uranium is ^{235}U which occurs naturally in uranium ore with a typical elemental composition

of 0.7 %. Dependent on the type of reactor, natural or enriched uranium (approximately 3-5 % ^{235}U) is used. When the fuel has reached the end of its useful life it is removed from the reactor and is either discarded as solid high-level waste (open NFC) or reprocessed to extract remaining fissile fuel (closed NFC). Open NFC waste contains both fission products and transuranic isotopes whereas closed NFC waste, which is in aqueous form after dissolution, contains a mixture of fission and corrosion products, minor actinides, transmutation products and process contaminates. [7]

The development of the nuclear industry brought into focus the various detrimental effects of ionising radiation produced by nuclear waste. Radiation is a generic name given to any transmission of energy in the form of electromagnetic waves (X-rays, gamma) or stream of particles (alpha, beta, neutrons). The cells of biological material exposed to ionising radiation undergo a sequence of chemical changes to its constituent atoms and molecules. The size and significance of the changes coincide to the level of exposure and could be enough to destroy the cells or to damage them irreparably resulting in clinical symptoms of illness in an individual. [8] The danger of nuclear waste is clearly seen in the deterministic (skin damage, hair loss, sterility, death) and stochastic effects (cancer) of radiation exposure. A nuclear waste management system was developed to isolate radionuclides to protect both the public and the environment.

Radioactive waste is separated into distinct categories dependent on the level of radiation the waste emits. The higher the concentration of radionuclides the waste contains the higher the hazard. However, radionuclides at the same concentrations possess different levels of hazards due to their individual decay mechanisms and specific activities. Radioactive waste accompanied by high levels of radiation requires immobilisation and shielding by remote

handling to reduce the potential for the migration or dispersion of contaminants including radionuclides. [9] Newly discharged spent nuclear fuel is intensely radioactive and generates significant amounts of heat. Management of spent fuel is easier if the fuel is temporarily stored to allow short lived radionuclides to decay away. Nuclear power stations typically contain storage facilities such as fuel ponds or shielded dry storage units into which used fuel is transferred after discharge from the reactor. After this period of short-term storage high activity wastes are converted to a chemically stable form of glass (vitrification), packaged in steel or copper drums for increased corrosion resistance along with a water-resistant buffer. The resultant conditioned waste is stored in deep stable geological formations providing long term isolation and containment. Management, storage and reprocessing of nuclear wastes create radioactive effluent which can enter the environment through controlled discharge or accidental release. A small fraction of the activity generated through fission of reactor fuel is emitted to the environment under normal plant operations, the effluent can originate from several sources within the nuclear plant including: fission of residual uranium contained on the exterior of fuel rods (tramp uranium), leaks from failed fuel rods, activation of materials in reactor cooling water and erosion of activated cooling system components. [10] Radioactive liquid effluents also arise from the reprocessing of nuclear waste and can originate from the fuel storage pond, reprocessing condensates, and decontamination washings. These wastes are typically concentrated by evaporation and held in tank storage until they can be safely discharged. [11] Commonly reported radionuclides found in liquid effluent released from nuclear plants are shown in Table 1.1: [12]

Radionuclide	Approximate Half Lives
^{51}Cr	28 days
^{54}Mn	312 days
^{55}Fe	2.7 years
^{60}Co	5.3 years
^{90}Sr	29 years
^{95}Nb	35 days
^{137}Cs	30 years
^{131}I	8 days

Table 1.1: commonly reported radionuclides in liquid effluent release from nuclear plants.
[12]

Without correct treatment dissolved radionuclides may enter the aquatic environment via rivers and groundwater, these can then potentially accumulate and concentrate in the food chain when taken up by marine life or vegetation, increasing the risk of human exposure to hazardous radioactive nuclides. Given the serious impact on human health radionuclides pose, the decontamination of radioactive effluent should be a critical technical, political, and social issue. Innovative and effective technologies and methods are required for the handling and decontamination of hazardous radioactive effluent, specifically, the treatment of long-lived gamma emitting radionuclides ^{60}Co, ^{90}Sr and ^{137}Cs. Thus, follows a comprehensive review of current technologies for the decontamination of radioactive effluent. The critical analysis of the various treatment methods currently researched aims to elucidate the benefits and drawbacks of each. Ultimately, one should always aspire to minimum volume stabilized and solidified radioactive waste with low as reasonably practicable impact on environmental and human health. Therefore, the principles of handling radioactive effluent should always be kept in mind when determining the selection, design, and operation of any potential treatment system.

1.3 - Current research for the treatment of radioactive effluent

1.3.1 - Adsorption and ion exchange

Adsorption and ion exchange are considered viable techniques for the removal of radionuclides from effluent as they are highly efficient, easy to operate and relatively cheap. The term adsorption refers to the adhesion of contaminants (adsorbate) to a surface (adsorbent). The sorption–desorption process can occur at the interface between any two phases e.g. liquid–solid, gas–solid, gas–liquid or liquid–liquid. Varying factors may influence the adsorption process including dissolved and non-dissolved organic matter content, surface tension of the aqueous phase, system pH, buffering capacity and ionic strength, characteristics of adsorbent and competition for its sorption sites, degree of precipitation and temperature fluctuations, interaction mechanisms and contribution of different types of binding phases, sorbent solubility and concentration of the contaminant. [13] Various types of adsorbents have been developed for the treatment of radioactive effluent, including clay minerals, carbon-based materials, graphene oxides, zeolite-based materials, metal-organic framework materials and layered double hydroxides. [14] Current research is focused on the improvement of the chemical, mechanical and thermal stability of adsorbent materials to improve their selectivity towards radionuclides. Metal oxide nano-adsorbents display high efficiency and capacity for the adsorption of heavy metals and are currently used for their removal from aqueous systems. A novel inorganic nanocomposite material Al_2O_3-ZrO_2-CeO_2 has been prepared by a sol-gel polymeric technique and its radionuclide separation capabilities were tested for simulated radioactive waste effluent containing a mixture of caesium and strontium. [15] High adsorption of Cs and Sr was achieved with a maximum adsorption of 94 % and 44 % respectively after 1 hour between pH 6-8. However, the %

sorption for Cs and Sr was significantly reduced with the addition of ions Na, Mg and Cr. Discharged radioactive effluent is likely to contain a wide variety of ions therefore the real-world effectiveness of the nanocomposite (considering the detrimental effect from competitive ions) to separate and adsorb radionuclides could be somewhat reduced. The pH range of radioactive effluent could potentially fall outside the pH range experimentally observed, with the % adsorption falling significantly at lower pH values and with no data for pH >8 the effectiveness of the nanocomposite for radioactive effluent treatment is again reduced or unknown. As the maximum adsorption capacity of the nanocomposite for Cs and Sr is not achieved until an hour of contact time it could be that this would be too slow if the adsorbent was used to stop the spread of radionuclide to the surrounding environment from an accidental release of radioactive effluent.

Newly developed chemically modified magnetic nanomaterials have shown good adsorption capacity for heavy metal ions and can be extracted from water using an external magnetic field. Specific surface modifications are utilised to target heavy metal radionuclides for their removal from effluent. Modified magnetic nanomaterials can be removed from effluent after adsorption has taken place and either concentrated and discarded or regenerated for reuse. The nano adsorbent nano zero valent iron (NZVI) has been surface modified with diethylenetriamine (DETA) to prevent surface oxidation and 2-pyridinecarboxaldehyde (PY) for selective heavy metal radionuclide adsorption to form (NZVI-DETA-PY) and tested for its adsorption capabilities of ^{60}Co in simulated radioactive effluent. [16] The NZVI-DETA-PY nanocomposite exhibited impressive ^{60}Co (0.01 mol L^{-1}) removal from simulated radioactive effluent with % extraction at 96.20 % after 30 minutes at pH 7. The potential chemical bonding mechanism is illustrated below:
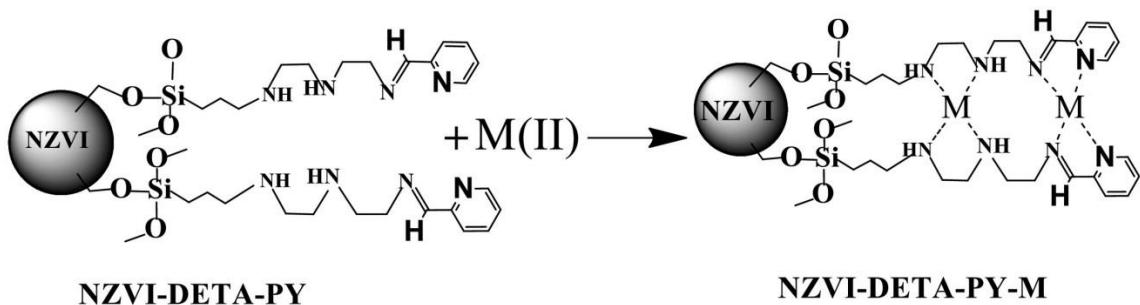
Figure 1.1: Chemical bonding of metal ion on the surface of NZVI-DETA-PY. Reproduced from Mahmoud *et al.* [16]

Interference of other ions in solution (chloride and sulphate) improves the adsorption capacity of ^{60}Co to NZVI-DETA-PY nanocomposite however lower pH values reduce adsorption and there is no adsorption data for pH values >7. Good thermal stability and efficient absorbance capacity suggests NZVI-DETA-PY nanocomposite could be effectively utilised for ^{60}Co removal from radioactive effluent and its proven ability to be regenerated and reused is of added benefit. However further research is required to test NZVI-DETA-PY nanocomposites affinity to ^{60}Co at pH values >7 and its affinity towards other radionuclides which are also commonly found in radioactive effluent.

Current research for modified silica-based nanomaterials focuses on catalysis, separation, and selective adsorption due to their flexibility for modification, high adsorption capacity and high surface area as well as their good thermal and mechanical stability. A Prussian blue functionalised SiO_2 nanomaterial (SiO_2-Fe-CN) has been created via a novel and simple preparation route and its adsorption capacity for Ce and Co contained in nuclear effluent and Ce, Co, Sr contained in HNO_3 acidic solutions were experimentally determined. [17] SiO_2-Fe-CN showed good adsorption capacity for Ce and Co in nuclear effluent (95.7 % for Ce and 88.88 % for Co after 120 minutes) with a linear increased adsorption capacity from pH 1.5 to pH 7.5. Removal efficiency for Ce and Co in 1 M HNO_3 is comparable to nuclear effluent however it is

significantly lower at both lower (0.01 M) and higher (3 M) concentrations. Very low adsorption is seen for Sr (<5 %) at all concentrations, this would suggest this nanomaterial shows very low affinity for Sr in acidic conditions however this property could be utilised if the separation of Co and Ce from Sr in a solution with HNO_3 is desired. The novel nanomaterials reviewed above show great potential for the application of absorption and ion exchange specifically for the hazardous gamma emitting radionuclides typically found in radioactive effluent. Research will continue to produce more analogues of the wide variety of adsorbents and ion exchange materials currently available with the aim of optimising their surfaces to increase their selectivity for targeted ions, increasing their functionality over a wider range of pH values and improving their durability under the more realistic harsher environmental conditions they would be subject to under operational activities or accidental release scenarios. Further research is required to test the adsorption capacity of developed materials under these harsher process conditions and when subject to larger amounts of radiation. An ideal radionuclide adsorbent or ion exchange material should have maximum adsorption or exchange capacity for all the hazardous radionuclides with longer half-life's which are likely to persist in the environment. They should be stable and effective under all the environmental conditions they are likely to be exposed to and should have the ability to be easily regenerated and reused in a way which is not detrimental to their purpose.

1.3.2 – Oxidation

Photo-catalytic advanced oxidation processes are a recent addition to a variety of techniques currently researched for the removal of radionuclides from radioactive effluent. Research utilising this radionuclide removal technique is very much in its infancy and therefore literature of experimentally proven methods is scarce but still worth evaluating.

Photocatalytic modifications enhance the adsorptive capacity of selected nanomaterials (which have already shown affinity to target radionuclides) when exposed to UV light. The mechanism of increased adsorption is suggested to be photocatalytic reduction of the nanomaterial which modifies its structure for greater capacity [18]. Prussian blue has been modified with TiO_2 (PB/TiO_2) for significantly enhanced ^{137}Cs adsorption capacity under UV radiation as illustrated below: [19]
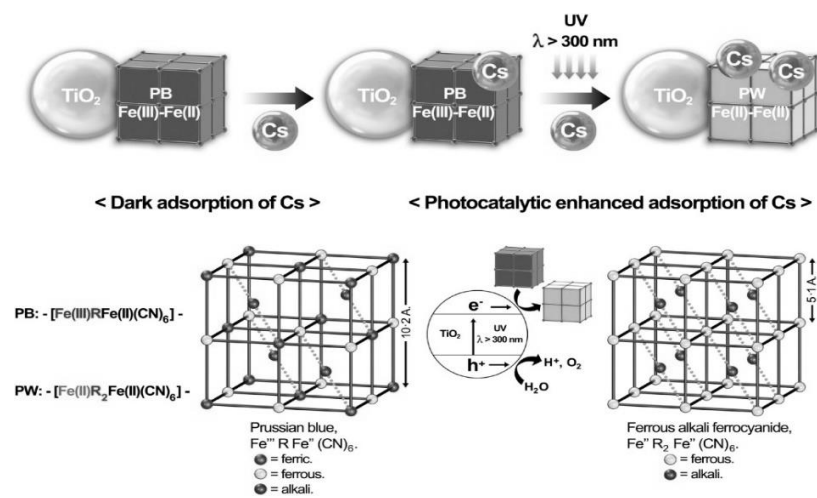
Figure 1.2: Schematic of dark and photocatalytic-enhanced adsorption of Cs ions by PB/TiO2 were the reduction of PB leads to formation of Prussian white (PW). Reproduced from Kim *et al.* [19]

As desorption of ^{137}Cs from PB can be induced by electrochemical oxidation it's enhancement with TiO_2 achieves both an increased adsorption capacity in comparison to conventional transition metal hexacyanoferrates and a method of removing the radionuclide from the adsorbent without the use of other chemical reagents, eliminating the production of additional waste. Additional experimentation is required to determine PB/TiO_2 adsorption capacity to other radionuclides of concern, over a wider range of pH values and to determine its selectivity to target radionuclides when other potentially competitive ions are introduced into the system. Advanced oxidation processes for radionuclide adsorption are still in initial

stages of development with current experiments conducted under controlled conditions which are not representative of industrial processes; therefore, some form of process validation on a larger scale should occur when completing future research.

1.3.3 - Precipitation and flocculation

Chemical precipitation is a simple and comparatively low-cost technique for the decontamination of radioactive effluent with the advantage of high efficiency removal when dealing with large volumes. The application of precipitation allows for the separation and concentration of radioactive contamination from a large volume of effluent which significantly reduces the quantity of radioactive waste to be dealt with which reduces operational cost and radiological risk. As most of the radioactivity is both precipitated and concentrated into a radioactive sludge by chosen chemical agents, it can be separated from a large volume of effluent and can be removed following the discharge of the decontaminated effluent. 35 m^3 of radioactive effluent containing ^{137}Cs and ^{60}Co has been treated in such way using potassium ferrocyanide, nickel nitrate and ferric nitrate. [20] 97.2 % of the total volume of effluent was treated and discharged as normal wastewater and 98 % of ^{137}Cs was removed at pH 9. The radioactive sludge formed through the precipitation of the radionuclides had a total volume of 0.98 m^3 significantly reducing the volume of waste to be treated. The transportation of the radioactive waste for solidification and final disposal was therefore safer and more economically viable than transporting the whole liquid volume pre-precipitation.

Precipitation has been combined with floatation to produce a successful solid-liquid separation technique for ^{137}Cs in low level radioactive effluent. [21] Permissible discharge limits for ^{137}Cs are achieved over a range of pH values within 30 seconds using sodium tetraphenylborate (TPB) as a precipitating agent with the addition of a Fe (III) solution. The

surfactants sodium laurel sulphate (SLS) and cetylpyridinium chloride (CPC) act as flotation agents based on the pH value of the solution. With the iron oxide coated CsTPB being positively charged at pH values less than 8 and therefore attracted to the anionic surfactant SLS and negatively charged at values greater than 8, hence the attraction cationic surfactant CPC as illustrated below:
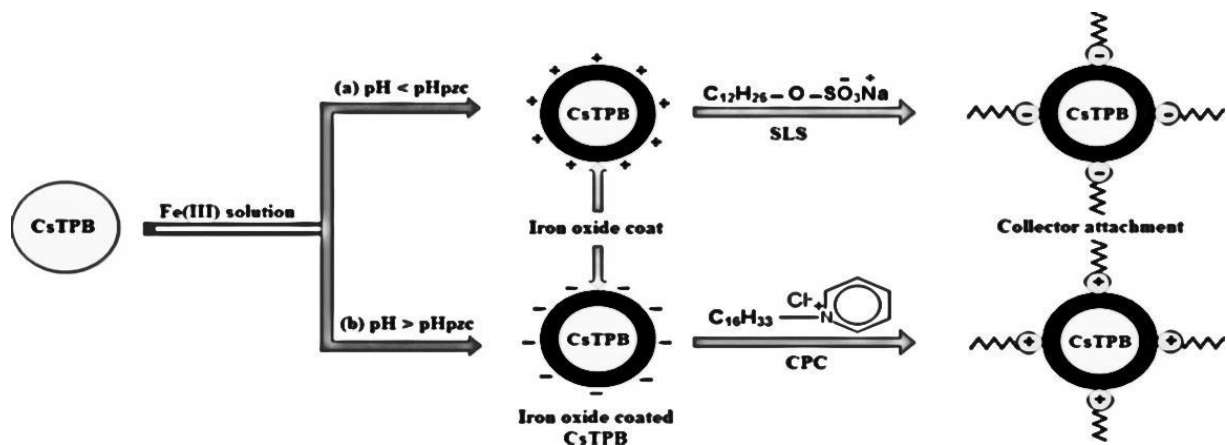
Figure 1.3: Schematic representation of collector attachment to the iron oxide coated CsTPB. Reproduced from Soliman *et al*. [21]

The decontamination factor for the flotation technique is superior in comparison to the other separation techniques tested which included decantation, centrifugation, and membrane filtration. Selectivity of NaTPB for ^{137}Cs may be an issue if other competitive ions are present in the radioactive effluent. Affinity and efficiency of Cs capture for NaTPB in the presence of other potentially competitive ions typically found in radioactive effluent should be researched further. The application of NaTPB in the high-level radioactive waste may be limited due to potential radiolytic decomposition of TPB when exposed to high levels of radiation.

Typical challenges associated with chemical precipitation are the production of potentially large quantities of radioactive slurries which require further processing before being discarded safely and the difficulty of the formation of insoluble precipitates in radioactive

effluent which contain low concentrations of radionuclides. Any precipitates which are formed are likely to be of a very small size and require flocculation for improved settlement. Flocculation is the process whereby destabilized particles or particles formed as a result of destabilisation (coagulation) are induced to come together forming agglomerates, with the aid of a flocculent this process can be accelerated as the solution is further destabilised; flocculation differs from precipitation in that flocculants are suspended in solution prior to flocculation and are not dissolved in solution. [22] Addition of a polyacrylamide-based polymer flocculent has been shown to increase the settling rate and increase the removal of ^{137}Cs and ^{90}Sr from low level radioactive effluent. The cationic flocculent is utilised for the aggregation of fine particles as well as improved removal of ^{90}Sr which improved the decontamination factor of radioactive effluent in comparison with a non-flocculent assisted co-precipitation technique. [23] Aluminosilicate and polyferric sulphate (PFS) which are both typical inorganic water purification media were chosen for their high efficiency and radiation stability and have been used in a practical context as an adsorbent and coagulant for the clean-up of the Taiwan research reactor spent fuel pond. [24] The granular synthetic aluminosilicate adsorbent was introduced to remove the ^{137}Cs and ^{90}Sr and the suspended solids were precipitated using PFS coagulants combined with calcium hydroxide in the spent fuel pond then removed mechanically with a specially designed unit. The decontamination of the spent fuel pond water using this technique resulted in a 95 % reduction of total radioactivity.

1.3.4 – Electrochemical

Various electrochemical separation methods including electro-adsorption, electro-dialysis and electro-deionization have been studied to produce technologies for the decontamination of radioactive effluent. Electrochemical techniques typically display higher adsorption

capacities compared to conventional ion exchange mechanisms and can be regenerated without the use of additional chemicals which would produce more unnecessary radioactive waste. Electrical exchange of ions can be easily controlled by electrode potential allowing for adsorption and desorption at the user's discretion without the need for other chemicals or filtration for the removal of adsorbed radionuclides which reduces cost. A copper hexacyanoferrate / multi-walled carbon nanotube (CuHCF/MWCNT) hybrid electrochemical separation system has been developed for the removal of Cs from effluent. [25] Uptake and release of Cs is controlled by switching applied potentials between an anode and cathode. Rapid ion exchange is achieved with CuHCF/MWCNT achieving a maximum adsorption capacity of 310 mg g^{-1} in a 50 µM Cs solution which is superior in comparison to a tested conventional adsorption system (230 mg g^{-1}). CuHCF/MWCNT adsorption of Cs is electrochemically reversible with the hybrid displaying an uptake capacity of 85 % after 100 cycles of adsorption and regeneration. This system would be beneficial for the removal of ^{137}Cs in radioactive effluent; however its selectivity for other radionuclides potentially contained in an effluent which would require removal is not known, multiple specific adsorption hybrids would be a less efficient cleaning strategy than one adsorbent capable of removing a variety of nuclides. Desorption of radionuclides allowing for decontamination and reuse of the adsorbent is an advantage over traditional single use adsorbents however the required electrical energy for regeneration may be detrimental to its economic viability.

Adsorbents and ion exchange mechanisms are currently widely used as methods for radionuclide treatment in effluent due to their low cost, thermal stability, selective compatibility and as seen above can be enhanced by electrochemical processes to increase ion adsorption and reduce secondary waste volumes. Electrochemical-switched ion exchange (ESIX) is one such method which can be employed for targeted radionuclide removal. Reduced

graphene oxide (RGO) supported nickel hexacyanoferrate (NiHCF) nanoparticles have been developed with high selective adsorption for Cs. [26] Ion exchange can be controlled by applied potentials with reverse potential desorbing the adsorbed Cs ion allowing for renewal and reuse of the nanoparticle. High adsorption capacity for Cs is achieved (320 mg g^{-1}) which is greater than other hexacyanoferrate materials tested and pure NiHCFs (235 mg g^{-1}). High reuse potential for the nanoparticle is also demonstrated with a 92 % ion-exchange capability after 160 cycles of Cs adsorption/desorption. RGO is used as a support as it is cheap, has good conductivity and has a large surface area which further enhances the Cs adsorption efficiency and capacity of the nanomaterial. It would appear that the characteristics of the carbon supports utilised in the above research are desirable for the application of radionuclide adsorption, however the deposited nanoparticles in the research covered displayed selective adsorption of Cs with no data to suggest affinity towards other radionuclides of concern e.g. Sr and Co. Therefore, further research is required to create a carbon-based support retaining these desirable characteristics but modified to adsorb and desorb a range of radionuclides, preferentially ones with long half-lifes (Cs, Sr, Co) which are typically found in radioactive effluent. This would be a more favourable approach as all radionuclides could be removed from effluent at the same time with the support able to withstand operational processes reducing both cost and waste.

Chalk river unidentified deposit (CRUD) is a corrosion product produced from nuclear power plants with a composition related to the activated construction material of reactor systems. One of the radionuclides it is likely to contain is ^{60}Co which then becomes a component of effluent during the decommissioning and decontamination phases. An advanced electro kinetic process combined with chemical decontamination has been utilised to remove CRUD from effluent. Oxalic acid was used for CRUD removal, and the Co ions from $CoFe_2O_4$

(Simulated CRUD) where transferred to a titanium cathode in an electro kinetic reactor. The combined system using a cation exchange membrane and zeolite for adsorption shows high efficiency for CRUD removal whilst also reducing secondary waste (typically produced from standard chemical decontamination methods), a schematic diagram of the decontamination system is shown below: [27]
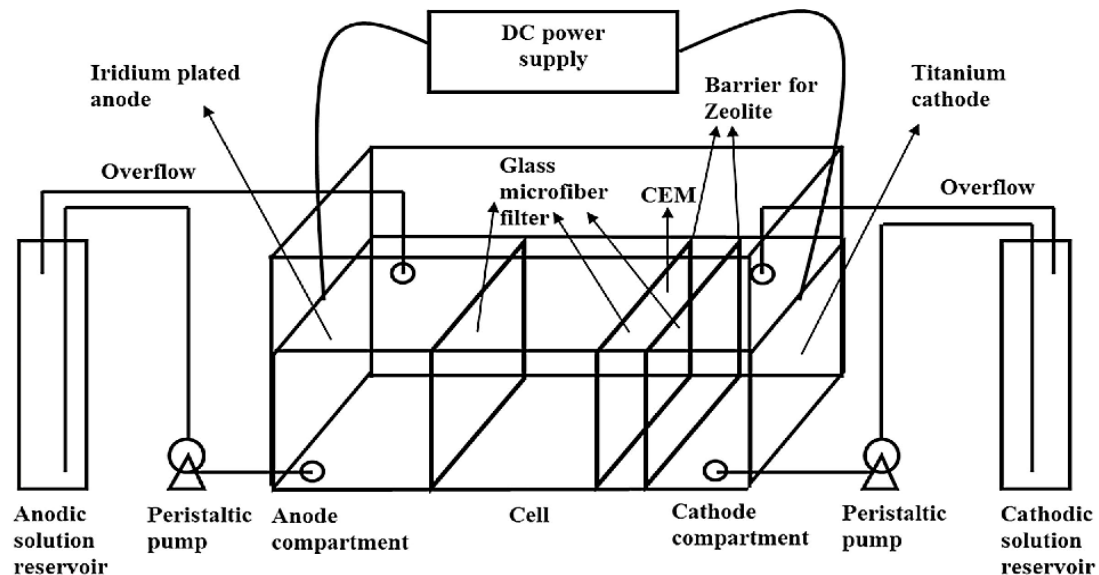
Figure 1.4: Schematic diagram of the rectangular reactor. Reproduced from Kim *et al.* [27]

The combined chemical electro-kinetic (EK) process removed 1.6 times more Co compared to a standard chemical decontamination method. The amount of secondary waste produced in the EK method was significantly less than the standard chemical decontamination method as the cobalt ions migrated towards the cathode compartment concentrating them in the cathodic electrolyte. Co is then removed from the system after adsorption on the zeolite barrier by removal of the barrier from the EK reactor, producing a smaller quantity of concentrated secondary solid waste. How practical and cost effective a decontamination system such as the one described is yet to be seen with further research required in an industrial setting. Large contaminated metal components which are to be decommissioned

would need to be cut into reasonably sized pieces based on the size of the EK reactor which could produce further contamination and additional expenses. The energy cost of such a system may not be economically viable and consumables such as the anodic and cathodic materials could be considerably expensive whilst also contributing to additional contaminated waste. Degradation of oxalic acid may occur under radiation reducing its effectiveness for the removal of CRUD, further research would be required as simulated CRUD was used for the purposes of this research.

1.3.5 - Biological methods

Various microorganisms and organic material such as bacteria, fungi, cellulose etc. may be used or modified for use as environmentally friendly treatments for radioactive effluent. Radionuclides may be removed from the effluent through several mechanisms such as biotransformation, bio-sorption, bioaccumulation, bio-precipitation, and bio-solubilisation. [28] A novel fungus-Fe_3O_4 bio-nanocomposite has been successfully synthesized via a low-cost self-assembly technique using mycelium (penicillium-sp) as a living template for growth. The sorption ability of the fungus-Fe_3O_4 towards Sr (II), U (VI) and Th (IV) was evaluated. [29] The bio-nanocomposites maximum sorption capacity for Sr (II), U (VI) and Th (IV) was calculated to be 100.9, 223.9 and 280.8 mg/g respectively at 303 K which was significantly higher compared to a standard nano-Fe_3O_4 adsorbent and higher than most adsorbents tested in other research. The functional groups on the mycelium (alcohol, acetyl, and carboxyl) increased the absorbance capacity for the studied ions, improved the incorporation of the Fe_3O_4 into the fungal structure and enhanced its dispersion. The mycelium exhibited strong mechanical properties allowing for continued use for a period of more than two months and inhibited the dissolution of Fe_3O_4 providing structural stability under acidic conditions. The

magnetite component of the bio-nanocomposite allowed for easy magnetic separation from solution and displayed excellent regeneration performance maintaining a high sorption capacity after five radionuclide adsorption / desorption cycles. Renewable bio-nanocomposites which are easy to synthesise, have low cost magnetic separation mechanisms and display good regeneration performance may be effective in the removal of radionuclides in radioactive effluent. However high-level radioactivity can destroy and modify the genetic structure of cells which could lead to process failure. More research would be required to establish the stability and efficiency of bio-nanocomposites when exposed to varying amounts of radiation.

A common approach when aiming to produce a highly efficient adsorbent is to start with a material with good adsorbent properties and then modify the material with the aim of improving its absorbance capacity or selectivity. Synthetically attaching chemical appendages to an adsorbent material is one such way this may be achieved. The benefits of using natural organic structures as foundations for chemically modified adsorbents are numerous, for example their isolation is usually derived from natural materials which cuts costs and reduces waste. A novel organic–inorganic nanocomposite cellulose/HO_7Sb_3 has been chemically prepared by sol–gel mixing of organic poly cellulose into inorganic $Sb(OH)_5$ and its absorption capacity tested for ^{140}La, ^{60}Co and ^{137}Cs in aqueous solutions. [30] Synthetic preparation of the modified cellulose is shown below:
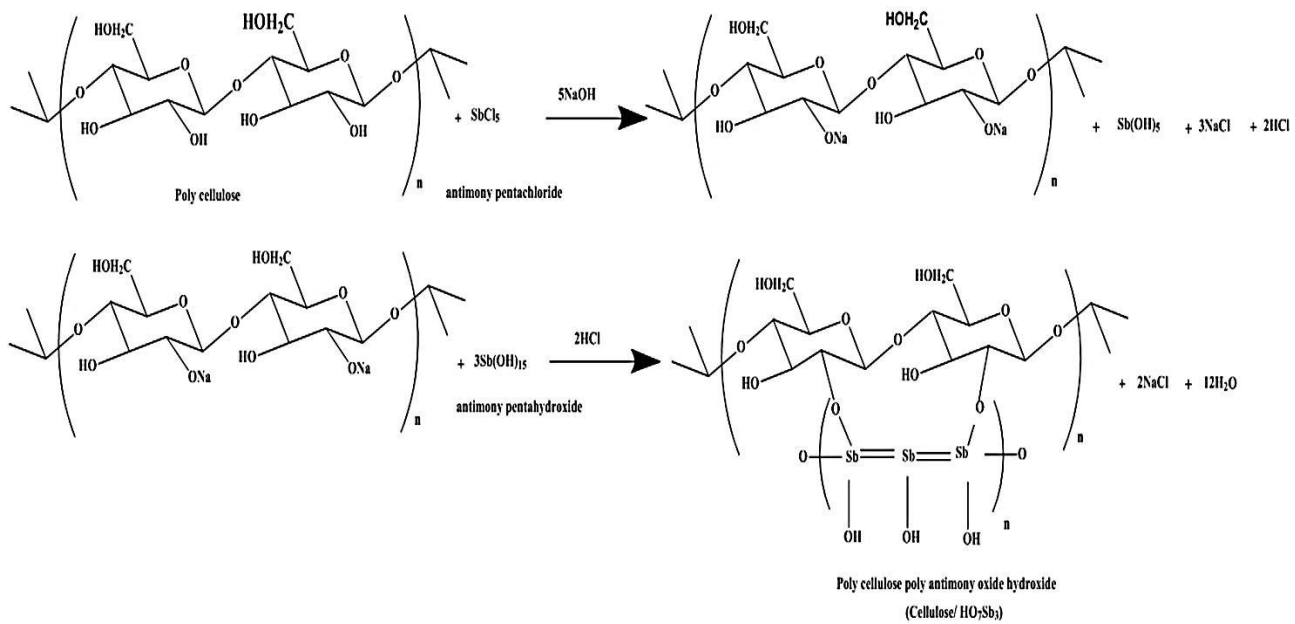
Figure 1.5: An example of chemical modification to a natural adsorbent material. Reproduced from Abdel-Galil *et al*. [30]

As seen in Figure 1.5 the synthesized cellulose/HO_7Sb_3 nanocomposite contains multiple bifunctional ion-exchange groups (C–OH and Sb–OH). The large number of hydroxyl groups increases the effectiveness of cellulose to bind with metal ions therefore improving its adsorptive capacity for the radioisotopes tested. Batch adsorption experiments showed high removal and decontamination efficiency for the nanocomposite with removal of 99.1 % for La^{3+}, 95.5 % for Co^{2+} and 46.8 % for Cs^+ from solution. The removal of the radionuclides from solution by the nanocomposite increased with increasing pH, contact time, sorbent dose and reaction temperatures. However, increasing the radionuclide concentration and introducing competitive ions (Na^+, Zn^{2+}, Ce^{3+} and EDTA) reduced ion removal capacity. Increased exposure to gamma radiation also reduced removal capacity with a 20 % loss at 50 kGy and 96 % loss at 150 kGy suggesting a breakdown in the nanocomposite structure at higher radiation levels.

An optimum solution for a strategic biological radionuclide remediation method would be to use a natural organic substance which requires no form of synthetic alteration but still has a

high radionuclide absorbance capacity. As some of the radionuclides which require treatment e.g. ^{137}Cs and ^{60}Co are essential trace elements which play vital biological roles in plants, they can be bio-accumulated in natural processes and therefore be removed from nuclear effluent. The phytoremediation efficiency of a live floating plant water hyacinth (*eichhornia crassipes*) has been examined for ^{137}Cs and ^{60}Co contaminated effluent. [31] High removal rates for ^{60}Co (~100 %) are reported while the highest removal value of ^{137}Cs (~80 %) was observed whilst directly exposed to sunlight and only when in solution with ^{60}Co. This would suggest the bioaccumulation mechanism requires both metals to be present to function which could limit the usability of the plant in effluents containing only ^{137}Cs. ^{60}Co adsorption is reduced by the presence of ^{137}Cs suggesting competitive ion adsorption which could reduce efficiency of removal in multi-radionuclide containing effluent. As with the other reviewed biological methods an increase in radiation reduces uptake capacity of radionuclides with the uptake rate of ^{137}Cs inversely proportional to initial activity. Sunlight exposure is necessary for increased uptake which may limit usability depending on effluent treatment method design. Benefits of using *eichhornia crassipes* specifically are based on its undesirable presence within the natural ecosystem. The water hyacinth stops sunlight reaching submerged plants therefore negatively effecting aquatic biosystems. Repurposing a disruptive natural organism for the remediation of radioactive effluent is both beneficial for the environment and due to its high abundance and cost effectiveness. Due to the biological nature of the treatment method any waste produced could be easily concentrated (perhaps by drying into powder form) therefore reducing the amount of secondary waste.

1.3.6 - Membrane separation

Membranes act as molecular sieves as their membrane pore size allows for the permeation and diffusion of particles. Tuning of the molecular pore size allows for the targeted retention (in the case of nuclear effluent remediation) of radionuclides. Retention and concentration of radionuclides allows for them to be separated from a waste stream and be discarded as radioactive waste. Membrane fouling is a persistent issue associated with membrane separation techniques. Fouling of the membrane leads to reduced removal efficiency and can cause the frequent discontinuation of operational processes for system maintenance. The polymer membranes which are used as the sieving mechanism can also be damaged by operational processes and higher levels of radiation exposure can cause the breakdown in their chemical structure. Therefore, current research is focused on the production of membranes which can deal with harsh operational conditions and exposure to large quantities of radiation whilst improving their selectivity towards target radionuclides. A novel polyvinylidene fluoride (PVDF) membrane has been created by post fabrication tethering of hydrophilic SiO_2 nanoparticles (NPs) and copper ferrocyanide (CuFC) layers onto its membrane surface (Figure 1.6) to improve its Cs removal efficiency from natural surface water. [32] The modified membrane showed high selectivity for the removal of Cs achieving an absorbance capacity of 1440.4 mg m^2 and retained the Cs whilst remaining structurally stable over a wide range of pH values and subjugated to sonicated stress treatments. The membrane also proved capable of being regenerated with H_2O_2 and N_2H_4 with reusability a main advantage over some of the previously mentioned methods reducing both cost and waste. Competitive adsorption is an issue here like other methods with the filter having a reduced rejection rate for Cs in the presence of K^+, Na^+, Ca^{2+} and Mg^{2+} ions. As the Cs ions are

filtered and separated rapidly, the issues seen with other nano-adsorbent materials such as their tendency to aggregate and their lack of reusability are if not eliminated but reduced significantly via this methodology.
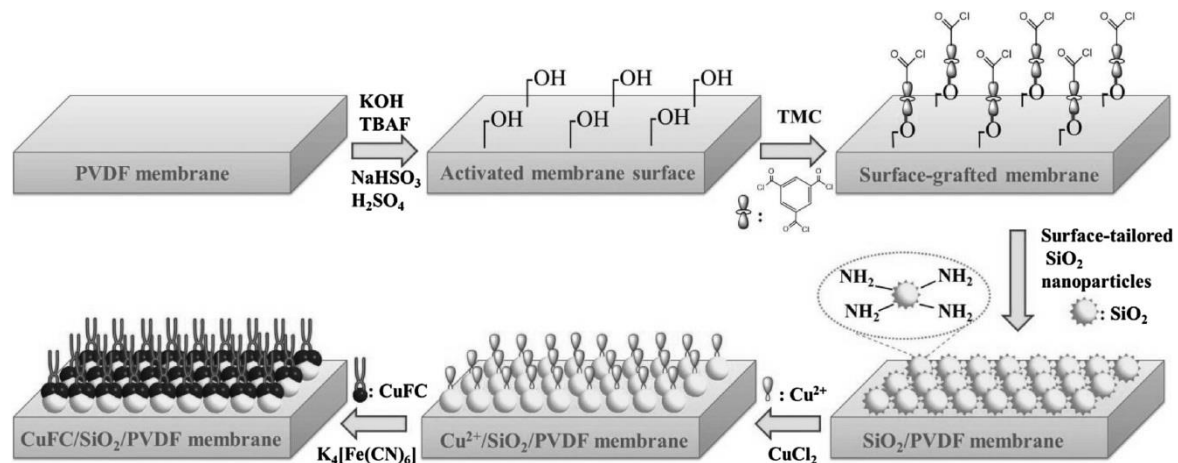
Figure 1.6: Schematic representation for the modification of a PVDF membrane to improve its removal efficiency for Cs. Reproduced from Yu *et al*. [32]

This research shows how the modification of adsorptive materials can be functionalised to improve their selectivity towards target ions whilst demonstrating practical usability for the treatment of radioactive effluent through process stability. Additional or more advantageous modifications to the PVDF membrane would include enhanced membrane permeability and an elimination of the need or a reduction in frequency of the requirement to regenerate the membrane by introducing mechanisms to combat structural degradation. Enhanced anti-fowling properties without reduction in adsorptive performance and ion rejection can be achieved by modifying PVDF with poly (vinyl pyrrolidone) (PVP). [33] PVP of a small molecular size was used to improve membrane pore size and the subsequent cross linking because of the synthesis mechanism improved the membrane hydrophilicity. Pore modification increased membrane flux (allowable flow rate) from 130 L m^{-2} h^{-1} to 170 L m^{-2} h^{-1}. An increase in hydrophilicity improved the contact angle, increasing the contact time of the Cs ions in

solution to the membrane surface. Simulated fowling of the modified membrane showed significantly lower flux reduction compared to an unmodified PVDF membrane with flux recovery rates of 98 % observed for the modified and 46 % for the unmodified membranes. No reduction in Cs ion rejection was seen and the flux recovery ratio after washing was higher in comparison between the modified and unmodified membrane suggesting the modification can be used as a method to both improve membrane survivability and reduce the frequency of cleaning operations. The anti-fouling ability and increased membrane flux of this modification could potentially be used in conjunction with other modifications which improve ion filtration to produce a separation mechanism which has increased ion removal, improved processing ability and requires less frequent cleaning, saving time and reducing cost. The practicalities of introducing membrane technologies into processes should be considered, including factors associated with performance variations with scale up and implementation. The implications of radiation on membrane performance along with removal efficiencies when dealing with effluent containing low concentrations of radionuclide should be known before process implementation to mitigate decreased efficiency or process failure.

Reverse osmosis (RO) is currently extensively used in desalination processes, the treatment of industrial chemical effluent and radioactive effluent. The evaluation of process performances over longer periods of time when membranes are exposed to radiation has been studied at both laboratory and industrial scale in order to establish performance difference when novel organic RO membranes are produced and implemented into process, highlighting how factors which may not be present in the initial laboratory research or are insignificant at small scales, effect membrane performance. [34] The validation of the separation performance for a reverse osmosis membrane (given nomenclature SW30 HR) with both active and inactive Cs showed a similar retention value of 96 %. Scale up to a 2.6

m^2 spiral wound membrane did not reduce retention capacity showing equivalent retentions of 96 % for Cs and 99 % for Sr in comparison to the lab scale membrane. However lower flux values (reduced flow rate and cross flow velocity) resulted in a reduced ability of the membrane to process the radioactive effluent suggesting optimisation of hydrodynamic parameters should be taken into consideration when implementing a membrane in a process dealing with larger volumes of effluent. Aging of the spiral wound membrane via gamma radiation showed limiting effects on permeability and retention, therefore the radiation levels the membrane is likely to be exposed to in a specific process should be taken into account when determining its suitability, durability and effective removal performance within a process over a period of effluent treatment. Design of the membrane including its chemical and physical configuration should be adapted for maximum performance based on learned degradation mechanisms through further scale up research of laboratory scale synthesised membranes. Laboratory scale experiments which describe fouling and scaling mechanisms should also be considered when determining the applicability of a membrane for a decontamination process, as seen in most of the reviewed treatment methods, the components of radioactive effluent such as competitive ions can produce a reduction in treatment performance. It is prudent to evaluate the methods currently employed and novel research completed to produce an effective treatment for radioactive effluent.

1.3.7 – Summary of reviewed technologies for radioactive effluent treatment

As seen in the reviewed literature there are a variety of treatment solutions each with their own advantages and disadvantages. The advantages and disadvantages of the various methods for the treatment of radioactive effluent reviewed above are summarised below in Table 1.2:

Methods	Advantages	Disadvantages
Adsorption and ion exchange	• Practical • Highly efficient • Variety of materials available for targeted removal	• Handling of contaminated products difficult • Reduced efficiency from competitive ions • Slow rate of absorbance • Lack of regeneration capability
Oxidation	• Typically, environmentally friendly • Complete oxidation can be achieved	• Energy intensive (Cost) • Operational practicalities
Precipitation and flocculation	• Relatively cheap • Capability of treating large volumes of effluent with high concentration of radionuclides	• Produces large amounts of secondary radioactive waste
Electrochemical	• Typically, environmentally friendly • Relatively safe operationally	• Costly as energy intensive • Not very efficient with low concentrations of ions
Biological	• Typically, environmentally friendly • Relatively cheap • Ability to regenerate • Low amounts of secondary waste	• Biological components less likely to function at high radiation levels
Membrane separation	• Capability of treating large volumes of effluent • High efficiency removal	• Can be expensive • Membrane fouling • If membrane has organic components may be damaged by radiation

Table 1.2: Advantages and disadvantages of reviewed technologies for the treatment of radioactive effluent

In conclusion, based on the reviewed literature adsorption is an ideal method for the treatment of radioactive effluent. Specific adsorbents can be selected and modified appropriately to produce high adsorbent efficiency with fast adsorbent rates. They can be made with sustainable materials using optimised processes to reduce environmental impact

and secondary wastes. Low cost adsorbent materials which have a variety of potential modification routes will increase the economic viability of using modified adsorbents for radioactive effluent treatment. Selecting and improving adsorbents surface area and chemical characteristics will allow for large volumes of effluent to be treated producing smaller amounts of secondary waste therefore reducing environmental impact, improving nuclear safety, and reducing overall cost. Biological components can be avoided by using alternative modifications which aren't degraded to the same extent during radiation exposure. External sources of energy aren't required for effective adsorption which will reduce overall operational cost.

1.4 - Modified graphene oxide as a radionuclide adsorbent

Graphene oxide (GO) can be obtained from the oxidation of graphite, which when sonicated in a polar solvent yield GO sheets which are a continuous and atomically thin two-dimensional array of carbon atoms that are functionalised with epoxy and hydroxyl groups on the carbon basal plane and carboxyl groups around the edges as shown below in figure 1.7: [35]
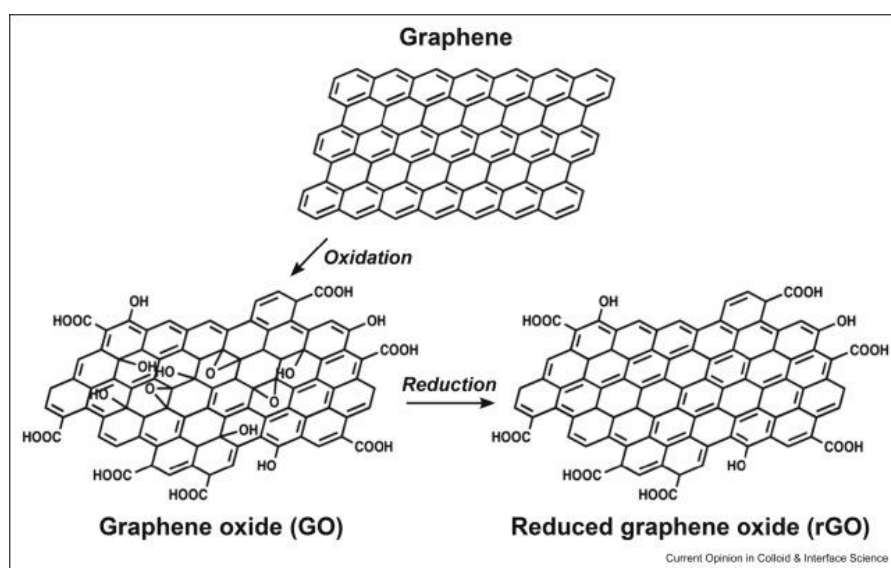
Figure 1.7: Idealised structures of graphene, graphene oxide and reduced graphene oxide. Reproduced from McCoy *et al*. [35]

Studies relating to the potential applications for GO have been conducted in variety of research disciplines because of its unique physicochemical properties such as high surface area, high chemical stability, large pore volume structure and excellent mechanical strength. [36] The interactions of heavy metal ions and radionuclides with GO and GO based materials have been studied under various experimental conditions with results showing high adsorption capacities which can be directly related to GO's large surface area and abundance of functional groups which improve the selective adsorption and concentration of target ions and radionuclides in aqueous solutions. [37] [38] Chemical functionalization of the graphene oxide surface can further enhance its adsorption capabilities were functionalization is defined as a route for the addition of new properties, structures or abilities via the alteration of a material in respect to its surface chemistry. [39] There has been an abundance of research focused on the functionalisation of graphene to improve its adsorbent capacity for radionuclides for the treatment of radioactive effluent and many surface modifications have been developed. [40] [41] [42] A modified graphene oxide adsorbent could be an exceptional treatment method for radioactive effluent based on its highlighted advantageous properties. With reference to the desired characteristics for an ideal method for the treatment of radioactive effluent GO and the functionalised GO derivatives researched display highly efficient adsorption capacities with relatively rapid adsorption rates. Their inherent excellent mechanical strength makes them robust enough to deal with the harshest operational conditions. Continuing research into alternative synthesis methods for GO and its modified analogues combined with lack of requirement for external energy sources to operate will reduce the overall cost of an effluent treatment using GO as an adsorbent. Due to GO's large surface area, large quantities of radioactive effluent will be able to be treated with small

quantities of GO which will reduce the amount of secondary waste produced and the negative impacts on adsorption performance from competitive ions should also be limited. The range of customisability for GO's surface means selective adaptations will provide solutions for individual needs over a variety of processes. Biological adaptations can be avoided with synthetic alternatives chosen for an application e.g. to withstand degradation when exposed to radiation. The ability for regeneration and reusability of GO derivatives has also been shown in most of the reviewed research again reducing cost and waste. Determination of the desired GO functionalisation should be based on the degree to which the surface modification improves the radionuclide adsorption capacity of GO in comparison to other potential surface modifications. Elucidation of radionuclide adsorption mechanisms on functionalised GO surfaces through computational and analytical tools would improve understanding as to which modifications would be best suited for the treatment of radioactive effluent. Computation of theoretical functionalised groups which may not be synthetically plausible could provide insight into which functional groups would provide the best adsorption ability and capacity of radionuclides for GO. Synthetically plausible analogues closely chemically matched to the idealised functionalised groups could then be created and tested in a laboratory to determine how effective they are in improving GO's ability to treat radioactive effluent. Ab Initio molecular dynamic simulations twinned with laboratory based experimental studies have already been completed to determine the adsorption capacity and mechanisms of a range of materials for radionuclides and heavy metal ions. [43] [44] [45] Various analytical techniques can be utilised for characterisation purposes and for experimental validation of the exact surface absorption site for radionuclides and heavy metal ions on the functionalised GO surface. Typical analytical equipment employed for these purposes include Raman and Fourier transform infrared spectroscopy (FTIR) for surface structure and types of

carbon-oxygen bonds, x-ray photoelectron spectroscopy (XPS) for elemental composition, x-ray powder diffraction (XRD) for degree of oxidation and how GO sheets interlay with each other, high resolution transmission electron microscopy (HR-TEM) and scanning transmission electron microscopy (STEM) for surface morphology and solid state NMR for site of adsorption for radionuclide or heavy metal ion on GO surface. [46] [47] [48]

Chapter 2: Theory

2.1 – Overview

Computational chemistry is the use of computers to solve the equations of a theory or model for the properties of a chemical system. Widespread use and rapid growth of computing power has facilitated the increased utilisation of simulation to improve the fundamental understanding of physical systems traditionally determined by theory and experimentation. The accuracy of models produced by theory is tested with experimentation and simulation helps to refine this process. Ultimately, anything which can be measured can be simulated, including properties of energies, chemical structures and the spectra produced from chemical systems. The computational component of this research utilises an open source molecular dynamics package named CP2K. CP2K is a quantum chemistry and solid state physics software package that can perform efficient and accurate atomistic simulations of solid state, liquid, molecular, periodic, material, crystal, and biological systems. This research uses CP2K to perform energy minimisation calculations (geometry optimisation) and ab-initio molecular dynamic simulations. There are various analytical techniques used in this research for material characterisation and for the identification of the surface location of ion adsorption. Thus, follows a comprehensive account of the underlying theories for CP2K and the analytical techniques utilised in this research.

2.2 - General theory for computational chemistry

This section will provide a brief overview of computational chemistry. The reader can find a more in-depth analysis of the theory contained in the references provided.

2.2.1 - The Schrödinger Equation

The wave function of a system may be determined by solving the time-independent Schrödinger equation: [49]

$$\hat{H}\Psi = E\Psi \quad (1)$$

Were $\hat{H}$ is the Hamiltonian operator, Ψ is the wave function and E is the energy level of the system. Exact solutions for many electron systems are impossible to solve therefore an approximation of the solution is used to determine the ground state of the system.

2.2.2 - The Hamiltonian

The Hamiltonian operator corresponds to the total energy of the system: [50]

$$\hat{H} = \hat{T} + \hat{V} \quad (2)$$

Where $\hat{T}$ is the kinetic energy operator and $\hat{V}$ is the potential energy operator.

2.2.3 - The Variation Principle

The variation principle is used to determine the approximate ground state wave functions for a system; the energy of the approximate wave function is given by: [51]

$$E\Phi = \frac{<\Phi|\hat{H}|\Phi>}{<\Phi|\Phi>} \quad (3)$$

The energy of an approximate ground state function is greater than or equal to the exact ground state energy:

$$E\Phi > E0 \quad (4)$$

Were E0 is the exact ground state energy.

For all Φ where Φ is the approximate ground state wave function.

2.2.4 - The Born-Oppenheimer Approximation

The Schrödinger Equation for an arbitrary molecule can't be solved for N > 2 where N is the number of charged particles. However, the wave function for a molecule can be separated into electronic and nuclear components. The mass of a nuclei of an atom is significantly larger than the mass of an electron. Therefore, the nuclei will move incredibly slowly in comparison to electrons. Therefore, an approximation can be made that the positions of the nuclei are fixed relative to the electrons. The kinetic energy of the nuclei is 0. The nuclei can now be described as classic point particles. [52] As the nuclear kinetic energy is now 0 and the nuclear-nuclear repulsion are constant the molecular Hamiltonian is adapted to describe electron kinetic energy, electron nuclear attraction and electron-electron repulsion. An electronic Hamiltonian is derived to obtain an electronic wave function:

$$\hat{H}e = -\sum_i \frac{1}{2}\nabla_i^2 - \sum_{iA} \frac{Z_A}{r_{iA}} + \sum_{i<j} \frac{1}{r_{ij}} \ (5)$$

Were i is the electron, ∇_i^2 is the Laplacian operator, A represents the nucleus and Z is charge.

2.2.5 - Basis Sets

Basis sets are sets of basis functions which mathematically describe the molecular orbitals of a system. A linear combination of atomic orbital (LCAO) are used to describe the molecular orbitals for molecular calculations, these are written as: [53]

$$\Phi(r) = \sum_\alpha C_{\alpha i}\, \varphi_\alpha \ (6)$$

Where Φ is the molecular orbital, φ_α are the atomic orbitals and $C_{\alpha i}$ are the expansion coefficients used to determine the minimum energy molecular orbitals. (In CP2K, molecular

optimised basis sets (DZVP-MOLOPT-GTH) are used). These basis sets are optimised on atomic configurations and molecular calculations.

2.2.6 – Pseudopotentials

Pseudopotentials are used to reduce the size of basis sets which help reduce calculation time. Core electrons are eliminated therefore less orbitals are required to be calculated reducing the number of degrees of freedom. Pseudopotentials utilised in CP2K are based on frozen core approximation and atomic calculations. Inactive electronic degrees of freedom in the Hamiltonian are replaced by an effective potential, one may do this as core electrons are chemically inert and do not overlap with different atoms; the wave functions utilised are from atomic reference calculations. [54]

2.2.7 - Hartree product

The Hartree product is an initial step to describe the wave function of a set of electrons based on the premise that electrons do not repel each other. Thus, the electronic Hamiltonian can be written as: [55]

$$\widehat{H}e = \sum_{i=1}^{N} \hat{h}(i) \ (7)$$

Were $\hat{h}(i)$ is an electron energy operator defined as:

$$\hat{h}(i) = -\frac{1}{2}\nabla_i^2 - \sum_{A=1}^{M} \frac{Z_A}{r_{iA}} \ (8)$$

For each individual electron there is a spin orbital $\chi(\vec{\chi}i)$ which is an Eigen function of $\hat{h}(i)$:

$$\hat{h}(i)\chi(\vec{\chi}i) = \in \chi(\vec{\chi}i) \ (9)$$

Were ∈ is the orbital energy. The wave function can be written as a product of all the individual electrons:

$$\Psi(\vec{\chi}_1, \vec{\chi}_2, \ldots, \vec{\chi}_n) = \chi_1(\vec{\chi}_1)\chi_2(\vec{\chi}_2) \ldots X_N(\vec{X}_N) \quad (10)$$

Therefore, the electrons are independent and uncorrelated as there is no interaction between them, and their motions do not affect each other. The problem with the Hartree product is that the electrons are indistinguishable therefore the Hartree product needs to be rewritten in a format to satisfy the anti-symmetry principle. [56]

2.2.8 - Slater Determinants

Slater determinants are for the systematic representation of anti-symmetric wave functions. The rows represent the individual electronic coordinates and the columns represent the individual spin orbitals; formalising to an arbitrary number of electrons: [57]

$$\Psi(1,2,\ldots,N) = \frac{1}{\sqrt{N!}} \begin{bmatrix} \chi_1(1) & \chi_2(1) & \cdots & \chi_N(1) \\ \chi_1(2) & \chi_2(2) & \cdots & \chi_N(2) \\ \vdots & \vdots & \ddots & \vdots \\ \chi_1(N) & \chi_2(N) & \cdots & \chi_N(N) \end{bmatrix} \quad (11)$$

Where the normalisation constant $\frac{1}{\sqrt{N!}}$ describes all the different permutations of $1 \rightarrow N$. This is consistent with the Pauli Exclusion Principle i.e. in any determinate where two columns or rows are the same ($\Psi = 0$).

2.2.9 - Hartree Fock approximation

The electronic Hamiltonian describes operators for one and two electron coordinates:

$$\hat{H}e = \sum_{i=1}^{N} -\frac{1}{2}\nabla_i^2 - \sum_{i=1}^{N}\sum_{A=1}^{M} \frac{Z_A}{r_{iA}} + \sum_{i=1}^{N}\sum_{j=i+1}^{N} \frac{1}{r_{ij}} \quad (12)$$

The one electron operators are separable operators as they can be factored into equation 7. The two-electron operator is non separable as it cannot be factored into an expression (many body problem) therefore an approximate is used and an average is taken over a 'mean field' of other electrons: [58]

$$\hat{f}(i) = \hat{h}(i) + \hat{v}^{HF}(i) \ (13)$$

Where $\hat{f}(i)$ is the Fock operator, $\hat{h}$ is the core Hamiltonian and $\hat{v}^{HF}$ is the mean field operator for electron (i). The Fock operator acts on a spin orbital in a system and yields an orbital energy acting on the spin orbital:

$$f(i)\chi_1(X_1) = \epsilon_i \ \chi_1(X_1) (14)$$

This is a pseudo-eigenvalue problem and the electrons are averaged over the total electron density and are no longer explicitly described. The Hatree Fock energy (ground state determinate energy) is given as:

$$E_0 = \sum_i h_i + \sum_{i<j} J_{ij} - K_{ij} \ (15)$$

Where h_i is the core Hamiltonian Integral (comprised of kinetic energy and nuclear attraction), J_{ij} is the coulomb operator and K_{ij} is the exchange operator. The Hartree Fock energy is minimised until self-consistency between the energies of the initial and generated molecular orbitals are the same to within a tolerance value. [59]

2.2.10 - Density functional theory (DFT)

CP2K uses a Gaussian and / augmented plane wave approach to DFT. DFT is a method of obtaining the ground state electron structure of a many body system by deriving the position

of atomic nuclei and the ground state energy from its electronic density rather than its wave function.

2.3 – Implementation of DFT to CP2K

The following section will expand on how the fundamental principles of computational chemistry discussed are implemented into CP2K. All references for the implementation can be found here: https://manual.cp2k.org/cp2k-6_1-branch/references.html

2.3.1 - Gaussian and plane wave methods (GPW)

Kohn-Sham (KS) DFT is comprised of three main theorems: The Hohenberg-Kohn theorem (existence theorem), Hohenberg-Kohn theorem II (variation principle) and the Kohn-Sham theorem which is a non-intercalating reference system which gives an orbital picture. [60] This is a method which works with orbitals and has a variation principle which should be exact. The variation principle component of KS-DFT includes the minimum energy functional of orbitals:

$$\text{Min } E(\{\Phi_i\}) \text{ (16)}$$

Were the orbitals must fulfil two constraints, firstly the orthogonality constraint:

$$\int \Phi_i(r)\Phi_j(r)dr = \delta_{ij} \text{ (17)}$$

And secondly that the total number of electrons is defined:

$$\int p(r)dr = N \text{ (18)}$$

The energy functional is dependent on the orbitals and its mathematical form accounts for the kinetic energy, external energy, classical coulomb energy, and exchange correlation functional:

$$E(\{\Phi_i\}) = -\sum_i \frac{f_i}{2} \int \Phi_i \nabla_i \Phi_i dr + \int V_{ext}(r)p(r)dr \quad (19)$$

$$+\frac{1}{2} \int \int \frac{p(r)p(r)'}{|r-r'|} drdr' + E_{XC}[p] \quad (20)$$

$$p(r) = \sum_i f_i |\Phi_i(r)|^2 \quad (21)$$

Were equation (19) is a combination of kinetic energy (E_{kin}) and the energy of electron-nuclei interaction (E_{ext}); the external energy is the interaction of the electron density with the nuclei and is implemented as a pseudopotential in the GPW method:

$$E_{kin} = -\frac{1}{2} \sum_i f_i (\Phi_i | \nabla^2 | \Phi_i|) \quad (22)$$

$$E_{ext} = \int V_{ext}(r)_p(r)dr \quad (23)$$

Equation (20) is a combination of the Hartree energy (E_H) and non-classical coulomb exchange energy (E_{xc}):

$$E_H = \int \int \frac{\rho(r)\rho(r')}{|r-r'|} dr'dr \quad (24)$$

$$E_{xc} = \int F[p]dr \quad (25)$$

And equation (21) includes both the orbital orthogonality (26) and electron number constraints given as a function of the orbitals (27):

$$\left(\Phi_i \middle| \Phi_j\right) = \delta_{ij} \quad (26)$$

$$\sum_i f_i\left(\Phi_i \middle| \Phi_j\right) = N \quad (27)$$

The implementation of KS-DFT is achieved by:

Using a LCAO (φ_α):

$$\Phi_{i(r)} = \sum_\alpha C_{\alpha i}\varphi_\alpha(r) \quad (28)$$

The overlap for the non-orthogonal basis functions:

$$S_{\alpha\beta} = \int dr\varphi_\alpha^{Ж}(r)\varphi_\beta(r) \quad (29)$$

The orthogonality constraint given as a function of the coefficient C:

$$\int dr\Phi_i^{Ж}(r)\Phi_j(r) = \sum_{\alpha\beta} C_{\alpha i}^{Ж}S_{\alpha\beta}C_{\beta j} = \delta_{ij} \quad (30)$$

Density matrix given as a function of the coefficient C:

$$p_{\alpha\beta} = \sum_i f_i\, C_{\alpha i}C_{\beta i}^{Ж} \quad (31)$$

The density can be written with the density matrix:

$$p(r) = \sum_{\alpha\beta} P_{\alpha\beta}\varphi_\alpha(r)\varphi_\beta^{Ж}(r) \quad (32)$$

The energy minimisation goes over the coefficient C:

$$E = \text{Min}_C[E_{kin}(c) + E_{ext}(\rho) + E_H(\rho) + E_{xc}(\rho)] \quad (33)$$

Minimisation over the coefficient C under the constraint of orthogonality given in equation (30) using a basis set representation changes the problem from analysis to linear algebra. The basis-functions used are Gaussian functions which are in the form of a Gaussian:

$$\varphi(r) = r^l \, Y_{lm}(\hat{r}) \exp\left[-\alpha(r - A)^2\right] \quad (34)$$

Were the exponent is centred at an atomic function which is multiplied by a spherical harmonic function; The Gauss functions are contracted (Linear combination of the Gauss functions are two basis functions):

$$x(r) = \sum_K d_K \varphi_K(r) \quad (35)$$

Were d_K are the contraction coefficients with fixed exponents.

The advantage of using Gaussian type orbitals include: [60]

- They are atomic orbital like therefore the basis set is compact

- Analytical integration over Gaussian operators are possible which are easy to perform

- They are optimal for regular grids (The Fourier transform of a Gaussian is a Gaussian function) i.e. numerical integration of a Gaussian has an exponential convergence

Disadvantages include: [61]

- Non-orthogonal basis, so all energy expressions contain overlap matrixes and inverse overlap matrixes

- Basis set superposition error (BSSE) which arise from calculations of interaction energies and adsorption energies with small basis sets

- Molecules and solids require different basis sets

In summary, calculation of KS-DFT with GTO basis sets requires analytical integration of kinetic energy, external potential, coulomb and overlap integrals and numerical integration using regular grids of XC energy and integrals. Analytical integration of coulomb four centre electron repulsion integrals (ERI) is very CPU and memory intensive.

2.3.2 - Hartree Energy

To avoid calculation of ERI, all the electrostatic terms are combined including electron-electron interaction (36), electron-core interaction (37) and ion-ion interaction (38):

$$E_{coulomb} = \left[\frac{1}{2} \iint \frac{p(r)p(r')}{|r - r'|} drdr' \right] \ (36)$$

$$- \sum_A Z_A \int \frac{p(r)}{|r - R_A|} dr \ (37)$$

$$+ \sum_{A<B} \frac{Z_A Z_B}{|R_A - R_B|} \ (38)$$

The total charge density of the system is the electronic charge and Gaussian atomic charges; not as point charges but as a Gaussian distribution. Each atom has a positive charge with a defined width (α):

$$\rho_{tot}(r) = \rho_e(r) + \sum_A \rho_A(r) \ (39)$$

$$\rho_A(r) = Z_A \left(\frac{\alpha}{\pi} \right)^{\frac{3}{2}} \exp \left(-\alpha(r - A)^2 \right) (40)$$

The Hartree term now incorporates the total charge density however, several correction terms are required because of the incorporation:

$$E_{coulomb} = \frac{1}{2} \iint \frac{p_{tot}(r)p_{tot}(r')}{|r - r'|} drdr' \ (41)$$

A correction for the interaction of the electrons with nuclear charge as there is no longer a point charge hence complementary error function:

$$-\sum_A Z_A \int \frac{\text{erfc}\left(\alpha(r - R_A)\right)}{|r - R_A|} p_e(r)dr \ (42)$$

A pair correction for overlapping Gaussian orbitals:

$$+\sum_{A<B} E_{pair}(R_A - R_B) \ (43)$$

An atomic self-interaction correction as the Gaussian distribution will interact with itself in the long-range interaction (Hartree):

$$-\sum_A E_{self} \ (44)$$

2.3.3 - Periodic boundary conditions (PBC)

PBC's are used to reduce the number of calculations required in the condensed phase as an enormous amount of bulk calculations are required without PBC's to achieve reasonable results. Therefore, elimination of surface effects makes the calculations more efficient. [62] CP2K implementation uses gamma point simulation to avoid Brillouin zone sampling (by integration of Brillouin zone by single point integration) and K point sampling. With K points 0, 0, and 0:

$$(\alpha|\vartheta|\beta) \rightarrow \sum_L \left(\alpha(0)|\vartheta|\beta(L)\right) \ (45)$$

2.3.4 - Plane Waves (PW)

PW's are another basis set of PBC's, the functions are orthogonal and independent of atomic positions and are defined as: [63]

$$\rho(r) = \frac{1}{\sqrt{\Omega}} \exp[iG.r] \ (46)$$

Definition of PW's and therefore PBC's are done by defining a box matrix which will be the computational box given by three vectors:

Box matrix: $h = [a_1, a_2, a_3]$ (direct lattice)

The box volume Ω is the determinate h: $\Omega = \det h$

Direct lattice vectors can be defined by integers I, J and K:

$$L = i.a_1 + j.a_2 + k.a_3$$

The reciprocal lattice is the inverse of the h matrix (transpose) with (b) vectors which are orthogonal duals to the (a) vectors:

$$2\pi(h^t)^{-1} = [b_1, b_2, b_3] \ (47)$$

$$bi.aj = 2\pi\delta ij \ (48)$$

The reciprocal lattice vectors which are used in the plane waves are integer multiples of the b vector: $G = i.b_1 + j.b_2 + k.b_3$. The plane wave can therefore be defined by the three indices i, j and k. In summary, the plane waves are now periodic with respect to box h, they are orthonormal (integration over the box with two G values gives 0) and are complete with an infinite number of G factors:

$$\Psi(r) = \Psi(r + L) = \frac{1}{\sqrt{\Omega}} \sum_G \Psi(G) \exp[iG.r] \ (49)$$

However, a cut off is used as opposed to an infinite number of plane waves and is defined by the kinetic energy of a plane wave:

$$\frac{1}{2}G^2 \leq E_{cut} \quad (50)$$

Where the cut off (E_{cut}) is defined as the inclusion of all plane waves with kinetic energy less than the cut off energy. Regular grids in reciprocal space can be defined in real space using fast Fourier transform (N_{log} Compared to N^2 operations).

2.3.5 - Pseudopotential implementation

- An atomic calculation is performed

- $\Phi_i^v(r)$ and $\in_i$ (atomic and electron reference state)

- Conversion of the wave function into its pseudo form $\Phi_i^v \rightarrow \Phi_i^{ps}$

Potential is calculated from the solution of the atomic problem:

$$\left(T + V_i(r)\right)\Phi_i^{PS}(r) = \in_i \Phi_i^{PS}(r) \quad (51)$$

The pseudopotential is then calculated by subtracting the full potential from the Hartree and exchange correlation potential:

$$V_i^{PS}(r) = V_i(r) - V_H\left(n_{ps}\right) - V_{XC}\left(n_{ps}\right) \quad (52)$$

For accuracy semi-localised pseudopotentials are used which depend on the L quantum number i.e. different pseudopotentials for S functions, P functions etc:

$$V^{PS}(r, r') = \sum_{L=0}^{\infty} V_L^{PS}(r)|Y_L\rangle\langle Y_L| \quad (53)$$

Implementation uses both a local pseudopotential ($V_{loc}^{PS}(r)$) and non-local pseudopotential ($\Delta V_L^{PS}(r)$):

$$V^{PS}(r, r') = V_{loc}^{PS}(r) + \sum_{L=0}^{Lmax} \Delta V_L^{PS}(r)|Y_L\rangle\langle Y_L| \quad (54)$$

Implemented in CP2K as fully non-local form allowing for analytical integration and fast Fourier transforms:

$$V_{pp}(r) = V_{loc}(r) + \sum_{L} \sum_{ij} |P_i^L\rangle h_{ij}^L \langle P_j^L| \quad (55)$$

With Gaussian form of the localised and non-localised parts where $\bar{r} = \frac{r}{rc}$:

$$V_{loc}(r) = -\frac{Z_{ion}}{r} erf\left[\frac{\bar{r}}{\sqrt{2}}\right] + exp\left[-\frac{\bar{r}^2}{2}\right] [C_1 + C_2\bar{r}^2 + C_3\bar{r}^3 + C_4\bar{r}^4] \quad (56)$$

$$P_L^i(r) = N_{iL}(r_l) exp\left[-\frac{r^2}{2r_l^2}\right] \quad (57)$$

2.3.6 - Ab initio molecular dynamics (AIMD)

In AIMD Newton's equations of motion are solved with a classical system of particles which interact with forces. Newton's equation of motion for a set of classical point particles in a potential is given as: [64]

$$M_I\ddot{R}_I = -\frac{dV(R)}{dR_I} \quad (58)$$

Mass times by acceleration is equal to force when force is derived from an electronic structure calculation. The total energy is a constant of motion. The equation of motion for a given number of particles (N) in a volume (V) generates a micro canonical ensemble. The total energy equals the kinetic energy plus the potential energy, kinetic energy is related to temperature and is calculated from the velocities of the atoms in the system: [65]

$$T(\dot{R}) = \sum_{I=1}^{N} \frac{M_I}{2}\dot{R}^2 \quad (59)$$

Potential energy is the total energy derived from the electronic structure calculation; the total energy can be used as an indication for the numerical accuracy of the simulation (total energy is a constant of motion). The Lagrange equation is implemented in CP2K as an equivalent to Newton's equation of motion for a Hamiltonian system as it is equivalent in Cartesian coordinates but is more general and adaptable. The Lagrangian is kinetic energy minus potential energy:

$$\mathcal{L}(R, \dot{R}) = T(\dot{R}) - V(R) \quad (60)$$

(Hamiltonian kinetic energy + potential)

$$\frac{d}{dt}\frac{\partial \mathcal{L}}{\partial \dot{R}} = \frac{\partial \mathcal{L}}{\partial R} \quad (61)$$

Integration of the equations of motion (differential equations) from a start time and end time (discrete time intervals) gives the trajectory of the particles in a system, computation of these discrete time intervals is completed using time steps in the general format: (X = R or V) $X(t) \rightarrow X(t + T) \rightarrow X(t + 2T) \rightarrow$ etc. The velocity verlet algorithm is used to identify the position of a particle based on the velocity of the forces at a given time step, in summary: [66]

$$R(t + T) = R(t) + TV(t) + \frac{T^2}{2M}f(t) \quad (62)$$

$$V(t + T) = V(t) + \frac{T}{2M}[f(t) + f(t + T)] \quad (63)$$

2.3.7 - Born Oppenheimer Molecular Dynamics

In each time step an electronic structure calculation is solved using the Born Oppenheimer approximation. [67] The SCF problem is solved by minimisation of the KS energy function and the orthogonality constraints which gives the potential:

$$V(R) = \min_\Phi \left[E_{KS}(\{\Phi(r)\}; R) + \text{const.} \right] \ (64)$$

The forces are calculated by taking the derivative of the KS energy with respect to the force

position assuming convergence of the wave function:

$$f_{KS}(R) = \frac{d_{\min_\Phi} E_{KS}(\{\Phi(r)\}, R)}{dR} \ (65)$$

2.3.8 - Gaussian Augmented Plane Waves (GAPW)

Plane waves are used for condensed matter, extended basis sets with periodic boundary

conditions. Gaussian type orbitals are localised basis sets centred at atomic positions. [68] A

mixed method is utilised in CP2K were the expansion is made in GTO and for certain

calculations e.g. Poisson equations, plane waves are used to describe the density in reciprocal

space as it is more computationally efficient to calculate the term in this way. Therefore, a

mixed GPW method is used with an auxiliary basis set to represent density. GAPW is a method

of separating the contribution of the two methods of GTO and PW but does not describe all

terms i.e. separated into "Hard" (high density fluctuation $\therefore$ GTO) and "soft" (low density

fluctuation $\therefore$ PW). Core electrons are defined explicitly at the interspatial regions between

hard and soft borders with the density calculations partitioned to avoid double counting. Hard

and soft densities are represented across the entire space and distinguished mathematically.

This is visualised below using formaldehyde as an example:
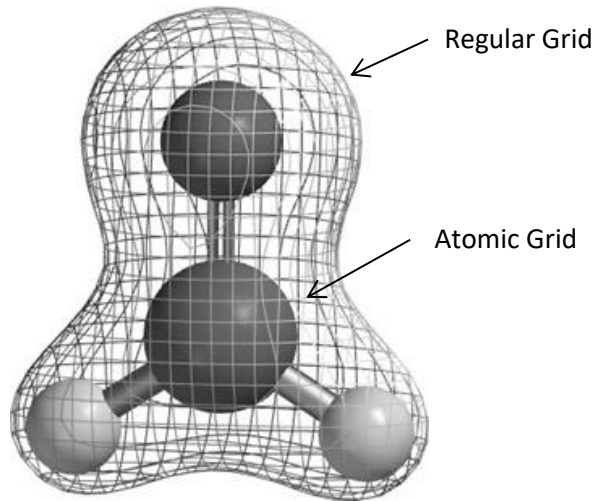
Figure 2.1: Visualisation of hard and soft densities using formaldehyde as an example. [69]

2.4 - Analytical and Computational Techniques

The following section will briefly outline the theory behind the function of the analytical techniques employed in this research for material characterisation, calculation of ion adsorption capacity and elucidation of surface adsorption location. The software utilised for the creation, execution and visualisation of simulations is also listed.

2.4.1 – FTIR Spectroscopy

Fourier transform is a mathematical method for decomposing a function of time (in this application an electronic signal) into its constituent frequencies: [70]

$$f(x) = \int_{-\infty}^{\infty} F(\sigma)e^{+i2\pi\sigma x}d\sigma \equiv \tilde{F}(\sigma) \ (66)$$

IR Spectroscopy studies the interaction between infrared radiation and matter. Infrared radiation is electromagnetic radiation with a longer wavelength than visible light and therefore has less energy and a smaller wavenumber. Infrared light interacts with matter by passing through sample material and dependent on its energy can trigger the vibration of specific molecular bonds (absorption). [71] Any energy absorbed by a molecule will be missing

from the original IR beam. IR light produced from a source after either being reflected or absorbed through a sample will be transmitted and can be captured by a detector resulting in the production of an electronic signal. FTIR utilises an interferometer which directs an IR beam to a beam splitter. The beam is split and directed to a fixed and moving mirror. The IR beams are reflected to the beam splitter, recombined (causing interference) and directed at sample material. [72] Using this method the spectral information of all wavelengths is acquired simultaneously allowing the detector to produce a signal of light intensity relative to mirror position. A sample spectrum is produced by removing environmental influences by creating spectra without a sample present (blank) and the raw signal is mathematically Fourier transformed into a classical IR plot of light intensity versus wavenumber yielding a reference spectrum. The procedure is repeated with a sample present producing a sample spectrum. Combination of the two spectra by dividing the sample spectrum by the reference spectrum produces a transmission spectrum, for example:
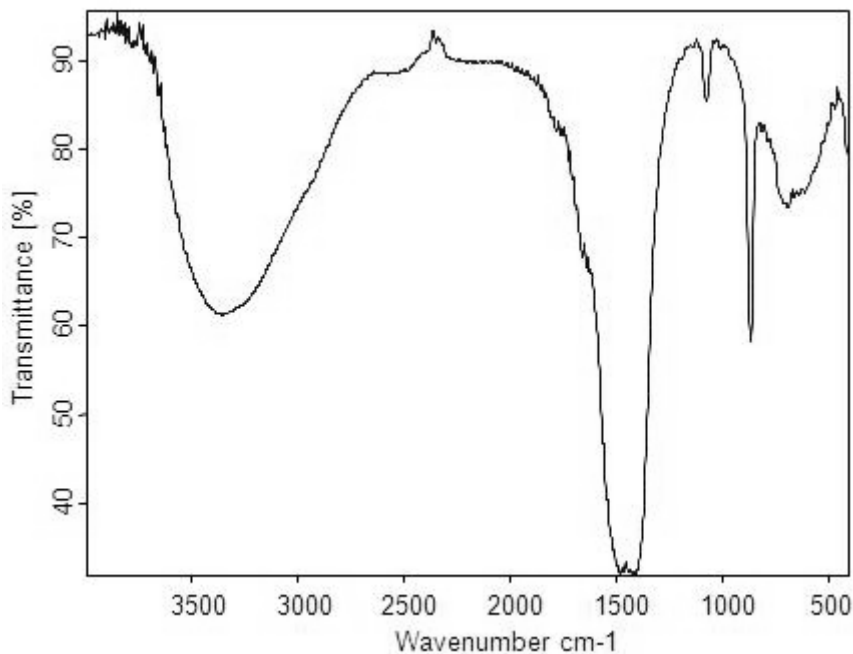
Figure 2.2: Example FTIR Spectrum. Reproduced from Birkner *et al.* [73]

The FTIR spectrum can be used to characterise material properties as absorption wavenumbers correspond to functional groups:

Absorbance (cm^{-1})	Type of vibration
1020-1310	C-O-C
1450-1600	C=C (Aromatic)
1550-1870	C=O
2000-2500	C≡N
3200-4000	O-H

Table 2.1: Example of IR vibration specific wavelength numbers. [74]

2.4.2 - Raman Spectroscopy

When a sample is exposed to monochromatic light in the visible region of the electromagnetic spectrum most of the light will be transmitted through the sample, a small proportion will be absorbed, and some will be scattered in all directions. The scattered light may be observed at a right angle to the incident beam. If the scattered light has the same frequency to the incident light frequency the scattering is referred to as Rayleigh scattering. However approximately 1% of the total scattered light occurs at frequencies different from the incident frequency, this is known as Raman scattering. [75] Raman scattering is a two-photon process. As electrons have different vibrational levels, they are defined by specific energy differences. An incident monochromatic light will interact with an electron in a sample and the electron will absorb energy from the incident photon and will move to a higher virtual state of energy. The energy transferred can be characterised:

$$\Delta E = h\nu = h\frac{c}{\lambda} = hc\tilde{\nu} \ (67)$$

Were ΔE is the difference in energy between two quantised states, h is Planks' constant and c is the velocity of light. Thus $\tilde{\nu}$ is directly proportional to energy transition. [76] Following energy transfer, the electron will move to a lower energy level by losing energy and will emit

a photon. The frequency of the photon is dependent on the quantity of energy lost by the electron as it reduces its energy level. A photon produced by an electron that does not return to its previous energy state after excitation will produce Raman scattering. If the final energy of the electron is less than the incident photon this will produce stokes line. If the frequency of the emitted photon is greater than the frequency of the incident photon this will produce anti-stokes line. [77] Raman spectra will yield a molecular fingerprint. A typical Raman spectrum (Figure 2.3) and example vibrational Raman shift bands (Table 2.2) are shown below:
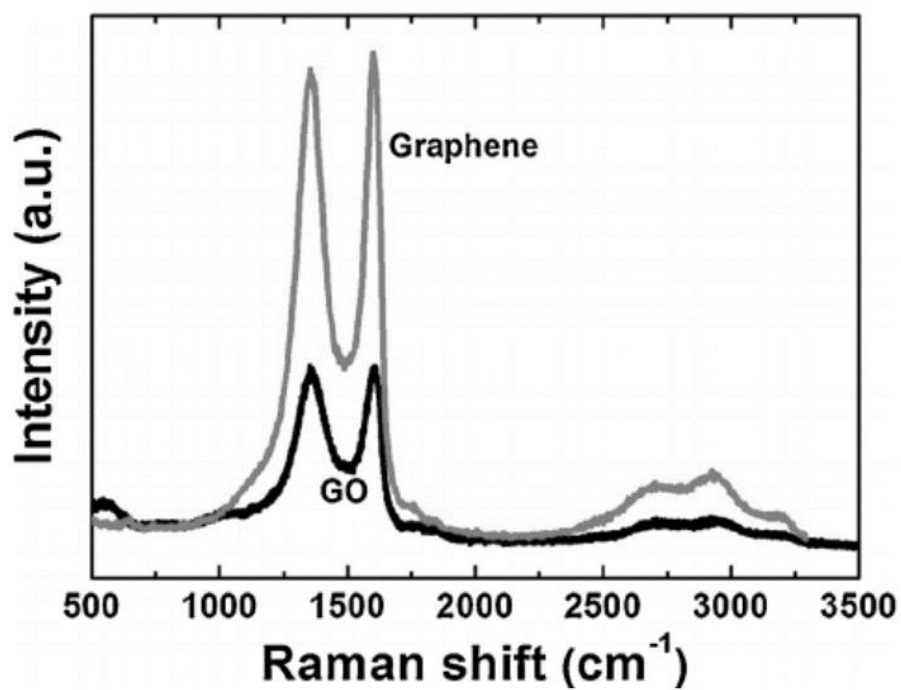
Figure 2.3: Raman spectrum of graphene oxide and graphene. Reproduced from Tuz-Johra *et al*. [78]

Raman Shift (cm^{-1})	Vibrational Bond
580-704	C-S
1730-1740	C=O
2245-2256	C≡N
2560-2590	S-H
3635-3645	O-H

Table 2.2: Example of Raman shifts corresponding to vibrational bonds [79]

2.4.3 – Raman Spectrum of Graphene, GO and RGO

The Raman spectrum of graphene can be explained through the interpretation of its electronic structure. The major peaks in graphene are shown at Raman shifts of approximately 1340 cm^{-1} (D peak) which is a defect activated peak, 1580 cm^{-1} (G Peak) which is a photon emission that corresponds to a high frequency photon and 2700 cm^{-1} (2D Peak) which is the overtone of the D peak although a defect is not required for production. A typical graphene spectrum with and without defects is shown below:
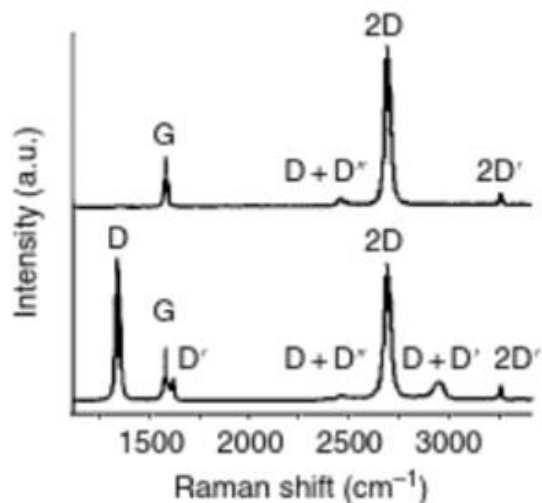
Figure 2.4: Raman Spectrum for Graphene (top) and with defects (bottom). Reproduced from Dimiev *et al*. [80]

The Raman spectrum of graphene changes with the introduction of defects to its structure. These defects include carbon framework disorder, misarranged carbon lattice atoms and missing or substituted atoms. The D peak evolution can be attributed to chemical functionalisation of Sp^2 carbon producing Sp^3 Carbon for GO. The D peak in RGO originates from structural defects within its carbon framework (removal of functional groups yields vacancies and rearranged carbon framework). A typical GO and RGO spectrum are shown below:
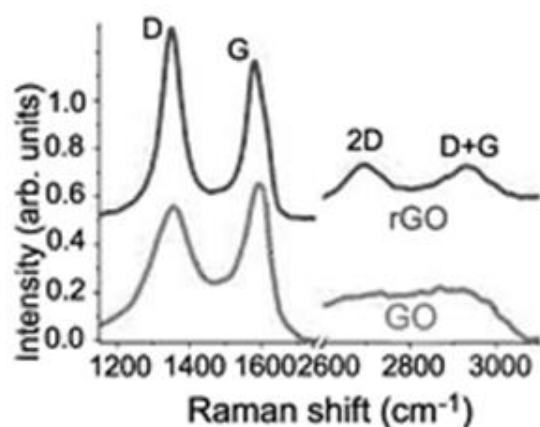
Figure 2.5: Raman Spectrum for GO (bottom) and RGO (top). Reproduced from Wu *et al*. [81]

2.4.4 - Scanning electron microscopy (SEM)

The Main components of an SEM include the column for electron beam generation, sample chamber, vacuum pump, monitor and control panels as illustrated below:
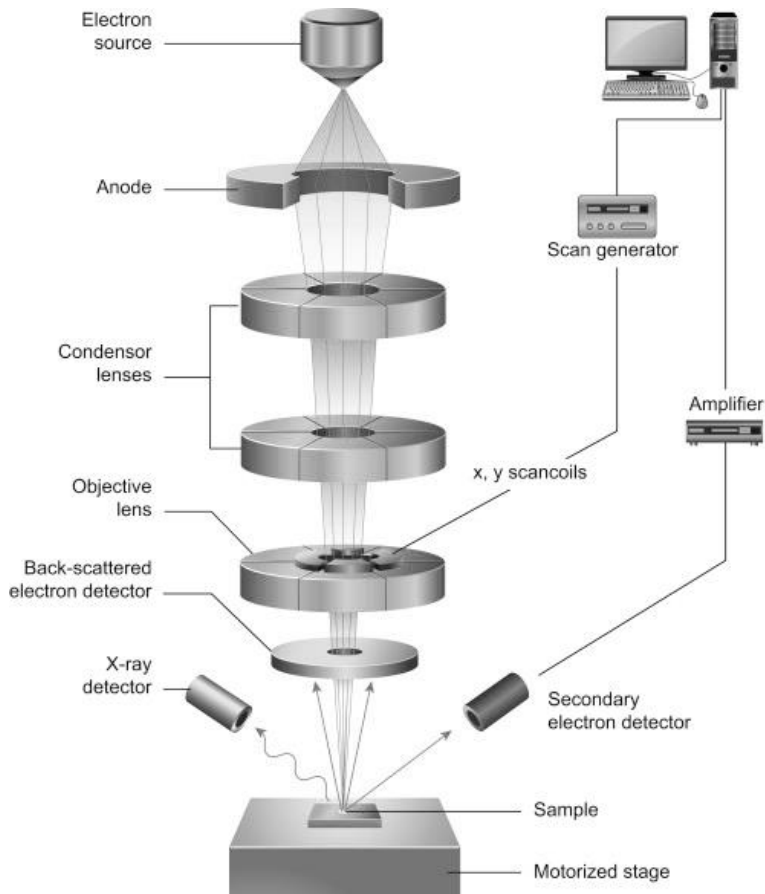
Figure 2.6: Simplified schematic of a scanning electron microscope. Reproduced from Inkson *et al*. [82]

The sample chamber is vented prior to analysis for pressure equalization. An electron beam is generated via a thermionic cathode (typically tungsten wire). Heated by an electrical current it will emit electrons into the vacuum where there is also an anode present. The strong electrical field between the cathode and anode accelerates the primary electrons downwards towards the sample. [83] An electromagnetic lens focuses the electron beam on the sample surface. These primary electrons knock out electrons from the sample material producing secondary electrons. A secondary electron detector will detect these secondary electrons emitted by the sample and deflected secondary electrons via an electromagnet. The deflected secondary electrons are attracted to a positively biased grid component of the secondary

electron detector; this allows for the generation of a magnified image of the sample by amplification and display of the signal on the monitor. [84]

2.4.5 - Energy Dispersive X-ray Spectrometry (EDS)

In EDS a sample is bombarded with electrons and excitation of the sample via a focused electron beam results in the emission of x-rays. The individual x-rays are collected by an x-ray detector and converted into a proportional electrical voltage. This allows for elemental analysis as the x-rays are characteristic of the components which are excited in the sample. Generated electrons are focused and accelerated at a sample. These electrons remove electrons from orbitals which are closer to the nucleus of atoms in the sample. The emitted electron is known as a secondary electron and the atom is now unstable. To stabilise, electrons from higher orbitals replace the removed electrons and, in the process, emit energy in the form of x-rays. [85] The x-ray energy is dependent on the difference in the energy between the orbitals. The x-ray energy from a specific element depends on which orbital lost an electron and which orbital the electron which replaced the secondary electron came from. Nomenclature of the electron 'shells' proceeds from the inner shell K, L, M, N, O, P and Q. Emission energy is denoted by the shell to which an electron is given, if from the closest shell then α, if from two shells away then β [86] e.g. electron moves from N to M shell then the transfer is denoted $M\alpha$. Ionisation energy is lower moving further away from the nucleus therefore $K\beta$ and $K\alpha$ has the greatest energy release which produce the strongest signals. Emission energies for specific elements are known through research. Experiential parameters which determine one's ability to characterise a samples elemental composition include:

- Choosing an appropriate beam energy for the primary electrons (an adequate number of x-rays need to be produced)

- Determination of detection limit (typically elemental limits are 0.1% by weight)

- Use correct working distance (detector should be in direct path with x-rays)

An example EDS spectrum is shown below:
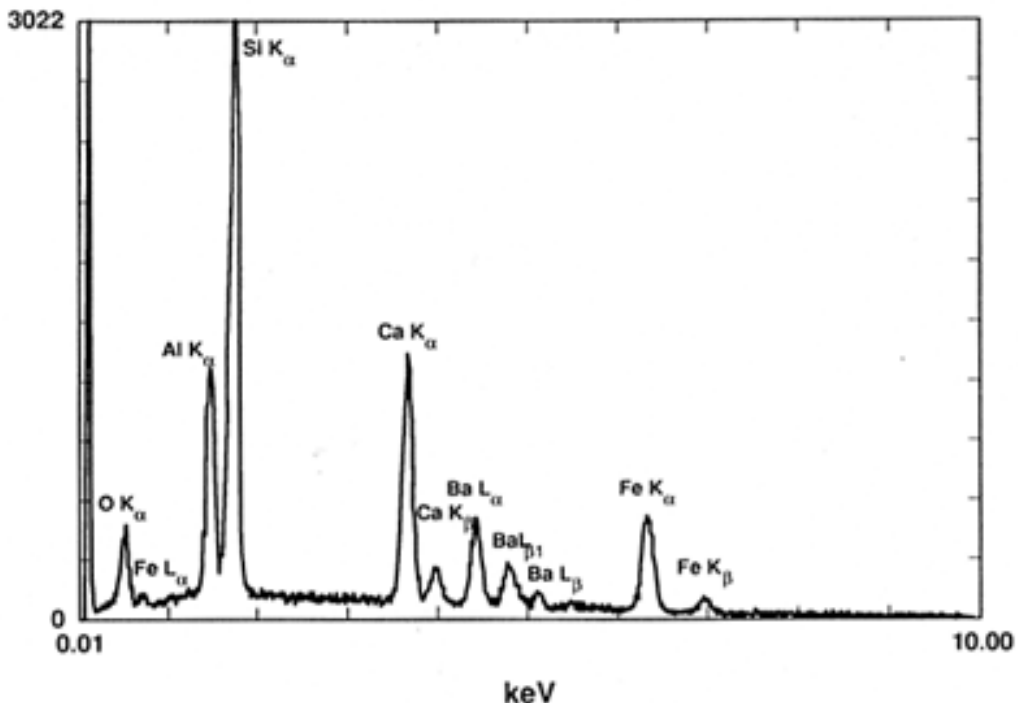
Figure 2.7: Example EDS Spectrum showing multiple elements and their emission energies. Reproduced from Inkson *et al.* [87]

2.4.6 - Inductively Coupled Plasma (ICP)

ICP is a multi-elemental analytical technique and provides efficient and comprehensive elemental compositional characterisation and thus is used for the detection of trace elements (ppm - ppb range). The analytical equipment generally consists of a sampler, waste line, nebuliser, and plasma gas flow tube (Argon), ICP torch, axial (for low concentration) and radial (for higher concentrations) detectors. A schematic of a typical ICP-OES is shown below:
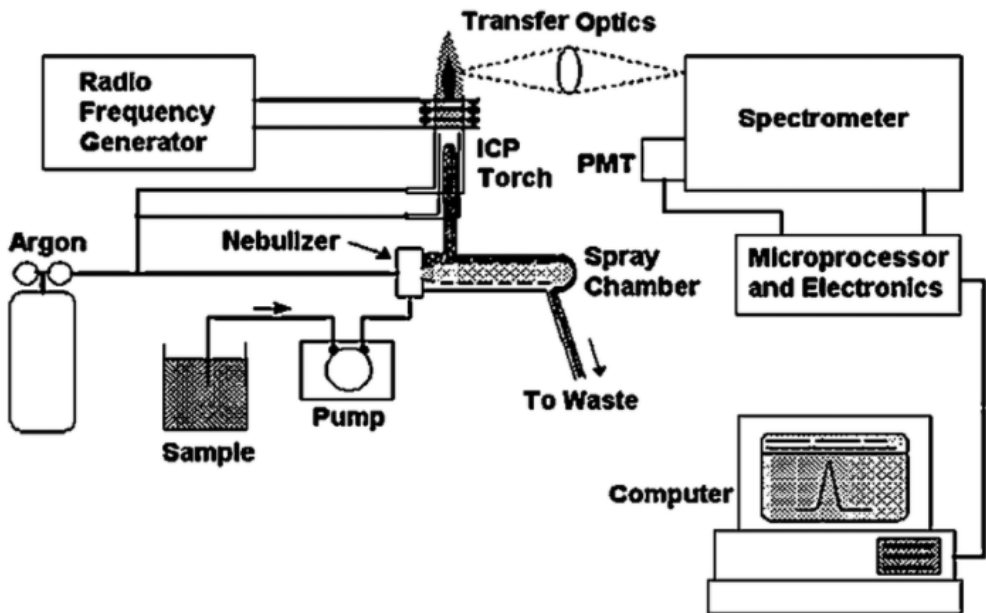
Figure 2.8: Schematic of Inductively Coupled Plasma Mass Spectrometer ICP-OES. Reproduced from Pingping, S. [88]

The inductively coupled plasma (where plasma is an electrically neutral gas made up of positive ions and free electrons) is created by flowing argon gas into the ICP torch where electrical power is used to generate a radio frequency. The spark from the tesla coil causes ionisation of the argon gas were the resistance of the electrons from the ionised gas against the magnetic field causes intense heat, thus plasma is created. [89] Samples introduced into the system are converted into aerosol form and transported to the opening at the base of the plasma where they are thermally atomised. The atoms contained in the sample which are now ionised will be in an excited state when leaving the plasma. The excited atoms will return to their ground state after the emission of a photon of an atom specific wavelength, as atomic emission spectroscopy is based on the principle that excited atoms and ions emit radiation of a characteristic wavelength when electrons return to lower energy orbitals. [90]. ICP-OES incorporate a polychromator which allows for the observation of multiple wavelengths at the same time. As light from the plasma enters the polychromator, it is selectively focused

through an entrance slit which is then focused onto a prism which separates the light by wavelength. After passing through optical elements (gratings) which order the separated light and improve resolution of the spectrum, a mirror collects and focuses the dispersed spectrum onto a detector. Identification of the wavelengths present in the atomic emission spectrum permits qualitative analysis. The intensity of the spectral lines is related to the amount of the element in the sample thus the quantity of the element present can be determined permitting quantitative analysis. Quantitative analysis may be performed by preparing a series of standards and calibrating the instrument against them to produce calibration graphs. The graphs can be used to quantify elements in the sample which are contained in known amounts in the calibration standards; done electronically by the analytical software.

2.4.7 - Nuclear Magnetic Resonance (NMR)

NMR is based on the principle that the nucleus of an atom placed in a magnetic field whilst exposed to electromagnetic radiation will resonate at a specific frequency corresponding to that of the radiation. [91] NMR uses radio frequency (RF) on the electromagnetic spectrum. A simplified labelled diagram showing the major components of an NMR spectrometer are shown below:
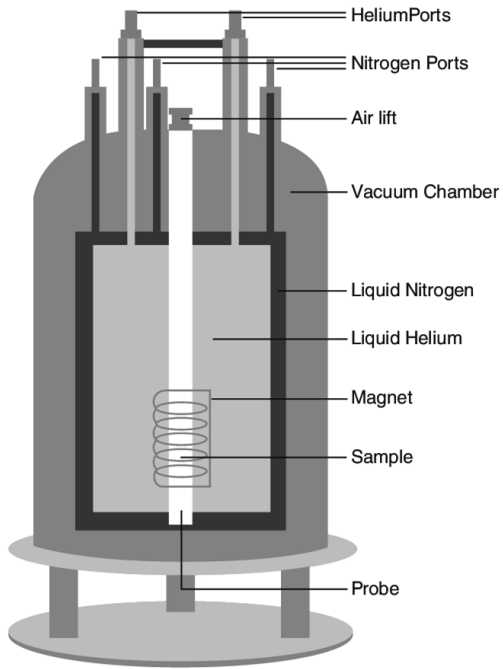
Figure 2.9: Schematic diagram detailing the main components of an NMR spectrometer. Reproduced from Antcliffe et al. [92]

Samples are inserted into the instrument from above. The sample is dropped and surrounded by radio frequency emitters and signal detection coils. Superconducting magnets surround the coils which generate the applied field. These are cooled by liquid helium to minus 296 °C to function effectively. [93] Liquid nitrogen surrounds the liquid helium to prevent boil off. A vacuum is generated around the liquid nitrogen for further insulation to mitigate evaporation.

NMR requires nuclei with the property of spin. This property arises when a nucleus has an odd number of protons and / or neutrons. Nuclei with these properties are detectable by NMR and are denoted spin-active or NMR active. Spin has the value (I) which can be either an integer or half integer. Nuclei with both an odd number of protons and neutrons have integer spin. Nuclei with an odd number of protons or neutrons but not both have half integer spins. Application of a magnetic field to a sample will align the nuclei spin states. The total number of spin states of nuclei is given by $2I + 1$. [94] The applied magnetic field (B_o) is applied along the Z axis. Two spin states for a spin ½ nucleus can either be aligned (lower

energy) or aligned against (higher energy) the magnetic field. The difference in the energy between the two spin states is denoted ΔE which will change dependent on the applied magnetic field strength. An NMR spectrum is produced by the application of energy in the form of varying frequencies of RF radiation to the system. Nuclei will only absorb energy which is the same as ΔE. Given $E = h\nu$ a specific energy corresponds to a specific frequency. The frequency adsorbed results in resonance producing a peak on a spectrum of frequency. [95]

2.4.8 – ^{13}C SSNMR of GO

Solid state ^{13}C NMR is utilised for the charicterisation of GO functional groups by inspection of the various chemical environments which exist on the surface of the carbon based graphene sheet as ^{13}C atom has spin ½ which is NMR active. Given the low natural abundance of ^{13}C and its lower magnetic moment (in comparison to ^{1}H), water dispersed GO flakes are not suitable for accurate analysis therefore graphene oxide is analysed in solid state using relatively long acquisition times to produce useful spectra. ^{13}C NMR analysis of graphene oxide shows that the carbon atoms are predominately hybridised and oxidised mostly in the form of hydroxyl and epoxides with carbonyl groups and lactols. The remaining minority are Sp^2 hybridised with ester and ketone functionalised groups. [96] A typical one dimentional (1D) ^{13}C magic angle spinning (MAS) spectra of graphene oxide is shown below:
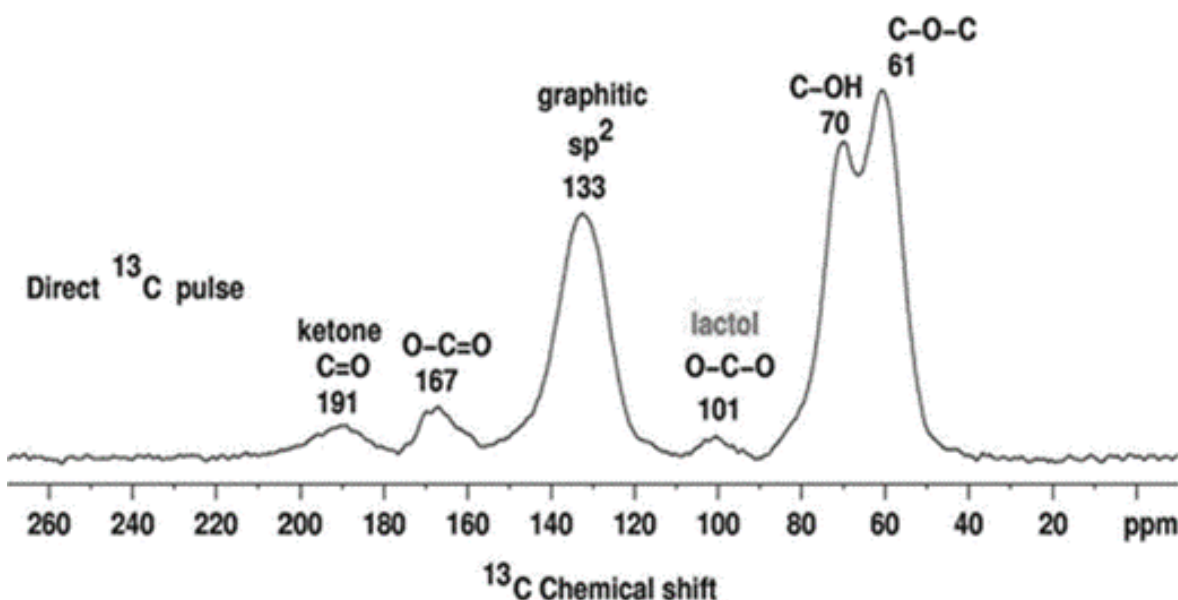
Figure 2.10: Typical 1D ^{13}C MAS SSNMR Spectrum of graphene oxide. Reproduced from Gao et al. [97]

MAS is used to reduce line broadening and increase the reliability for the recording of the NMR spectra, this is achieved by reducing dipolar interactions and anisotropy of nuclei by roatating the probe at up to 70 KHz at the magic angle of 54.74 ° in relation to the external magnetic field. [98]

2.5 – Software Packages

The following software packages were utilised in this research:

CP2K (https://www.cp2k.org/)

CP2K is a quantum chemistry and solid-state physics software package which provides state-of-the-art methods for efficient and accurate atomistic simulations of solid state, liquid, molecular, periodic, material, crystal, and biological systems. CP2K provides a general framework for different modelling methods such as DFT using the mixed Gaussian and plane waves approaches GPW and GAPW. CP2K can do simulations of molecular dynamics, meta-dynamics, Monte Carlo, Ehrenfest dynamics, vibrational analysis, core level spectroscopy,

energy minimization, and transition state optimization. [99] CP2K was utilised in this research for chemical structure energy optimisation and AIMD simulations.

Visual Molecular Dynamics (VMD) (https://www.ks.uiuc.edu/Research/vmd/)

VMD is a molecular visualization program for displaying, animating, and analysing large biomolecular systems using 3-D graphics and built-in scripting. [100] VMD was used in this research to visualise the optimised structures and the AIMD simulations produced from CP2K software in the form of .xyz files.

GaussView (https://gaussian.com/gaussview6/)

GaussView is a graphical interface which aids in the creation of Gaussian input files and enables the user to run Gaussian calculations from a graphical interface without the need for using a command line instruction and helps in the interpretation of Gaussian output. [101] GuassView was used in this research to construct, modify, and visualise all analogues of graphene oxide.

Putty (https://www.chiark.greenend.org.uk/~sgtatham/putty/latest.html)

PuTTY is a client program for the SSH, Telnet and Rlogin network protocols. These protocols are all used to run a remote session on a computer, over a network. PuTTY implements the client end of that session: the end at which the session is displayed, rather than the end at which it runs. [102] Putty was used in this research to remote access the HEC via VPN for the purposes of viewing and editing input files and submitting jobs in CP2K.

VMware (https://www.vmware.com/uk/products/workstation-player.html)

VMware Workstation Player enables a second, isolated operating system to be run on a single PC. [103] VMware was used in this research to access Linux OS on a windows PC to use GaussView.

Opentext^{TM} Exceed and Exceed 3D (https://www.opentext.co.uk/products-and-solutions/products/specialty-technologies/connectivity/exceed-3d)

OpenText™ Exceed™ is a secure, high-performance X Window server designed for environments were users need to access X Window applications securely and reliably from Microsoft Windows and Citrix® virtual desktops over the LAN. OpenText™ Exceed™ 3D is an add-on to OpenText Exceed for rendering OpenGL-based 3D graphics applications over a remote connection. Exceed 3D enables users to access graphical 3D applications running on UNIX®, Linux®, or other X11 desktops from a Microsoft® Windows® PC. [104] Exceed 3D was used in this research to open and edit text files when logged into HEC through Putty.

Chapter 3: Graphene Synthesis and Characterisation

3.1- Initial production of small quantities of graphene

Graphene oxide and reduced graphene oxide was produced in the laboratory using a modified version of Thomas *et al.* [105] Hummers method. Initially a small quantity (1/5th the mass produced in the literature) was prepared to prove the safety of the synthesis and the quality of the graphene variants. Hummers graphene oxide and reduced graphene oxide will here out be denoted HGO and RGO respectively.

3.1.1 – Initial production of small quantities of HGO

1.009 g graphite, 0.910 g KNO$_3$ and 35 ml of conc. H$_2$SO$_4$ where added to a 500 ml glass beaker. The glass beaker was placed in a plastic container containing ice water. 4.512 g of KMnO$_4$ was added over a 70-minute period. The solution was left stirring for 24 hours. 110 ml of 5 % H$_2$SO$_4$ was added over a 30-minute period and stirred for 1 hour. 12 ml of 20 vol H$_2$O$_2$ was added over a period of 5 minutes and stirred for 1 hour. 100 ml of 3 % H$_2$SO$_4$ / 0.5 % H$_2$O$_2$ was added and was left stirring for a 48-hour period. The resulting solution was centrifuged at 5000 rpm for 20 minutes. The separated solid was removed and placed in a clean glass beaker. 100 ml of 3 % H$_2$SO$_4$ / 0.5 % H$_2$O$_2$ was added. The resulting solution was centrifuged again. The same sequence was repeated once more so that the initial solid had been centrifuged three times with a H$_2$SO$_4$ / H$_2$O$_2$ solution. The resulting solid was then centrifuged for another 3 times using the same method but with demineralised water instead. The resulting solid was then dried in an oven at 60 °C for a 48-hour period. It was noted upon sample collection from the oven that the stipulated temperature threshold mechanism had failed, and the oven thermometer read 80 °C.

3.1.2 – Initial production of small quantities of RGO

0.150 g of Hummers graphene oxide as produced in 3.1.1 was added to a 500 ml glass beaker with 100 ml of demineralised water and 5 ml of $N_2H_4.H_2O$ and stirred for 3 hours. The resulting solution was centrifuged at 5000 rpm for 20 minutes. The solid was separated and washed with demineralised water. The solid was centrifuged and washed three times in total. The resulting solid was then dried in an oven at 60 °C for a 48-hour period.

3.1.3 – Characterisation of first attempt HGO and RGO

The prepared HGO and RGO were characterised via FTIR spectroscopy using an Agilent Technologies Cary 630 FTIR Spectrometer and analysed using Agilent MicroLab PC software and Raman spectroscopy using a Horiba LabRAM' micro Raman system to determine the types of carbon-oxygen and carbon-carbon bonds typically exhibited in graphene and reduced graphene oxide as well as to probe the quality of the graphene sheets. The FTIR (Figure 3.1 and 3.2) and Raman spectra (Figure 3.3 and 3.4) produced for HGO and RGO are shown below:
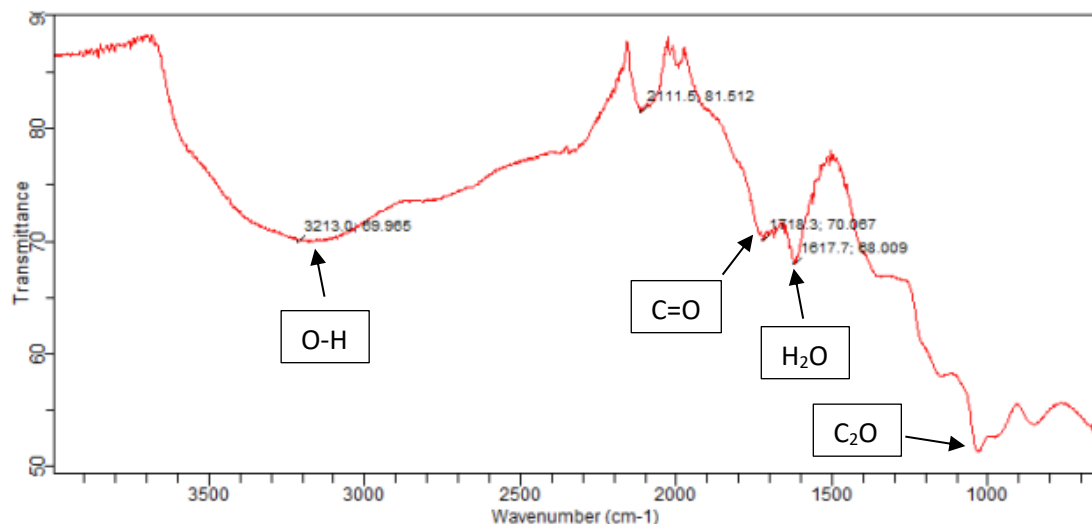
Figure 3.1: FTIR Spectrum for the initial production of HGO

The broad peak shown at 3213 cm^{-1} indicates the stretching of an O-H bond and can be attributed to the presence of hydroxyl groups. The peak observed at 1718 cm^{-1} signifies the presence of carbonyl groups. The peak shown at 1617 cm^{-1} represents the bending modes of H_2O integrated into the GO structure. The peak at approximately 1175 cm^{-1} may indicate epoxide bending. The peak at approximately 1050 cm^{-1} corresponds to C-O stretching.
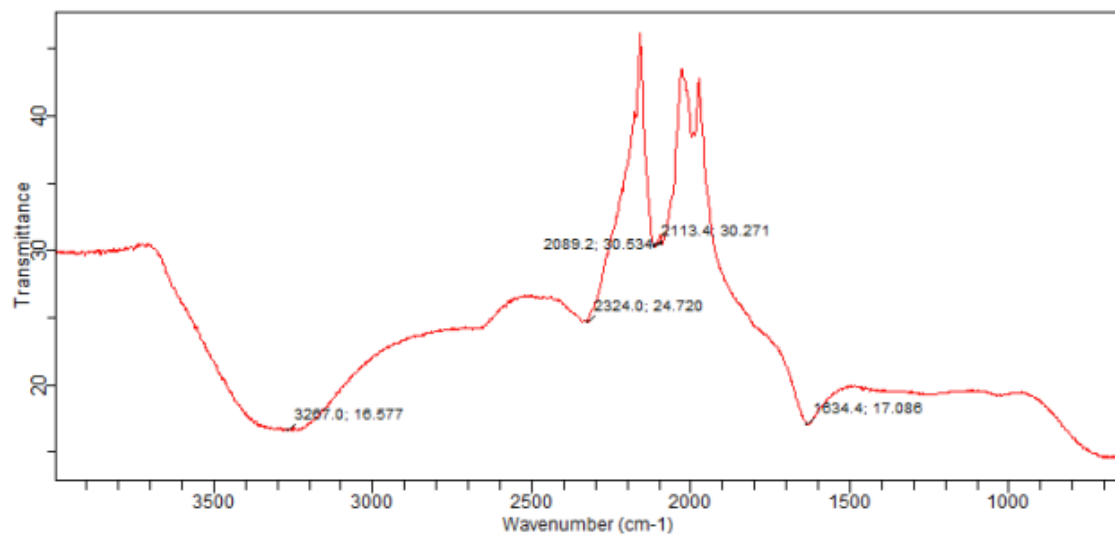
Figure 3.2: FTIR Spectrum for the initial production of RGO

The removal of all peaks below 1634 cm^{-1} suggests the reduction of most of the oxygen containing groups on the GO. The presence of H_2O integrated into the RGO structure can be seen at 1634 cm^{-1} with complimentary broad peak at 3267 cm $^{-1}$. The peak at 2324 cm^{-1} may indicate residual CO_2.
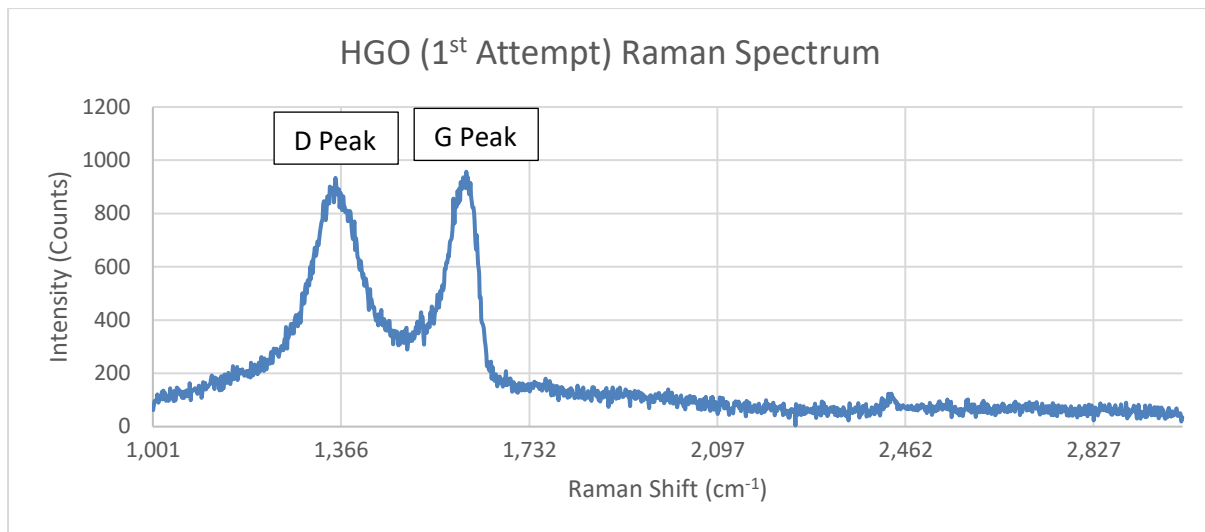
Figure 3.3: Raman Spectrum for the initial production of HGO

The D peak for HGO is seen at 1325 cm $^{-1}$ and G peak at 1600 cm $^{-1}$. The broadness of the peaks represents a moderate degree of defects within its structure. The lower intensity of the D peak to the G peak suggests the sample retains a large portion of Sp^2 conformation. The lack of Sp^3 conformation for this sample may be due to deoxygenation via decomposition as the oven temperature when drying exceeded the stipulated drying temperature of 60°C.
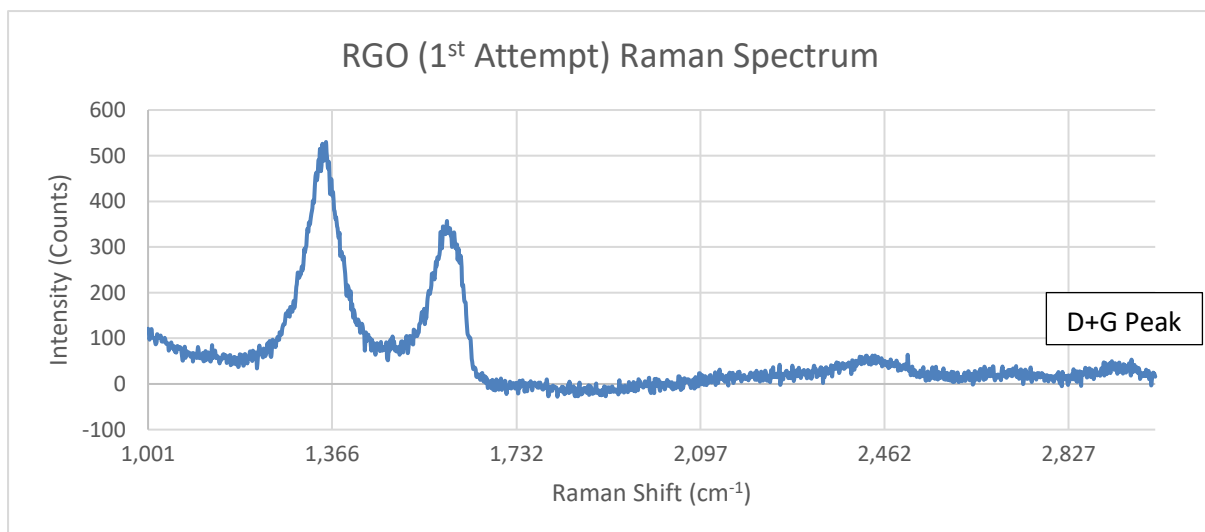
Figure 3.4: Raman Spectrum for the initial production of RGO

The D peak for RGO is shown at 1325 cm^{-1}. This is larger than the G peak shown at 1600 cm^{-1}. A Slight D+G is shown peak at 2950 cm^{-1}. It is suggested that the HGO sample was moderately functionalised when prepared as following reduction, the characteristic carbon framework defects from the removal of these functionalised groups are seen in the D peak for RGO. The lack of functionalisation seen in the HGO Raman spectrum is most likely from thermal decomposition due to exceeding the drying temperature threshold for a significant period.

3.2 – Further production of HGO and RGO

As the initial preparation was deemed safe using small quantities and the analytical data suggested the sample contained key characteristics of GO and RGO, a larger quantity of HGO and RGO was prepared with more in-depth analysis for further characterisation.

3.2.1 - Production of HGO

The production of HGO proceeded in two separate 1L glass beakers given the masses and volumes involved. Products from beakers 1 and 2 were combined and yielded 9.585 g of dried HGO.

Method

2.504 g (beaker 1) 2.517 g (beaker 2) graphite, 2.250 g (beaker 1) 2.261 g (beaker 2) KNO$_3$ and 85 ml of conc. H$_2$SO$_4$ was added to each of the glass beakers. The glass beakers were placed in a plastic container containing ice water. 11.266 g (beaker 1) 11.255 g (beaker 2) of KMnO$_4$ was added over a 70-minute period. The solutions were left stirring for 24 hours. 275 ml of 5 % H$_2$SO$_4$ was added to each beaker over a 30-minute period and stirred for 1 hour. 32.5 ml of 20 vol H$_2$O$_2$ was added to each beaker over a period of 5 minutes and stirred for 1 hour. 100

ml of 3 % H_2SO_4 / 0.5 % H_2O_2 was added to each beaker and was left stirring for a 48-hour period. The resulting solutions were centrifuged at 5000 rpm for 20 minutes. The separated solids were removed and placed in clean glass beakers. 500 ml of 3 % H_2SO_4 / 0.5 % H_2O_2 was added to each glass beaker. The resulting solutions were centrifuged again. The same sequence was repeated once more so that the initial solids had been centrifuged three times with a H_2SO_4 / H_2O_2 solution. The resulting solids were then centrifuged for another 3 times using the same method but with demineralised water instead. The resulting solids were combined and then dried in an oven at 60 °C for a 48-hour period.

3.2.2 - Production of RGO

0.75 g of HGO was added to a 1 L glass beaker with 500 ml of demineralised water and 25 ml of $N_2H_4.H_2O$ and stirred for 3 hours. The resulting solution was centrifuged at 5000 rpm for 20 minutes. The solid was separated and washed with demineralised water. The solid was centrifuged and washed three times in total. The resulting solid was then dried in an oven at 60 °C for a 48-hour period.

3.2.3 – Characterisation of HGO and RGO

HGO and RGO were characterised via FTIR, Raman, SEM, EDS, and Solid-State NMR (SSNMR).

FTIR Spectroscopy

The FTIR spectrum for HGO is shown below in Figure 3.5:
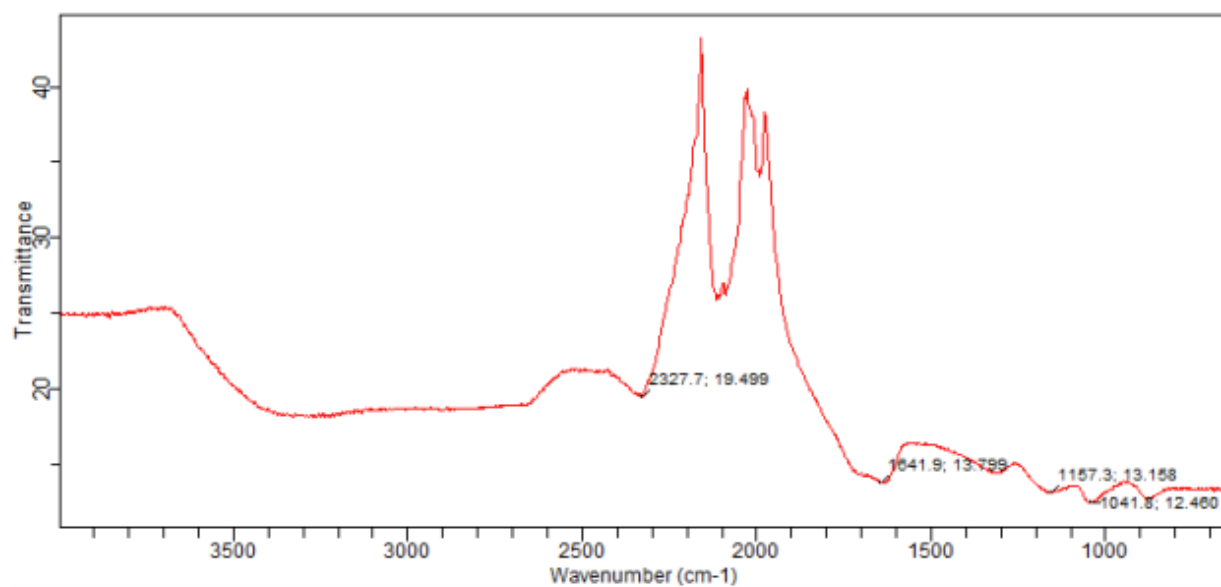
Figure 3.5: FTIR spectrum for HGO

The broad peak between 2600 cm^{-1} and 3400 cm^{-1} which indicates the stretching of an O-H

bond is less defined. The peaks observed at 1718 cm^{-1} (R$_2$C=O), 1642 cm^{-1} (integrated H$_2$O)

1157 cm^{-1} (C$_2$O) and 1042 cm^{-1} (C-O) are also significantly less defined. The FTIR spectrum for

RGO is shown below in Figure 3.6:
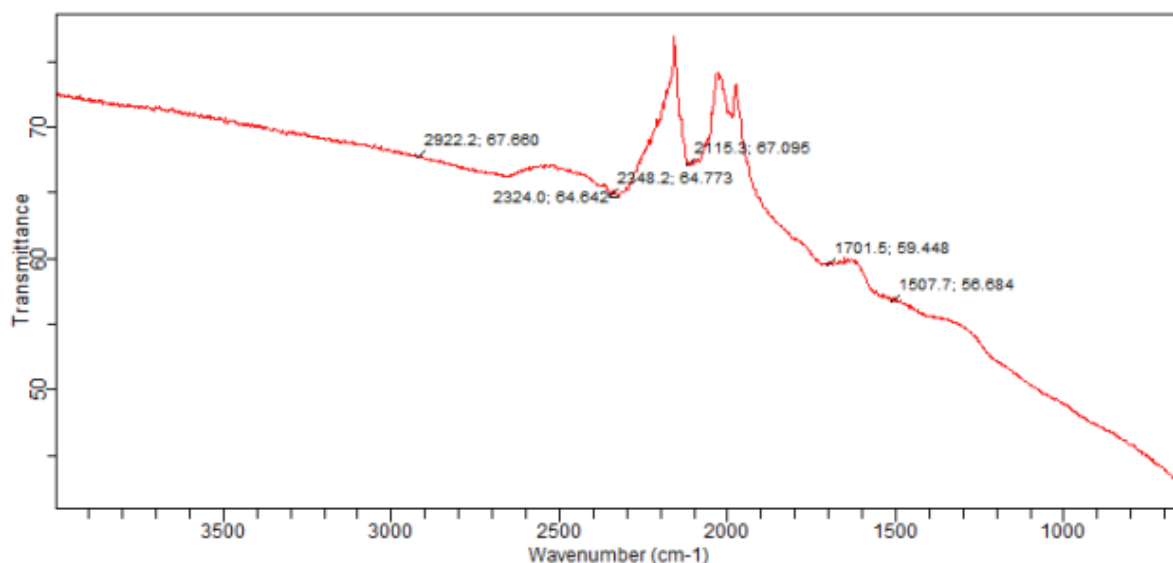
Figure 3.6: FTIR spectrum for RGO

All typical distinguishing features for GO are mostly removed. This suggests a lack of absorbance of any functional group other than the potential CO_2 absorbance seen at 2348 cm $^{-1}$.

Raman Spectroscopy

The Raman spectrum for HGO is shown below in Figure 3.7:
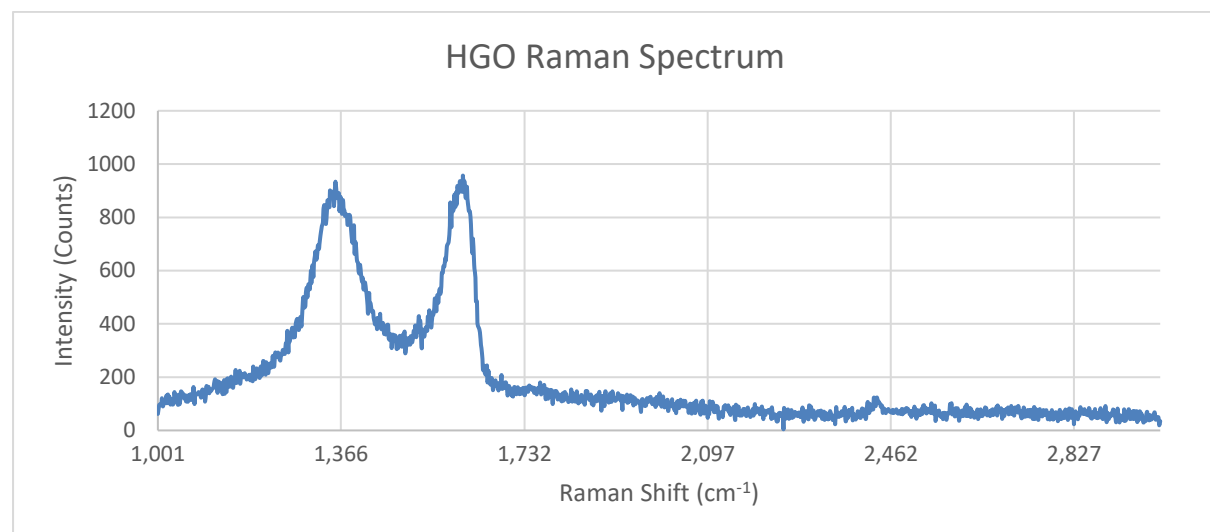
Figure 3.7: Raman Spectrum for HGO

The D peak for HGO is seen at 1325 cm $^{-1}$ and G peak at 1600 cm $^{-1}$. The broadness of the peaks and the reduction in 2D and D + G bands hight suggesting a significant degree of defect within its structure. Similar intensities between the D and G peaks suggest a similar Sp^2 and Sp^3 conformation.

The Raman spectrum for RGO is shown below in Figure 3.8:
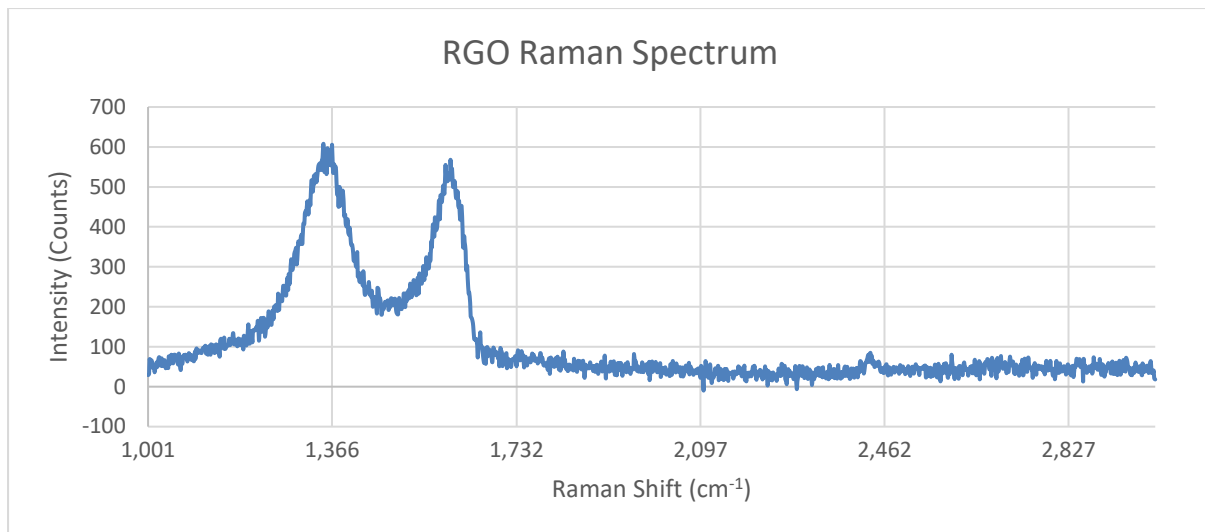
Figure 3.8: Raman Spectrum for RGO

The D peak for RGO is seen at 1325 cm $^{-1}$ and G peak at 1600 cm $^{-1}$. The broadness of the peaks and the reduction in 2D and D + G bands hight suggesting a significant degree of defect within its structure. The D peak is larger than the G peak suggesting that the removal of functionalisation from reduction has increased the levels of defects in the carbon framework of the graphene sheets.

SEM

A JSM-7800F Schottky Field Emission Scanning Electron Microscope was used to characterise the surface morphology of HGO and RGO; all SEM images are taken at 5 kV. SEM images of HGO are shown below at various magnifications:
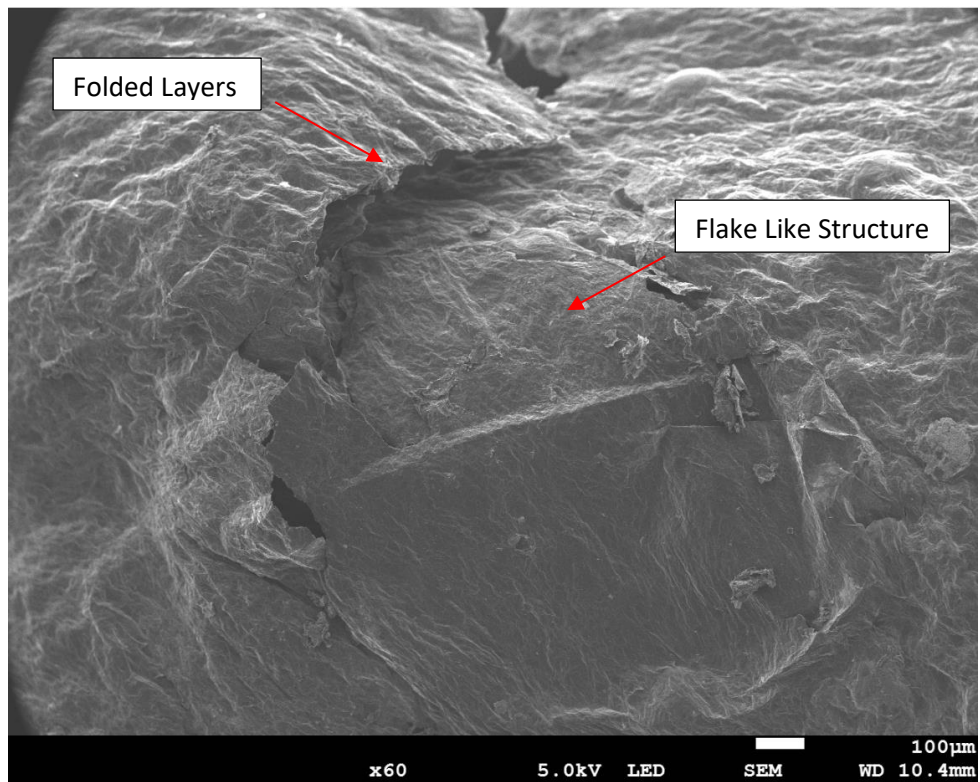
Figure 3.9: SEM image of HGO with x60 magnification
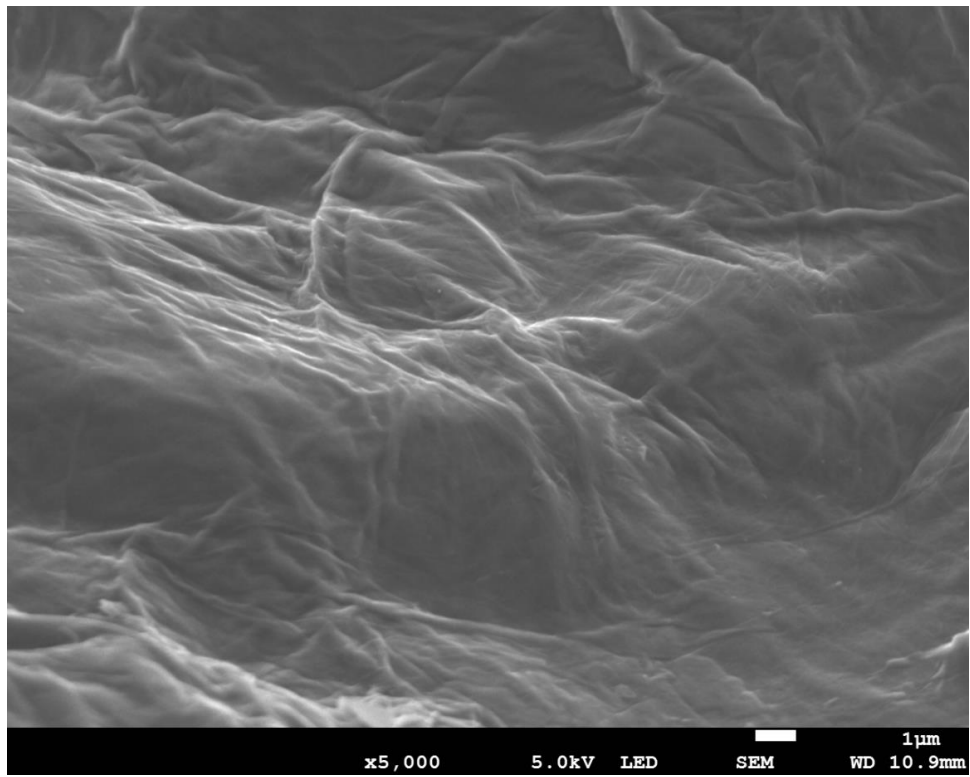
Figure 3.10: SEM image of HGO with x5000 magnification

Figures 3.9 and 3.10 show that HGO is a flake like heterogenous structure which is several layers thick. The 2D structure has edges which appear to fold. SEM images of RGO are shown below at various magnifications:
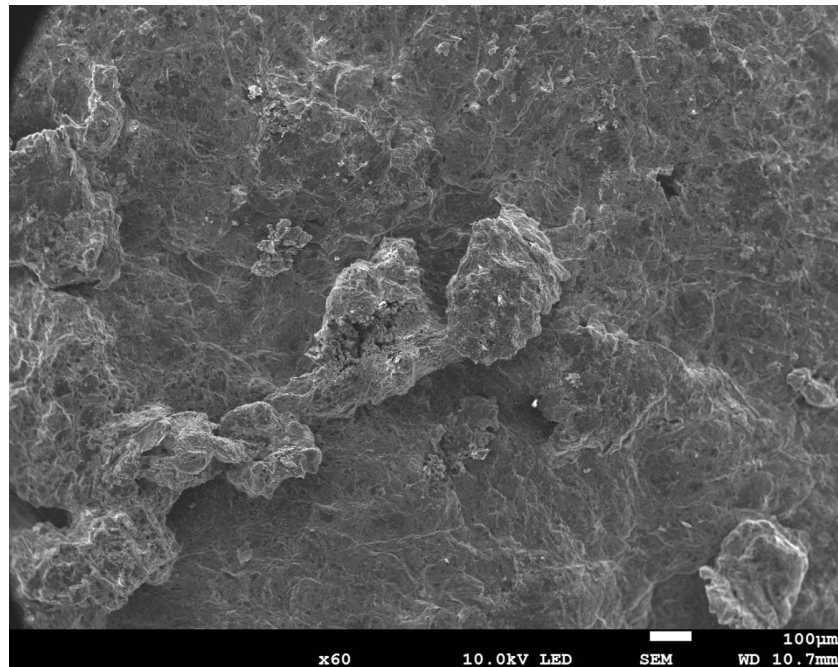
Figure 3.11: SEM image of RGO with x60 magnification
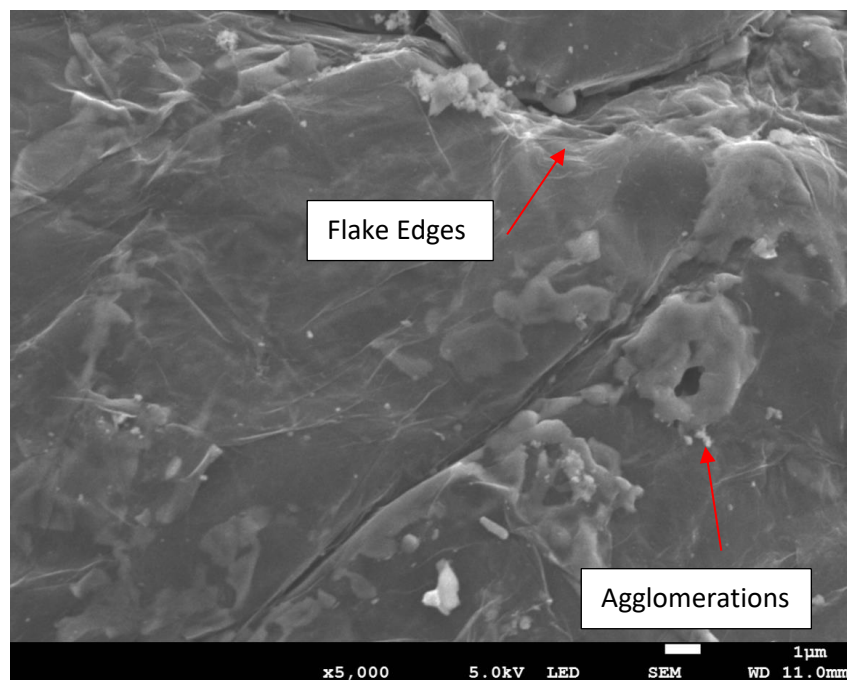
Figure 3.12: SEM image of RGO with x5000 magnification

Figures 3.11 and 3.12 show the flake like structure of RGO, although in comparison to HGO the flakes look flatter suggesting a reduced 2D structure. The flake edges can be clearly seen in Figure 3.12 and exhibit folding. The SEM images for RGO show a higher level of heterogeneity with sharp contrast between the its foundational flake structure and various agglomerations spread throughout the sample.

EDS

EDS analysis was conducted using an Oxford Instruments X-Max 50 EDS System. The point and identifications are taken at x2000 magnification. An EDS layered image for HGO is shown below:
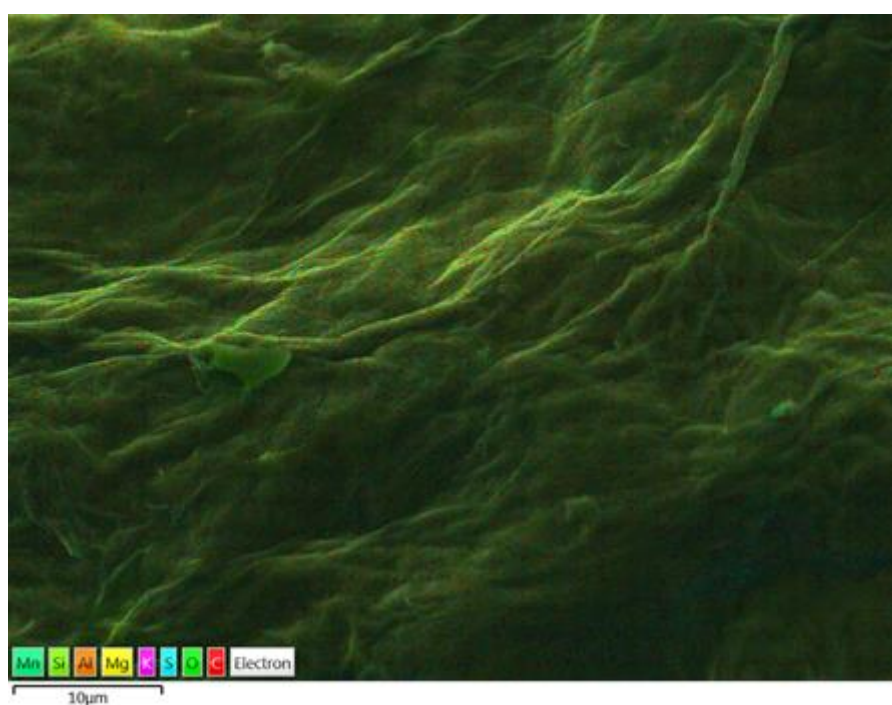
Figure 3.13: EDS layered image of HGO with colour key for elemental identification

Figure 3.13 shows that the HGO sample analysed is highly oxidised with oxygen distributed across the entire carbon surface. No obvious contamination can be seen on this portion of the sample. Quantitative analysis was performed at various points across another portion of

the sample to evaluate its chemical constitution more thoroughly. An SEM image of a different portion of the HGO sample is shown below:
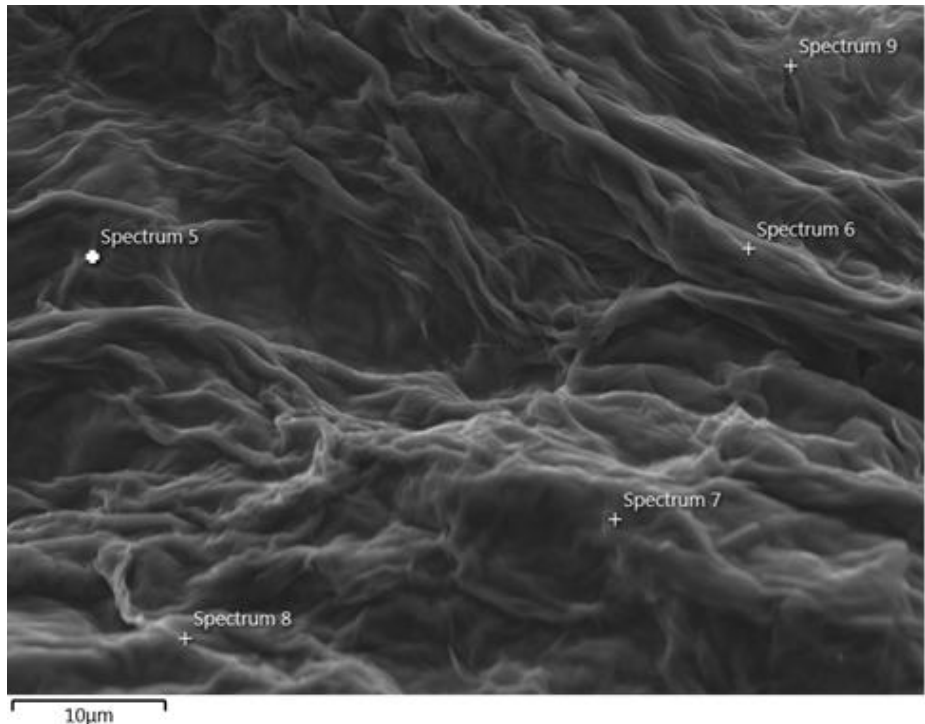
Figure 3.14: SEM image of HGO showing spectrum points at x2000 magnification

A total of 5 points were analysed on the HGO sample as shown in Figure 3.14 and the average elemental composition of the points are summarised in Table 3.1 below. Each individual quantitative analysis spectrum can be found in Appendix A.

Element (Weight%)	Spectrum					Average (Weight %)	Standard Deviation
	5	6	7	8	9		
C	28.7	48.3	43.8	49.1	41.8	42.3	7.34
O	15.4	29.6	27.6	29.3	25.4	25.4	5.24
S	45.9	18.0	22.8	18.1	27	26.3	10.32
Mn	5.9	2.9	3.5	2.0	3.5	3.5	1.29
K	0.9	0.7	0.8	1.1	0.7	0.8	0.15
Si	2.9	0.3	1.3	0.3	1.4	1.2	0.95

Table 3.1: EDS analysis taken from spectrum points shown in Figure 3.14

EDS results shown in Table 3.1 show a moderate level of oxidation but also a significant quantity of sulphur and a small quantity of manganese remaining within the HGO sample. This suggests that the washing regime employed to remove unwanted chemical constituents which originate from the synthesis of HGO was inadequate for the whole sample. An EDS layered image for RGO is shown below:
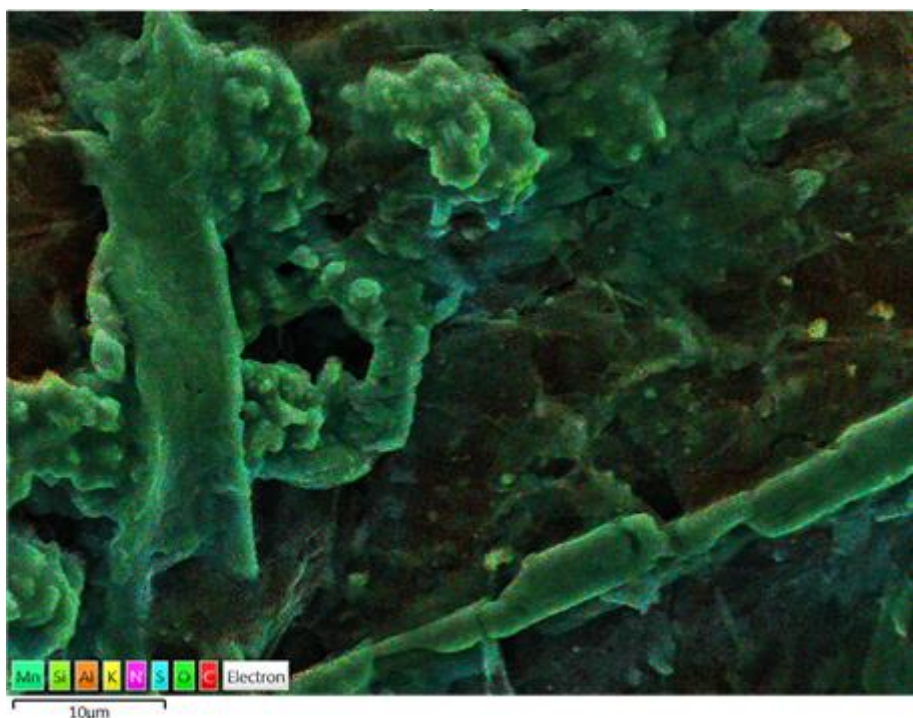
Figure 3.15: EDS layered image of RGO with colour key for elemental identification

Figure 3.15 shows large agglomerates on the surface of the RGO sample analysed and contains observable quantities of oxygen, nitrogen, and sulphur across the entire carbon surface. Quantitative analysis was performed at various points across another portion of the sample to evaluate it chemical constitution more thoroughly. An SEM image of a different portion of the RGO sample is shown below:
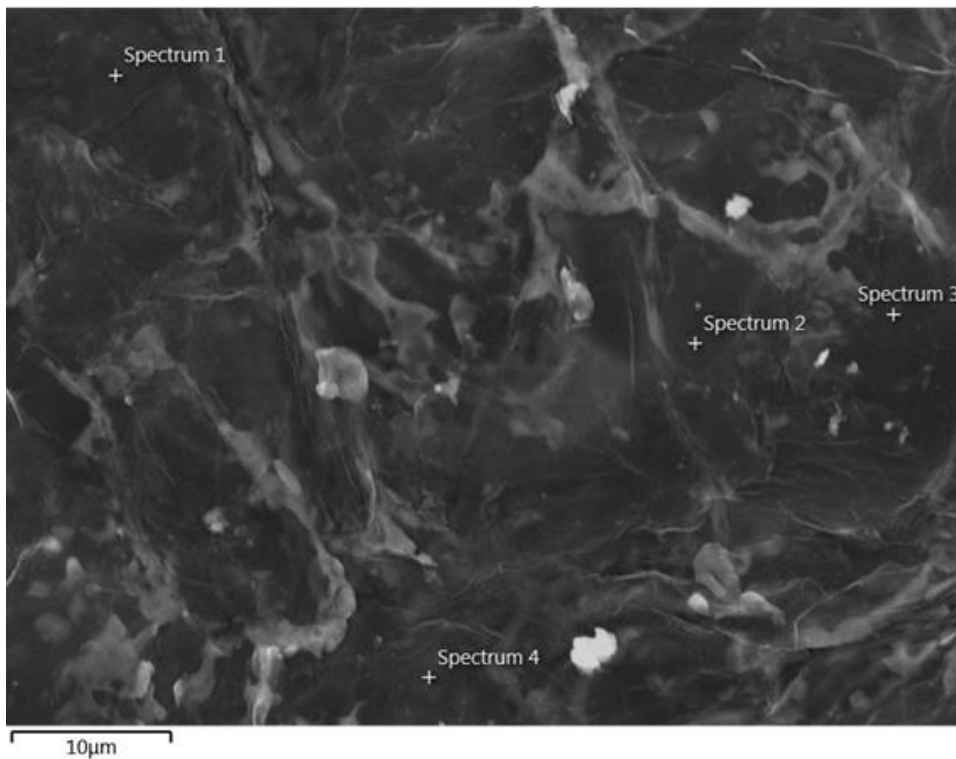
Figure 3.16: SEM image of RGO showing spectrum points at x2000 magnification

A total of 4 points were analysed on the RGO sample as shown in Figure 3.16 and the average elemental composition of the points are summarised in Table 3.2 below. Each individual quantitative analysis spectrum can be found in Appendix B.

Element (Weight%)	Spectrum				Average (Weight %)	Standard Deviation
	1	2	3	4		
C	74.6	70.0	77.2	54.7	69.1	8.72
O	11.1	14.9	13.5	10.7	12.5	1.73
S	8.9	10.2	9.2	22.2	12.6	5.55
Mn	3.7	2.1	3.4	7.1	4.1	1.85
K	1.3	1.5	1.1	4.0	2.0	1.18

Table 3.2: EDS analysis taken from spectrum points shown in Figure 3.16

EDS results shown in Table 3.2 of the RGO sample shown in Figure 3.16 show a lower level of oxidation and sulphur than the HGO sample shown in Figure 3.14 although a similar quantity of manganese remains. This suggest for this sample that reduction has occurred as the oxygen % is lower for the RGO sample in comparison to the HGO sample. As the sulphur % is also

lower this suggests that reduction process may have played a part in "cleaning" the surface. It could however be the case that the additional washing steps incorporated into the preparation of RGO is the cause for the removal of sulphur although the quantity of manganese stays consistent between HGO and RGO. The graphite used to create HGO and RGO was analysed via SEM and EDS to rule out possible contamination of starting synthesis materials. An EDS layered image for graphite is shown below:
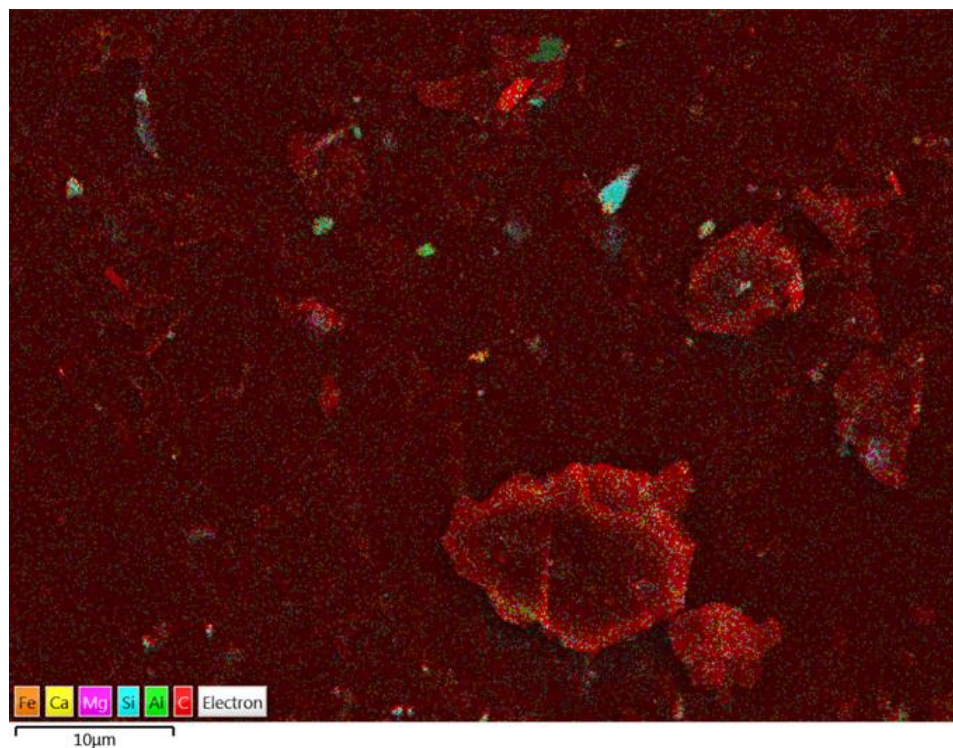
Figure 3.17: EDS layered image of graphite with colour key for elemental identification

Figure 3.17 shows that the graphite used to synthesise HGO and RGO is mostly carbon with trace amounts of silicon, calcium, and aluminium. This accounts for the small quantities of these contaminants found in the HGO and RGO samples. An SEM image of a different portion of the graphite sample is shown below:
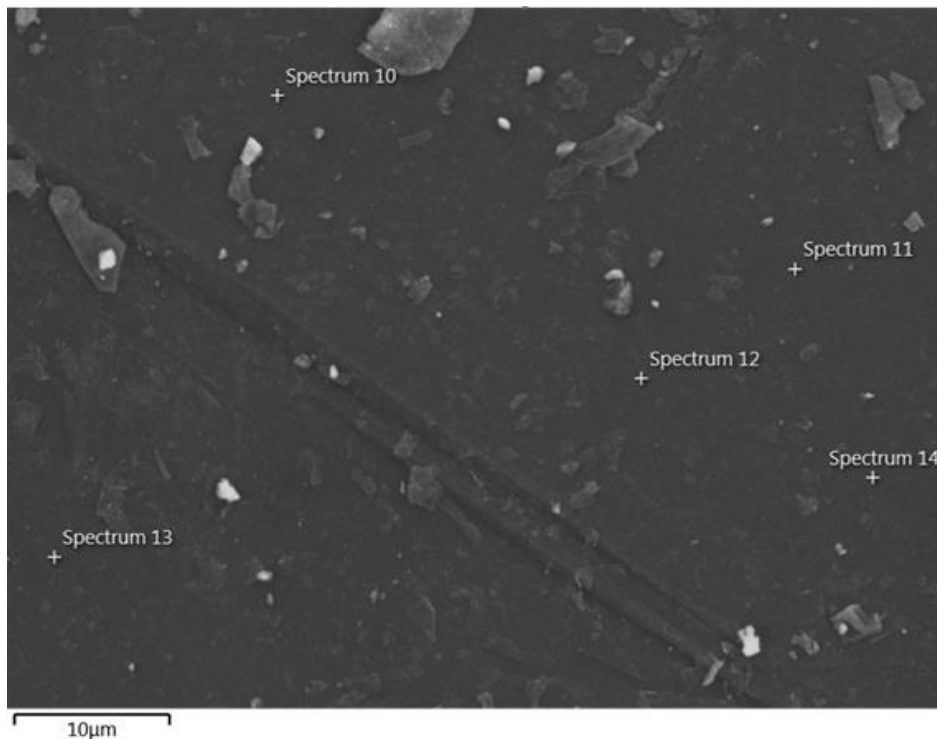
Figure 3.18: SEM image of Graphite showing spectrum points at x2000 magnification

A total of 5 points were analysed on the graphite sample as shown in Figure 3.18 and the average elemental composition of the points are summarised in Table 3.3 below. Each individual quantitative analysis spectrum can be found in Appendix C.

Element	Spectrum					Average (Weight %)	Standard Deviation
	10	11	12	13	14		
C	97.4	97.6	97.5	97.5	97.5	97.5	0.06
O	2.6	2.4	2.5	2.5	2.5	2.5	0.06

Table 3.3: EDS analysis taken from spectrum points shown in Figure 3.17

Table 3.3 and Figure 3.17 confirms that the graphite is almost exclusively carbon and oxygen with trace amounts of contaminates. EDS results show that the small traces of silicon contained in the HGO and RGO samples came from the graphite with which they were made. All other contamination came from the chemicals used for synthesis.

HGO and RGO samples were analysed for ^{13}C MAS SSNMR using a Bruker Avance III HD 400 spectrometer with a 3.2 mm triple channel MAS probe in double resonance mode. The samples were scanned 2784 times with a recycle delay of 30 seconds. The pulse length was 3.8 microseconds and MAS rate was 12.5 kHz. The SSNMR spectra for HGO is shown below:
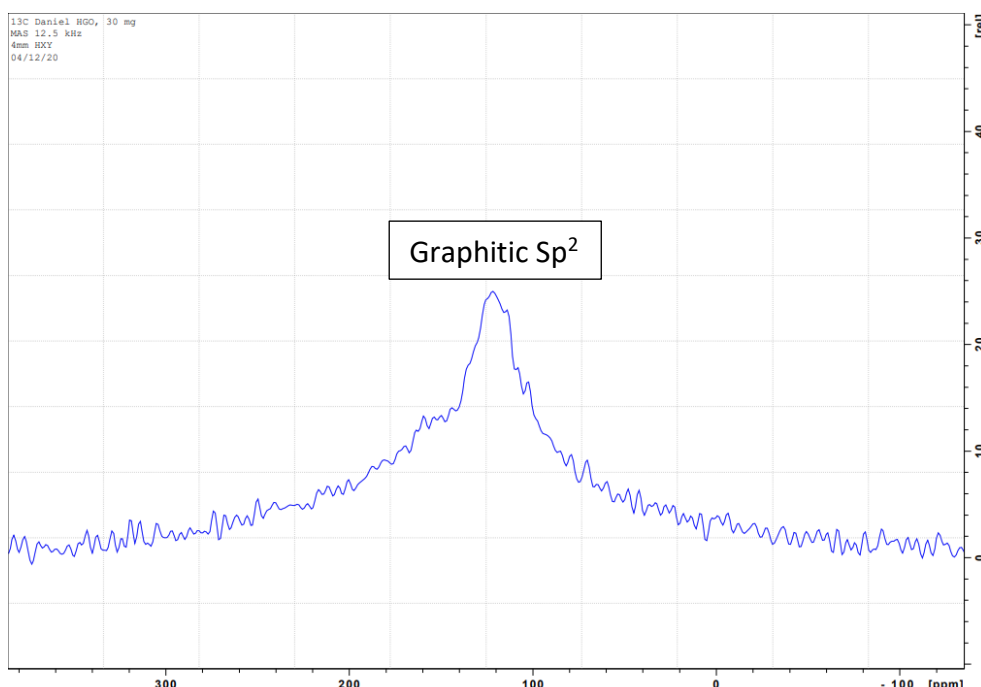
Figure 3.19: ^{13}C SSNMR spectrum of HGO

The Graphitic Sp^2 peak commonly seen at 130 ppm is clearly shown in Figure 3.19 however, other typically present oxygenated functionalities [106] such as epoxide at 61 ppm, hydroxyl at 70 ppm and ketone at 191 ppm are not visible. Given the comparative weakness and low absorption seen in the FTIR analysis of HGO (Figure 3.5) and the lack of functionality exhibited in the SSNRM it may be the case that there are few of these functional groups present in the HGO sample. The SSNMR spectrum for RGO is shown below:
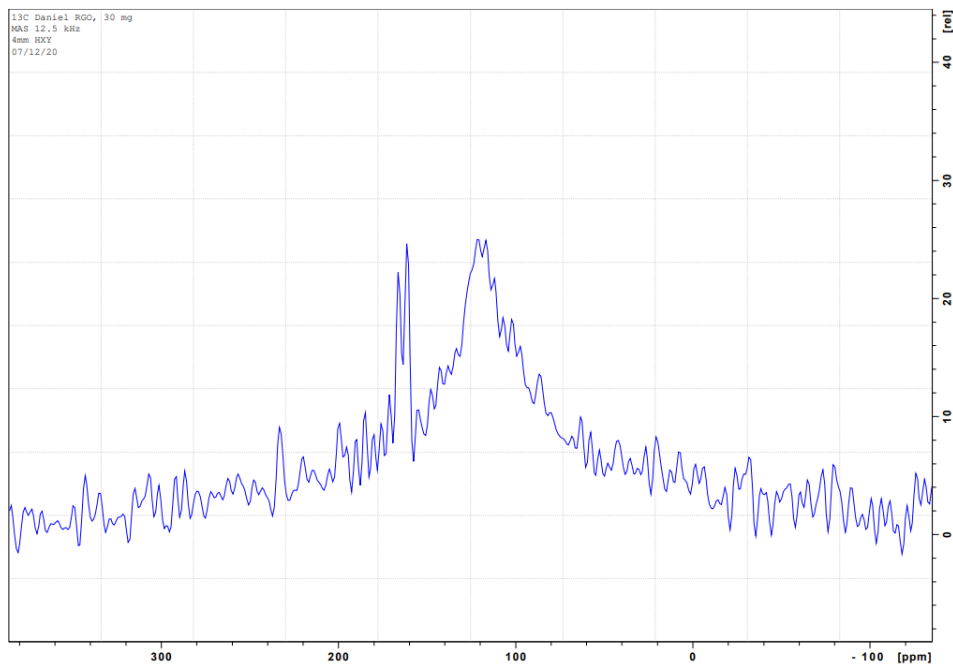
Figure 3.20: ^{13}C SSNMR spectrum of RGO

The graphitic peak for RGO is shifted slightly to the right at 120 ppm, this suggests a greater amount of Sp^2 conjugation which is consistent with the removal of carbon functionalisation via reduction. [107] The peak at 170 ppm corresponds to carboxyl groups [108] however these should have been removed following reduction and no carboxyl groups are present in the HGO spectra (Figure 3.19). The peak may be the result of amide formation as a reaction intermediate between hydrazine and oxygen functionalised groups during reduction which is consistent with the presence of nitrogen in the EDS layered image for RGO (Figure 3.15) and the relative chemical shift of amide carbonyls for ^{13}C NMR. [109]

3.3 – Reduction and characterisation of purchased graphene

Given the degree of contamination present within the synthesised HGO and RGO, GO flakes (GOgraphene) were purchased from William Blyth and subsequently reduced to compare the ion adsorptive capacity and adsorption location between the synthesised and bought GO

variants. The externally sourced graphene oxide and its reduced variant will here out be denoted BGO and BRGO respectively.

3.3.1 – Production of BRGO

0.747 g of BGO was added to a 1 L glass beaker with 500 ml of demineralised water and 25 ml of $N_2H_4.H_2O$ and stirred for 3 hours. The resulting solution was centrifuged at 5000 rpm for 20 minutes. The solid was separated and washed with demineralised water. The solid was centrifuged and washed three times in total. The resulting solid was then dried in an oven at 60 °C for a 48-hour period.

3.3.2 – Characterisation of BGO and BRGO

BGO and BRGO were characterised via FTIR, Raman, SEM, EDS, and Solid-State NMR (SSNMR).

FTIR Spectroscopy

The FTIR spectra for BGO and BRGO are shown below in Figures 3.21 and 3.22:
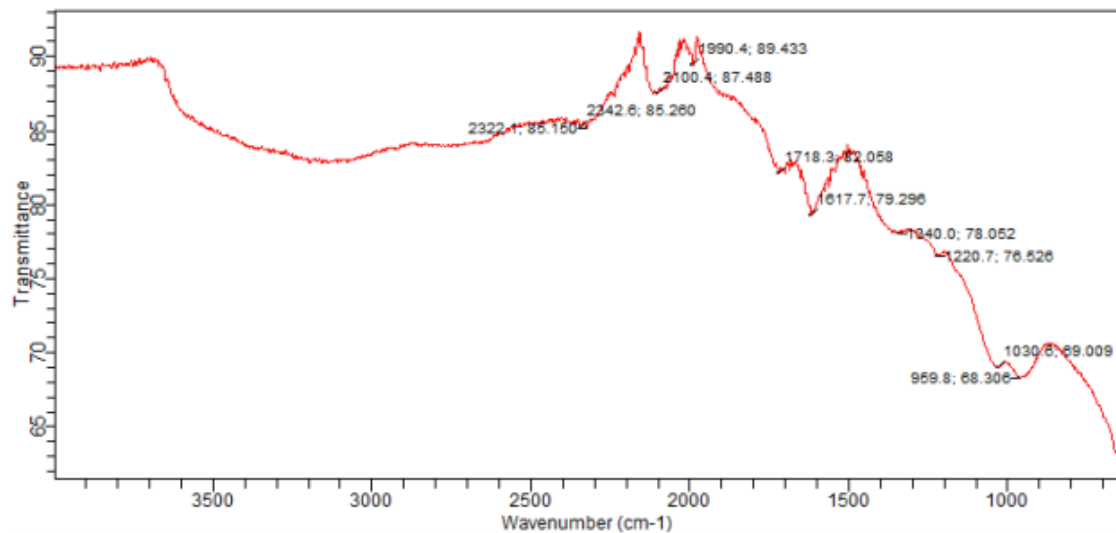
Figure 3.21: FTIR spectrum for BGO

All typical functionalities of GO are present. The broad peak between 3600 – 2400 cm^{-1} indicates the presence of hydroxyl groups. The peak observed at 1718 cm^{-1} signifies the presence of carbonyl groups. The peak shown at 1617 cm^{-1} represents the bending modes of H_2O integrated into the GO structure. The peak at approximately 1220 cm^{-1} indicates epoxide bending. The peak at approximately 1030 cm^{-1} corresponds to C-O stretching.
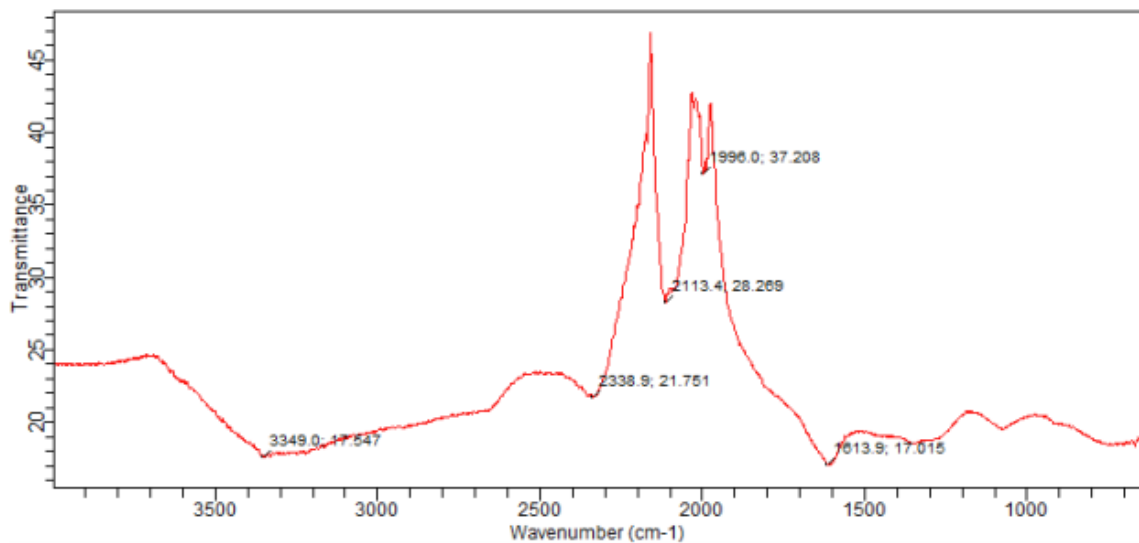
Figure 3.22: FTIR spectrum for BRGO

The removal of all peaks below 1600 cm^{-1} suggests the reduction of most of the oxygen containing groups on the GO. The presence of H_2O integrated into the RGO structure can be seen at 1613 cm^{-1} with complementary broad peak at 3349 cm $^{-1}$. The peak at 2338 cm^{-1} may indicate residual CO_2.

Raman Spectroscopy

The Raman spectra for BGO and BRGO are shown below in Figures 3.23 and 3.24:
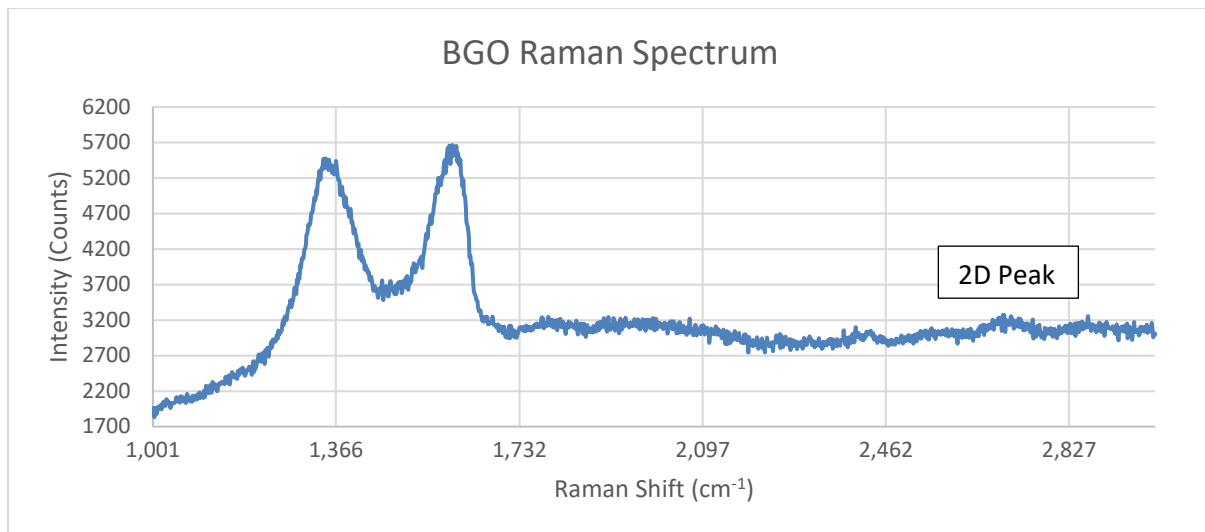
Figure 3.23: Raman Spectrum for BGO

The D peak for BGO is seen at 1325 cm $^{-1}$ and G peak at 1600 cm $^{-1}$. There is a slight 2D peak at 2700 cm $^{-1}$. The broadness of the peaks represents a moderate degree of defects within its structure. The similar intensity of the D peak to the G peak suggests the sample has achieved a large portion of Sp^3 confirmation. The Sp^3 confirmation may indicate a high amount of carbon functionalisation.
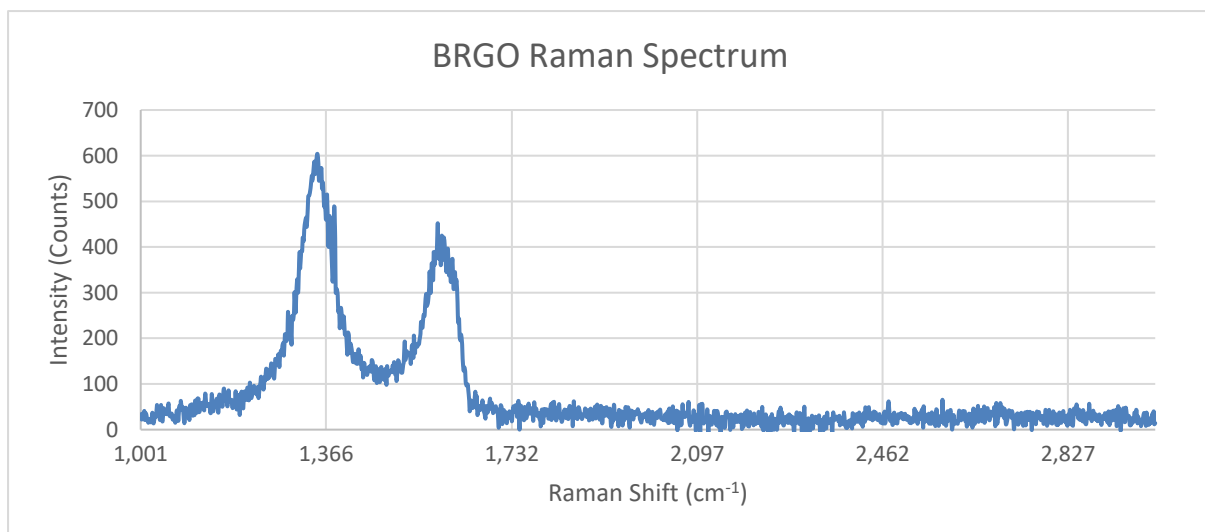
Figure 3.24: Raman Spectrum for BRGO

The D peak for BRGO is seen at 1325 cm $^{-1}$ and G peak at 1600 cm $^{-1}$. The broadness of the peaks and the reduction in 2D and D + G bands height suggests a greater degree of defect within its structure. The D peak is larger than the G peak suggesting that the removal of functionalisation from reduction has increased the levels of defects in the carbon framework of the graphene sheets.

SEM

SEM images of BGO are shown below at various magnifications:
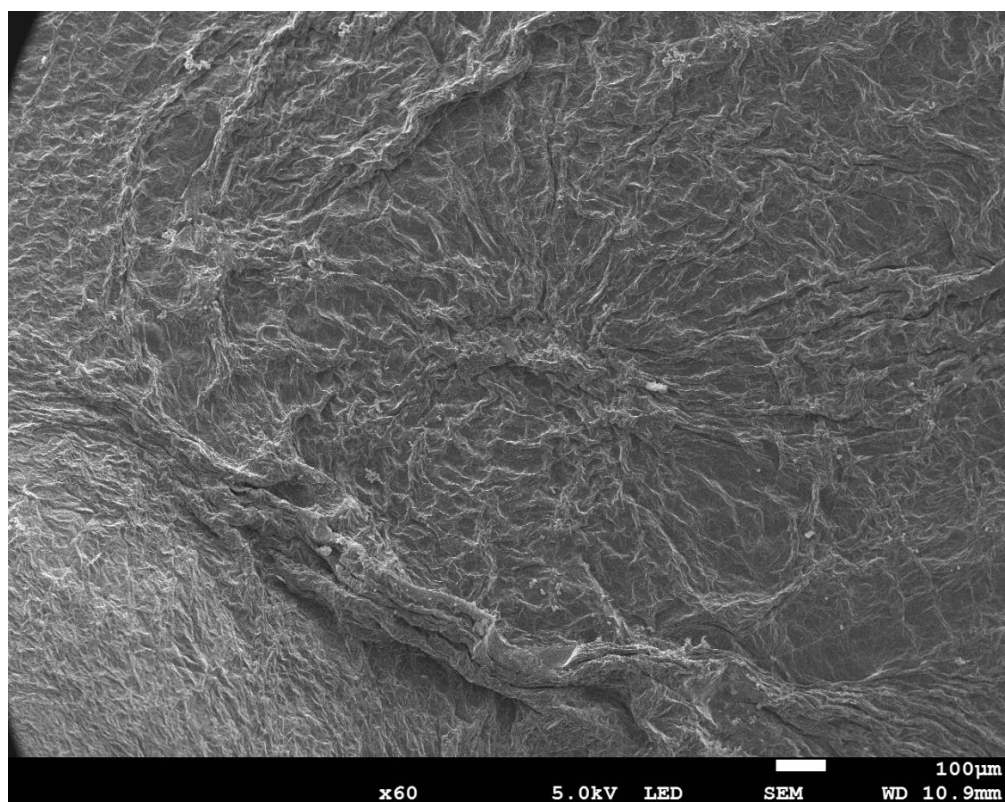
Figure 3.25: SEM image of BGO showing 100 μm with x60 magnification
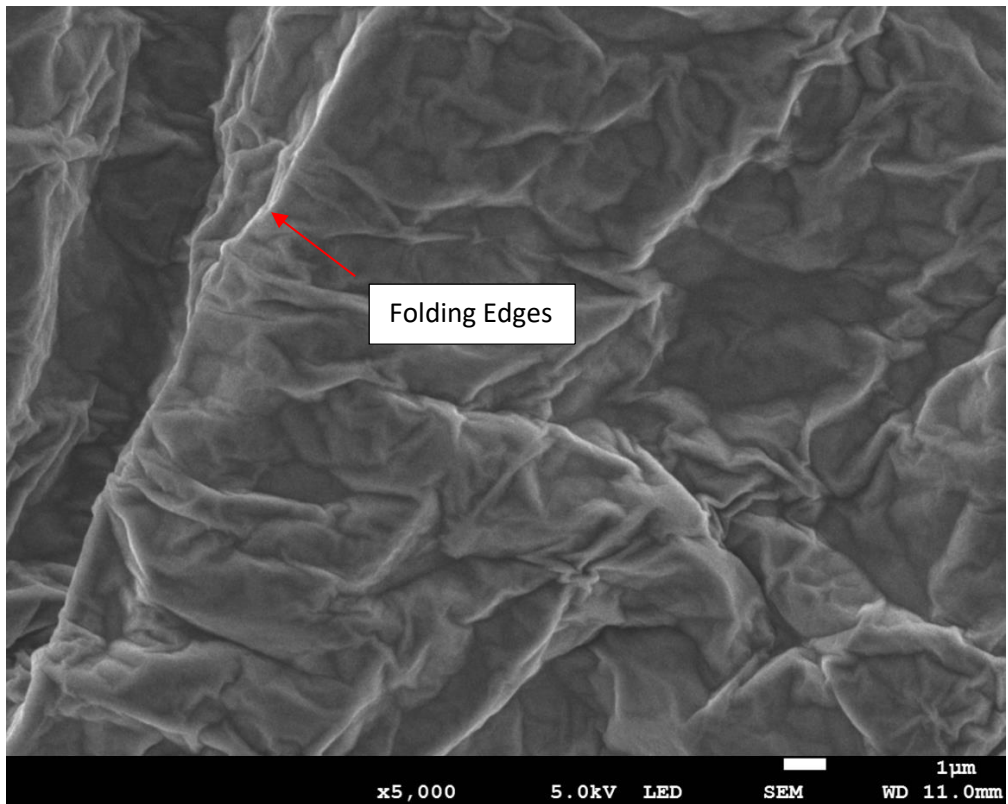
Figure 3.26: SEM image of BGO showing 1 μm with x5000 magnification

Figures 3.25 and 3.26 show that BGO is a flake like heterogenous structure which is several layers thick. The 2D structure has edges which appear to fold. SEM images of RGO are shown below at various magnifications:
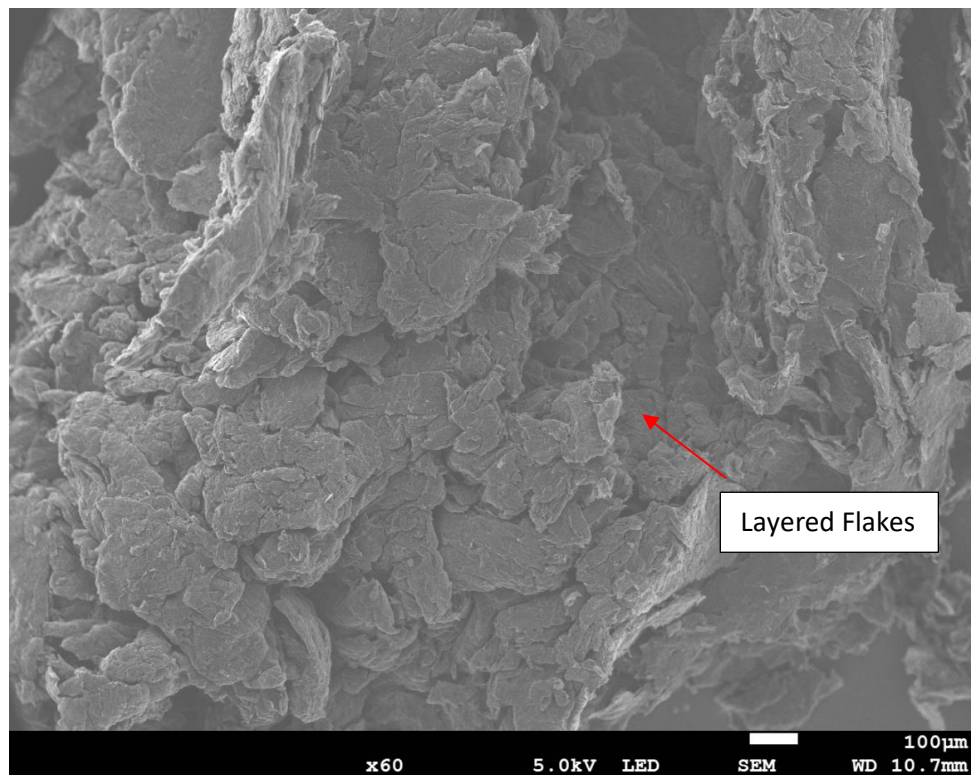
Figure 3.27: SEM image of BRGO showing 100 μm with x60 magnification
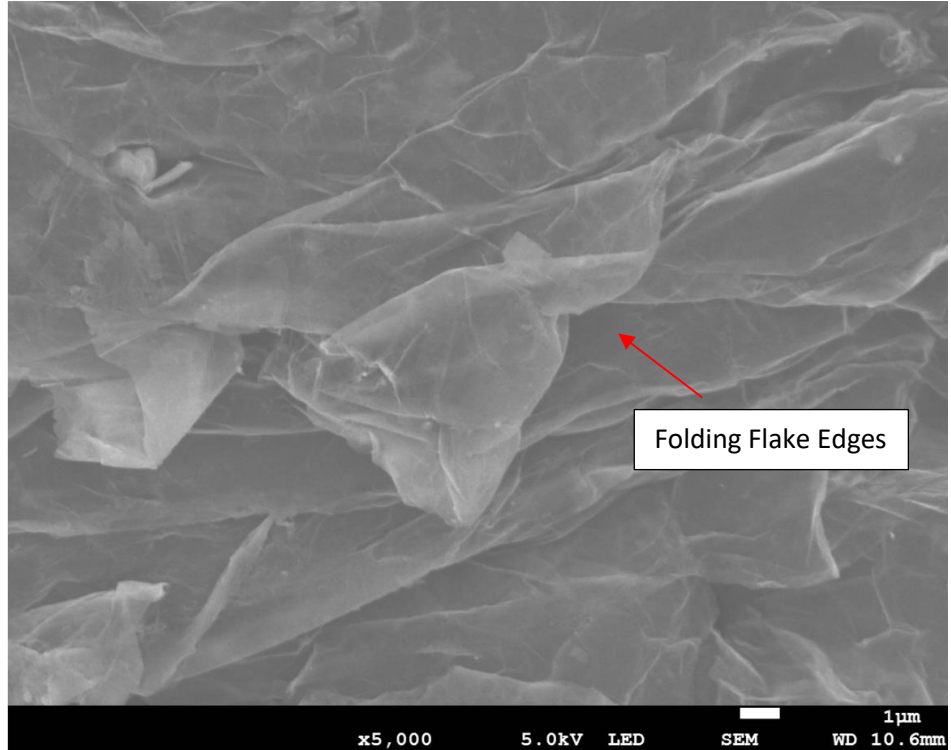
Figure 3.28: SEM image of BRGO showing 1 μm with x5000 magnification

Figures 3.26 and 3.27 show the flake like structure of BRGO. In comparison to BGO the flakes appear more fragmented. The flake edges exhibit folding. In comparison to RGO (Figures 3.11 and 3.12) the agglomerations spread throughout the sample aren't present in BRGO suggesting the agglomerates are most likely clusters of unwashed contamination originated from the synthesis of HGO.

EDS

An EDS layered image for BGO is shown below:
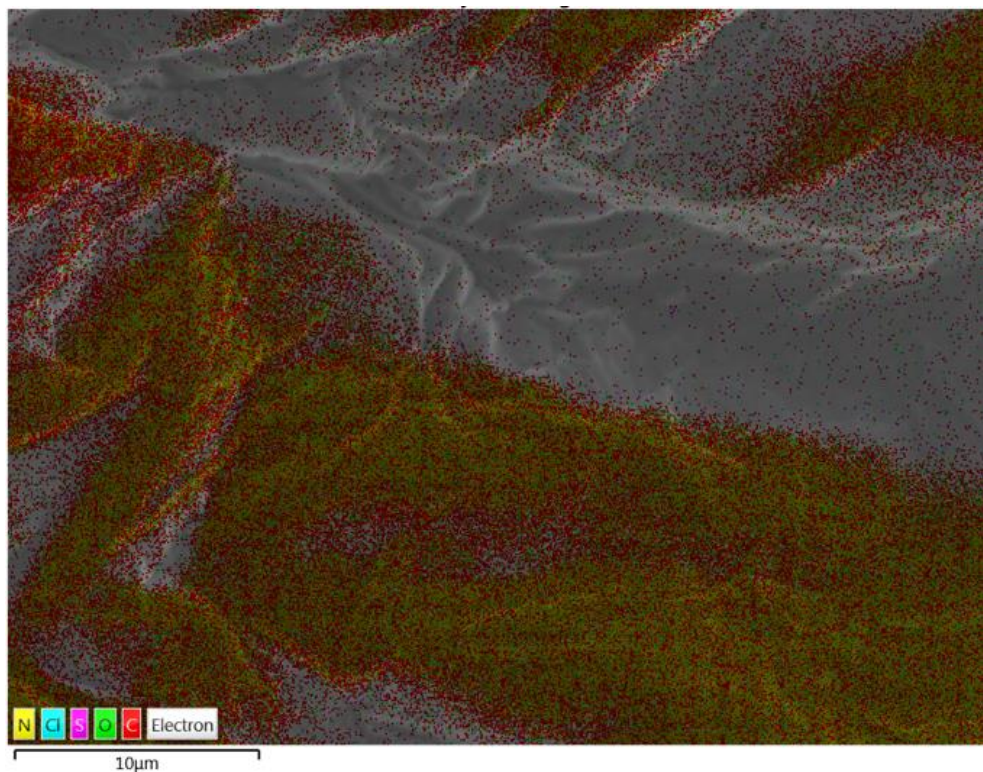
Figure 3.29: EDS layered image of BGO with colour key for elemental identification

Figure 3.29 shows that the BGO sample analysed is highly oxidised with oxygen distributed across the entire carbon surface. There is also a small amount of evenly distributed nitrogen present on the surface of this sample. Quantitative analysis of the same portion of this sample

was conducted to evaluate its chemical constitution more thoroughly. The EDS spectrum for

BGO is shown below:
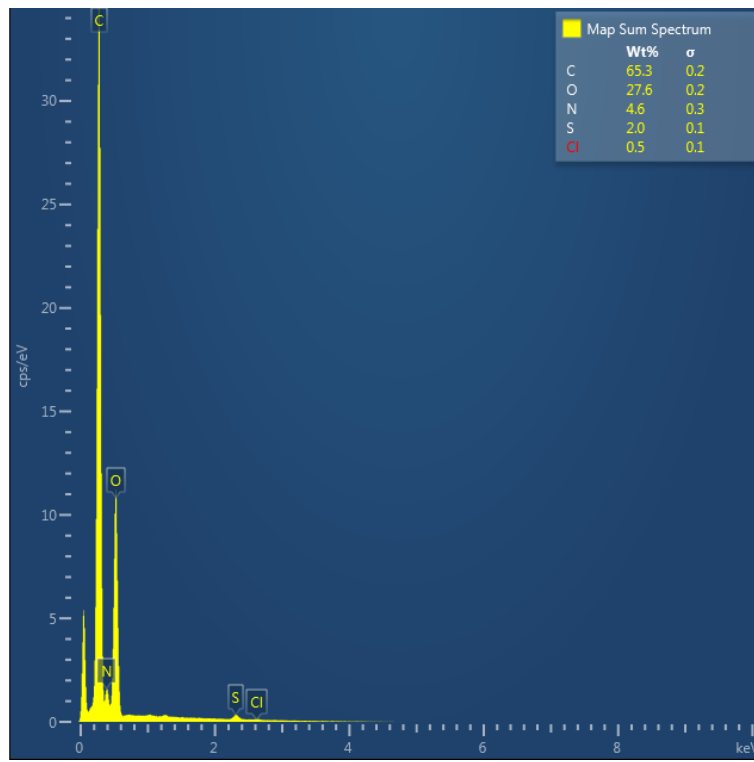
Figure 3.30: EDS Spectrum of BGO sample portion shown in Figure 3.29

Figure 3.30 shows that BGO is moderately oxygenated with small quantities of nitrogen and

sulphur contaminants. An EDS layered image for BRGO is shown below:
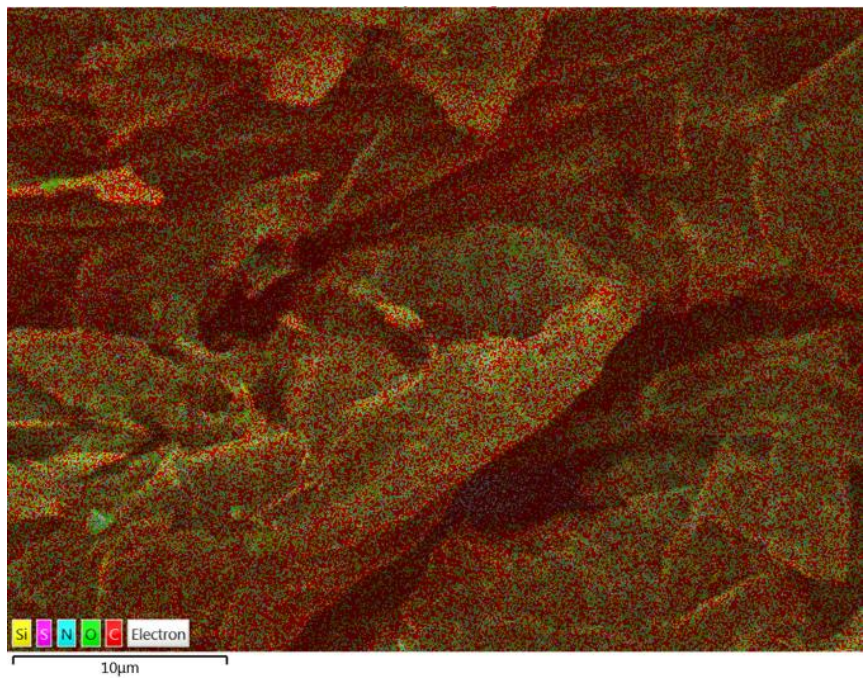
Figure 3.31: EDS layered image of BRGO with colour key for elemental identification

Figure 3.31 shows that the BRGO sample analysed is less oxidised in comparison to BGO suggesting reduction has been successful. Nitrogen is also present in small quantities distributed evenly on the surface of the sample. Quantitative analysis of the same portion of this sample was conducted to evaluate its chemical constitution more thoroughly. The EDS spectrum for BRGO is shown below:
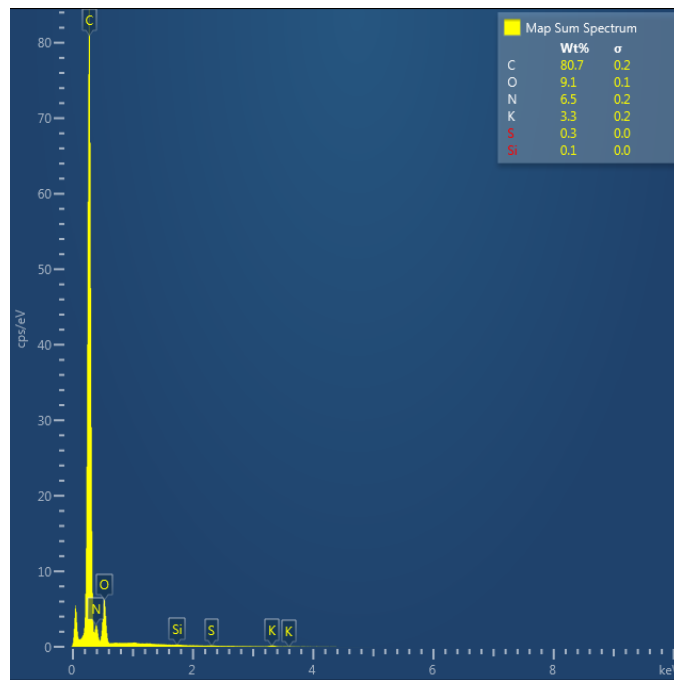
Figure 3.32: EDS Spectrum of BRGO sample portion shown in Figure 3.31

Figure 3.32 suggests that BRGO has been reduced effectively given the lower quantity of oxygen present within the EDS spectra in comparison to BGO. Small quantities of nitrogen and potassium contaminant are present in this BRGO sample. Given the even distribution of nitrogen across the surface of BGO and BRGO its origin is most likely a result of the synthetic process used.

^{13}C SSNMR

BGO and BRGO samples were analysed using ^{13}C MAS SSNMR. BGO was scanned 5520 times and BRGO 2784 times with a recycle delay of 30 seconds. The pulse length was 3.8 microseconds and MAS rate was 12.5 kHz. The SSNMR spectrum for BGO is shown below:
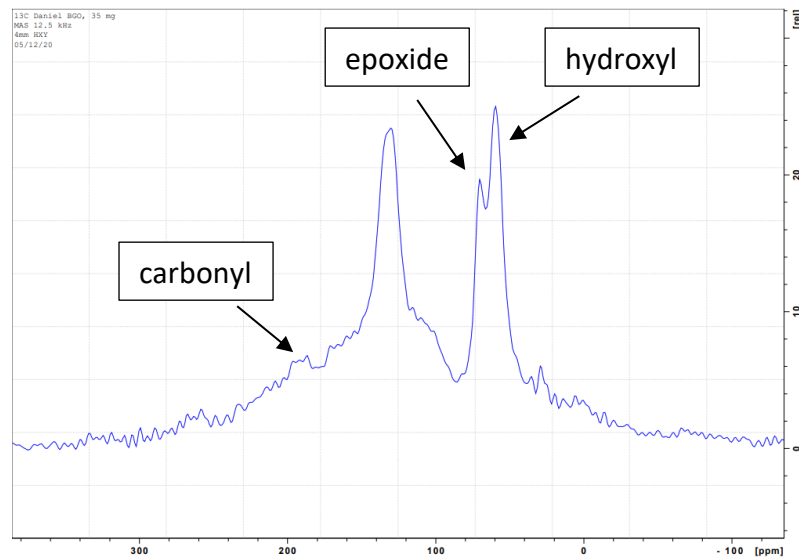
Figure 3.33: ^{13}C SSNMR spectrum of BGO

The graphitic Sp^2 peak can be seen at 130 ppm, peaks at 60 and 70 ppm show epoxide and hydroxyl groups respectively. The small broad peak at 190 ppm may indicate carbonyl functionality. The SSNMR spectra for RGO is shown below:
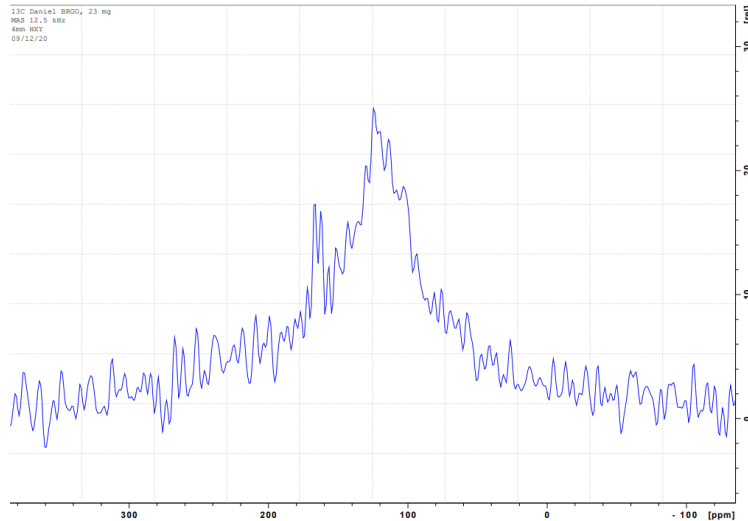
Figure 3.34: ^{13}C SSNMR spectrum of BRGO

The graphitic peak for RGO is shifted to 120 ppm suggesting successful reduction. The origin of the peak at 170 ppm which is also present in Figure 3.20 has already been discussed (3.2.3 ^{13}C SSNMR).

3.4 – Characterisation of a molecular sieve (MS)

To compare the adsorption capacity of HGO, RGO, BGO and RGO against a standard adsorbent a molecular sieve (A11535, 4A, powder) was purchased from Alfa Aesar. The chemical morphology and constitution of the powder was determined by SEM and EDS. SEM images of the MS are shown below at various magnifications:
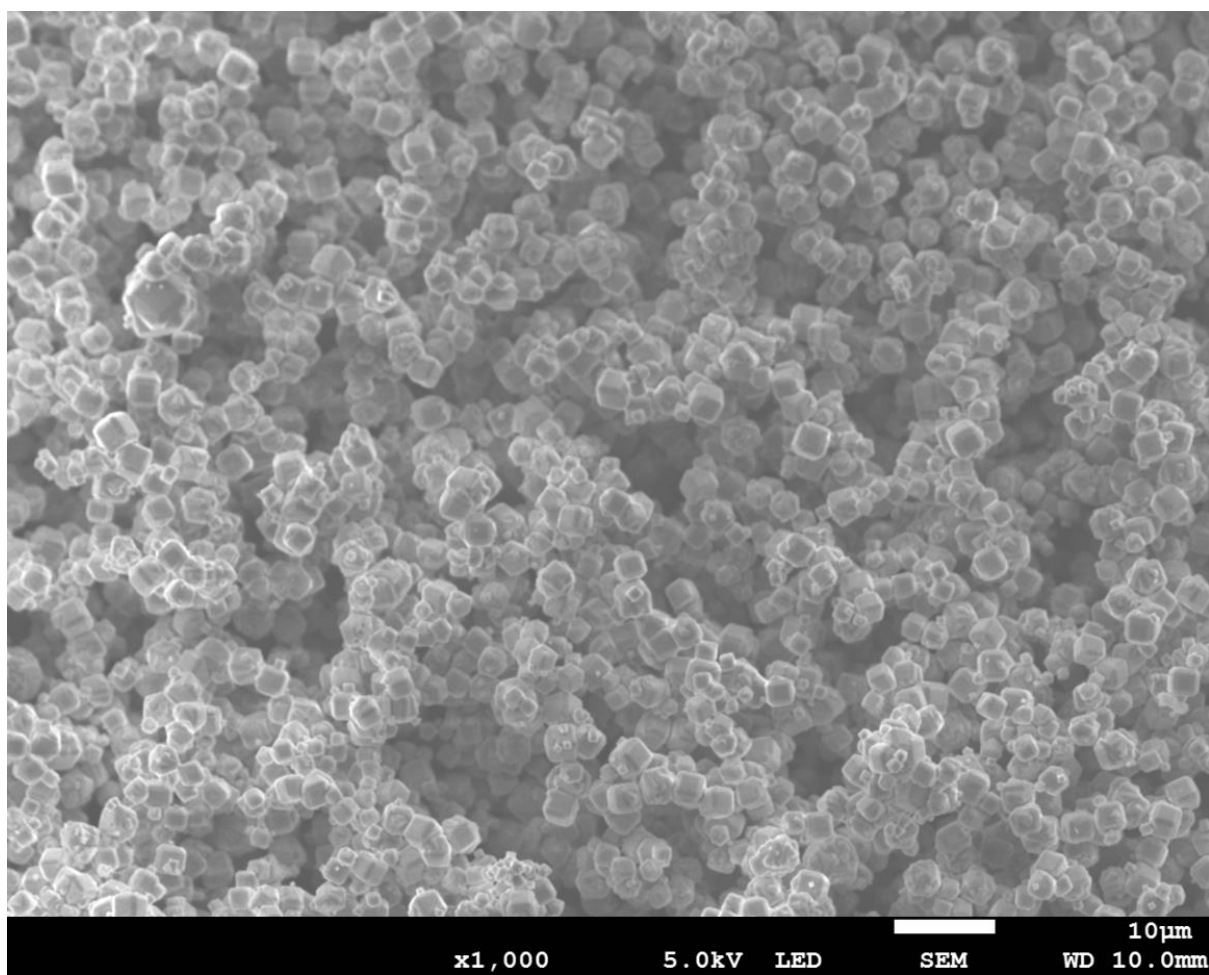
Figure 3.35: SEM image of MS showing 10 μm with x1000 magnification
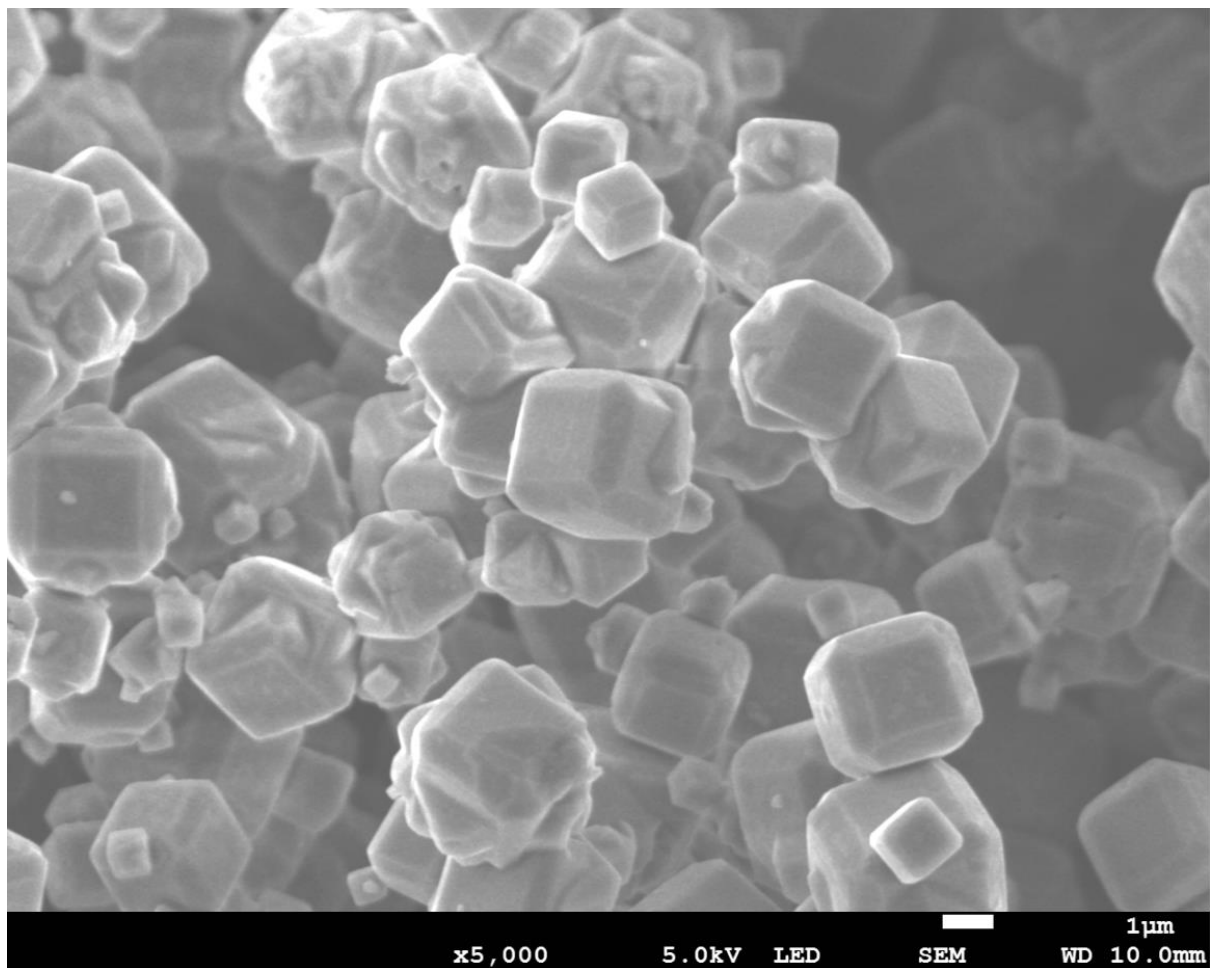
Figure 3.36: SEM image of MS showing 1 μm with x5000 magnification

Figures 3.35 and 3.36 show a uniform distribution of zeolite cubic crystals. The crystals vary in size and agglomeration of the crystals can be seen throughout the sample. The crystals form a complex network of various layers giving the adsorbent a large surface area.

EDS

An EDS layered image for the MS is shown below:
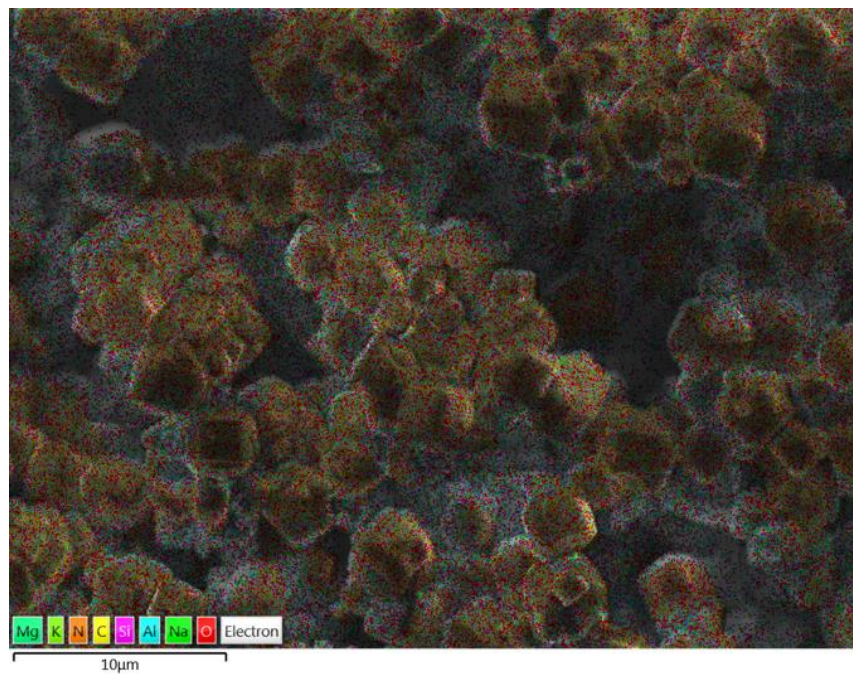
Figure 3.37: EDS layered image of MS with colour key for elemental identification

Figure 3.37 shows that the MS is predominately oxygen with even distribution throughout its structure. Sodium, Aluminium and Silicon constitute the remaining portion of the MS structure. The EDS spectrum for the MS is shown below:
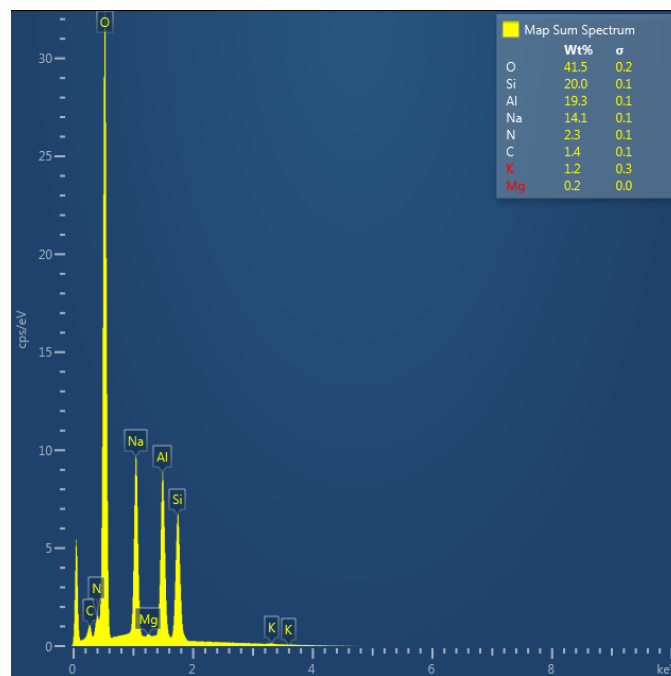
Figure 3.38: EDS Spectrum of BRGO sample portion shown in Figure 3.37

Chapter 4: Computational Models

4.1 – Model selection, creation, and limitations

To computationally determine the preferential adsorption locations and compare adsorption affinity of Cs and Sr ions for various surface modified analogues of graphene oxide, a series of single sheet graphene structures were created using GaussView. Each graphene sheet contains 49 carbon atoms and is surrounded by 50 water molecules. Given the periodic boundary conditions used within the computational model it was not possible to add functional groups to the edges of the graphene sheets. As the simulation is of a finite 2D region (graphene sheet) and this 2D region is repeated infinitely in 2 dimensions to create an infinite region. This results in the atoms on the edges of the finite 2D region being chemically bonded to the atoms on the edges in the repeat cell. This is the same for all the edges therefore functionalisation at the edges is not possible. The carboxyl groups which are typically found on the edges of graphene oxides sheets have instead been placed on the surface. Carbonyl groups have also been excluded from the edges and incorporated into the main body of the sheet through the deletion of carbon-carbon bonds. A total of 8 models have been prepared for simulation. 4.1.1 and 4.1.2 are models of HGO and RGO. 4.1.3, 4.1.4 and 4.1.5 are models taken from recent scientific literature on modified GO derivatives for various applications. 4.1.6, 4.1.7 and 4.1.8 are models developed from concepts which may not be synthetically plausible but may potentially elucidate the role targeted functionalisation of graphene oxide has in respect to ion adsorption.

4.1.1 – Reduced graphene oxide (RGO)

The RGO model used for AIMD simulation is based on a ≈ 10 % oxidised model of graphene

oxide and contains carboxyl, hydroxyl, epoxide, and carbonyl groups as shown below in Figure

4.1:
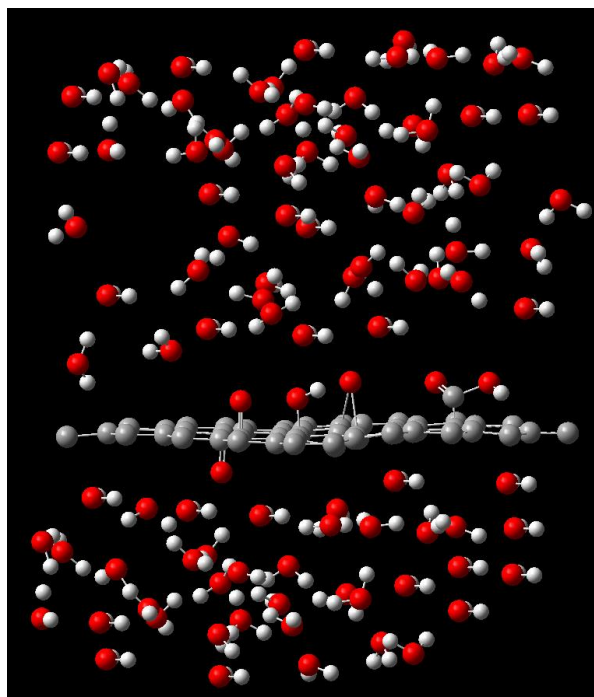
Figure 4.1: RGO model prepared in GaussView

4.1.2 – Hummers graphene oxide (HGO)

The HGO model used for AIMD simulation is based on a ≈ 20 % oxidised model of graphene

oxide which contains the same functional groups of RGO but in a greater abundance across

its surface, as shown below in Figure 4.2:
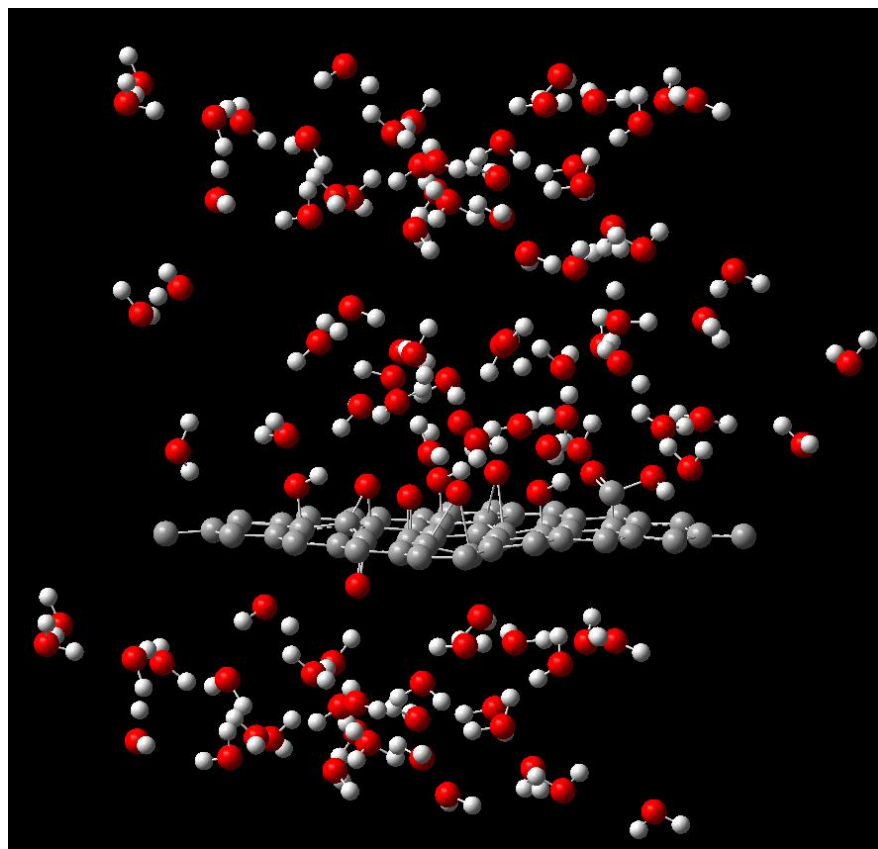
Figure 4.2: HGO model prepared in GaussView

4.1.3 – Fluorine functionalised graphene oxide (FFGO)

The FFGO structure is derived from the synthesis of fluorinated graphene oxide via a deoxyflourination reaction as conducted by Aguilar-Bolados et al. [110] The reaction uses diethylaminodifluorosulfinium tetrafluoroborate to replace oxygenated functional groups with fluorine as shown below in Figure 4.3:
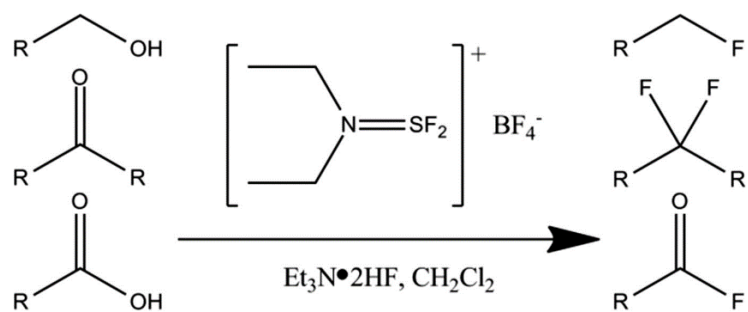
Figure 4.3: Fluorination of GO functional groups. [110]

The FFGO model is based on ≈ 5 % fluorination as achieved in the research and is shown below in Figure 4.4:
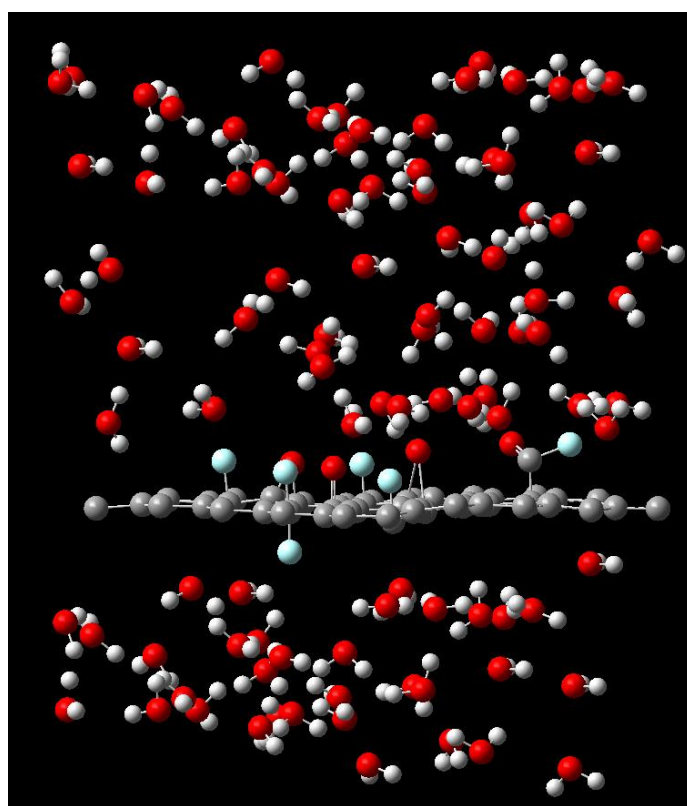
Figure 4.4: FFGO model prepared in GaussView

The model was chosen because it is a simple reaction and produces GO which contains both fluorinated and oxygenated functional groups. It is envisaged that the fluorinated groups will increase the electrostatic attraction of the GO sheet to the positively charged ions in solution.

4.1.4 – Nitrile functionalised reduced graphene oxide (NFRGO)

The NFRGO structure is derived from the synthesis of nitrile group functionalised graphene via a cycloaddition with tetracyanoethylene oxide as conducted by Peng et al. [111] The nitrile functionalisation of graphene is illustrated below in Figure 4.5:
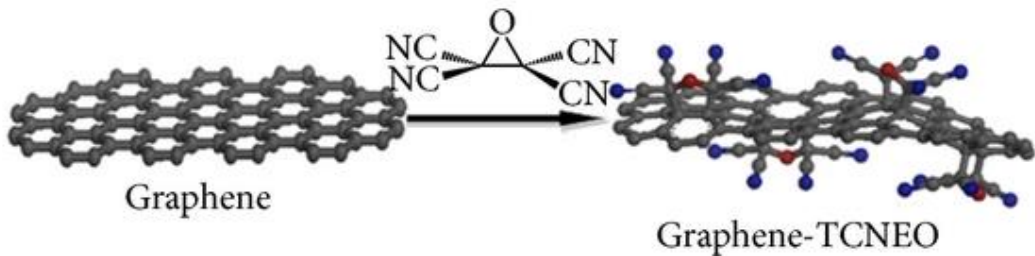
Figure 4.5: Addition of Nitrile groups to Graphene. [111]

The NFRGO model used is based on reduced graphene oxide functionalised with a single TCNEO group as shown below in Figure 4.6:
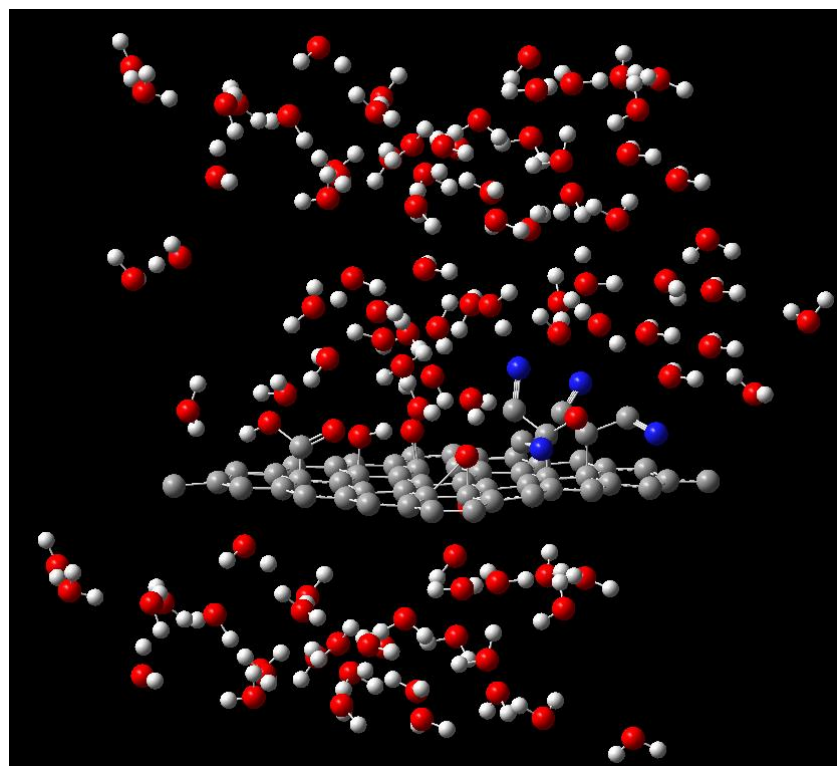
Figure 4.6: NFRGO model prepared in GaussView

The model was chosen to compare any attractive effect to positively charged ions in solution between the nitrile groups and the oxygen containing groups in reduced graphene oxide. It is envisaged that the nitrile groups being points of negative charge due to their lone pairs of

electrons and their electronegative nitrogen will be attractive to positive charged ions in solution.

4.1.5 – Sulfonated functionalised reduced graphene oxide (SFRGO)

The SFRGO structure is derived from the synthesis of sulfinic acid group functionalised graphene oxide via sulfonation with an aryl diazonium salt as conducted by Mao-Ping et al. [112] The reaction scheme is shown below in Figure 4.7:
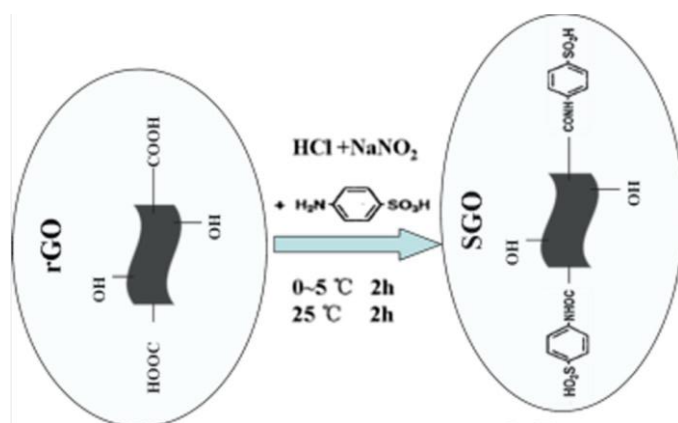
Figure 4.7: Addition of Nitrile groups to Graphene. [112]

The SFRGO model contains the sulfinic acid group on the surface of the RGO sheet in difference to the edge of the sheet as shown in Figure 4.7. This is due to the limitation of the computational model imposed by the periodic boundary conditions. The SFRGO model is shown below in Figure 4.8:
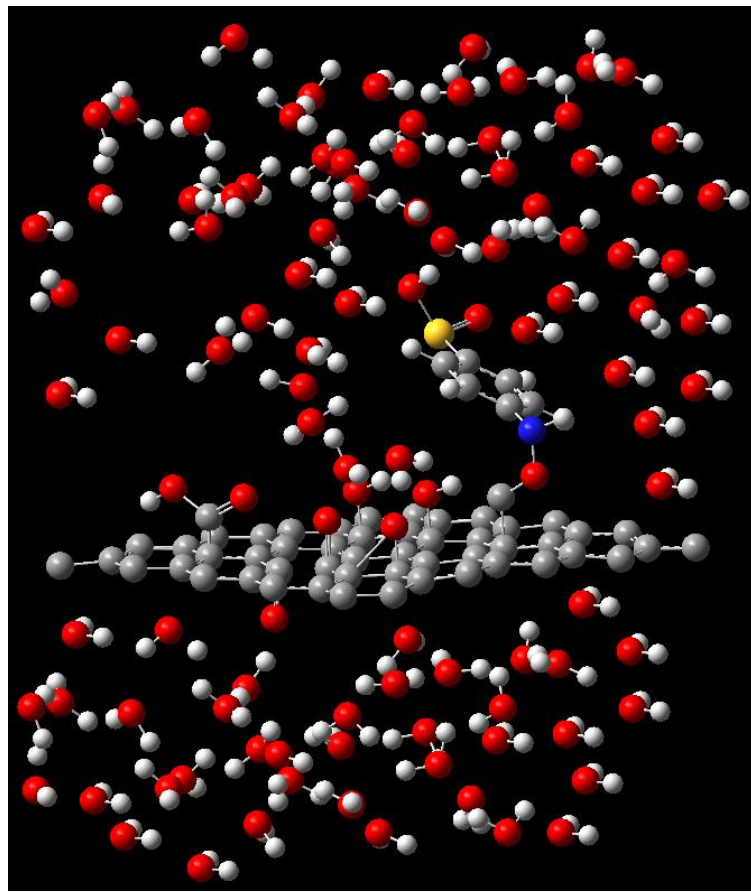
Figure 4.8: SFRGO model prepared in GaussView

It is envisaged that the sulfinic acid group will increase the electrostatic attraction of the GO sheet to the positively charged ions in solution.

4.1.6 – Fluorinated graphene oxide (FGO)

The FGO structure has an even distribution of four trifluoromethyl groups attached to the graphene sheet. The FGO model is shown below in Figure 4.9:
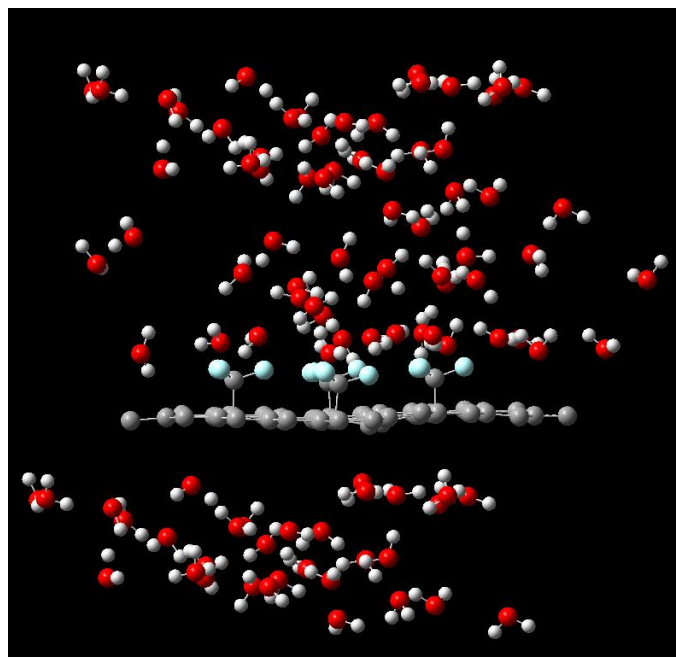
Figure 4.9: FGO model prepared in GaussView

4.1.7 – Nitrile group graphene oxide (NGO)

The NGO structure has an even distribution of six nitrile groups attached to the graphene sheet. The NGO model is shown below in Figure 4.10:
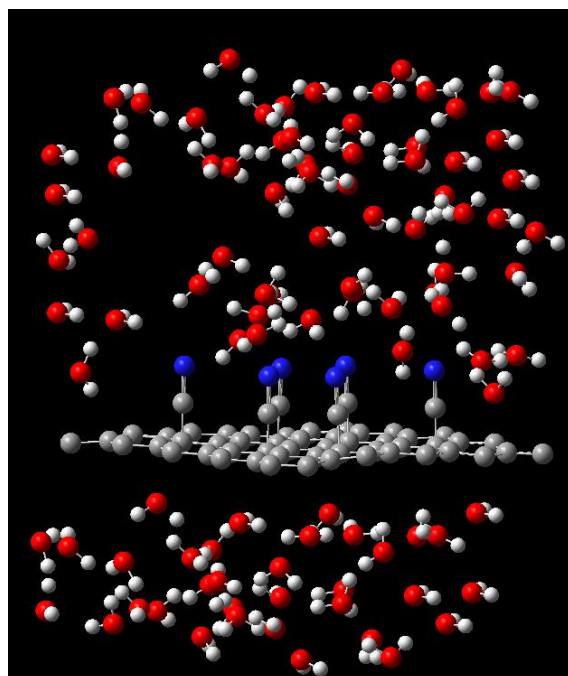
Figure 4.10: NGO model prepared in GaussView

4.1.8 – Sulphonic group graphene oxide (SGO)

The SGO structure has an even distribution of four sulphonic acid groups attached to the graphene sheet. The SGO model is shown below in Figure 4.11:
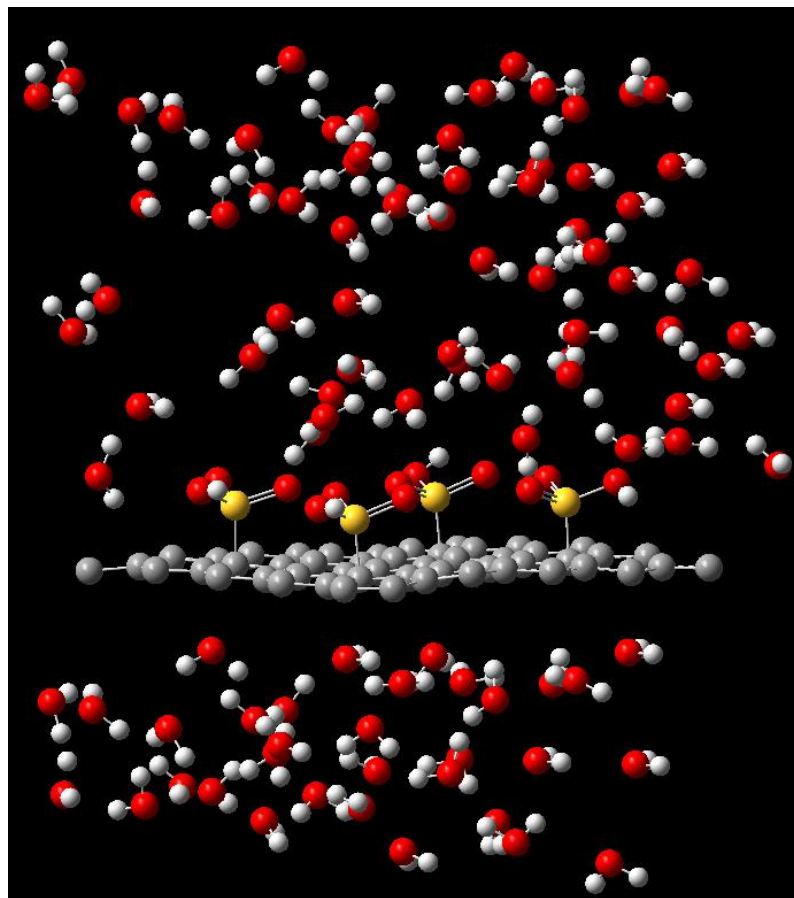
Figure 4.11: SGO model prepared in GaussView

Chapter 5: Computational and Experimental Methods

5.1 – Computational

Following the construction of the graphene derivatives, caesium hydroxide and strontium hydroxide were added separately into the computational models. The caesium and strontium ions were placed in three different locations for each graphene derivative and the corresponding derivative was given the notation A, B or C to reflect the position. The positions do not correspond to specific coordinates but provide approximate locations as to where the ions are placed within the computational box. The three positions are far away from the graphene surface (denoted A), closer to the graphene surface (denoted B) and underneath the graphene surface which is most functionalised (denoted C). The positions were chosen to simulate the behaviour of the ions at various distances to each graphene sheet variant. Following the addition of the ions a geometry optimisation was performed using CP2K. This is an energy minimisation calculation to determine the arrangement of atoms were their net inter-atomic forces are acceptably close to zero and their position on the potential energy surface is a stationary point. [113] The optimised structure is used for the AIMD simulations as the optimised structure has the most realistic conformation. The input code for the optimisations is shown in Appendix D. Tables 5.1 and 5.2 below show a summary of the attempted optimisations for all graphene derivatives with each ion and its location and states whether the optimisations were successful or unsuccessful:

Caesium

Structure	Ion Position		
	A	B	C
RGO	Successful	Failed	Failed
HGO	Successful	Successful	Failed
FFGO	Successful	Failed	Failed
NFRGO	Failed	Failed	Failed
SFRGO	Failed	Failed	Failed
FGO	Failed	Failed	Failed
NGO	Successful	Failed	Failed
SGO	Failed	Failed	Failed

Table 5.1: Status of optimisation of models containing Cs^+ ion

Strontium

Structure	Ion Position		
	A	B	C
RGO	Successful	Successful	Successful
HGO	Successful	Successful	Successful
FFGO	Successful	Successful	Failed
NFRGO	Successful	Successful	Failed
SFRGO	Failed	Failed	Failed
FGO	Failed	Failed	Failed
NGO	Successful	Successful	Successful
SGO	Successful	Successful	Failed

Table 5.2: Status of optimisation of models containing Sr^{2+} ion

Optimisations were unsuccessful due to ill conditioned matrix's by Cholesky decomposition failure. This problem was alleviated by increasing the size of the computational box (Appendix D, line ABC, value C) on a trial and error basis. The C value was increased by 0.250 until the optimisation was successful. The successfully optimised structures containing Cs^+ are shown below (Cs^+ displayed in the colour dark brown by GaussView software):
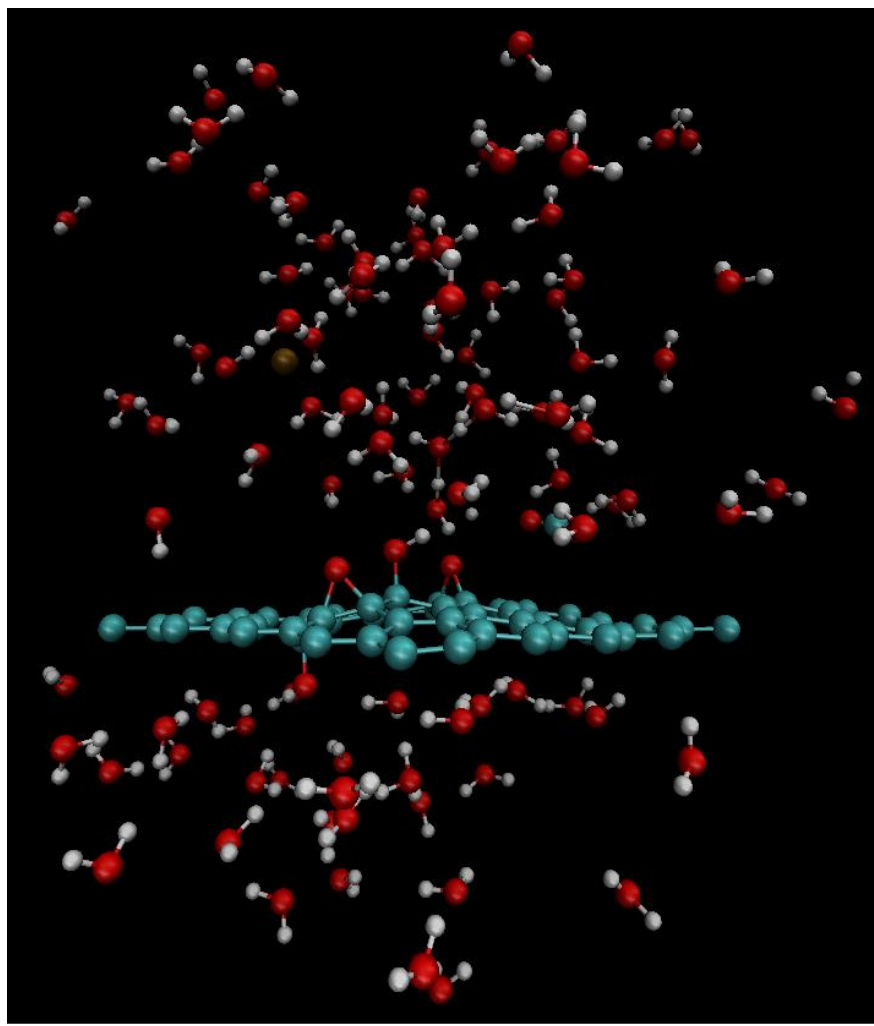
Figure 5.1: Optimised RGO model showing Cs$^+$ ion at position A
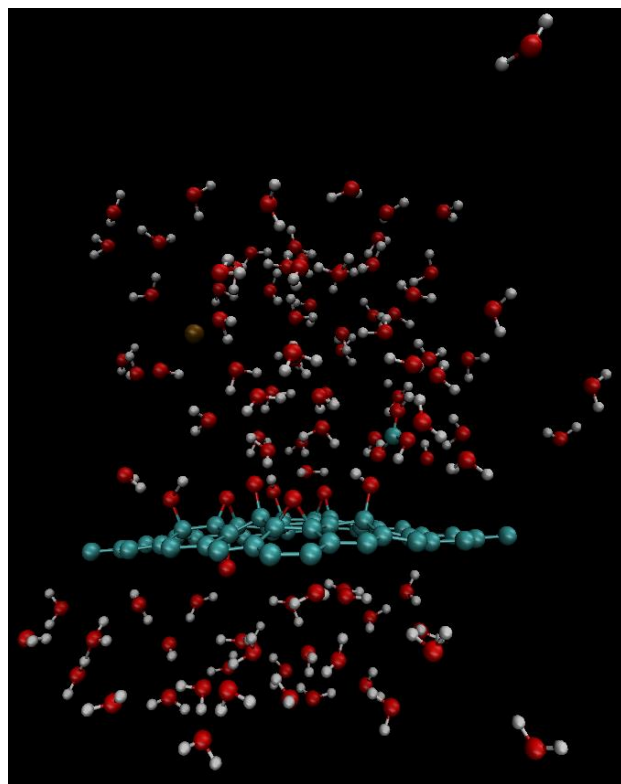
Figure 5.2: Optimised HGO model showing Cs$^+$ ion at position A
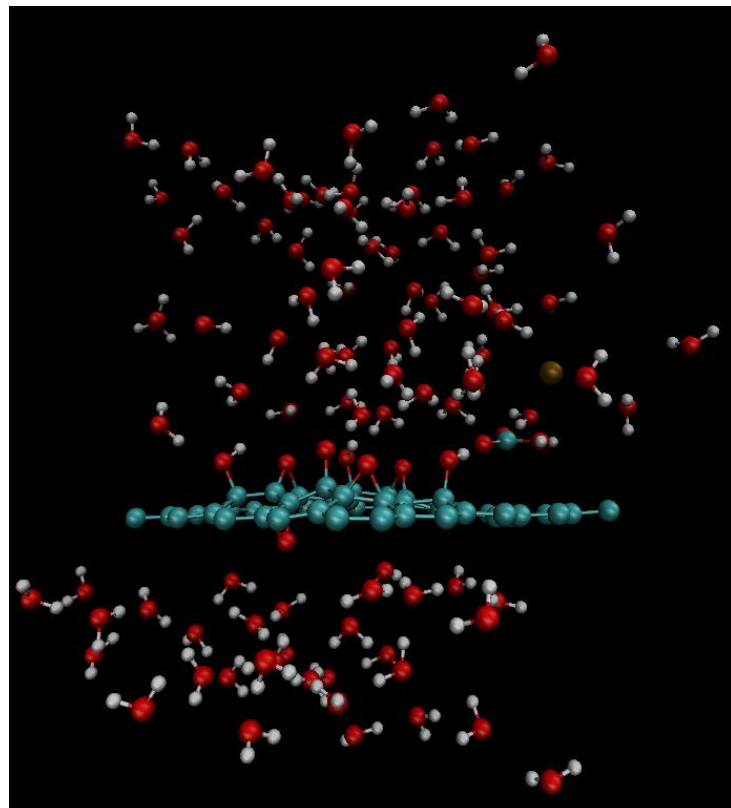
Figure 5.3: Optimised HGO model showing Cs$^+$ ion at position B
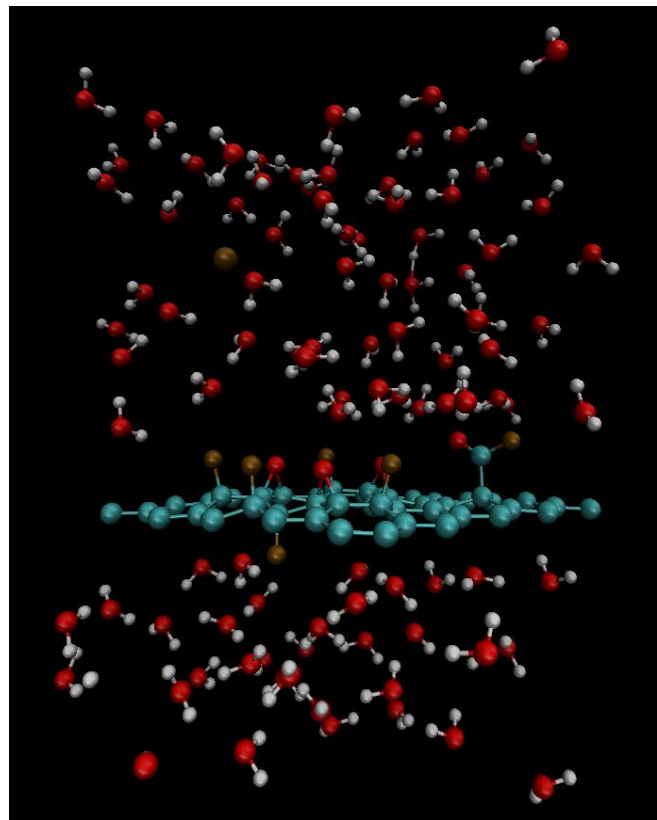
Figure 5.4: Optimised FFGO model showing Cs$^+$ ion at position A
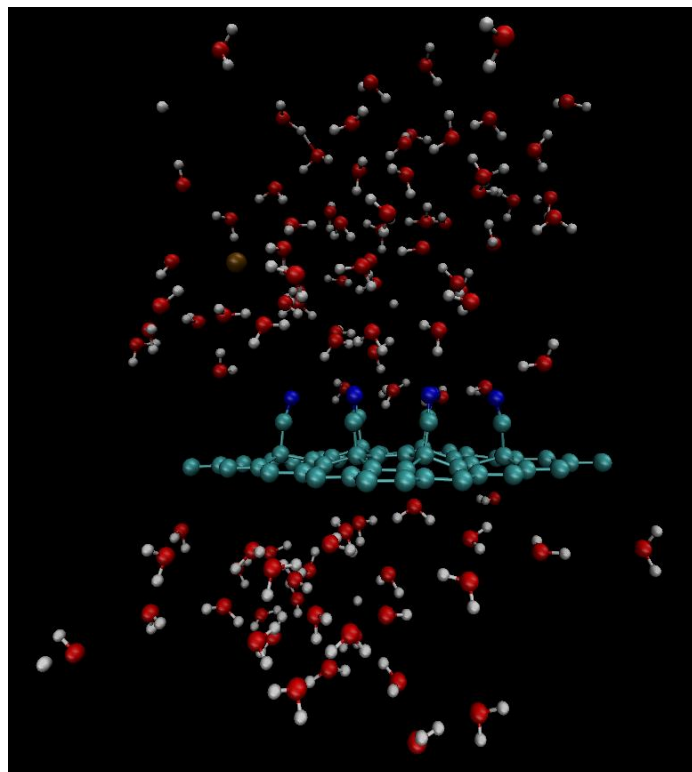
Figure 5.5: Optimised NGO model showing Cs$^+$ ion at position A

The successfully optimised structures containing Sr^{2+} are shown below (Sr^{2+} displayed in the colour dark brown by GaussView software):
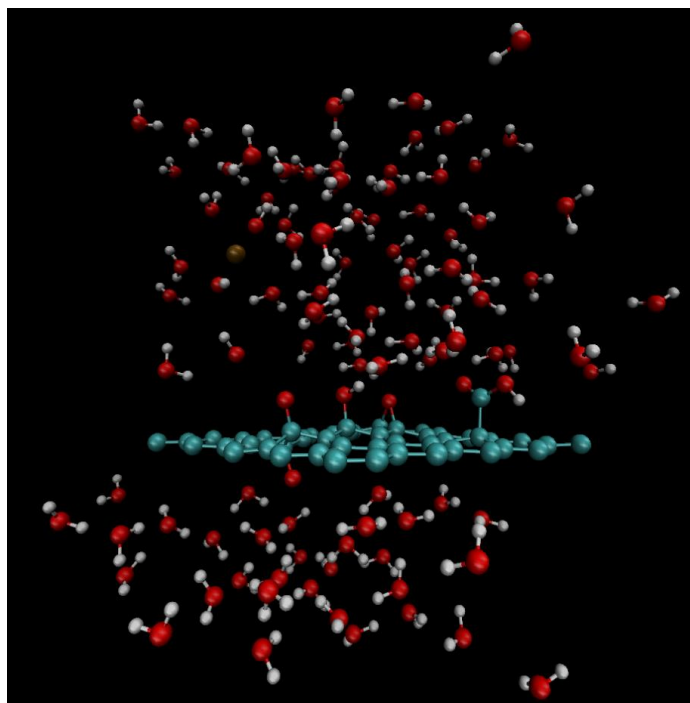
Figure 5.6: Optimised RGO model showing Sr^{2+} ion at position A
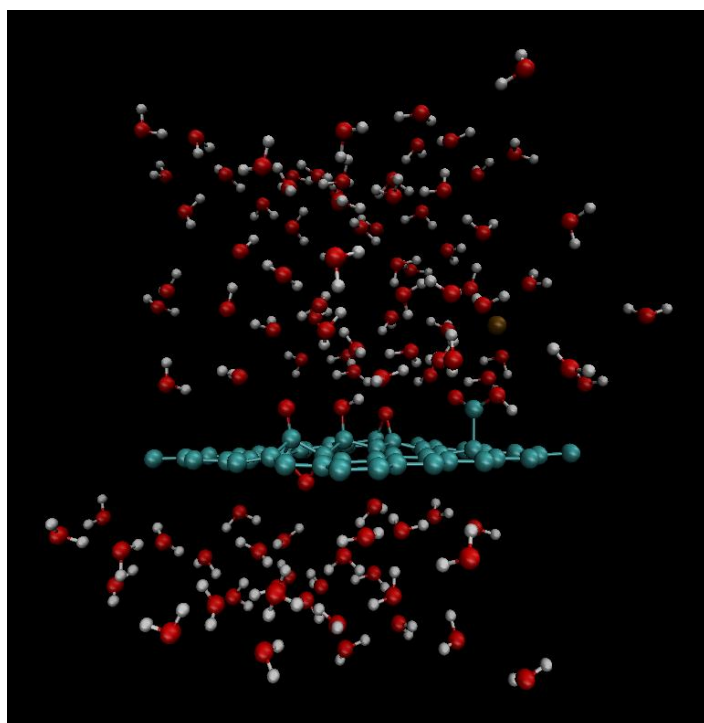
Figure 5.7: Optimised RGO model showing Sr^{2+} ion at position B
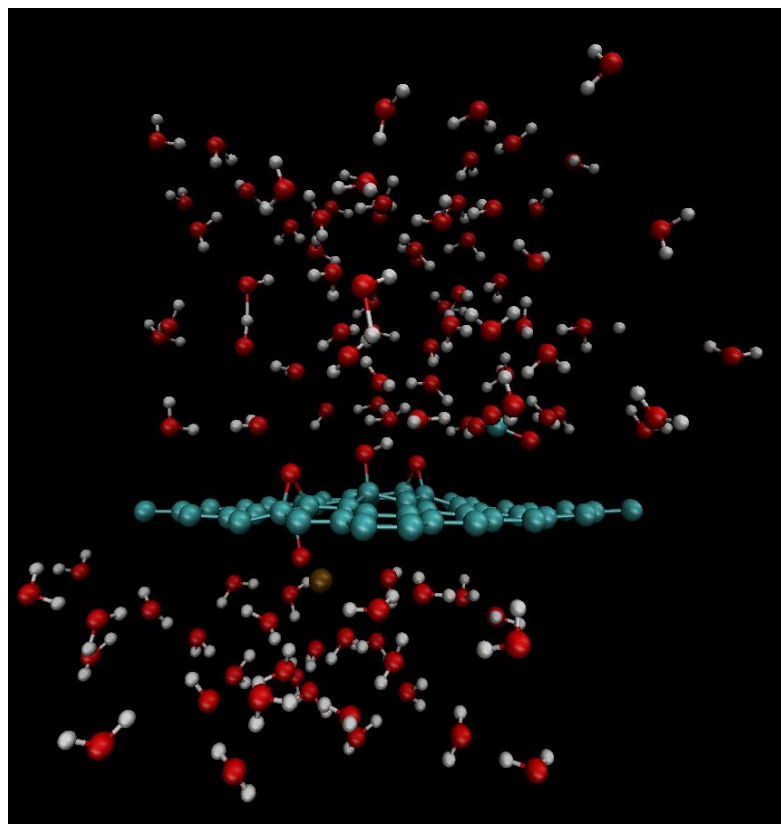
Figure 5.8: Optimised RGO model showing Sr^{2+} ion at position C
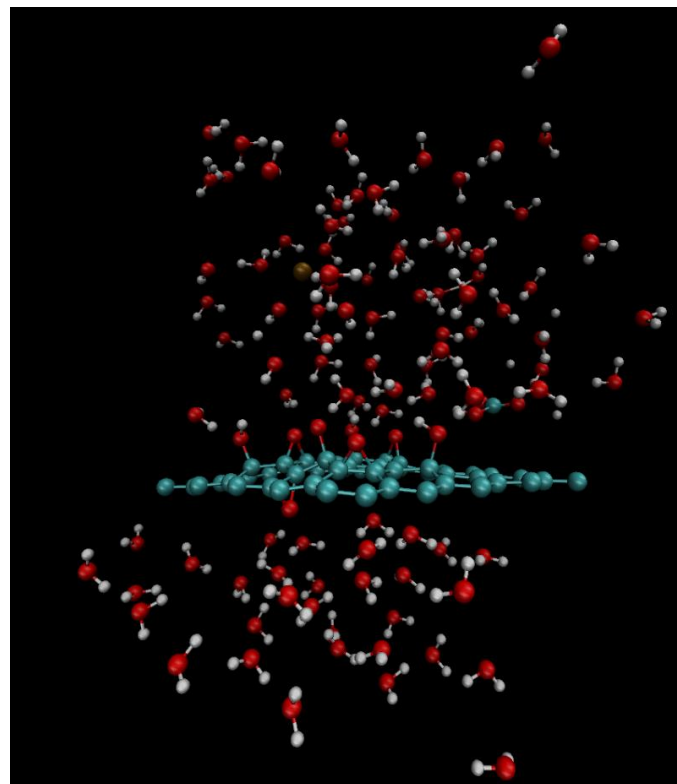
Figure 5.9: Optimised HGO model showing Sr^{2+} ion at position A
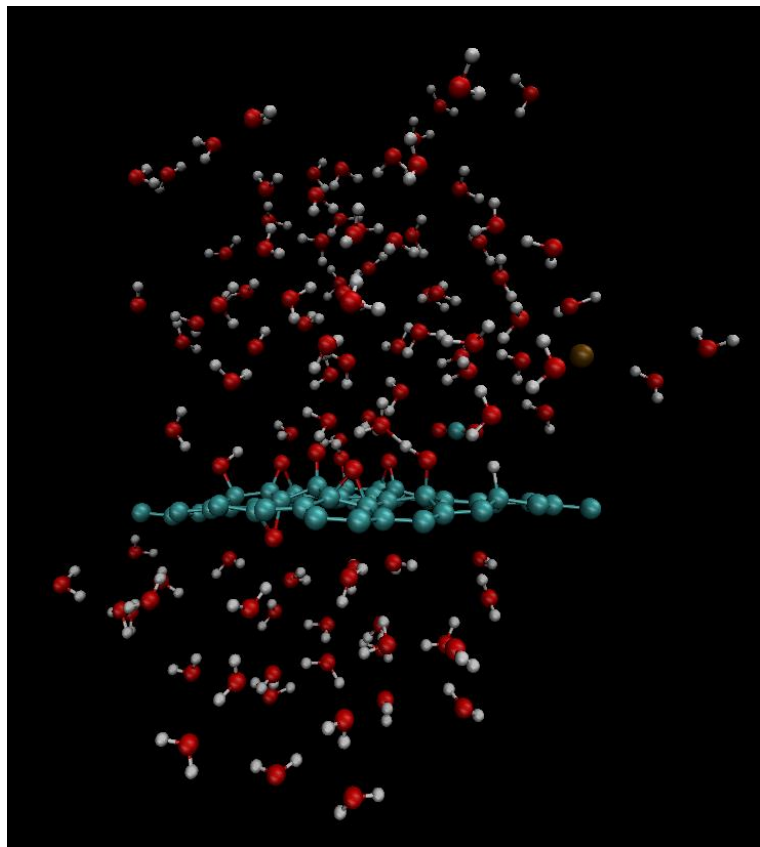
Figure 5.10: Optimised HGO model showing Sr^{2+} ion at position B
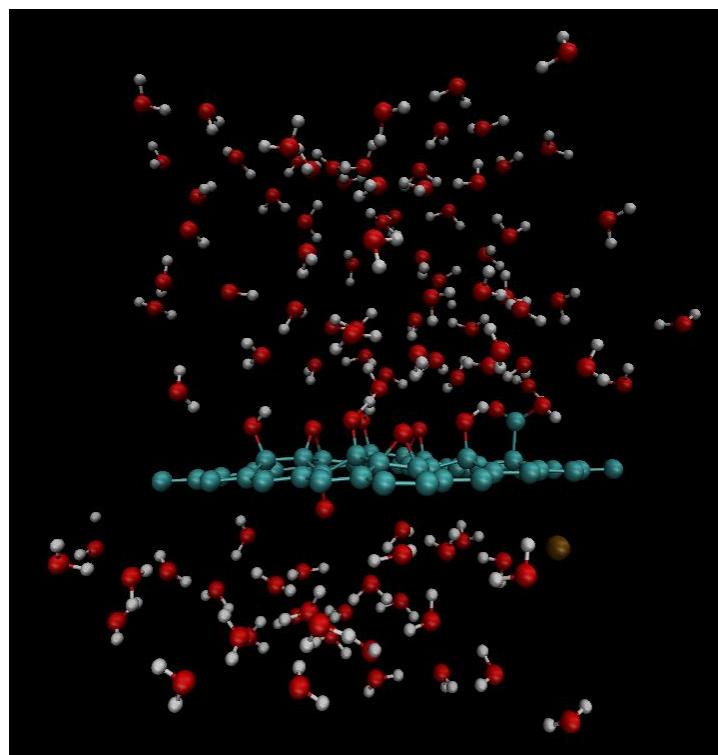
Figure 5.11: Optimised HGO model showing Sr^{2+} ion at position C
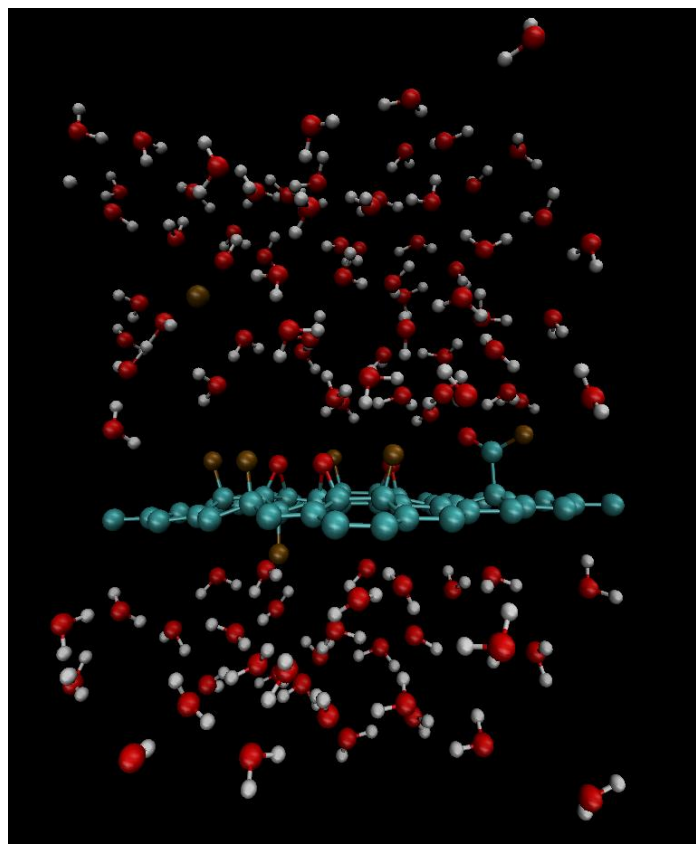
Figure 5.12: Optimised FFGO model showing Sr^{2+} ion at position A
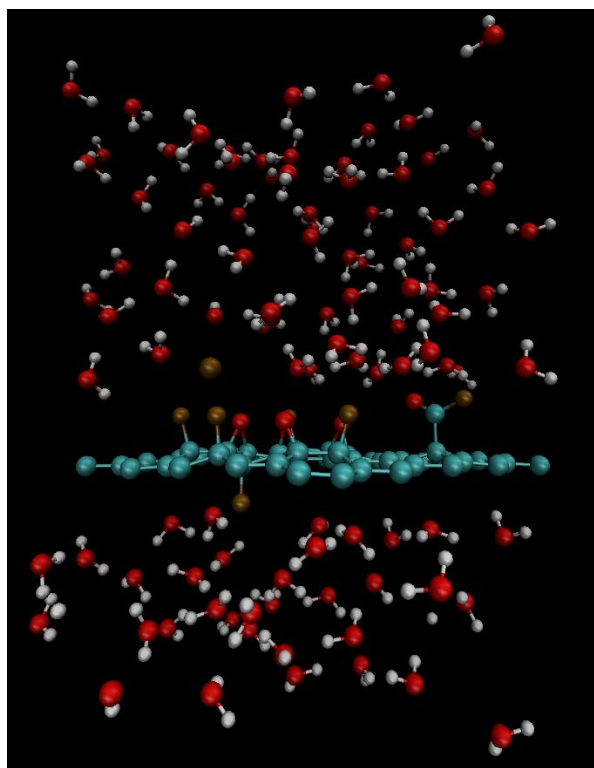
Figure 5.13: Optimised FFGO model showing Sr^{2+} ion at position B
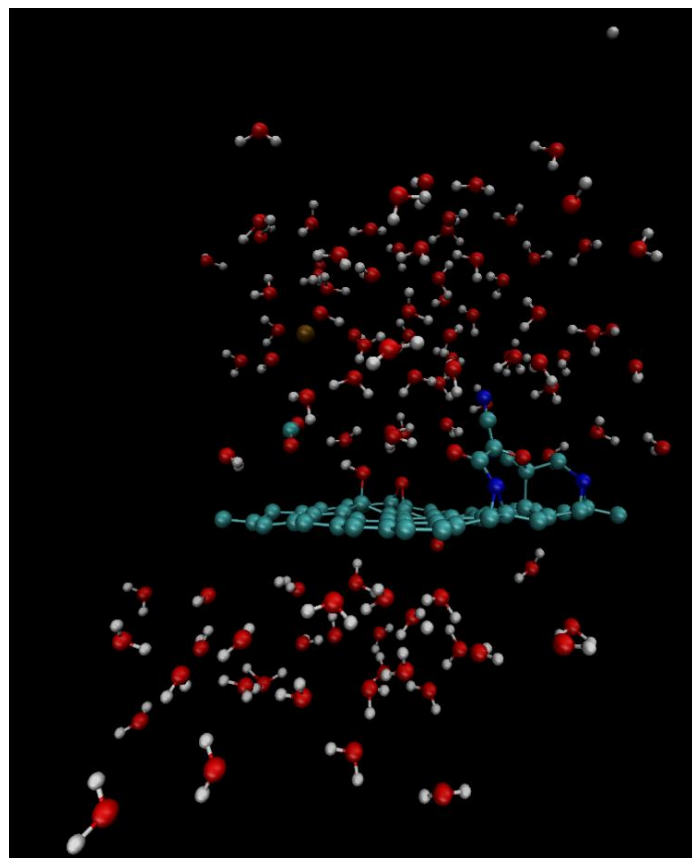
Figure 5.14: Optimised NFRGO model showing Sr^{2+} ion at position A
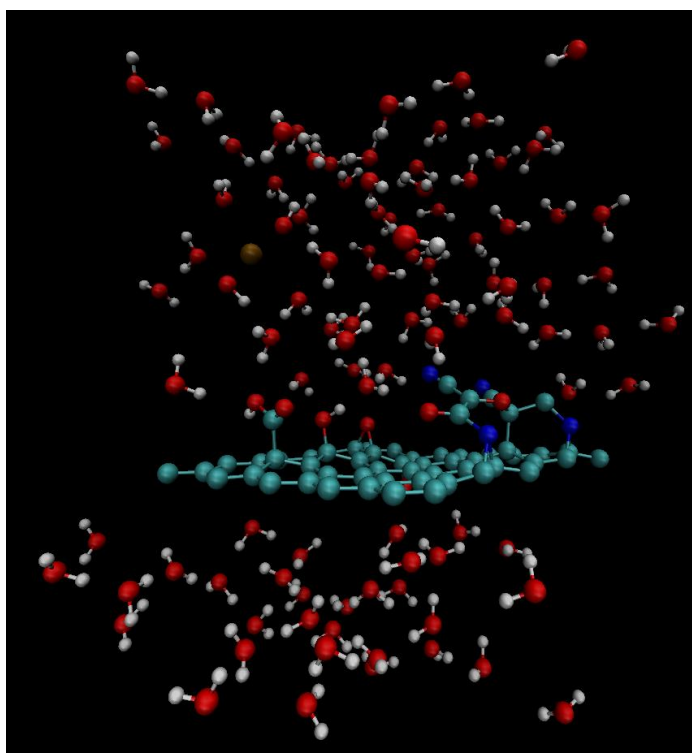
Figure 5.15: Optimised NFRGO model showing Sr^{2+} ion at position B
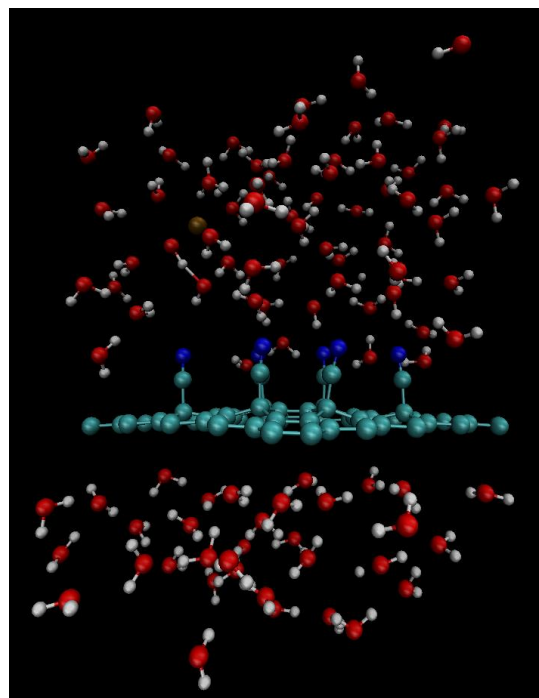
Figure 5.16: Optimised NGO model showing Sr^{2+} ion at position A
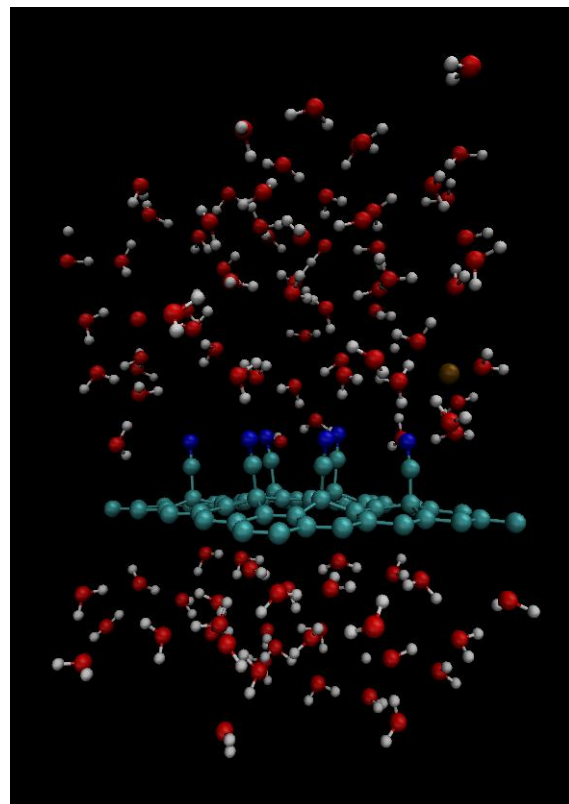
Figure 5.17: Optimised NGO model showing Sr^{2+} ion at position B
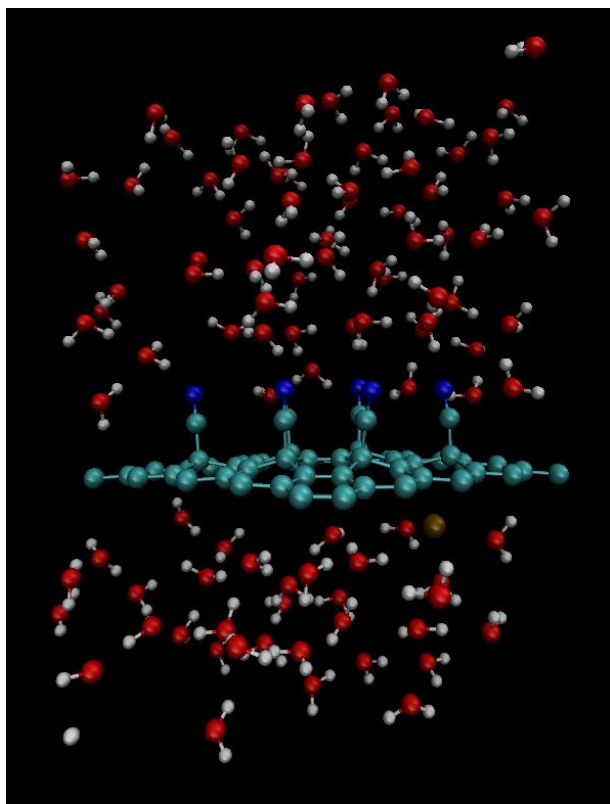
Figure 5.18: Optimised NGO model showing Sr^{2+} ion at position C
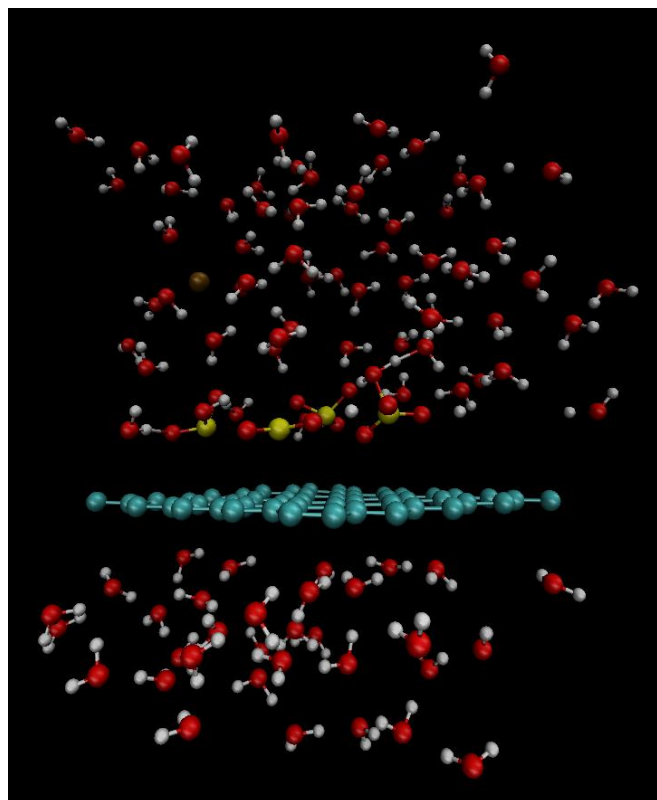
Figure 5.19: Optimised SGO model showing Sr^{2+} ion at position A
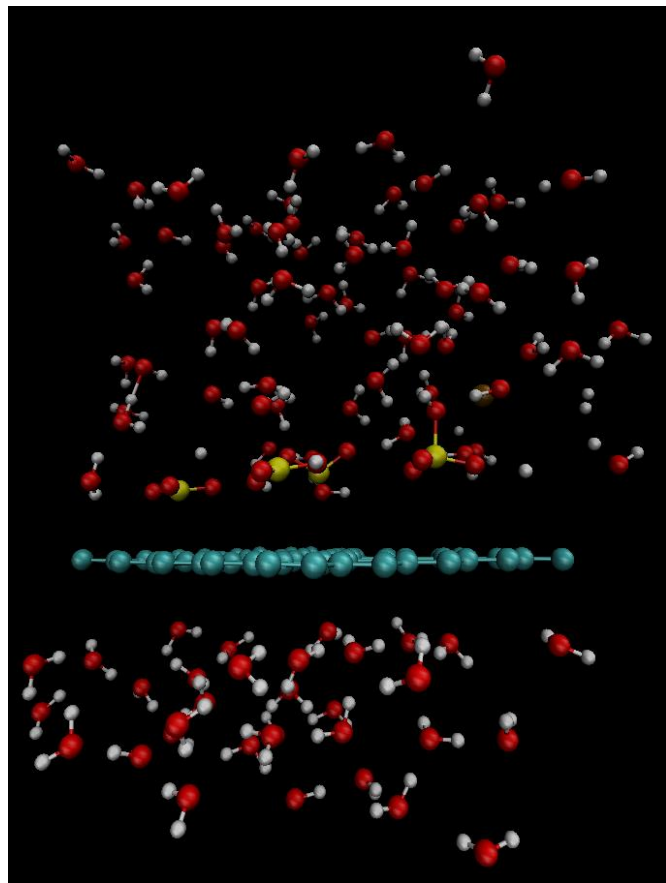
Figure 5.20: Optimised SGO model showing Sr^{2+} ion at position B

Following successful optimisation, AIMD simulations were performed using the same computational box size. The coordinate file generated from the optimisation was used as the input coordinate file for the AIMD simulation. The AIMD simulations were performed for 40000 timesteps with each timestep being 5 femtoseconds. Simulations which failed during the initial 40000 timestep simulation were restarted at a timestep in which the system was stable and prior to any rapid change in energy which would suggest break down in system stability. Simulations which failed were restarted for another 40000 timesteps hence why some of the simulations have greater than 40000 timesteps in total simulation time. AIMD simulations were performed at temperatures of 400K but this was adapted were appropriate if initial system stability could not be achieved at this temperature. 400 K was chosen as the original minimum simulation temperature as generalised gradient approximation DFT results

in frozen water at 300 K. However, 300 K was used if the system temperature greatly increased over the first few hundred timesteps and 500 K was used if the system temperature greatly decreased over the first few hundred timesteps. The temperature was subsequently changed back to 400K after 2000 timesteps once the system established stability. If system stability could not be achieved by adapting the initial temperature input, then the optimisation for the system was reperformed with a different computational box size to attempt to rectify the issue. The input code used for the AIMD simulations is shown in Appendix E.

5.2 – Filtration

Adsorption experiments were performed by filtering solutions of Cs and Sr through samples of HGO, RGO, BGO, BRGO and the MS using a sintered funnel attached to a Buchner flask subject to a vacuum as shown below in Figure 5.21:

Figure 5.21: Sintered funnel attached to Buckner flask subjected to vacuum

Cs and Sr solutions were also filtered through the funnel without a sample to act as a standard comparison. Cs(OH).xH$_2$O and Sr(OH)$_2$.8H$_2$O were used to give suitable concentrations for each ion. Approximations for the quantity of sample were determined based on the required mass needed to completely cover the surface of the sintered funnel once the sample had been ground using a mortar and pestle to achieve an evenly distributed sample layer as shown below in Figure 5.22:

Figure 5.22: Flakes of HGO contained in sintered funnel after being ground

Concentrations of Cs and Sr were determined by the oxygen % of the graphene derivatives so that there would be an equal molar concentration of the ion filtered through a sample with an equal molar concentration of oxygen, for example:

BGO

Mass required for even distribution over sintered funnel = 0.075 g

Mass of oxygen based on EDS analysis = 0.021 g

Moles of oxygen = 1.3125×10^{-3}

Mass of strontium = 0.114975 g

Mass multiplier (Sr to $Sr(OH)_2.8H_2O$) = 3.032

Mass of $Sr(OH)_2.8H_2O$ = 0.349 g

All masses of $Cs(OH).xH_2O$ and $Sr(OH)_2.8H_2O$ were dissolved in 200 ml of deionised water except for $Sr(OH)_2.8H_2O$ filtered through HGO which was dissolved in 1.2 L given its solubility of 4.1 g/L. Half the mass of the HGO sample was filtered against 600 ml of $Sr(OH)_2.8H_2O$ solution, 25 ml of each of the 600 ml filtrate were retained for ICP analysis to determine % ion adsorption. $Cs(OH).xH_2O$ and $Sr(OH)_2.8H_2O$ were filtered through the MS as approximately equivalent quantities. Each filtration was repeated three times using unfiltered samples from the stock samples. The filtrate was added slowly as to not dislodge the sample from the base of the sintered funnel to avoid the formation of sample gaps with the aim to achieve full saturation of the sample and prevent the filtrate bypassing the sample. 50 ml of the filtrate from each sample was retained for ICP analysis to determine % ion adsorption. The masses of each sample and masses of $Cs(OH).xH_2O$ and $Sr(OH)_2.8H_2O$ per volume used for each filtration are shown below in tables 5.3 and 5.4:

Sample	Sample Mass (g)	Filtrate	Filtrate Mass (g)	Filtrate Volume (ml)
No 1	0	$Cs(OH).xH_2O$	0.2735	200
No 2	0	$Cs(OH).xH_2O$	0.2741	200
No 3	0	$Cs(OH).xH_2O$	0.2736	200
HGO 1	0.7616	$Cs(OH).xH_2O$	3.2027	200
HGO 2	0.7621	$Cs(OH).xH_2O$	3.2034	200
HGO 3	0.7619	$Cs(OH).xH_2O$	3.2026	200
RGO 1	0.1753	$Cs(OH).xH_2O$	0.2190	200
RGO 2	0.1758	$Cs(OH).xH_2O$	0.2186	200
RGO 3	0.1754	$Cs(OH).xH_2O$	0.2192	200
BGO 1	0.0752	$Cs(OH).xH_2O$	0.2386	200
BGO 2	0.0755	$Cs(OH).xH_2O$	0.2391	200
BGO 3	0.0761	$Cs(OH).xH_2O$	0.2385	200
BRGO 1	0.1907	$Cs(OH).xH_2O$	0.1951	200
BRGO 2	0.1912	$Cs(OH).xH_2O$	0.1949	200
BRGO 3	0.1909	$Cs(OH).xH_2O$	0.1953	200
MS 1	1.0037	$Cs(OH).xH_2O$	1.0022	200
MS 2	1.0009	$Cs(OH).xH_2O$	1.0019	200
MS 3	1.0028	$Cs(OH).xH_2O$	1.0005	200

Table 5.3: Sample masses and $Cs(OH).xH_2O$ mass and volume used for filtration

Figure 5.23: MS contained in sintered funnel

Sample	Sample Mass (g)	Filtrate	Filtrate Mass (g)	Filtrate Volume (ml)
No 1	0	$Sr(OH)_2.8H_2O$	0.2014	200
No 2	0	$Sr(OH)_2.8H_2O$	0.2018	200
No 3	0	$Sr(OH)_2.8H_2O$	0.2017	200
HGO 1	0.7523	$Sr(OH)_2.8H_2O$	4.6178	1200
HGO 2	0.7551	$Sr(OH)_2.8H_2O$	4.638	1200
HGO 3	0.7564	$Sr(OH)_2.8H_2O$	4.646	1200
RGO 1	0.1753	$Sr(OH)_2.8H_2O$	0.3191	200
RGO 2	0.1759	$Sr(OH)_2.8H_2O$	0.3202	200
RGO 3	0.1748	$Sr(OH)_2.8H_2O$	0.3197	200
BGO 1	0.0751	$Sr(OH)_2.8H_2O$	0.3498	200
BGO 2	0.0759	$Sr(OH)_2.8H_2O$	0.3491	200
BGO 3	0.0754	$Sr(OH)_2.8H_2O$	0.3502	200
BRGO 1	0.1914	$Sr(OH)_2.8H_2O$	0.2854	200
BRGO 2	0.1921	$Sr(OH)_2.8H_2O$	0.2853	200
BRGO 3	0.1923	$Sr(OH)_2.8H_2O$	0.2847	200
MS 1	1.0004	$Sr(OH)_2.8H_2O$	1.0002	200
MS 2	1.0011	$Sr(OH)_2.8H_2O$	1.0002	200
MS 3	1.0009	$Sr(OH)_2.8H_2O$	1.0005	200

Table 5.4: Sample masses and $Sr(OH)_2.8H_2O$ mass and volume used for filtration

Following filtration, a portion of the ion exposed solid sample was taken for ^{13}C SSNMR analysis for spectra comparison with stock samples.

Chapter 6: Results

6.1 – AIMD Simulations

Completed AIMD simulations generated. xyz coordinate files which contain the ion locations for each time step in each simulation. These files were uploaded to VMD to visualise the evolution of the systems over time. The ion trajectories were overlayed on the optimised structures to show their movements over the duration of the simulations. The Z coordinates (vertical movement) for each ion was taken at every 100th timestep and have been presented in graph form. The trajectories for each ion in their successful AIMD simulation shown in VMD and the change in their Z coordinate in graph form are presented below.

6.1.1 – Simulations with Cs^+
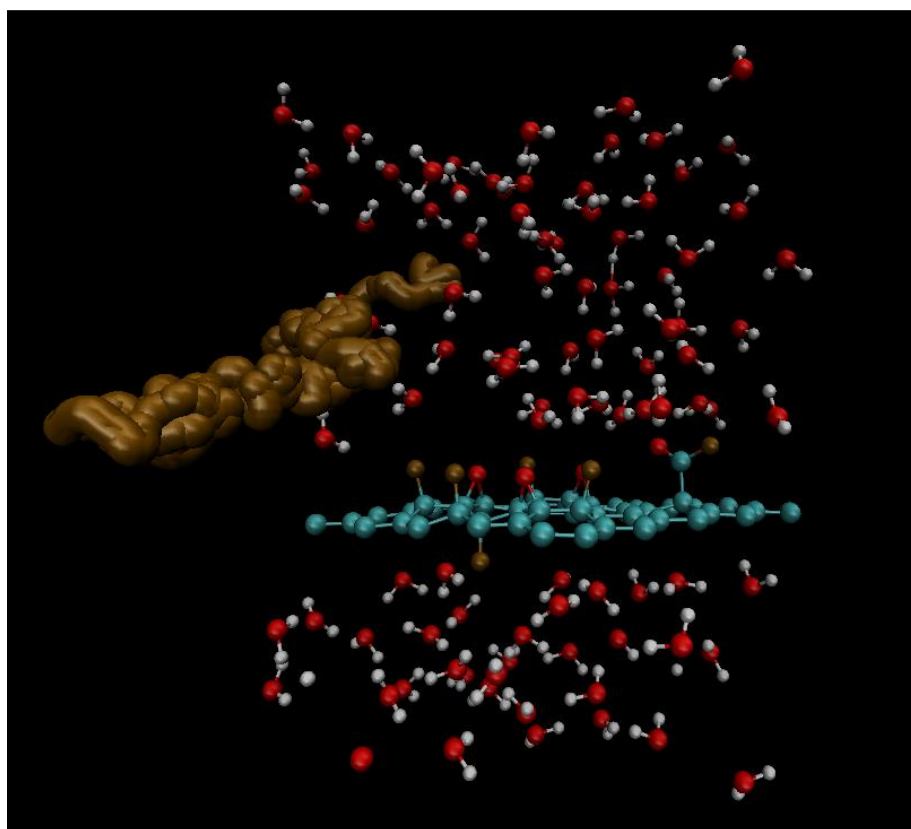
Figure 6.1: Cs FFGO (A) AIMD trajectory shown in VMD

Change in Cs Z coordinate over time with Fluorine Functionalised Graphene Oxide (A)
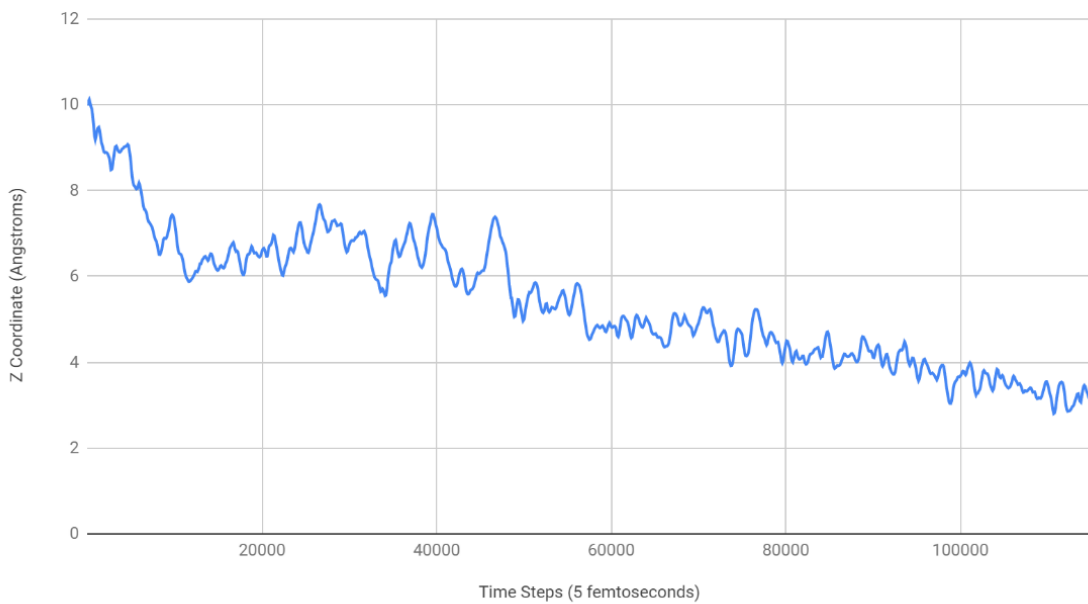
Figure 6.2: Cs FFGO (A) AIMD change in Cs Z coordinate over 115000 timesteps

Figure 6.1 shows that the Cs ions trajectory moving outside the computational box which is allowable given the periodic boundary conditions imposed on the system. The ions trajectory is towards the surface of the FFGO however the exact location of the ion on the surface cannot be determined based on the representation of the simulation. Figure 6.2 shows a significant movement (approximately 7 angstroms) in the Z coordinate of the ion suggesting strong attraction of the ion to the FFGO surface. All functional groups appear stable and remain on the graphene sheet throughout the entirety of the simulation.
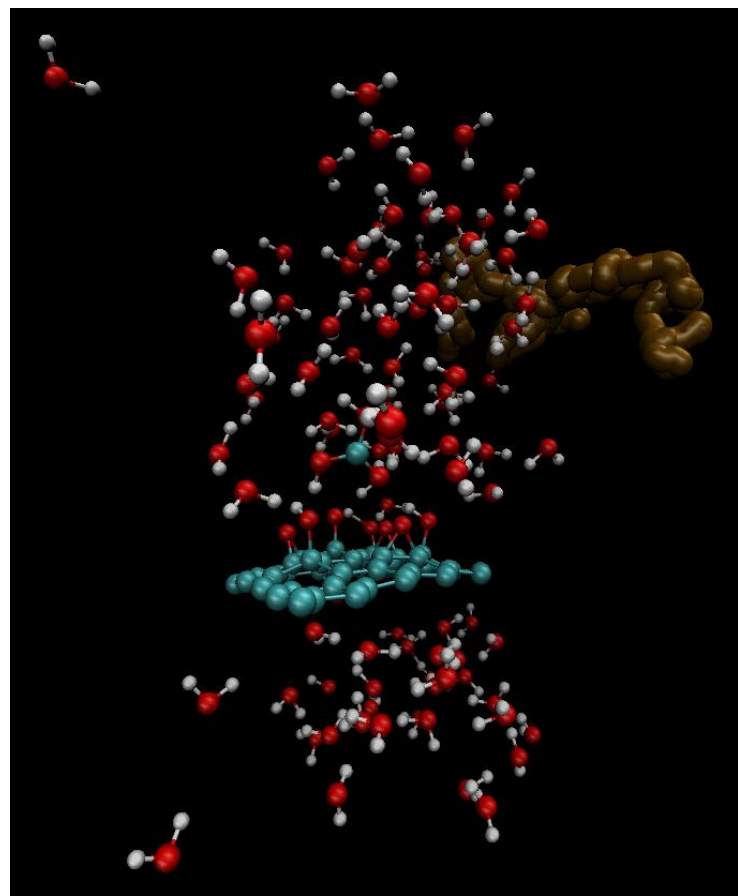
Figure 6.3: Side on view of Cs HGO (A) AIMD trajectory shown in VMD
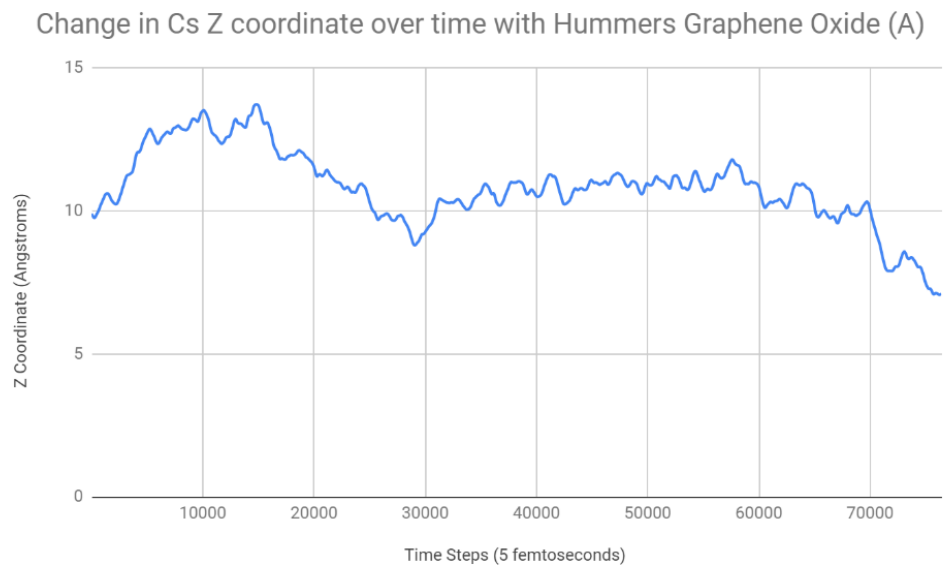
Figure 6.4: Cs HGO (A) AIMD change in Cs Z coordinate over 76400 timesteps

Figure 6.3 shows that the carboxyl group for the HGO optimised structure has been removed from the graphene sheet surface and has formed a carboxylate ion in solution. The lack of stability of the carboxyl group on the surface of the graphene sheet adds further argument to the assumption that if carboxyl groups are present on graphene oxide then they likely occur exclusively on the edges of graphene oxide sheets. [114][115][116] Indeed all successful AIMD simulations within this research of structures containing carboxyl groups on the surface of graphene oxide sheets show similar instability, with the carboxyl group leaving the surface and forming an ion or molecule in solution. Figures 6.3 and 6.4 show an overall small degree of movement of the Cs ion towards HGO. With the ion moving towards the sheet following initial repulsion between 0 and 30,000 timesteps. However, the remaining timesteps show the ion moving away from HGO until completion of the simulation.
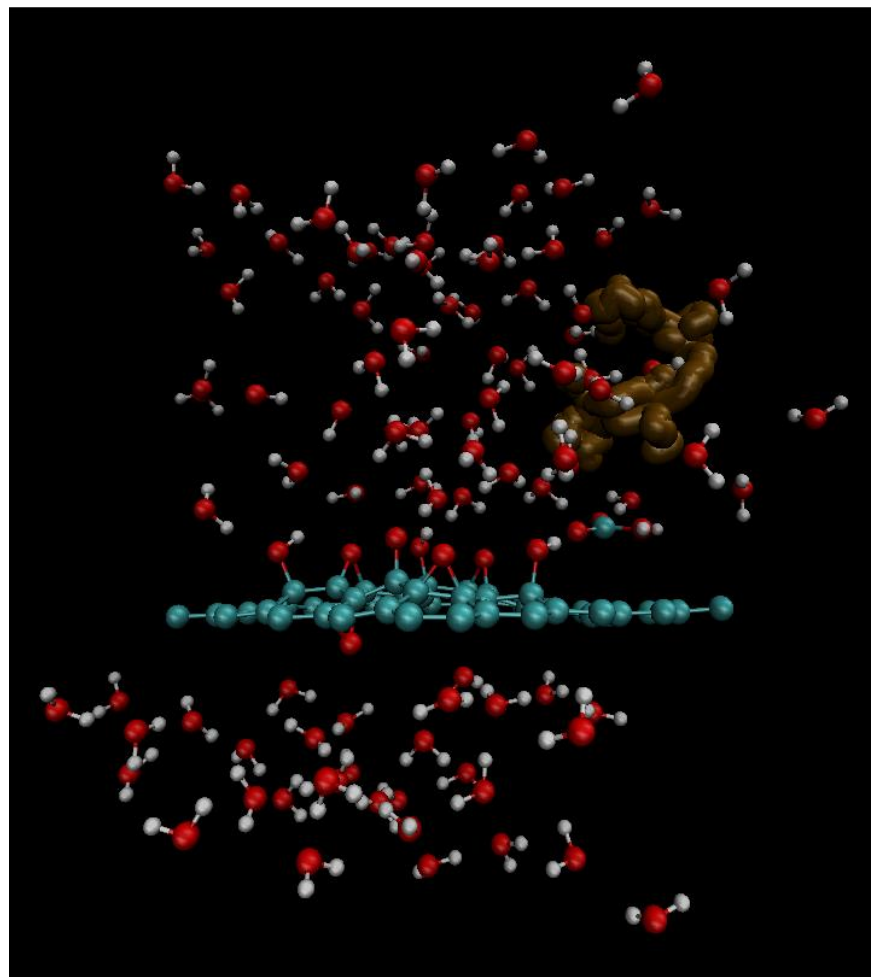
Figure 6.5: Cs HGO (B) AIMD trajectory shown in VMD

Change in Cs Z coordinate over time with Hummers Graphene Oxide (B)
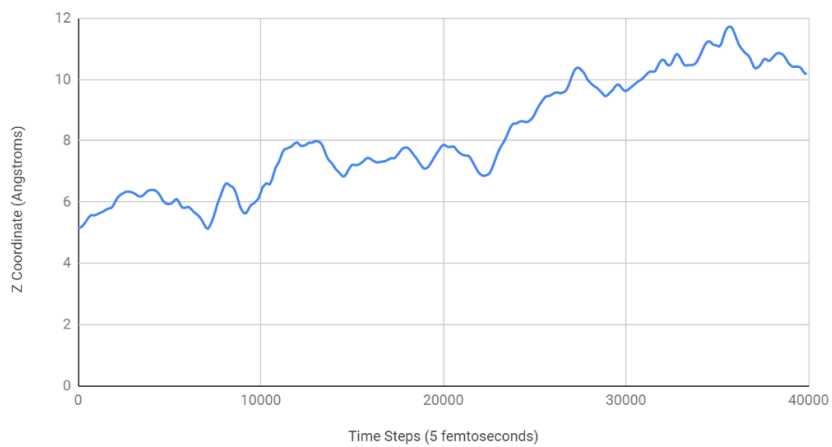
Figure 6.6: Cs HGO (B) AIMD change in Cs Z coordinate over 40000 timesteps

Figure 6.5 and 6.6 show that the Cs ion gradually moves away from HGO throughout the simulation. B position ions were placed close to the surface of the graphene sheets to highlight any attractive forces to the various functional groups across their surfaces. The relatively vertical trajectory of the ion over approximately 5 Å could suggest repulsive forces or a general lack of affinity for the ion to the functional groups. The formation of the carboxylate ion given its relative proximity to the Cs ion may have influenced its trajectory over the course of the simulation.
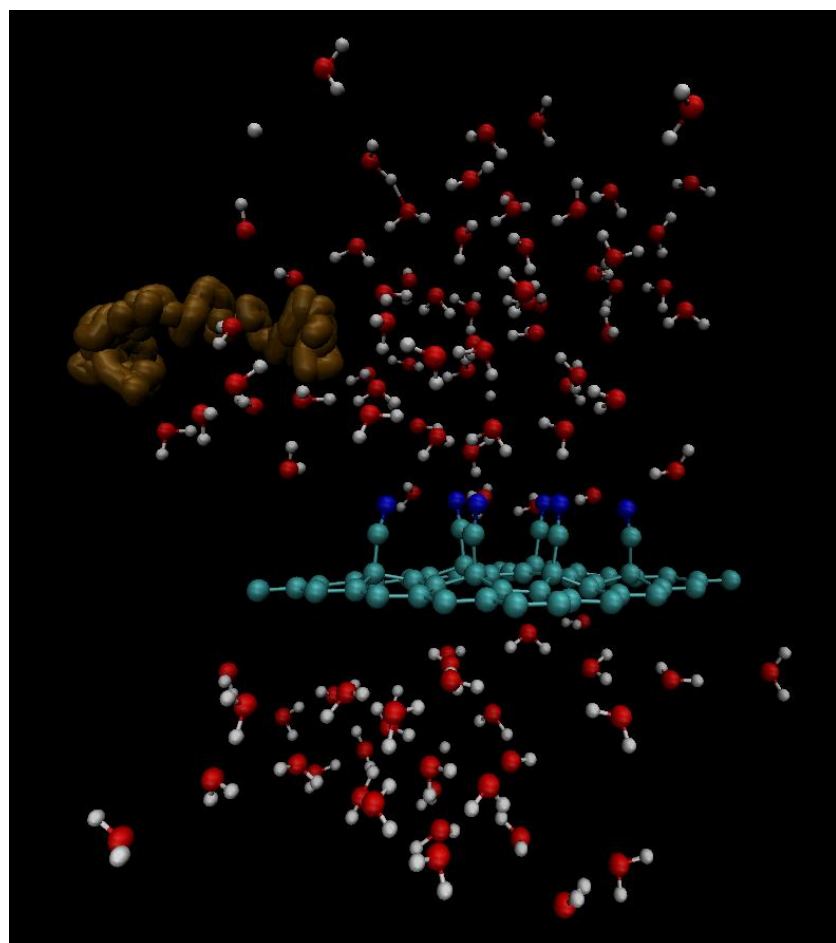
Figure 6.7: Cs NGO (A) AIMD trajectory shown in VMD

Change in Cs Z coordinate over time with Nitrogen Group Graphene Oxide (A)
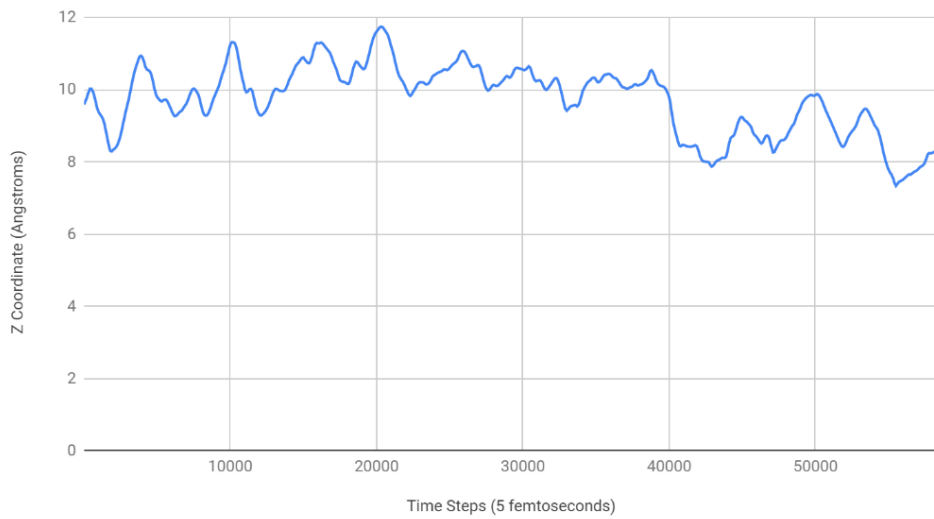
Figure 6.8: Cs NGO (A) AIMD change in Cs Z coordinate over 584000 timesteps

Figure 6.7 shows the Cs ion moving away from the graphene sheet over the course of the simulation. There is only a minor change in the starting and ending Z coordinate for the ion as shown in Figure 6.8. The nitrile groups remain stable throughout the entirety of the simulation.
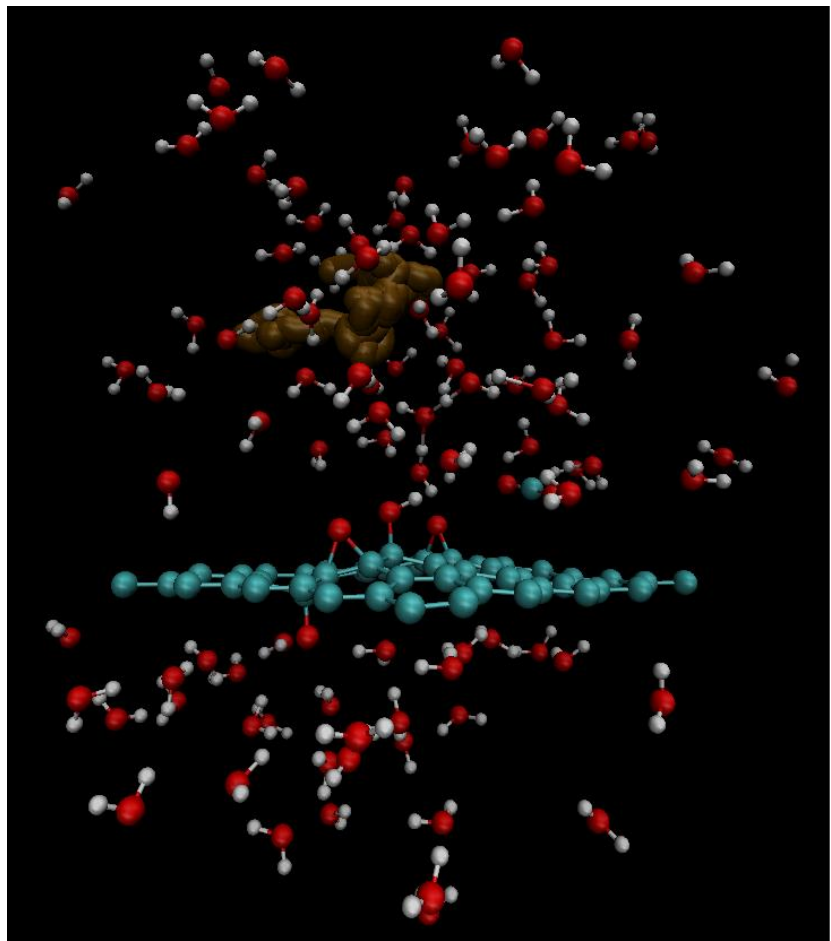
Figure 6.9: Cs RGO (A) AIMD trajectory shown in VMD
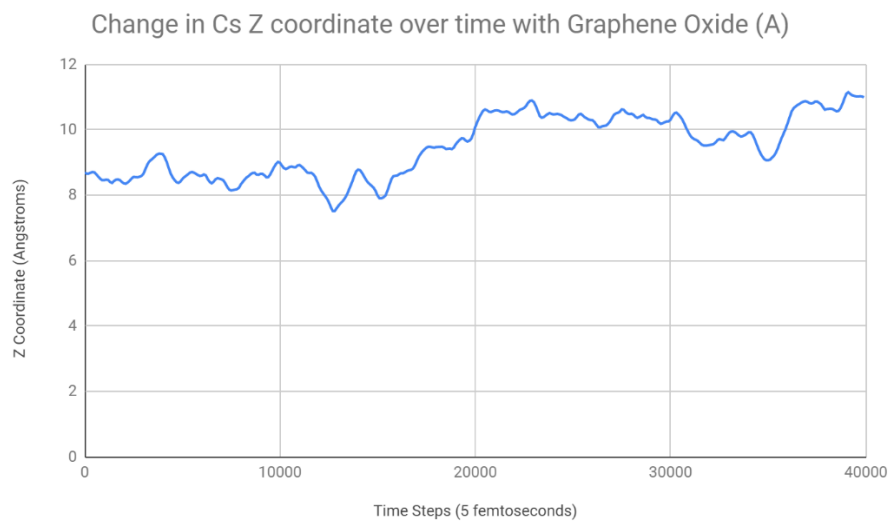
Figure 6.10: Cs RGO (A) AIMD change in Cs Z coordinate over 40000 timesteps

Figure 6.9 shows the formation of a carboxylate ion following optimisation and movement of the Cs ion away from the graphene sheet over the duration of the simulation. There is no significant change in the ions Z coordinate over the entirety of the simulation as shown in Figure 6.10.

6.1.2 – Simulations with Sr^{2+}
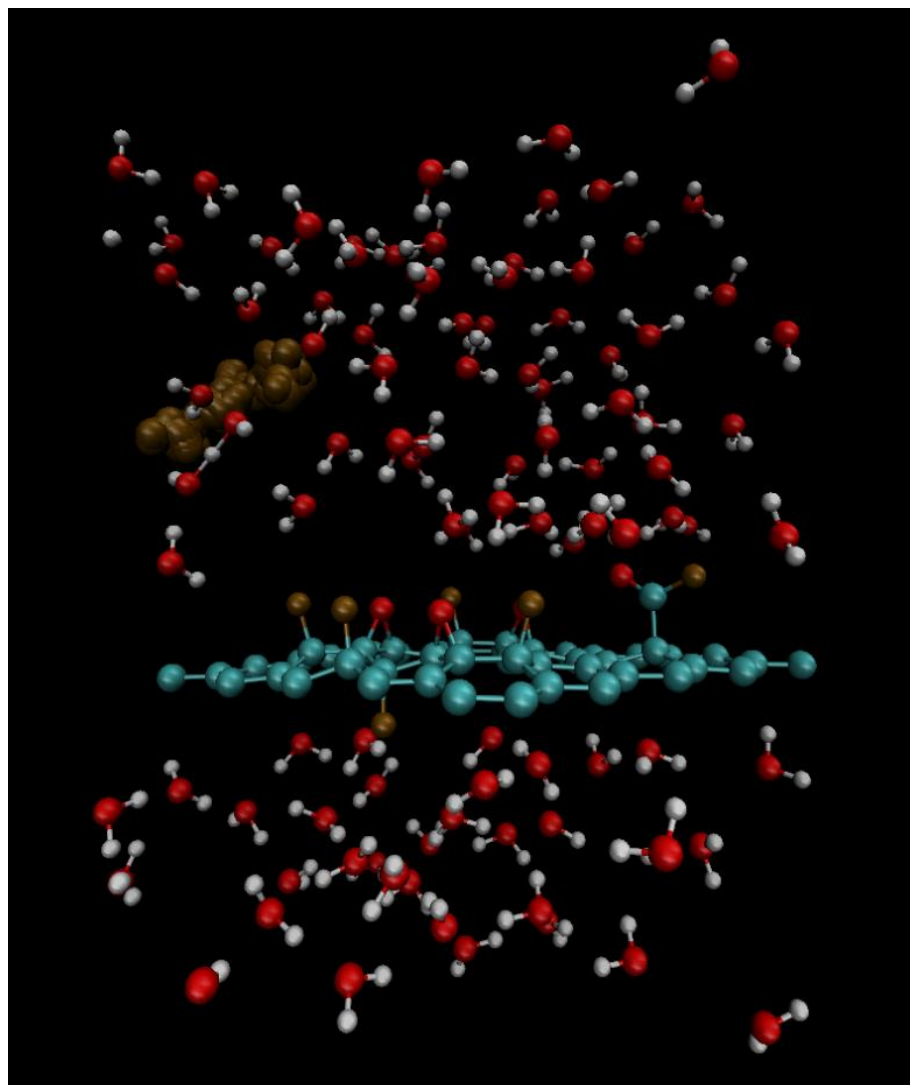
Figure 6.11: Sr FFGO (A) AIMD trajectory shown in VMD

Change in Sr Z coordinate over time with Fluorine Functionalised Graphene Oxide (A)
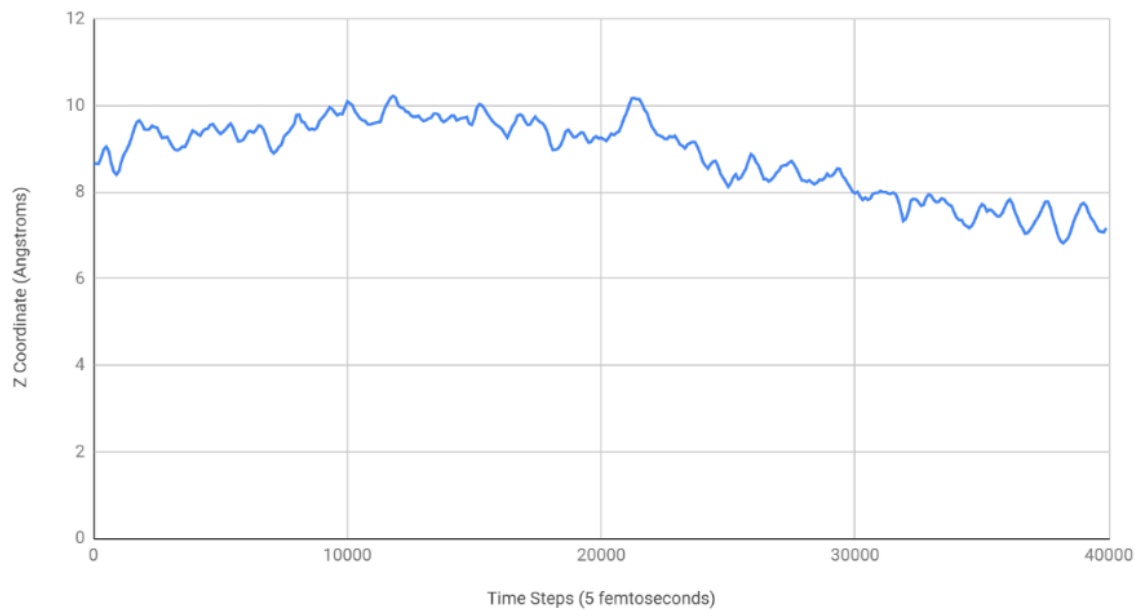
Figure 6.12: Sr FFGO (A) AIMD change in Sr Z coordinate over 40000 timesteps

Figures 6.11 and 6.12 shows the movement of the Sr ion towards the graphene sheet over the course of the simulation. The Sr ion appears to move in a similar fashion to the Cs atom as shown in AIMD simulation Figure 6.1. Continuation of the simulation may have yielded the same trajectory away from the graphene sheet which may suggest repulsive forces pushing the positively charged ions away from the surface. In similarity to Figure 6.1 all functionalised groups remain stable throughout the simulation.
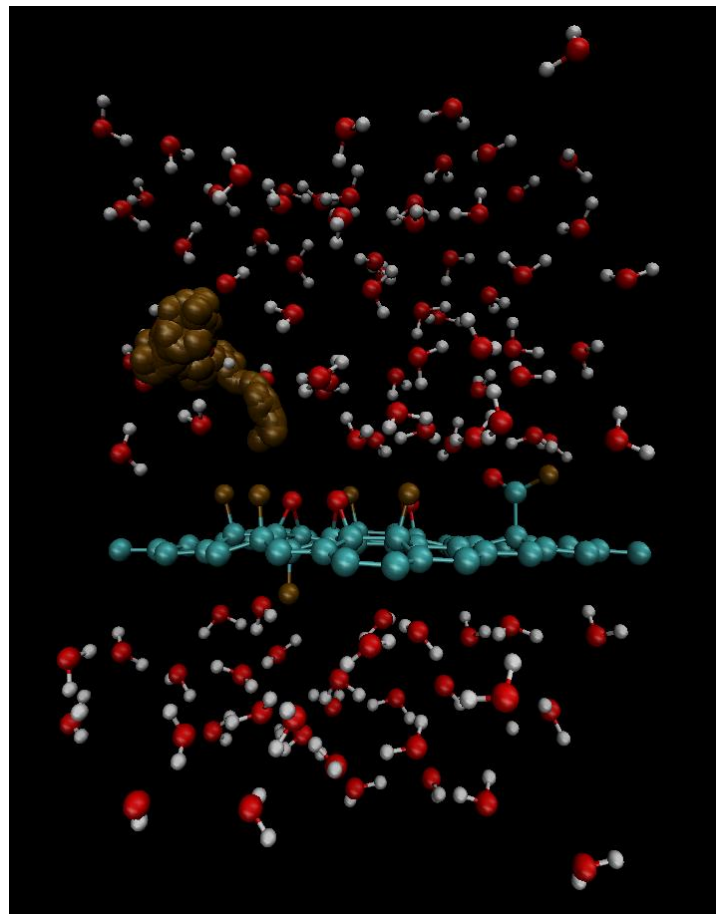
Figure 6.13: Sr FFGO (B) AIMD trajectory shown in VMD
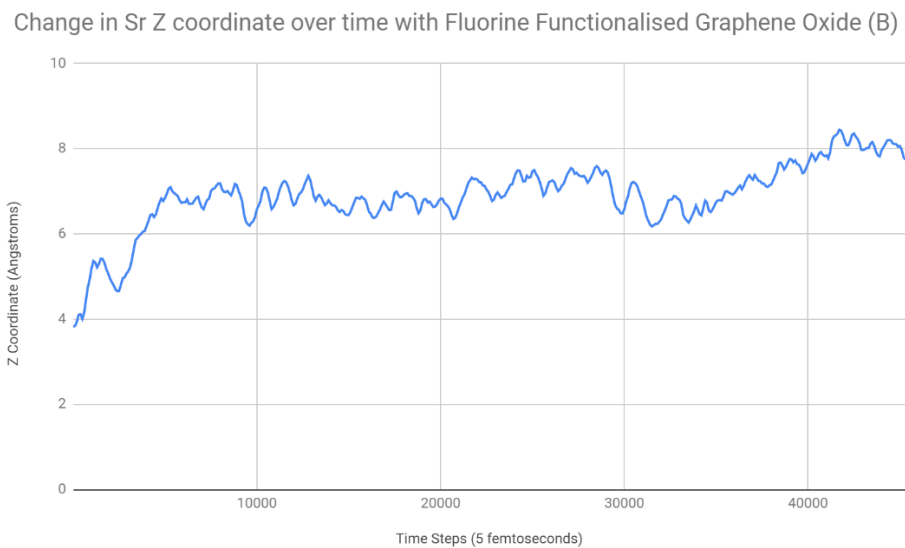
Figure 6.14: Sr FFGO (B) AIMD change in Sr Z coordinate over 45300 timesteps

Figures 6.13 and 6.14 show a substantial initial movement of the Sr ion away from the graphene sheet with the ion moving 3 Å in approximately 5000 timesteps. Over the remainder of the simulation the ion continues to move away from the graphene sheet.
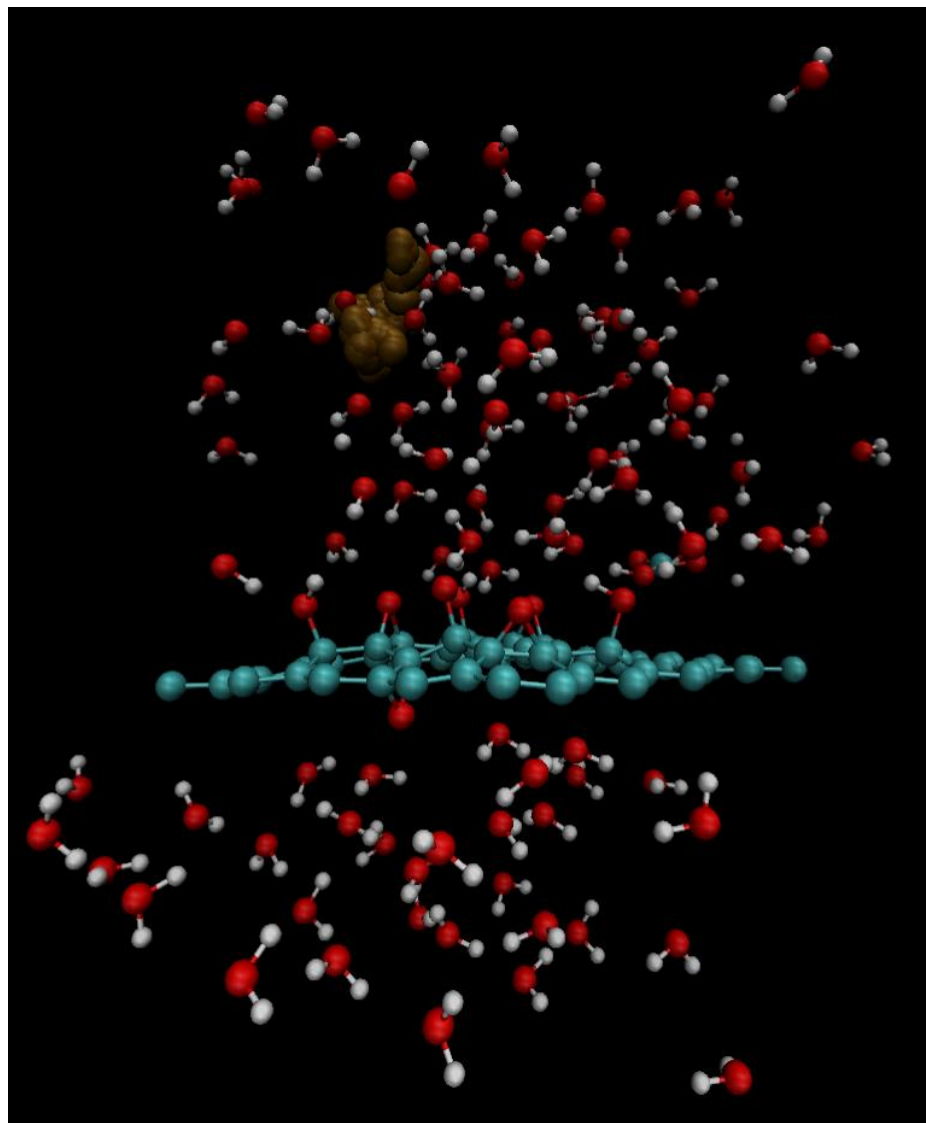
Figure 6.15: Sr HGO (A) AIMD trajectory shown in VMD
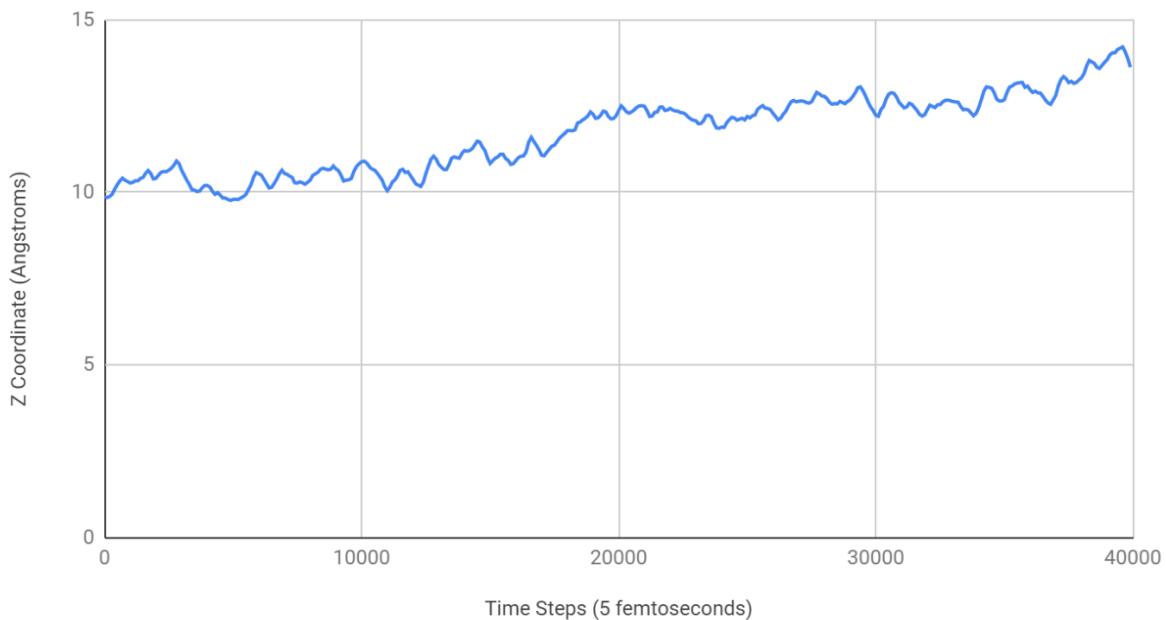
Figure 6.16: Sr HGO (A) AIMD change in Sr Z coordinate over 40000 timesteps

The instability of the carboxyl group on the graphene surface is seen in Figure 6.15 with the formation of a hydrogen carbonate. The Sr ion moves steadily away from the HGO surface over the duration of the simulation as shown in Figure 6.15 and 6.16, all other functional groups remain stable throughout the entirety of the simulation. Carbonyl groups incorporated into the structure of HGO appear to favour epoxide conformation as shown both above and below the plane of the GO sheet as seen in Figure 6.15. Preferential stability of epoxide in comparison to carbonyl functionality is consistent with spectral analysis for GO functional group location which suggests carbonyl functionality occurs most frequently within significant voids or on the periphery of the graphene oxide sheet. [117] However molecular dynamic simulations show the formation of carbonyl groups within the graphene basal plane are energetically favourable in comparison to other functional groups such as epoxides. [118] Carbonyl groups were incorporated into the structures of HGO and RGO developed in

GaussView however some change into epoxide groups following optimisation. The presence of both functional groups in the simulations suggests that both can exist within the regions of the graphene sheet into which they are inserted. The energetic preferability for the formation of epoxide groups could highlight the importance of graphene sheet deformation and the relative proximity of other functionalities on the stability of neighbouring carbonyl groups.
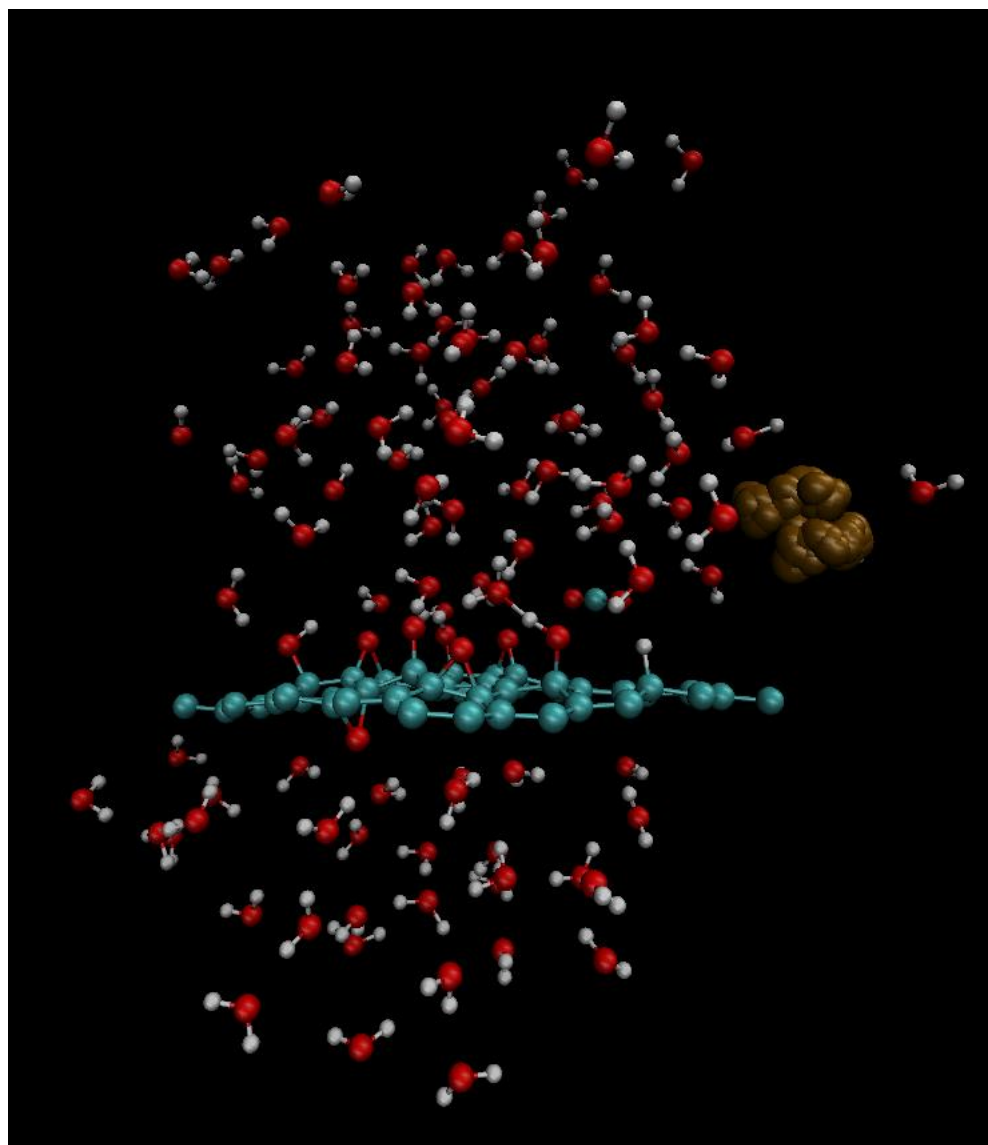
Figure 6.17: Sr HGO (B) AIMD trajectory shown in VMD

Change in Sr Z coordinate over time with Hummers Graphene Oxide (B)
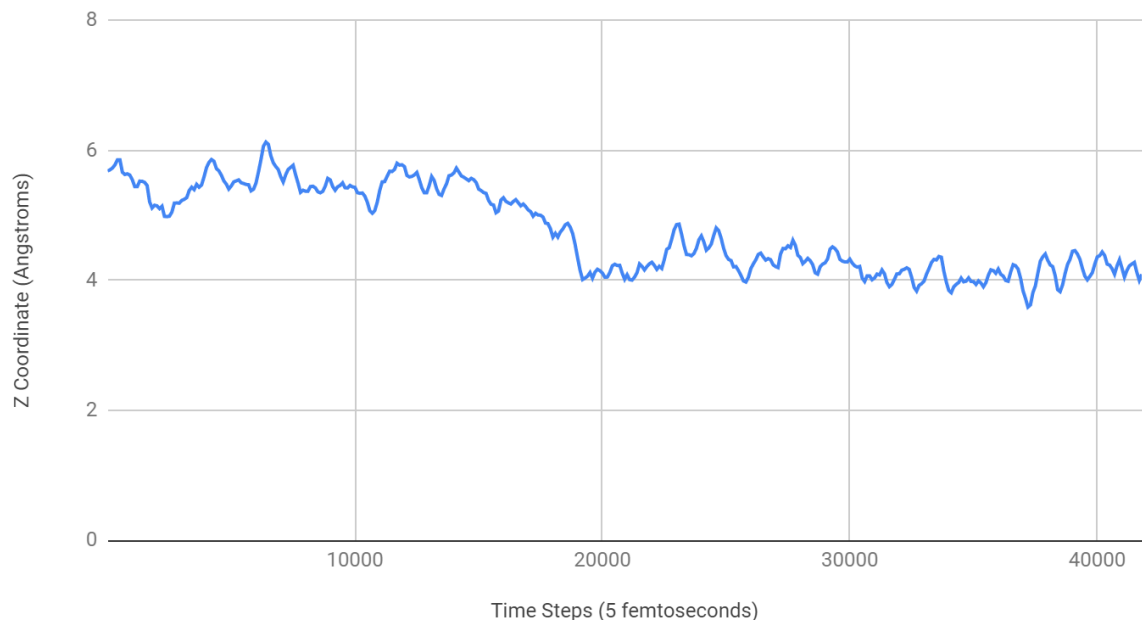
Figure 6.18: Sr HGO (B) AIMD change in Sr Z coordinate over 41800 timesteps

The instability of the carboxyl group is seen in Figure 6.17 with the formation of carbon dioxide. The hydrogen bond on the leaving site of the carboxyl group is illustrative and is part of a hydronium ion which can been seen for the full duration of the simulation. Over the course of the simulation the Sr ion moves closer in the Z coordinate but away in the X coordinate from the graphene sheet showing no attraction to any functionality suggesting random movement.
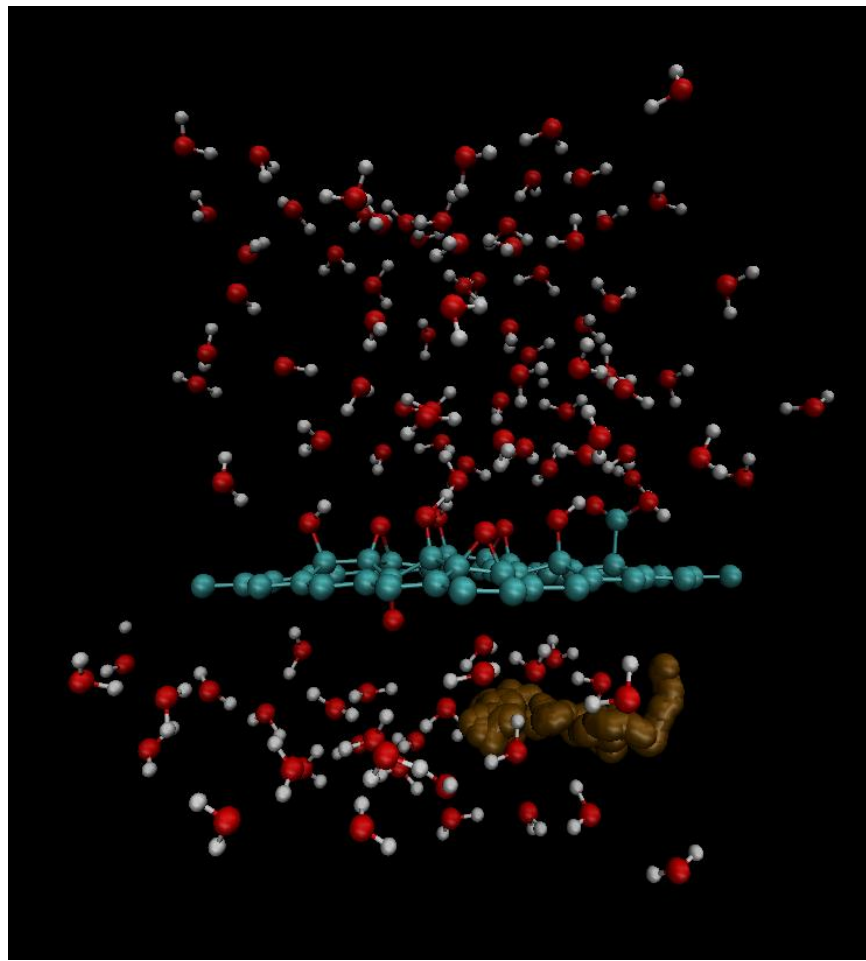
Figure 6.19: Sr HGO (C) AIMD trajectory shown in VMD
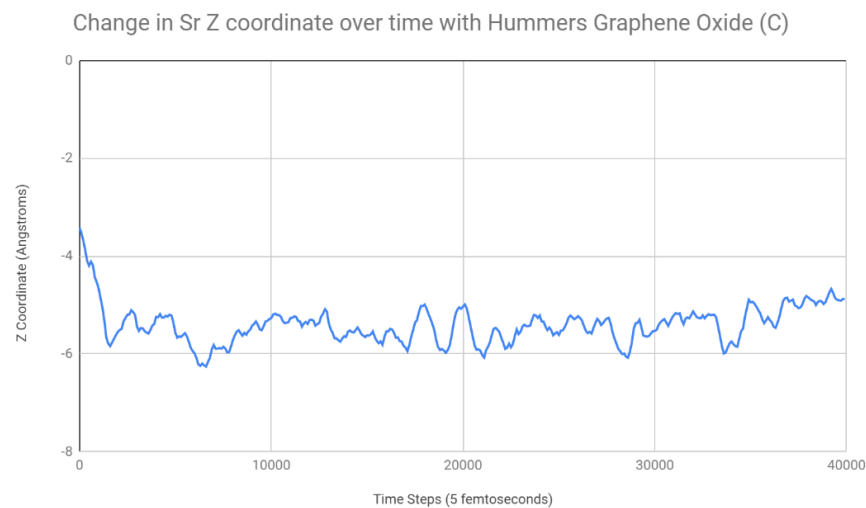
Figure 6.20: Sr HGO (C) AIMD change in Sr Z coordinate over 40000 timesteps

The carboxyl group shown in Figure 6.19 leaves the surface of the graphene sheet after 600 timesteps forming a carboxylate ion, the hydrogen then binds with a neighbouring water molecule to form carbon dioxide and a hydronium ion, the remaining functional groups maintain stability throughout the simulation. Figures 6.19 and 6.20 show a substantial (2.4 Å) rapid (1600 timesteps) initial movement of the Sr ion away from the graphene sheet. Following what is thought to be initial repulsion the Sr ion migrates towards the middle of the graphene sheet over the remainder of simulation. This may indicate potential attraction to the carbonyl group located on the underside of the graphene sheet as the ion gradually moves closer towards the sheet over the duration of the simulation as shown in Figure 6.20. Continuation of the simulation for a greater number of timesteps would be required to provide greater evidence for such a claim.
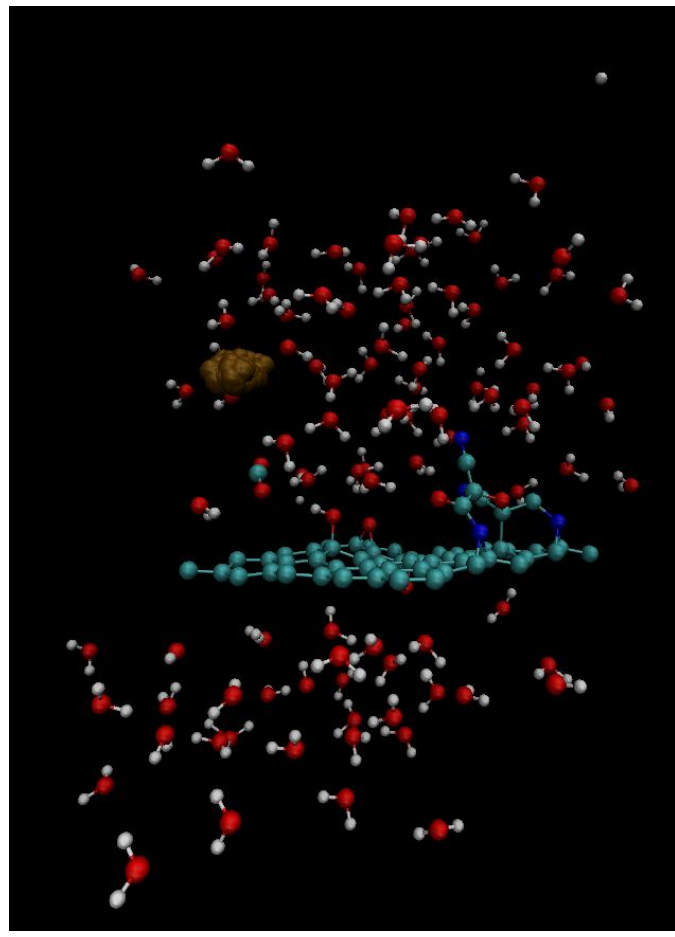
Figure 6.21: Sr NFRGO (A) AIMD trajectory shown in VMD

Change in Sr Z coordinate over time with Nitrogen Functionalised Reduced Graphene Oxide (A)
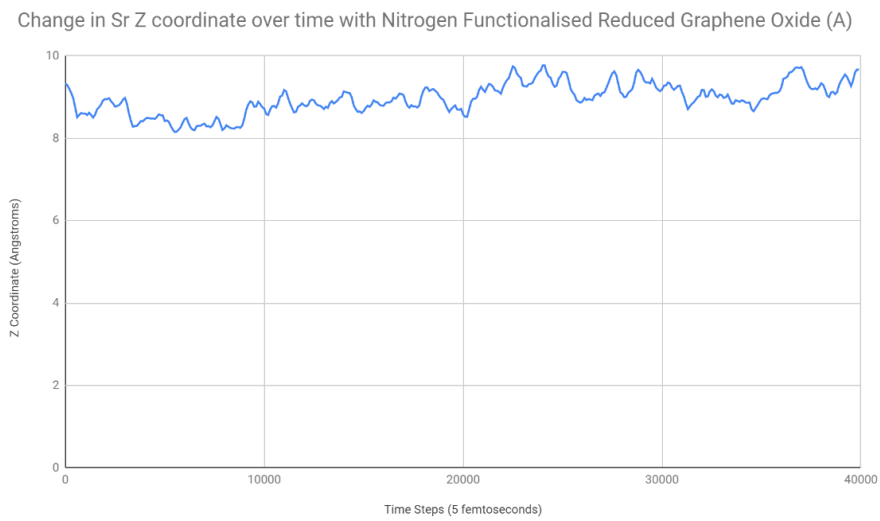
Figure 6.22: Sr NFRGO (A) AIMD change in Sr Z coordinate over 40000 timesteps

Figure 6.21 shows that the tetracyanoethylene oxide has interacted with the adjacent epoxide group on the graphene sheet, Figure 6.21 also shows that two of the nitrile groups have formed tertiary amines to the graphene sheet. The instability of the carboxylate group is shown by the formation of carbon dioxide. There is little movement of the Sr ion in any direction during the simulation.
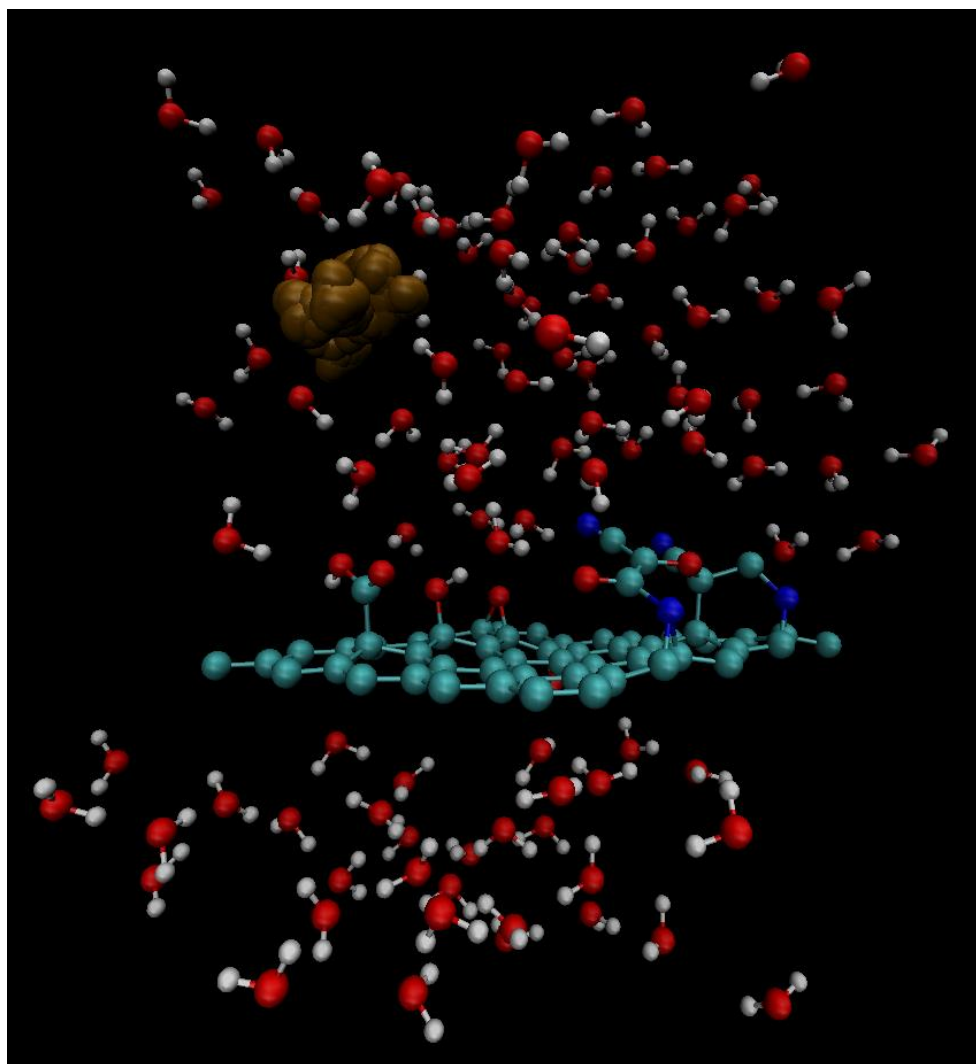
Figure 6.23: Sr NFRGO (B) AIMD trajectory shown in VMD

Change in Sr Z coordinate over time with Nitrogen Functionalised Reduced Graphene Oxide (B)
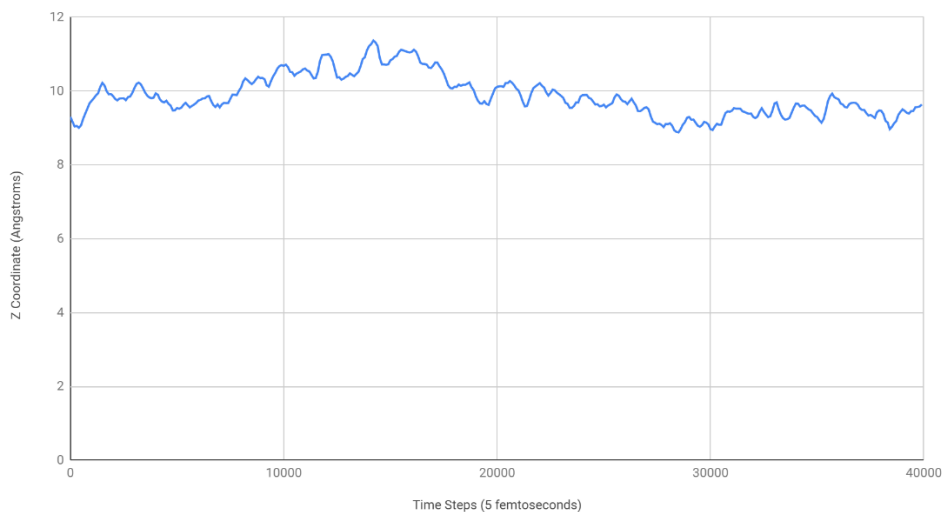
Figure 6.24: Sr NFRGO (B) AIMD change in Sr Z coordinate over 40000 timesteps

Figure 6.23 shows the tetracyanoethylene oxide has rearranged itself in the same way as in Figure 6.21 following optimisation. The carboxylate group is attached to the surface of the graphene sheet following optimisation but leaves after 500 timesteps as a carboxylate ion and then forms carbon dioxide with the hydrogen interacting with an adjacent water molecule to form a hydronium ion. There is a slightly greater movement of the Sr ion for this simulation, but the ion moves in a similar way without travelling in any specific direction.
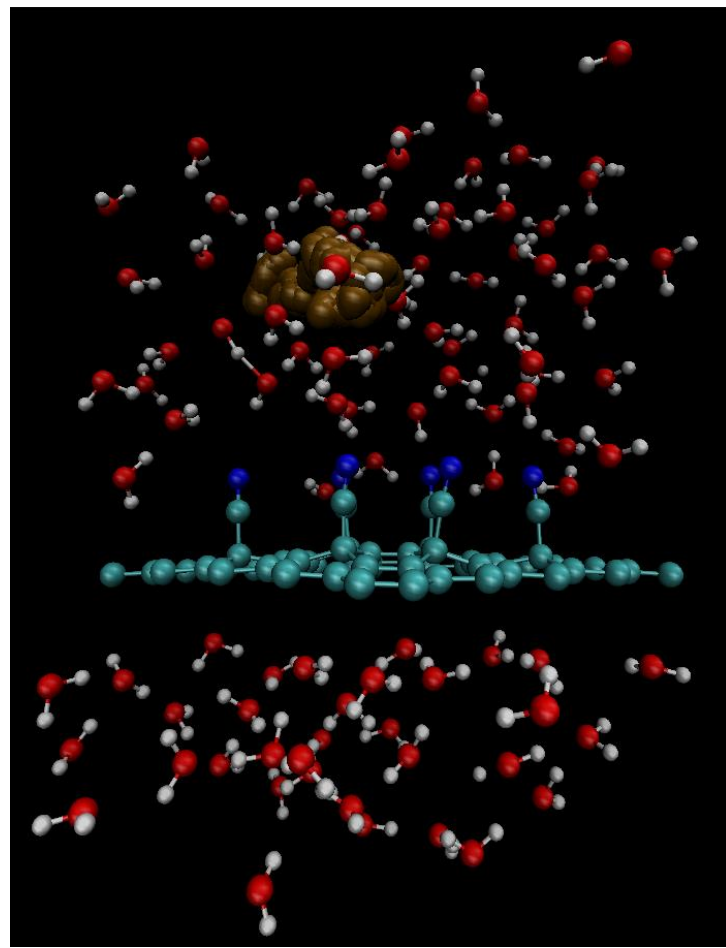
Figure 6.25: Sr NGO (A) AIMD trajectory shown in VMD

Change in Sr Z coordinate over time with Nitrogen Group Graphene Oxide (A)
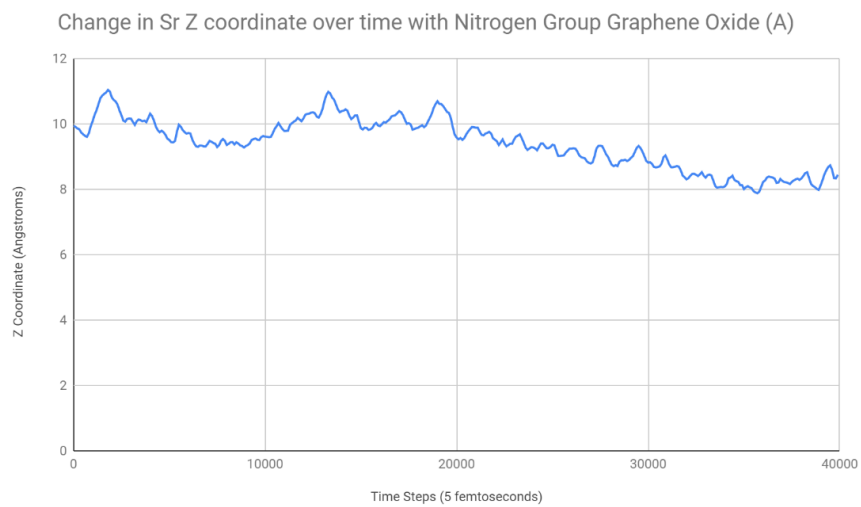
Figure 6.26: Sr NGO (B) AIMD change in Sr Z coordinate over 40000 timesteps

Figures 6.25 and 6.26 show a small amount of movement of the Sr ion over the duration of the simulation with the Sr ion gradually moving towards the graphene sheet. The nitrile groups remain stable throughout the simulation.
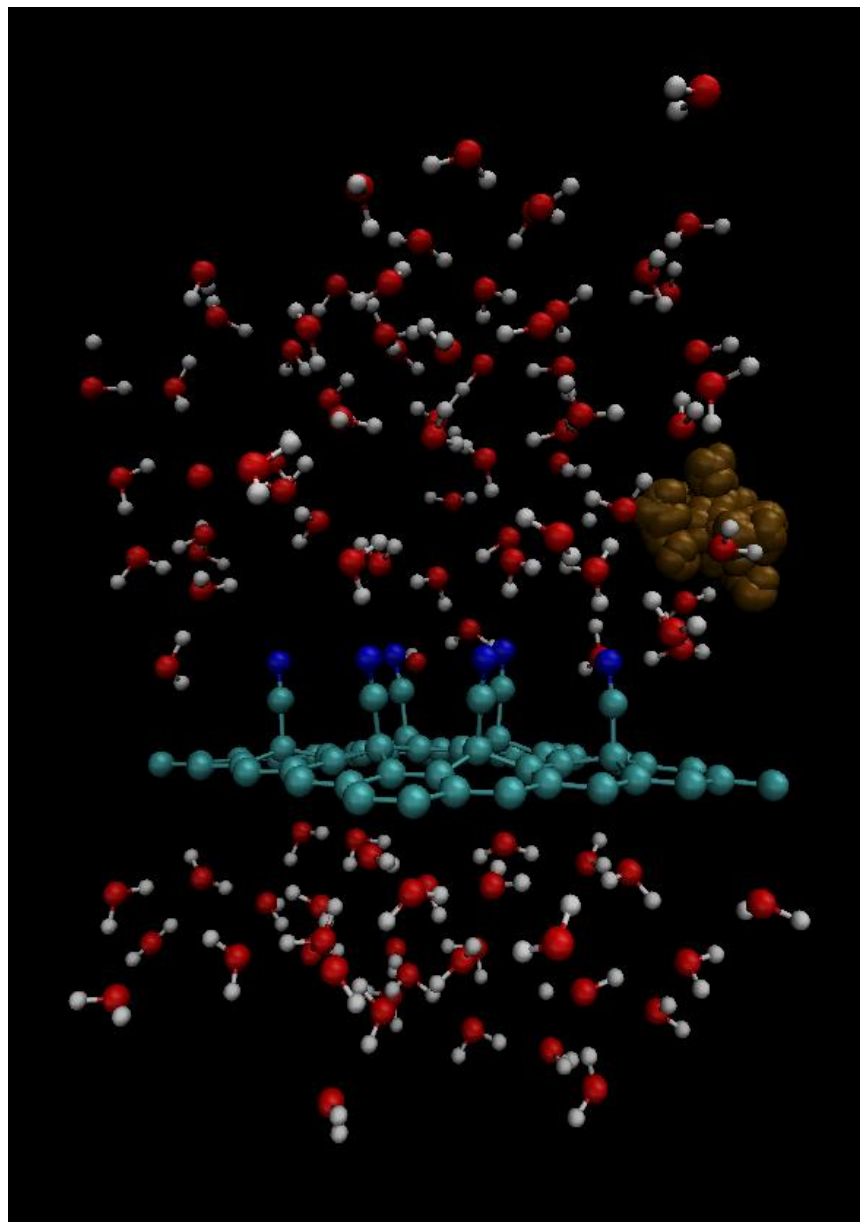
Figure 6.27: Sr NGO (A) AIMD trajectory shown in VMD
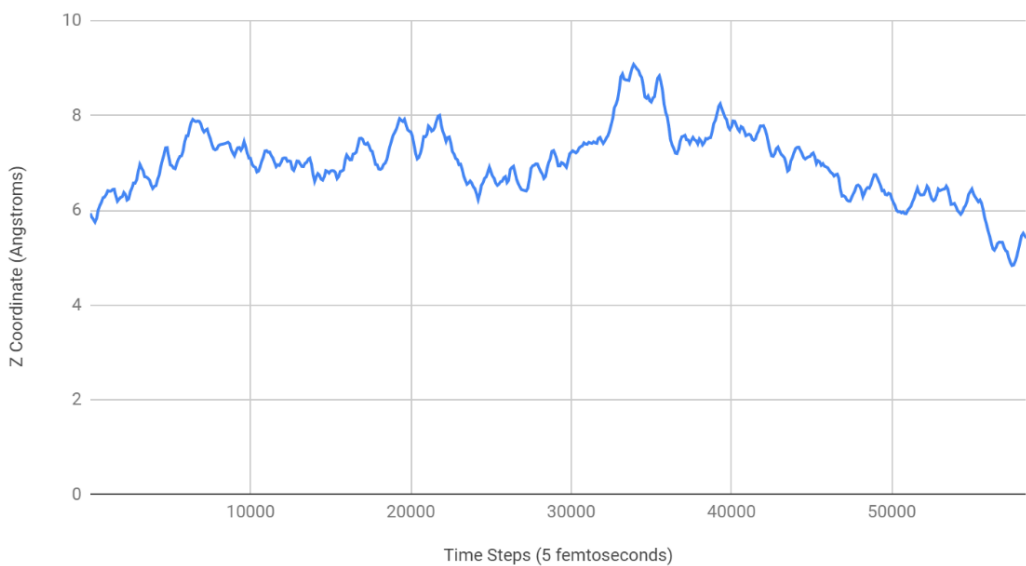
Figure 6.28: Sr NGO (B) AIMD change in Sr Z coordinate over 58400 timesteps

Figures 6.27 and 6.28 show a slightly higher amount of movement of the Sr ion over the duration of the simulation when the ion is placed closer towards the nitrile functional group. Over the duration of the simulation the Sr ion moves closer to the graphene sheet in the Z coordinate but appears to be moving towards the edge of the sheet and away from the closest nitrile group. Continuation of the simulation would be required to further clarify the trajectory of the ion.
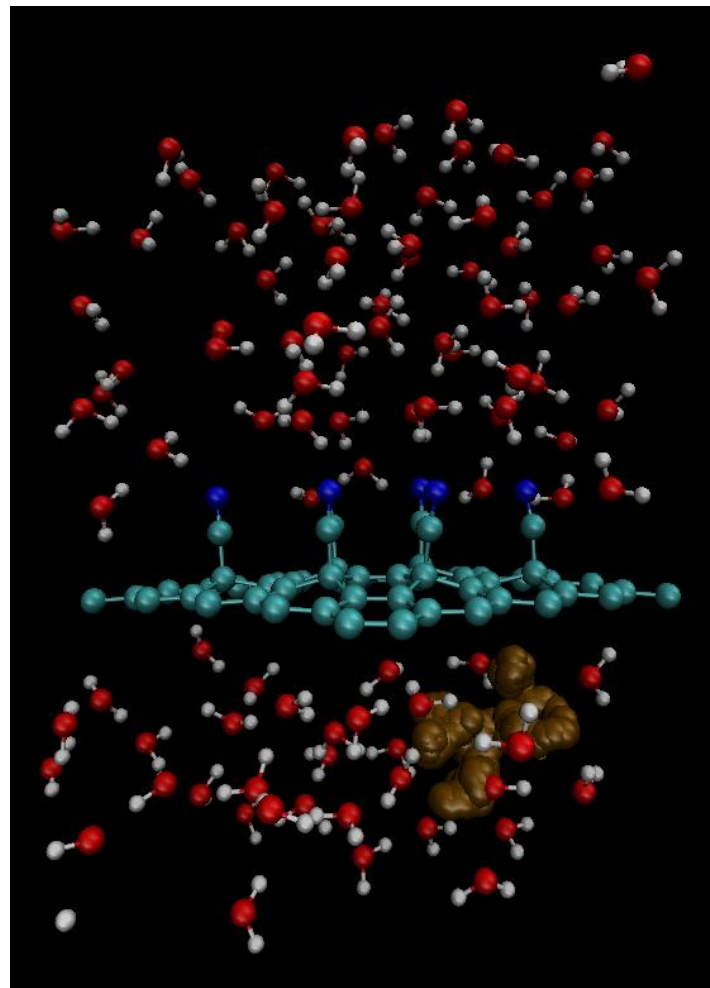
Figure 6.29: Sr NGO (C) AIMD trajectory shown in VMD
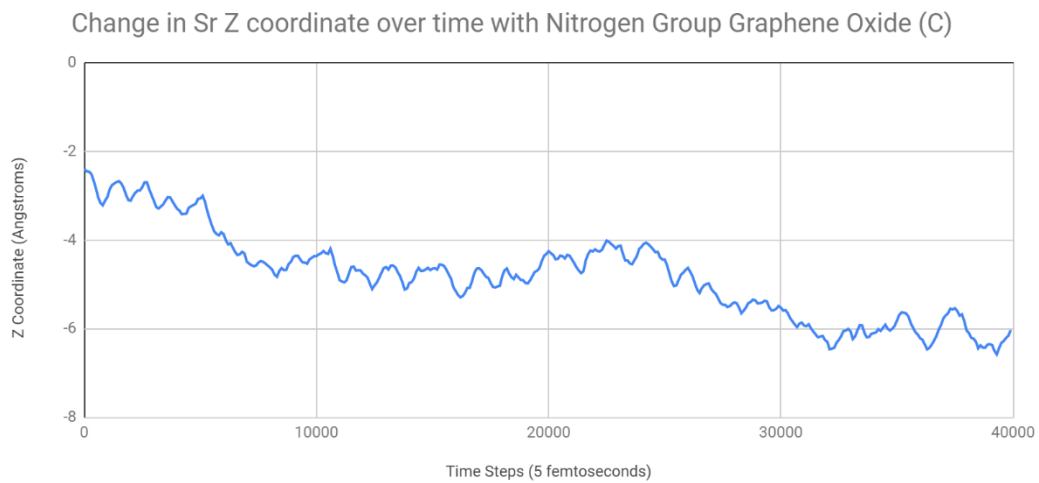
Figure 6.30: Sr NGO (C) AIMD change in Sr Z coordinate over 40000 timesteps

Figures 6.29 and 6.30 show gradual movement of the Sr ion away from the graphene sheet. This contrasts with the gradual movement of the Sr ion towards the graphene sheet in the previous simulations. Given the lack of functionality on the surface of the graphene sheet facing the ion in this simulation at position (C) it may be the case that there is some attractive force between the nitrile groups and the Sr ion which can be seen in the simulations where the ion is placed in the (A) and (B) positions.
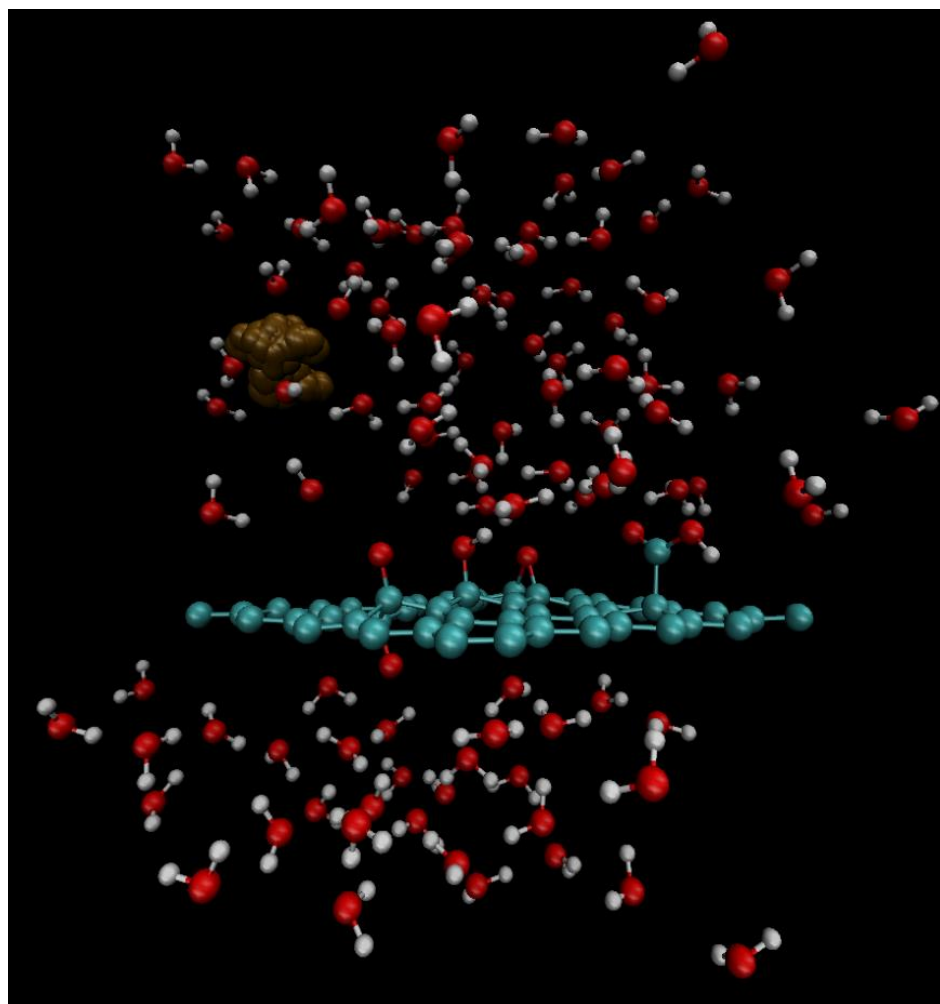
Figure 6.31: Sr RGO (A) AIMD trajectory shown in VMD
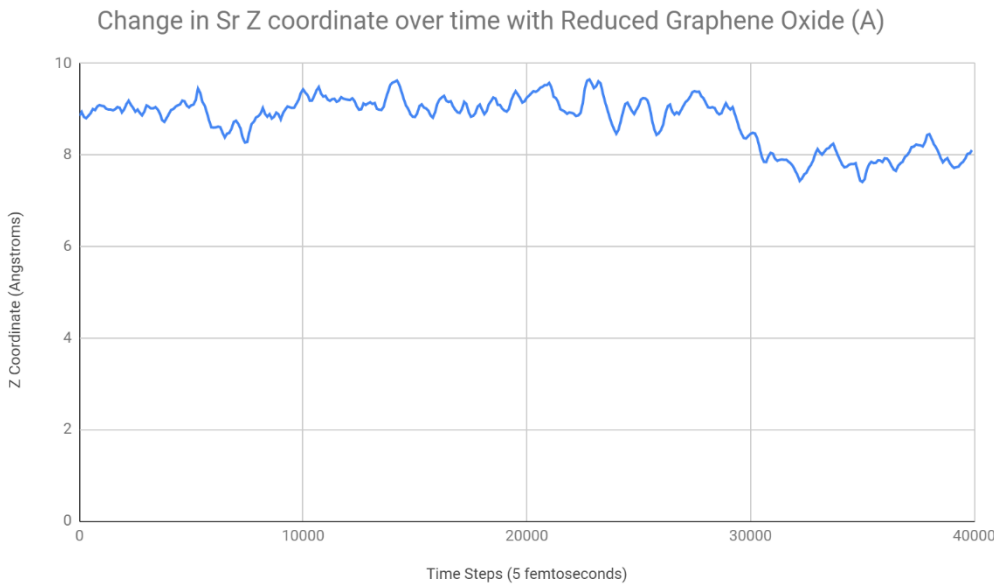
Figure 6.32: Sr RGO (A) AIMD change in Sr Z coordinate over 40000 timesteps

The Carboxyl group shown in Figure 6.31 leaves the surface of the graphene at approximately 1750 timesteps forming a carboxylate ion which goes on to form carbon dioxide and a hydronium ion as seen in previous simulations. Sr ion movement is limited as shown in Figures 6.31 and 6.32 with less than 1 Å change in Z coordinate.
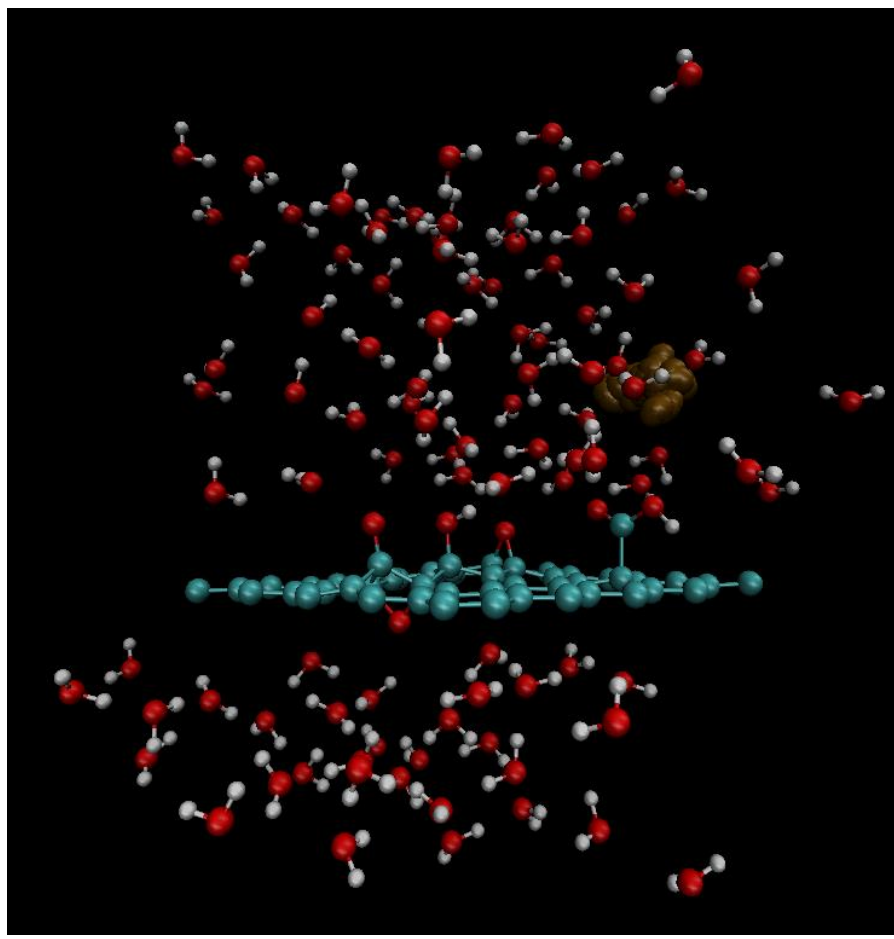
Figure 6.33: Sr RGO (B) AIMD trajectory shown in VMD

Change in Sr Z coordinate over time with Reduced Graphene Oxide (B)
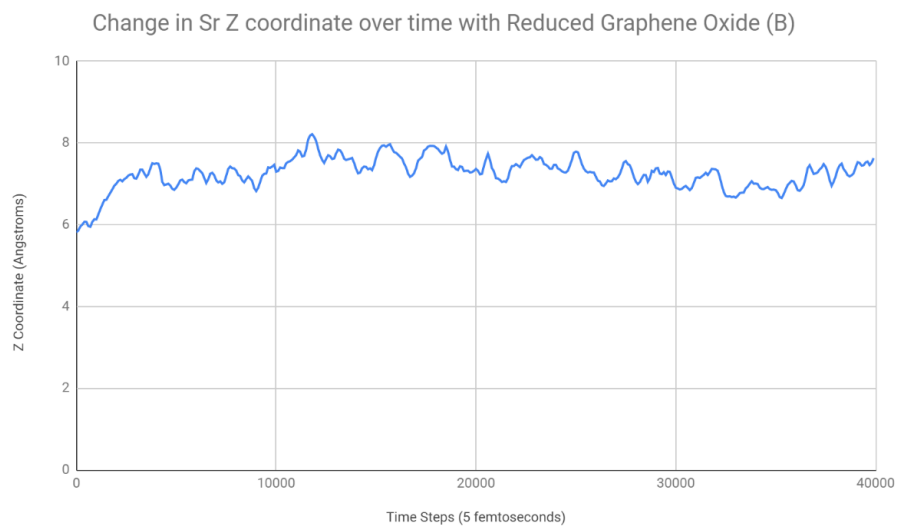
Figure 6.34: Sr RGO (B) AIMD change in Sr Z coordinate over 40000 timesteps

The carboxyl group shown in Figure 6.33 leaves the surface of the graphene at approximately 750 timesteps forming a carboxylate ion which goes on to form carbon dioxide and a hydronium ion as seen in previous simulations. Initial movement away from the graphene sheet as seen in Figure 6.34 may be the interaction of the ion with leaving carboxyl group. Following this initial change, the ion moves over short distances for the reminder of the simulation.
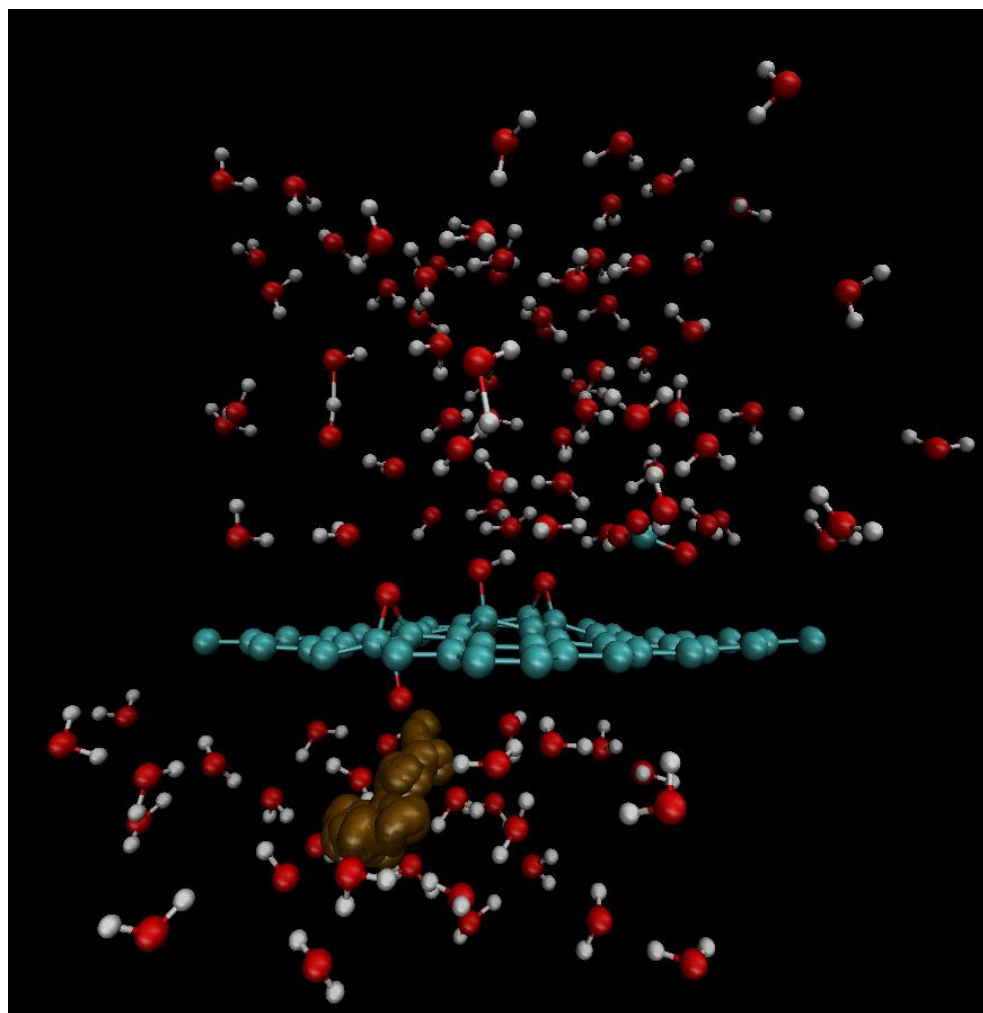
Figure 6.35: Sr RGO (C) AIMD trajectory shown in VMD

Change in Sr Z coordinate over time with Reduced Graphene Oxide (B)
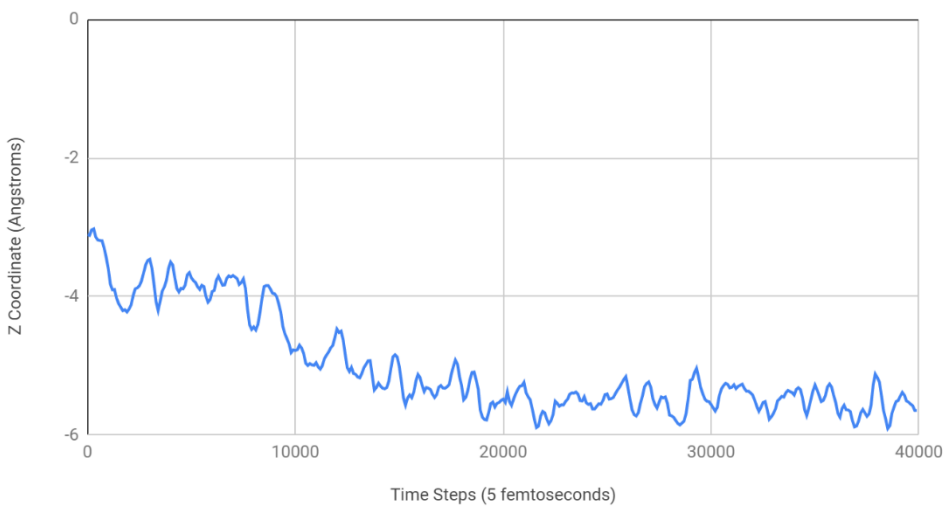
Figure 6.36: Sr RGO (C) AIMD change in Sr Z coordinate over 40000 timesteps

The carboxyl group has left the surface and formed a carboxylate ion following optimisation as shown in Figure 6.35, the ion proceeds to form carbon dioxide and a hydronium ion as seen in previous simulations. Figure 6.36 shows a rapid (1700 timesteps) and large (1.1 Å) movement of the Sr ion away from the carbonyl group to which it is placed in proximity at the beginning of the AIMD simulation. The Sr ion then continues to migrate away from the graphene surface finishing -2.54 Å in the Z coordinate from its starting point at the end of the simulation. This suggests repulsion between the Sr ion and the carbonyl group.
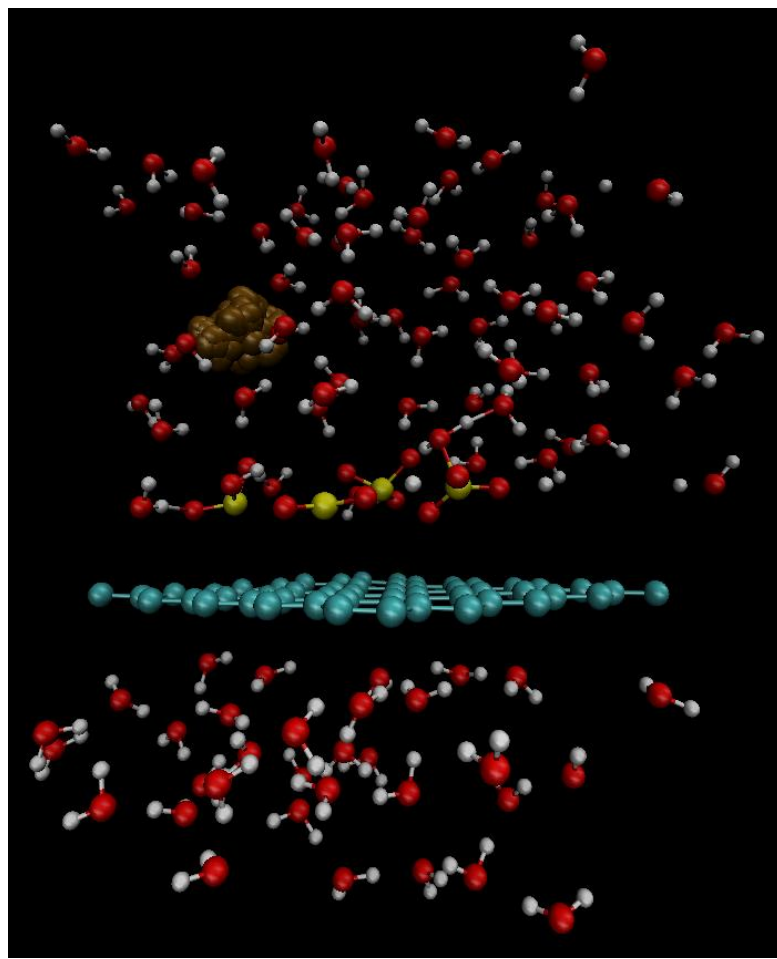
Figure 6.37: Sr SGO (A) AIMD trajectory shown in VMD
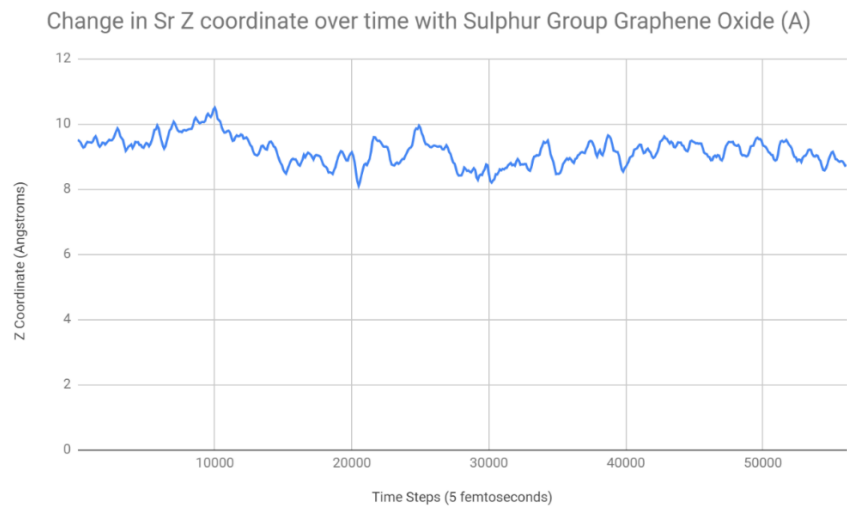
Figure 6.38: Sr SGO (A) AIMD change in Sr Z coordinate over 56100 timesteps

As seen in Figure 6.37 following optimisation all sulphonic acid groups have left the graphene sheet. Over the course of the simulation the groups go on to form various sulphur oxides including sulphur trioxide, hydrogen sulphite, hydrogen sulphate, sulphurous acid, and sulphuric acid. The sulphur oxides continuously migrate away from the graphene sheet during the simulation without interacting with the Sr ion.
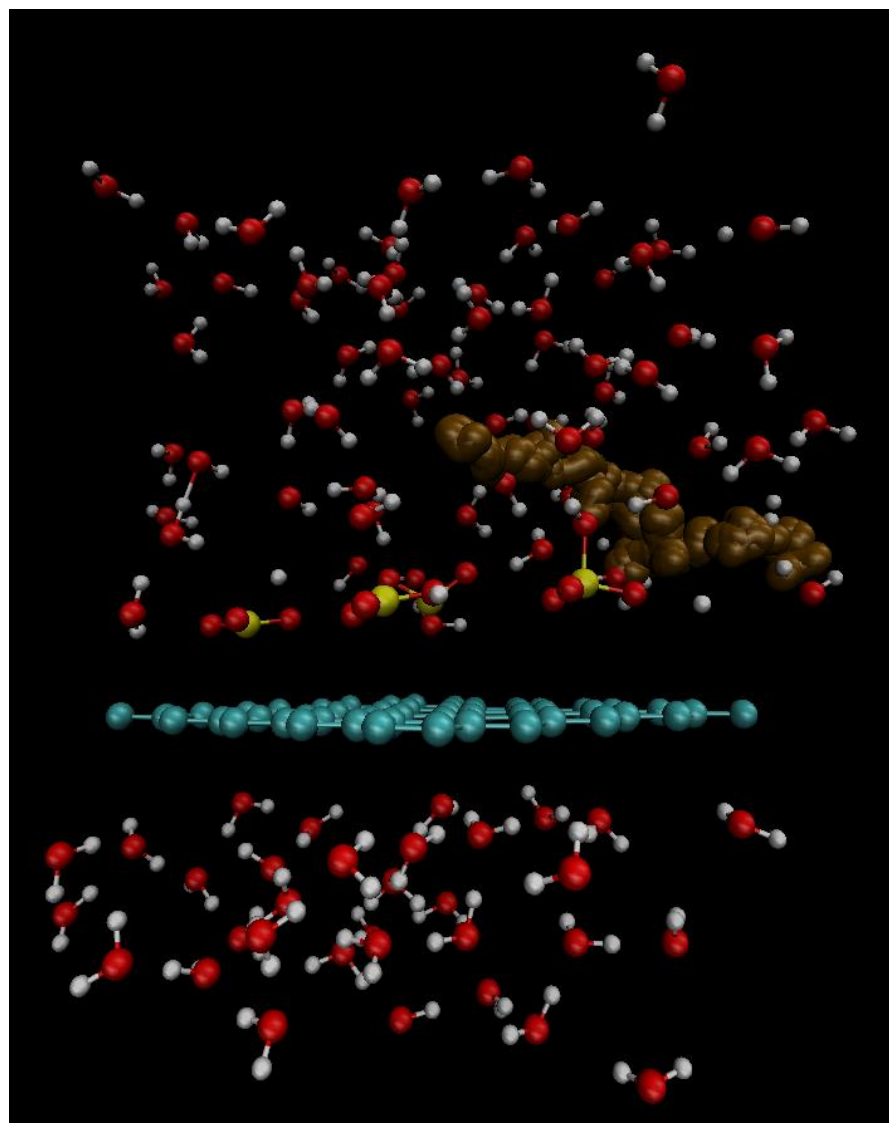
Figure 6.39: Sr SGO (B) AIMD trajectory shown in VMD

Change in Sr Z coordinate over time with Sulphur Group Graphene Oxide (B)
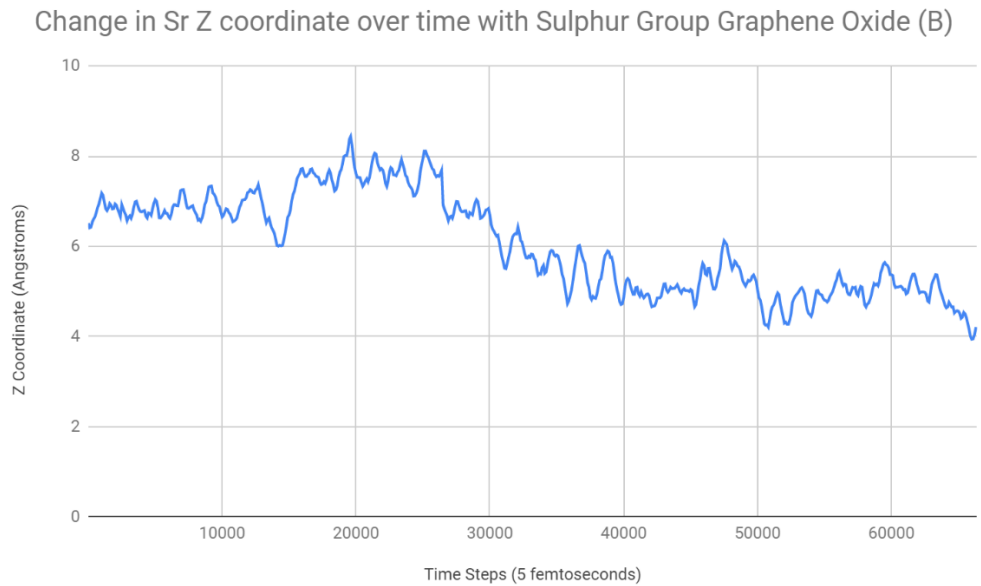
Figure 6.40: Sr SGO (B) AIMD change in Sr Z coordinate over 66400 timesteps

As seen in Figure 6.39 following optimisation all sulphonic acid groups have left the graphene sheet. The Sr ion at the start of the simulation is placed in proximity to a hydrogen sulphate ion. Over the course of the simulation the Sr ion migrates in proximity with the hydrogen sulphate ion away from the graphene sheet. This suggests there may be some affinity between the Sr ion to the hydrogen sulphate anion. The other sulphur oxides continuously migrate away from the graphene sheet during the simulation along the same trajectory as the Sr ion as shown in Figure 6.39.

6.2 – ^{13}C SSNMR Analysis

Samples taken as described in 5.2 following filtration of Cs and Sr solutions through BGO and BRGO were analysed by ^{13}C MAS SSNMR.

6.2.1 – Cs BGO

The ^{13}C SSNMR spectrum of a composite sample of BGO (67 mg wet) filtered with various concentrations of Cs(OH).xH2O solutions is shown below in Figure 6.41. The number of scans

is 2784 with a 1 second recycle delay, the pulse length is 3.8 microseconds with a MAS rate of 12.5 KHz. Figure 6.42 shows a comparison between the ^{13}C SSNMR of BGO and Cs exposed BGO.

13C Daniel BGO Cs, 67 mg (wet)
MAS 12.5 kHz
4mm HXY
18/12/20
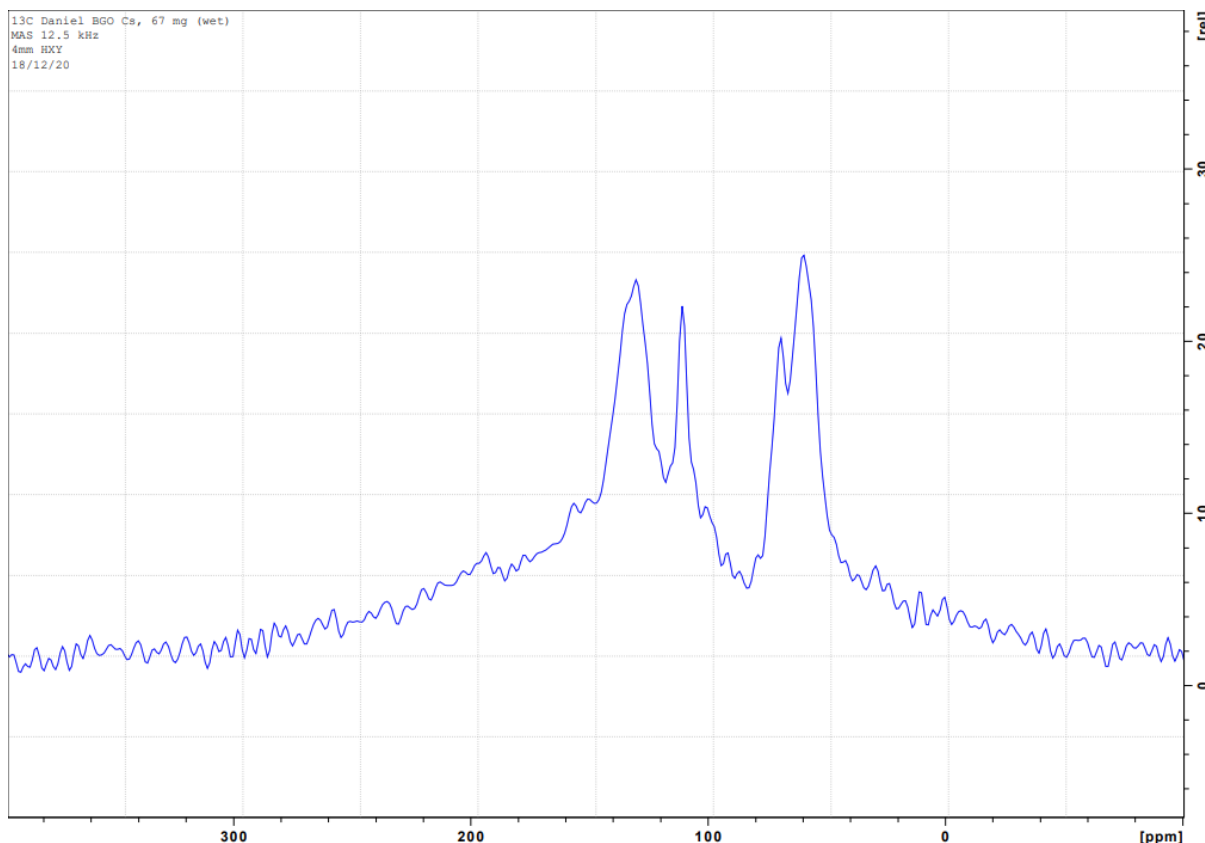
Figure 6.41: ^{13}C SSNMR spectrum of composite BGO filtered with Cs(OH).xH2O solutions

The distinct peak seen at 110 ppm most likely originates from the ($_2$FC-CF$_2$) bond in the PTFE tape [119] which was used to contain the moisture (which was still present in the sample following filtration) within the NMR sample introduction tube. This PTFE peak appears in all post filtered samples.
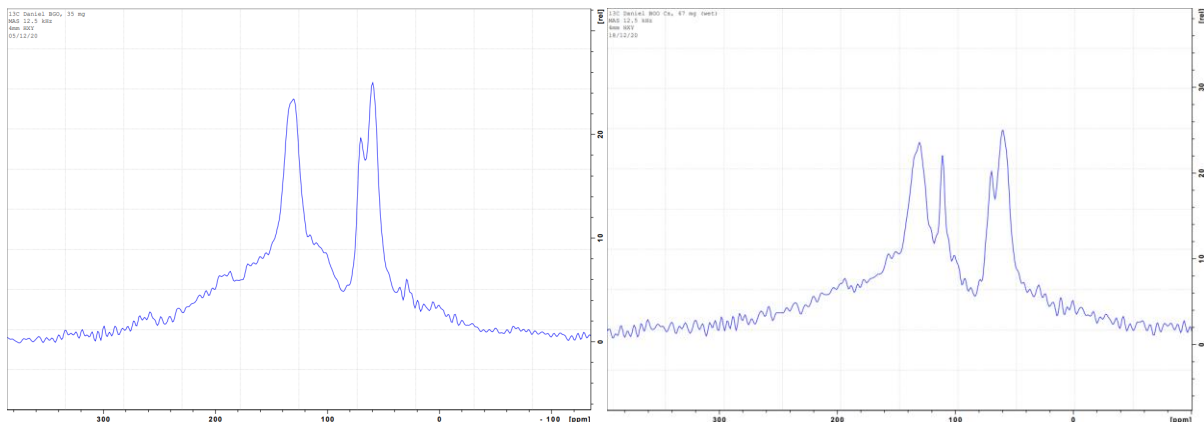
Figure 6.42: ^{13}C SSNMR spectrum comparison of BGO and Cs exposed BGO

Figure 6.42 shows that there is no significant shift in the ppm values or change in the relative intensities of the peaks corresponding to the BGO functional groups when BGO is exposed to Cs ions. This suggests that the Cs ions did not interact with any of the functional groups of BGO to an extent to which could be detected utilising this analytical technique with the parameters described.

6.2.2 – Cs BRGO

The ^{13}C SSNMR spectrum of a composite sample of BRGO (43 mg wet) filtered with various concentrations of Cs(OH).xH2O solutions is shown below in Figure 6.43 The number of scans is 2784 with a 1 second recycle delay, the pulse length is 3.8 microseconds with a MAS rate of 12.5 KHz. Figure 6.44 shows a comparison between the C^{13} SSNMR of BRGO and Cs exposed BRGO.
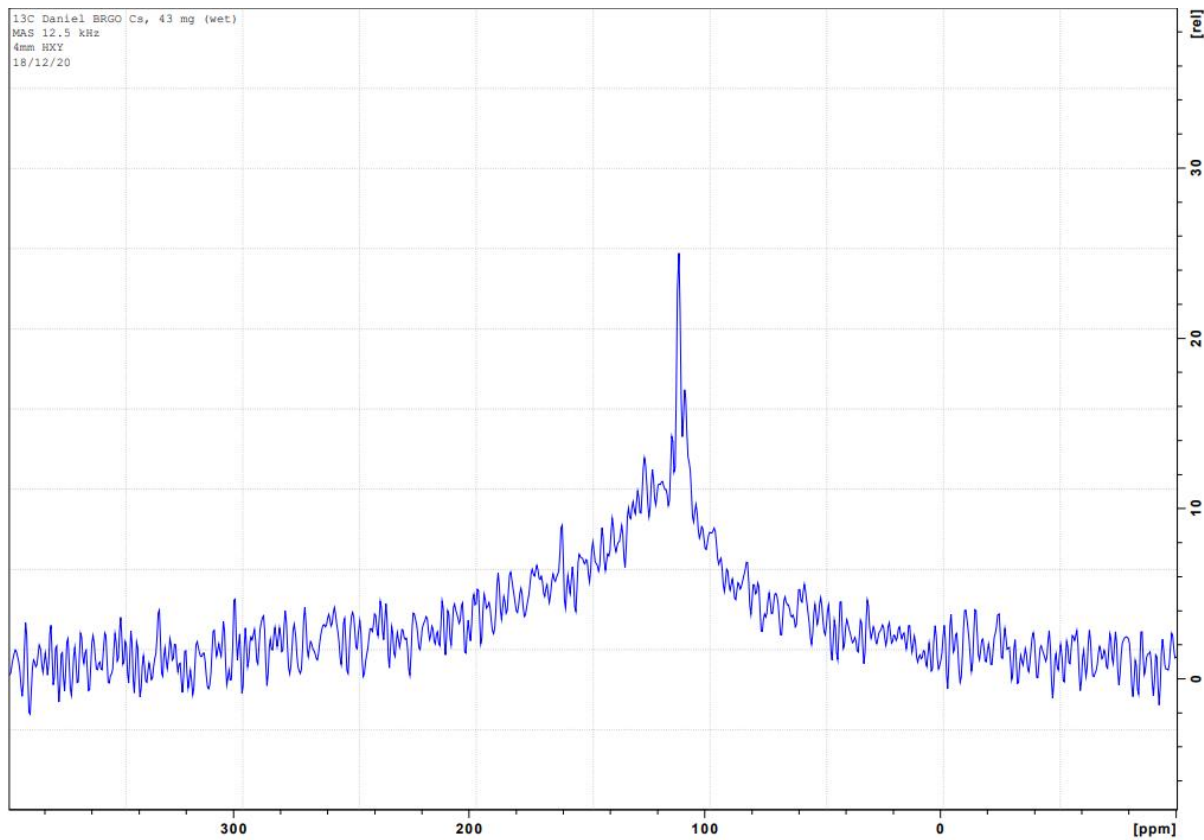
Figure 6.43: ^{13}C SSNMR spectrum of composite BRGO filtered with Cs(OH).xH2O solutions
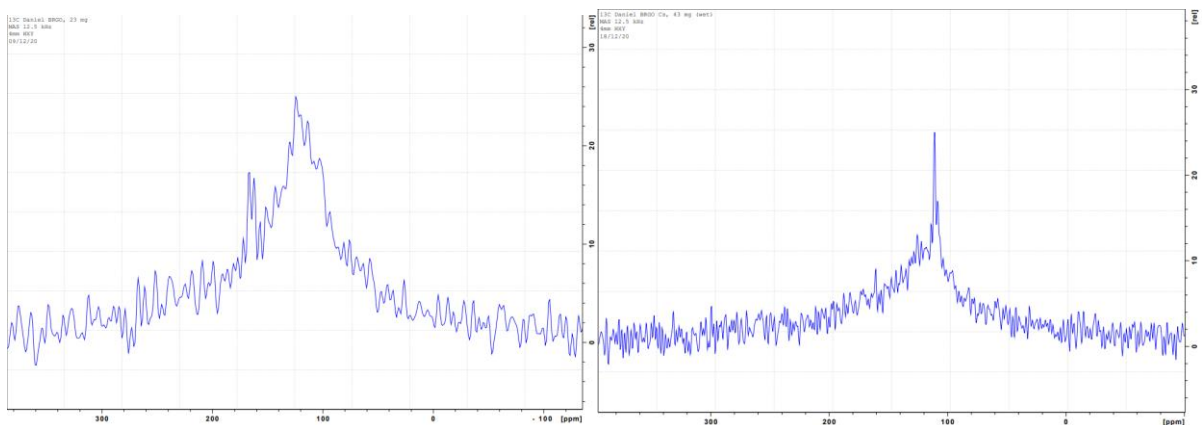
Figure 6.44: ^{13}C SSNMR spectra comparison of BRGO and Cs exposed BRGO

Figure 6.44 shows the removal of the peak at 170 ppm following the exposure of BRGO to Cs ions. This may be the result of the sample being further washed with a strong base which could have removed any residual amide carbonyl intermediate compounds remaining in the BRGO sample.

6.2.3 – Sr BGO

The ^{13}C SSNMR spectrum of a composite sample of BGO (86 mg wet) filtered with various concentrations of $Sr(OH)_2.8H_2O$ solutions is shown below in Figure 6.45. The number of scans is 2784 with a 1 second recycle delay, the pulse length is 3.8 microseconds with a MAS rate of 12.5 KHz. Figure 6.46 shows a comparison between the ^{13}C SSNMR of BGO and Sr exposed BGO.
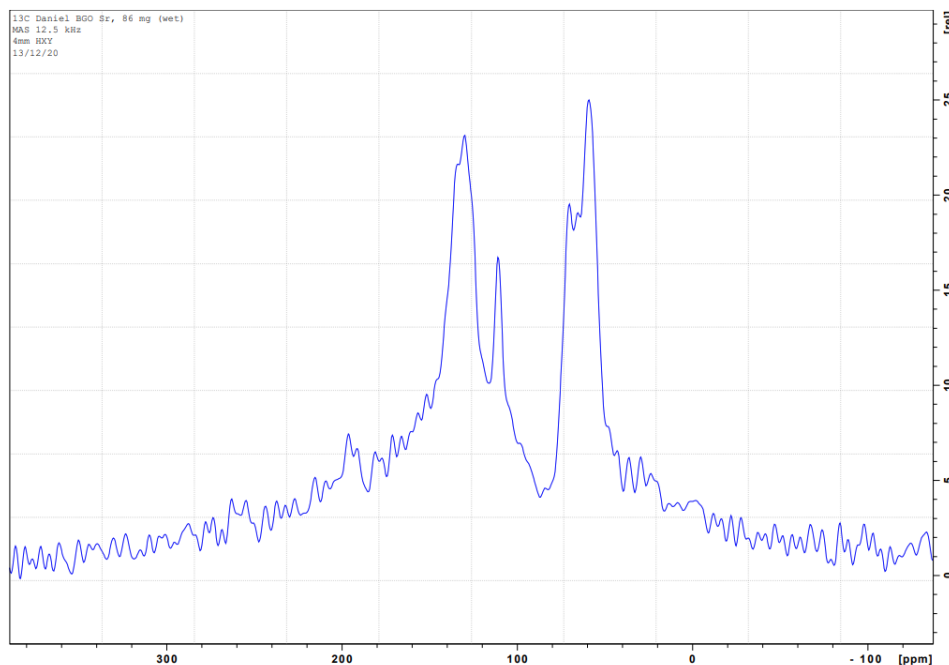
Figure 6.45: ^{13}C SSNMR spectrum of composite BGO filtered with $Sr(OH)_2.8H_2O$ solutions
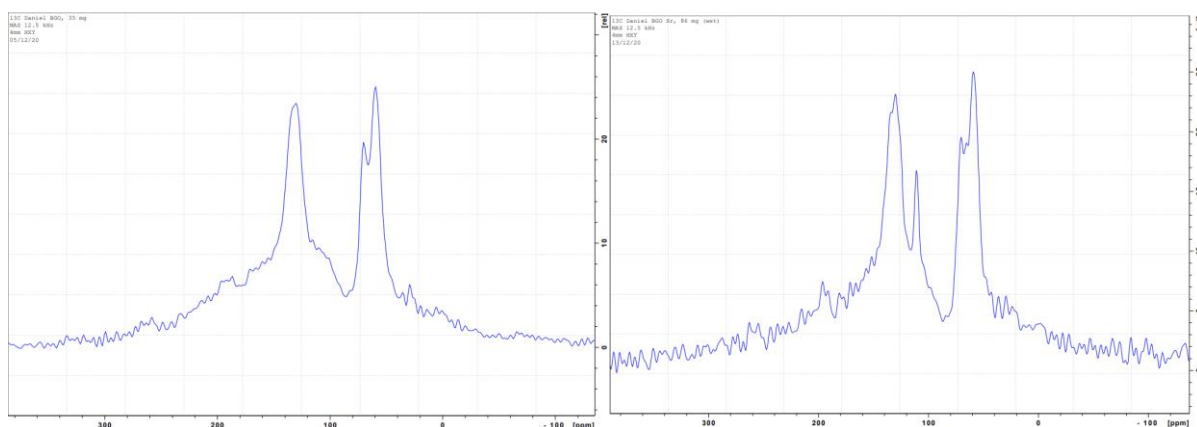
Figure 6.46: ^{13}C SSNMR spectra comparison of BGO and Sr exposed BGO

Figure 6.46 shows that there is no significant shift in the ppm values or change in the relative intensities of the peaks corresponding to the BGO functional groups when BGO is exposed to Sr ions. This suggests that the Sr ions did not interact with any of the functional groups of BGO to an extent to which could be detected utilising this analytical technique with the parameters described.

6.2.4 – Sr BRGO

The ^{13}C SSNMR spectrum of a composite sample of BRGO (23 mg wet) filtered with various concentrations of $Sr(OH)_2.8H_2O$ solutions is shown below in Figure 6.47. The number of scans is 2784 with a 1 second recycle delay, the pulse length is 3.8 microseconds with a MAS rate of 12.5 KHz. Figure 6.48 shows a comparison between the ^{13}C SSNMR of BRGO and Sr exposed BRGO.
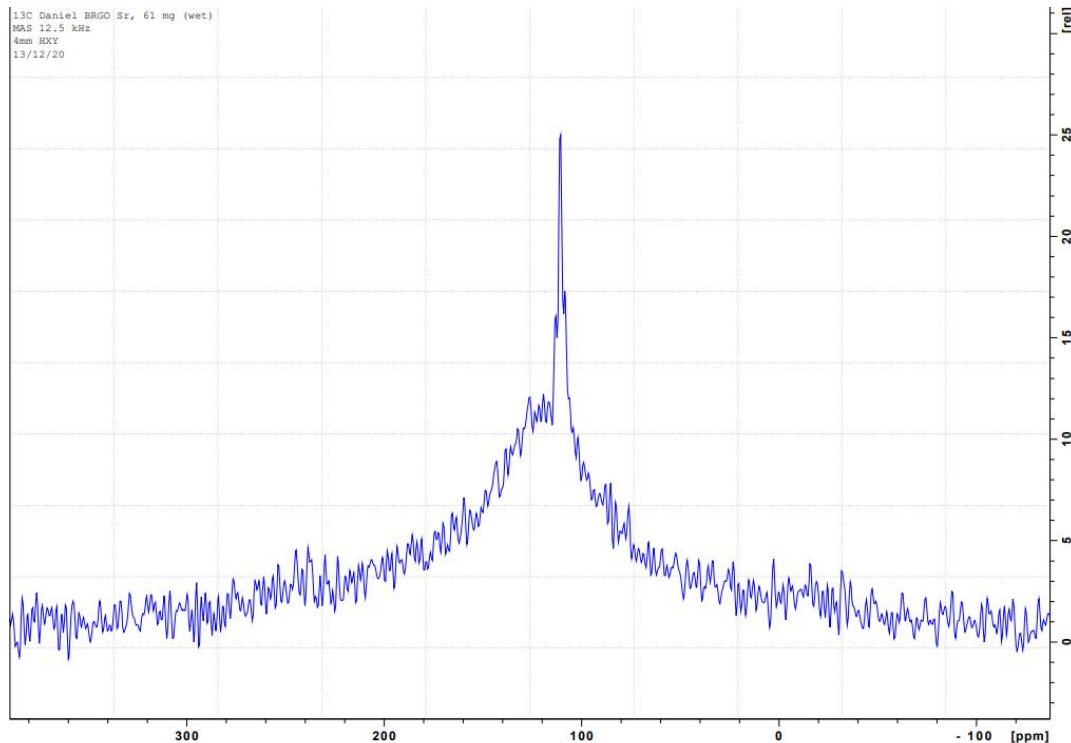
Figure 6.47: ^{13}C SSNMR spectrum of composite BRGO filtered with $Sr(OH)_2.8H_2O$ solutions
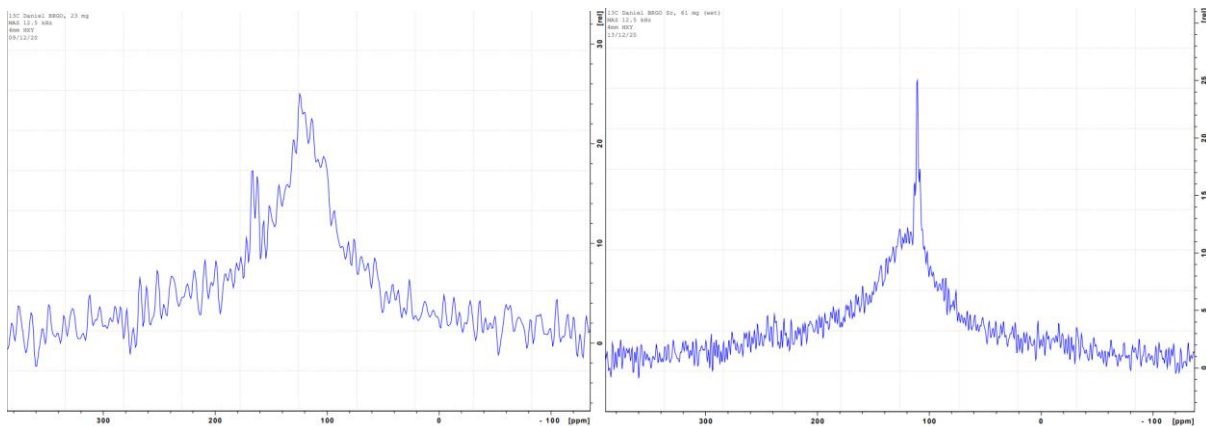
Figure 6.48: ^{13}C SSNMR spectrum comparison of BRGO and Sr exposed BRGO

Figure 6.48 shows the removal of the peak at 170 ppm following the exposure of BRGO to Sr ions. This may be the result of the sample being further washed with a strong base which could have removed any residual amide carbonyl intermediate compounds remaining in the BRGO sample.

6.3 – Filtrate ICP Analysis

ICP analysis was conducted using an Agliant 5100 ICP-OES UDV. The instrument was calibration checked using a wavelength calibration standard obtained from Agilent technologies. Standards and samples were matrix matched in an ≈ 3 % HNO$_3$ solution (60.4299 g/L) using Honeywell Fluka HNO$_3$ (≥ 69 %). Pipette error over a 10-weight average was calculated at 1.4 % which is within the detectable error limit for the instrument. The instrument was calibrated using a 6-point calibration including a blank. A second blank was used following calibration and prior to analysis to prevent inadvertent contamination of the first sample. A series of calibration standards were prepared by diluting the appropriate calibration standard for the sample set to produce a linear calibration. Standards and samples were analysed (replicates) 3 times using a pump speed of 3, with an uptake delay of 25 seconds and the rinse (H$_2$O) time was 30 seconds. The read time was 5 seconds with a

stabilisation time of 15 seconds. View mode was axial, nebuliser flow rate was 0.7 L/min, plasma flow rate was 12 L/min and auxiliary flow was 1 L/min.

6.3.1 – Sr

The strontium standard used to produce a linear calibration was sourced from Sigma Aldrich (Sr 9998 mg/L +/- 20 mg/L). A series of dilutions were performed to produce 1,2,5,10,15 and 25 ppm solutions of Sr in ≈ 3 % HNO_3. Each sample was diluted by a factor of 10 to ensure all samples fell within the calibration. The calibration graphs and typical peak shapes produced at various wavelengths for strontium are given in Appendix F. Taking into consideration calculated errors and peak resolution the quantitative analytical results have been taken from wavelength 232.236 nm. The sample analysis results are show below in Table 6.1:

Sample identification	Concentration of Sr prior to filtration (ppm)	Analysis results at 232.236 nm (ppm)	Actual Sr (ppm)	Reduction in Sr concentration (%)
Sr1	332	2.99	29.9	90.99
Sr2	333	3.02	30.2	90.93
Sr3	333	2.81	28.1	91.56
HG01	1269	9.98	99.8	92.14
HG02	1275	9.59	95.9	92.48
HG03	1277	10.09	100.9	92.10
RG01	526	4.66	46.6	91.14
RG02	528	4.54	45.4	91.40
RG03	527	4.42	44.2	91.61
BG01	577	4.35	43.5	92.46
BG02	576	4.54	45.4	92.12
BG03	578	4.69	46.9	91.89
BRG01	471	3.55	35.5	92.46
BRG02	471	3.59	35.9	92.38
BRG03	470	3.75	37.5	92.02
MS1	1650	1.59	15.9	99.04
MS2	1650	1.62	16.2	99.02
MS3	1650	1.29	12.9	99.22

Table 6.1: ICP-OES sample analysis results (Sr)

Table 6.1 shows that the majority (≈ 90 %) of Sr is removed by the sintered funnel. There is a slight increase (1-2 %) in Sr removal with the addition of the graphene derivatives. There does not appear to be any significant difference in Sr concentration reduction between the graphene derivatives which suggests that the level of oxidation in the samples is not a determining factor for the adsorption of Sr. The molecular sieve filtrate samples have significantly less Sr concentrations (≈ 99 %) than the graphene filtrate samples (≈ 92 %) suggesting the molecular sieve is a more effective adsorbent for Sr than the graphene derivatives.

6.3.2 – Cs

The caesium standard used to produce a linear calibration was sourced from HPS (Cs 10000 µg/ml +/- 30 µg/L). A series of dilutions were performed to produce 1,2,5,10,15 and 25 ppm solutions of Cs in ≈ 3 % HNO_3. All samples except HGO and MS were diluted by a factor of 10, HGO and MS were diluted by a factor of 100 to ensure all samples fell within the calibration. The calibration graphs and typical peak shapes produced at various wavelengths for caesium are given in Appendix G. Taking into consideration calculated errors and peak resolution the quantitative analytical results have been taken from wavelength 455.522 nm. The sample analysis results are show below in Table 6.2:

Sample identification	Concentration of Cs prior to filtration (ppm)	Analysis results at 455.522 nm (ppm)	Actual Cs (ppm)	Reduction in Cs concentration (%)
Sr1	970	11.66	116.6	87.98
Sr2	972	11.81	118.1	87.85
Sr3	970	12.71	127.1	86.90
HG01	11359	14.70	1470.0	87.06
HG02	11361	14.66	1466.0	87.10
HG03	11359	15.34	1534.0	86.49
RG01	777	9.91	99.1	87.24
RG02	775	9.69	96.9	87.50
RG03	777	9.69	96.9	87.54
BG01	846	11.04	110.4	86.95
BG02	848	11.05	110.5	86.97
BG03	846	10.77	107.7	87.27
BRG01	692	9.55	95.5	86.20
BRG02	691	9.64	96.4	86.05
BRG03	693	9.80	98.0	85.85
MS1	3554	2.69	269.0	92.43
MS2	3553	2.81	281.0	92.09
MS3	3548	2.75	275.0	92.25

Table 6.2: ICP-OES sample analysis results (Cs)

Table 6.2 shows that the majority ($\approx$ 87 %) of Cs is removed by the sintered funnel. There is no significant increase in Cs removal with the addition of the graphene derivatives. The molecular sieve filtrate samples have significantly less Cs concentrations ($\approx$ 92 %) than the graphene filtrate samples ($\approx$ 87 %) suggesting the molecular sieve is a more effective adsorbent for Cs than the graphene derivatives. In summary, the analytical results show little evidence of strong adsorption however, this is a preliminary measurement of the graphene membranes with little optimisation of the experimental setup or of the solution concentrations. There is some evidence for Sr^{2+} adsorption and this may suggest ion selectivity which could be useful for specific applications. Although there are clear limitations for high concentration solutions, the small differences in adsorption observed could be used to remove low concentrations of residual ions at later stages of a bespoke filtration process.

Chapter 7: Conclusions

7.1 – Simulations

Visualisation of the simulations performed within this research highlight the limitations of the periodic boundary conditions applied to the system. The inability to incorporate carbonyl and carboxyl groups to the edges of the graphene sheets leads to an inaccurate description of the structure of the graphene derivatives which should have functionality at the peripheries. This prevents the simulation and investigation of ion adsorption at the edges of the graphene sheets and introduces instability which is seen in the simulations which incorporate carboxyl groups on the surface of the graphene sheets. However, the instability of the carboxyl groups on the graphene sheets which decompose to carbon dioxide and a hydronium ion in each simulation to which it is incorporated provides further evidence that if carboxyl groups do exist within graphene oxide, they most likely only exist in a stable form on the edges of graphene oxide or within significant voids within the graphene sheets, which have not been simulated within this research. Carbonyl and epoxide functionalities appear interchangeably following optimisation of the oxygenated structures suggesting that both functionalities can exist within the main body of the graphene sheet, further simulations would be required to determine the mechanisms of preferential formation for either functionality.

There appears to be some form of attraction between a Cs ion and the surface of FFGO as seen in Figures 6.1 and 6.2. The Cs ion migrates into the adjacent computational cell and towards the surface of FFGO however the exact location of attraction cannot be determined based on the representation of the ion trajectory within VMD. Further research could be conducted to repeat the simulation with the ion placed at alternative locations which may

produce an ion trajectory within the starting cell. Reflective boundary conditions could be implemented to inhibit ion migration into adjacent cells. An alternative representation for ion trajectory may be used which may be capable of identifying the exact location on the surface of FFGO to which the Cs ion is attracted. Attraction of a Sr ion to a hydrogen sulphate ion can be seen in simulation SFRGO B (Figure 6.39). It is suggested that the Sr^{2+} ion is attracted to the relative negativity of the HSO_4^- ion as the two ions remain in proximity moving along the same trajectory with each other throughout the simulation. Inspection of the orientation of the HSO_4^- ion to the Sr^{2+} ion throughout the simulation suggests that the attraction between the two ions is via the regions of negative electrostatic potential which originate from the lone pair of electronegative oxygen atoms of HSO_4^-.

Strong initial repulsion of Sr ions can be seen between fluorinated (Figure 6.13) and carbonyl groups (Figure 6.35) when the ion is placed in proximity to the functional groups at the beginning of the simulation. This contrasts with the expected result that the positively charged anions will be attracted by electrostatic interaction to the electronegative functional groups on the graphene oxide surface. However, it may be the case that the expected processes occur on longer timescales which are not captured within the durations of the simulations performed in this thesis.

7.2 – Analytical

Characterisation of the graphene oxide prepared via the hummer's method shows how critical an effective washing method is for the removal of sulphur and the formation of the oxygen functionalities typically associated with graphene oxide. The lack of HGO functionalisation suggests that the removal of sulphur is key to the formation of these functionalities. The ^{13}C SSNMR spectra for RGO and BGO both show peaks at approximately

170 ppm which suggests the formation of hydrazide. Further NMR analysis and additional characterisation would be required to fully identify the origin of the peak.

Analysis of filtrate samples shows that Cs^+ was not absorbed by any of the graphene derivatives which could explain why there was no significant shift in the ppm values or change in the relative intensities of the peaks corresponding to the BGO functional groups within its ^{13}C SSNMR spectra. Filtrate samples containing Sr^{2+} show an increase in Sr^{2+} removal with the introduction of the graphene derivates. This suggests that some adsorption has taken place. However, there was no significant shift in the ppm values or change in the relative intensities of the peaks corresponding to the BGO functional groups within its ^{13}C SSNMR spectra. This may be explained by the relative low removal of Sr^{2+} by BGO as there has been an insufficient quantity adsorbed to effect a significant enough change which would be detectable on the NMR.

7.3 – Summary

The simulation component of this work has highlighted the complexity of graphene systems for ion capture applications and further work is required to explore this in more detail. Additional chemical systems and alternative computational approaches should be explored to observe ion attraction over longer timescales.

The experimental component has provided a good understanding of graphene synthesis and the chemical effects of the steps taken. The ion capture properties appear limited but could be developed further and studied in more detail by investigating a wider ion concentration range and alternative graphene functionalities.

7.4 – Future Work

The potential adsorptive capabilities of FFGO for Cs ions should be further explored both computationally and with physical adsorption experiments. Fluorinated functional groups on the FFGO surface can be separated and added individually to the GO surface computationally to investigate which functional group has the greatest affinity for Cs ions. GO can then be prepared using novel synthetic techniques to produce an FFGO variant with an abundance of the fluorinated functional group which has been shown to have good affinity to Cs ions. The variant can then be compared to a standard molecular adsorbent to determine adsorption capacity and efficiency.

Computational models should be developed so that edges of GO can be simulated. Carboxyl groups can then be implemented onto the GO edges which should remain stable and the interaction of these functional groups with Cs and Sr ions can then be investigated. This may be achieved by defining a ribbon or developing a cluster model with clearly defined GO edges within a computational box.

The presence of carboxyl groups appears critical to the adsorption capabilities of GO. Carboxyl groups are unstable on the basal plane of GO and therefore are only likely to exist on the edges of GO flakes. The design principles for GO adsorbents should therefore seek to increase the number of edges available within a given mass of GO which will increase the quantity of available carboxyl groups for ion adsorption. This could be achieved by reducing the size of the GO flakes as more flakes will have more edges and therefore a greater amount of carboxyl groups. Methods to enhance the oxidation at the edges of graphene sheets could also be researched to increase the concentration of oxygenated functionalities on the GO edges.

Bibliography

[1] Prăvălie, R, Bandoc, G. (2018). Nuclear energy: Between global electricity demand, worldwide decarbonisation imperativeness, and planetary environmental implications. Journal of Environmental Management, 209 (1), p81-92

[2] Letcher, T, M. (2019). 1 - Why do we have global warming? In: Managing Global Warming: An Interface of Technology and Human Issues. London: Elsevier, p3-15

[3] Martin, P.G. Tomkinson, N.G. Scott T.B. (2017). The future of nuclear security: Commitments and actions – Power generation and stewardship in the 21st century. Energy Policy, 110, p325-330

[4] York, R Bell, S, E. (2019). Energy transitions or additions: Why a transition from fossil fuels requires more than the growth of renewable energy. Energy Research & Social Science, 51, p40-43

[5] Myasoedov, B, F. Kalmykov, S, N. (2015). Nuclear power industry and the environment, Mendeleev Communications, 5 (5), p319-328

[6] Saling, J. (2001). Sources of Radwaste In: radioactive waste management. London: Taylor & Francis, p12-13

[7] Ojovan, M, I. Lee, W, E. (2014). Sources of nuclear waste in: An Introduction to Nuclear Waste Immobilisation. 2nd ed. Oxford: Elsevier, p75-76

[8] Martin, A. Haribson, S.A. (1979). Biological effects of radiation in: An introduction to radiation protection. 2nd ed. London: Springer science and media, p43-46

[9] Ojovan, M, I. Lee, W, E. (2005). Introduction to immobilisation in: An Introduction to Nuclear Waste Immobilisation. Oxford: Elsevier, p6-7

[10] Dlouhý, Z. (1982). 2 Characteristics of Radioactive Wastes, Studies in Environmental Science. 15, p30-64

[11] El-Hinnawi, E, E. (1982). Reprocessing. In: Nuclear Energy and the Environment: Environmental Sciences and Applications. Oxford: Pergamon Press, p147-148

[12] National Research Council, Division on Earth, and Life Studies, Nuclear and Radiation Studies Board, Committee on the Analysis of Cancer Risks in Populations near Nuclear Facilities. (2012). Effluent Releases from nuclear power plants and fuel cycle facilities in: Analysis of Cancer Risks in Populations near Nuclear Facilities. Washington: The national academies press, p38-39

[13] Roger, SF. (2018). Understanding Sorption Behavior and Properties of Radionuclides in the Environment. In: Rhaman, R, A. Principles and Applications in Nuclear Engineering - Radiation Effects, Thermal Hydraulics, Radionuclide Migration in the Environment. London: IntechOpen. p124-125

[14] Pengcheng, G. Zhanga, S. Xing, L. Wang X. Wen, T. Jehana, R. Alsaedi, A. Hayat, T. Wang, X. (2018). Recent advances in layered double hydroxide-based nanomaterials for the removal of radionuclides from aqueous solution. Environmental Pollution. 240, p493-505

[15] Attallah, M, F. Hassan, H, S. Youssef, M, A. (2019). Synthesis and sorption potential study of Al2O3ZrO2CeO2 composite material for removal of some radionuclides from radioactive waste effluent. Applied Radiation and Isotopes, 147, p40-47

[16] Mahmoud, M, E. Saad, E, A. Soliman, M, A. Abdelwahab, M, S. (2019). Removal of radioactive cobalt/zinc and some heavy metals from water using diethylenetriamine/2-pyridinecarboxaldehyde supported on NZVI. Micro chemical Journal, 145, p1102-1111

[17] Attallah, M, F. Abd-Elhamid, A, I. Ahmed, I, M. Aly, H, F. (2018). Possible use of synthesized nano silica functionalized by Prussian blue as sorbent for removal of certain radionuclides from liquid radioactive waste. Journal of Molecular Liquids, 261, p379-386

[18] Chi, H, A. Tsang, K, L. Zeng, Y. Zhao, W. Zhang, T. Zhan, Y. Xie, R. Leung, D, Y, C. Huang, H. (2019). Titanium oxide based photocatalytic materials development and their role of in the air pollutants degradation: Overview and forecast. Environment International, 125, p200-228

[19] Kim, H. Kim, M. Kim, W. Lee, W. Kim, S. (2018). Photocatalytic enhancement of cesium removal by Prussian blue-deposited TiO_2, Journal of Hazardous Materials, 357, p449-456

[20] Osmanlioglu, A, E. (2018). Decontamination of radioactive wastewater by two-staged chemical precipitation. Nuclear Engineering and Technology. 50 (6), p886-889

[21] Soliman, M, A. Rashad, G, M. Mahmoud, M, R. (2015). Fast and efficient cesium removal from simulated radioactive liquid waste by an isotope dilution–precipitate flotation process. Chemical Engineering Journal, 275, p342-350

[22] Bratby, J. (2006). Introduction In: Coagulation and Flocculation in Water and Wastewater Treatment. 2nd ed. London: IWA Publishing, p5-6

[23] Rout, T.K. Sengupta, D.K. Kaur, G. Kumar, S. (2006). Enhanced removal of dissolved metal ions in radioactive effluents by flocculation. International Journal of Mineral Processing, 80, p215-222

[24] Huang, CP. Wu, JY. Li, YJ. (2018). Treatment of spent nuclear fuel debris contaminated water in the Taiwan Research Reactor spent fuel pool. Progress in Nuclear Energy, 108, p26-33

[25] Zheng, Y. Qiao, J. Yuan, J. Shen, J. Wang, AJ. Niu, L. (2017). Electrochemical removal of radioactive cesium from nuclear waste using the dendritic copper hexacyanoferrate / carbon nanotube hybrids, Electrochimica Acta, 257, p172-180

[26] Jin, X. Huang, L. Yu, S. Ye, M. Yuan, J. Shen, J. Fang, K. Weng, X. (2019). Selective electrochemical removal of cesium ion based on nickel hexacyanoferrate/reduced graphene oxide hybrids. Separation and Purification Technology, 209, p65-72

[27] Kim, W, S. Nam, S. Chang, S. Kim, H. Um, W. (2018). Removal of Chalk River unidentified deposit (CRUD) radioactive waste by enhanced electro kinetic process. Journal of Industrial and Engineering Chemistry, 57, p89-96

[28] Zhang, X. Gu, P. Liu, Y. (2019). Decontamination of radioactive wastewater: State of the art and challenges forward. Chemosphere, 215, p543-553

[29] Ding, C. Cheng, W. Sun, Y. Wang, X. (2015). Novel fungus-Fe_3O_4 bio-nanocomposites as high-performance adsorbents for the removal of radionuclides. Journal of Hazardous Materials, 295, p127-137

[30] Abdel-Galil, E, A. Moloukhia, H. Abdel-Khalik, M. Mahrous, S, S. (2018). Synthesis and physico-chemical characterization of cellulose/HO_7Sb_3 nanocomposite as adsorbent for the removal of some radionuclides from aqueous solutions. Applied Radiation and Isotopes, 140, p363-373

[31] Saleh, H, M. (2012). Water hyacinth for phytoremediation of radioactive waste simulate contaminated with cesium and cobalt radionuclides. Nuclear Engineering and Design, 242, p425-432

[32] Ding, S. Zhang, L. Li, Y. Hou, L. (2019). Fabrication of a novel polyvinylidene fluoride membrane via binding SiO_2 nanoparticles and a copper ferrocyanide layer onto a membrane surface for selective removal of cesium. Journal of Hazardous Materials, 368, p292-299

[33] Yu, S. Zhang, X. Li, F. Zhao, X. (2018). Poly (vinyl pyrrolidone) modified poly (vinylidene fluoride) ultrafiltration membrane via a two-step surface grafting for radioactive wastewater treatment. Separation and Purification Technology, 194, p404-409

[34] Combernoux, N. Schrive, L. Labed, V. Wyart, Y. Carretier, E. Moulin, P. (2017). Treatment of radioactive liquid effluents by reverse osmosis membranes: From lab-scale to pilot-scale. Water Research, 123, p311-320

[35] McCoy, T.M. Turpin, G. Teo, B, M. Tabor, R.F. (2019). Graphene oxide: a surfactant or particle? Current Opinion in Colloid & Interface Science, 39, p98-109

[36] Wang, X. Yu, S. Jin, J. Wang, H. Alharbi, N, S. Alsaedi, A. Hayat, T. Wang, X. (2016). Application of graphene oxides and graphene oxide-based nanomaterials in radionuclide removal from aqueous solutions. Science Bulletin, 61, (20), p1583-1593

[37] Peng, W. Li, H. Liu, Y. Song, S. (2017). A review on heavy metal ions adsorption from water by graphene oxide and its composites. Journal of Molecular Liquids, 230, p496-504

[38] Lu, S. Sun, Y. Chen, C. (2019). Chapter 4 - Adsorption of radionuclides on carbon-based nanomaterials. Interface Science and Technology, 29, p141-215

[39] Lim, J.Y. Mubarak, N.M. Abdullah, E.C. Nizamuddin, S. Khalid, M. Inamuddin. (2018). Recent trends in the synthesis of graphene and graphene oxide-based nanomaterials for removal of heavy metals — A review. Journal of Industrial and Engineering Chemistry, 66, p29-44

[40] Chen, X. Wang, X. Wang, S. Qi, J. Xie, K. Liu, X. Li, J. (2017). Furfuryl alcohol functionalized graphene for sorption of radionuclides. Arabian Journal of Chemistry, 10, (6), p837-844

[41] Chen, H. Shao, D. Li, J. Wang, X. (2014). The uptake of radionuclides from aqueous solution by poly(amidoxime) modified reduced graphene oxide. Chemical Engineering Journal, 254, p623-634

[42] Ma, F. Li, Z. Zhao, H. Geng, Y.Zhou, W. Li, Q. Zhang, L. (2017). Potential application of graphene oxide membranes for removal of Cs(I) and Sr(II) from high level-liquid waste. Separation and Purification Technology, 188, p523-529

[43] Yuan, K. Taylor, S.D. Powell, B.A. Becker, U. (2017). An ab initio study of the adsorption of Eu^{3+}, Pu^{3+}, Am^{3+}, and Cm^{3+} hydroxide complexes on hematite (001) surface: Role of magnetism on adsorption. Surface Science, 664, p120-128

[44] Lago, D.C. Nuñez, M. Prado, M.O. (2016). Adsorption of CsCl on porous SiO2 glass surface: experimental results and ab-initio calculations. Journal of Non-Crystalline Solids, 440, p70-75

[45] Li, K. Zhao, Y. Zhang, P. He, C. Deng, J. Ding, S. Shi, W. (2016). Combined DFT and XPS investigation of iodine anions adsorption on the sulphur terminated (001) chalcopyrite surface. Applied Surface Science, 390, p412-421

[46] Rattana, S. Chaiyakun, N. Witit-anun, N. Nuntawong, P. Chindaudom, S. Oaew, C. Kedkeaw, C. Limsuwan, P. (2012). Preparation and characterization of graphene oxide nanosheets. Procedia Engineering, 32, p759-764

[47] Gebreegziabher, G.G. Asemahegne, A.S. Ayele, D.W. Dhakshnamoorthy, M. (2019). One-step synthesis and characterization of reduced graphene oxide using chemical exfoliation method. Materials Today Chemistry, 12, p233-239

[48] Das, T.K. Banerjee, S. Pandey, M. Vishwanadh, B. Kshirsagar, R.J. Sudarsan, V. (2017). Effect of surface functional groups on hydrogen adsorption properties of Pd dispersed reduced graphene oxide. International Journal of Hydrogen Energy, 42, p8032-8041

[49] Berezin, F, A. Shubin, M. (1991). The Schrödinger Equation. Dordrecht: Springer Science & Business Media, B.V, p6-7

[50] Greenberger, D. Hentschel, K. Weinert, F. (2009). Compendium of Quantum Physics: Concepts, Experiments, History and Philosophy. Berlin: Springer Science & Business Media, p271-272

[51] Epstein, S. (1974). The variation method in quantum chemistry. New York: Academic Press, p5-6

[52] Ramachandran, K.I. Deepa, G. Namboori, K. (2008). Computational Chemistry and Molecular Modeling: Principles and Applications. Berlin: Springer, p54-55

[53] Huzinaga, S. Andzelm, J. Radzio-Andzelm, E. Sakai, Y. Tatewaki, H. Klobukowski, M. (1984). Gaussian Basis Sets for Molecular Calculations. Amsterdam: Elsevier, p1-2

[54] Martin, R.M. (2004). Electronic Structure: Basic Theory and Practical Methods. Cambridge: Cambridge University Press, p204-205

[55] Reiher, M. Wolf, A. (2009). Relativistic Quantum Chemistry: The Fundamental Theory of Molecular Science. Weinheim: Wiley-VCH, p274-275

[56] Pilar, F.L. (1990). Elementary Quantum Chemistry. 2nd edition, New York: Dover Publications, p191-193

[57] Lowe, J.P. Peterson, K. (2006). Quantum Chemistry. 3rd edition, Elsevier: London, p137-138.

[58] Patterson, J. Bailey, B. (2010). Solid-State Physics: Introduction to the Theory. 2nd edition, Berlin: Springer, p119-120

[59] Zaleśny, R. Manthos, G. Papadopoulos, P. Mezey, G. Leszczynski, J. (2011). Linear-Scaling Techniques in Computational Chemistry and Physics: Methods and Applications. New York: Springer, p264-265

[60] Leszczynski, J. (2004). Computational Materials Science. Amsterdam: Elsevier, p171-173

[61] Ciarlet, P.G. (2003). Computational Chemistry. Amsterdam: Elsevier, p197-198

[62] Kabadshow, I. (2012). Periodic Boundary Conditions and the Error-controlled Fast Multipole Method. Julich: forschungszentrum Julich, p77-78

[63] Rankin, D.W.H. Mitzel, N. Morrison, C. (2013). Structural Methods in Molecular Inorganic Chemistry. Chichester: John Wiley & Sons, Ltd, p34-35

[64] Marx, D. Hutter, J. (2009). Ab Initio Molecular Dynamics: The Virtual Laboratory Approach. Cambridge: Cambridge University Press, p3-4

[65] Tuckerman, M. (2010). Statistical Mechanics: Theory and Molecular Simulation. Oxford: Oxford University Press, p10-11

[67] Marx, D. Hutter, J. (2009). Ab Initio Molecular Dynamics: The Virtual Laboratory Approach. Cambridge: Cambridge University Press, p24-25

[68] Labanowski, J.K. Andzelm, J.W. (1991). Density Functional Methods in Chemistry. New York: Springer-Verlag, p14-15

[69] Wells, C. (2014). What do the C=O molecular orbitals of acetaldehyde look like, compared with those of formaldehyde? Available: https://www.quora.com/What-do-the-C-O-molecular-orbitals-of-acetaldehyde-look-like-compared-with-those-of-formaldehyde.   Last accessed 22/12/2019

[70] Davis, S.P. Abrams, M.C. James, W. (2001). Fourier Transform Spectrometry. California: Academic Press, p41-42

[71] Smith, B.C. (2011). Fundamentals of Fourier Transform Infrared Spectroscopy. 2nd ed. Florida: Taylor & Francis, p5-6

[72] Smith, B.C. (2011). Fundamentals of Fourier Transform Infrared Spectroscopy. 2nd ed. Florida: Taylor & Francis, p15-16

[73] Birkner, N. Wang, Q. (2019). How an FTIR Spectrometer Operates. Available: https://chem.libretexts.org/Bookshelves/Physical_and_Theoretical_Chemistry_Textbook_M

aps/Supplemental_Modules_(Physical_and_Theoretical_Chemistry)/Spectroscopy/Vibration al_Spectroscopy/Infrared_Spectr. Last accessed 28/12/2019

[74] Socrates, G. (2001). Infrared and Raman Characteristic Group Frequencies: Tables and Charts. West Sussex: John Wiley & Sons, p12-13

[75] Schrader, B. (1995). Infrared and Raman Spectroscopy: Methods and Applications. Weinheim: VCH, p13-14

[76] Ferraro, J.R. Nakamoto, K. (1994). Introductory Raman Spectroscopy. London: Academic Press, p4-5

[77] Larkin, P. (2011). Infrared and Raman Spectroscopy: Principles and Spectral Interpretation. Oxford: Elsevier, p17-18

[78] Tuz Johra, F. Lee, J. Jung, W-G. (2014). Facile and safe graphene preparation on solution-based platform. Journal of Industrial and Engineering Chemistry. 20, p2883–2887.

[79] McCreery, R.L. (2000). Raman Spectroscopy for Chemical Analysis. New York: Wiley-Interscience, p19-20

[80] Dimiev, A.M. Eigler, S. (2016). Characterisation Techniques. In: Graphene Oxide: Fundamentals and Applications. West Sussex: John Wiley & Sons, Incorporated. p102-103

[81] Wu, J, B. Lin, M, L. Cong, X. Liu. HN. Tan, PH. (2018). Raman spectroscopy of graphene-based materials and its applications in related devices. Chemical Society Reviews. 47 (1), p1822-1873

[82] Inkson, B.J. (2016). Scanning electron microscopy (SEM) and transmission electron microscopy (TEM) for materials characterization. Materials Characterization Using Nondestructive Evaluation (NDE) Methods, p17-43

[83] Goldstein, J. Newbury, D.E. Echlin, P. Joy, D.C Romig, A. D. Jr Lyman, C.E Fiori, C. Lifshin, E. (1992). Scanning Electron Microscopy and X-Ray Microanalysis. New York: Plenum Press, p21-22

[84] Khursheed, A. (2011). Scanning Electron Microscope Optics and Spectrometers. Singapore: World Scientific, p2-5

[85] Bell, D.C Garratt-Reed, A.J. (2003). Energy Dispersive X-ray Analysis in the Electron Microscope. Oxford: BIOS Scientific Publishers Limited, p6-7

[86] Russ, J.C. (1984). Fundamentals of Energy Dispersive X-Ray Analysis. London: Butterworth & Co Ltd, p2-3

[87] Goodge, J. (2013). Energy-Dispersive X-Ray Spectroscopy (EDS). Available: https://serc.carleton.edu/research_education/geochemsheets/eds.html. Last accessed 08/01/2020

[88] Pingping, S. (2012). Sorption of Metal Ions to Wood, Pulp and Bark Materials. Available: https://www.researchgate.net/figure/The-principle-and-major-components-of-a-typical-ICP-OES-instrument-Boss-and-Fredeen_fig13_268258151. Last accessed 03/06/21

[89] Taylor, H.E. Taylor, H.M. (2001). Inductively Coupled Plasma-Mass Spectrometry: Practices and Techniques. London: Academic Press, p15-16

[90] Moore, G.L. (1989). Introduction to Inductively Coupled Plasma Atomic Emission Spectrometry. Amsterdam: Elsevier, p3-4

[91] Levitt, M.H. (2001). Spin Dynamics: Basics of Nuclear Magnetic Resonance. West Sussex: John Wiley & Sons LTD, p5-6

[92] Antcliffe, D. Gordon, A. (2016). Metabonomics and Intensive Care. Available: https://www.researchgate.net/publication/298906982_Metabonomics_and_Intensive_Care . Last accessed 19/01/2020

[93] Jacobsen, N.E. (2007). NMR Spectroscopy Explained: Simplified Theory, Applications and Examples for Organic Chemistry & Structural Biology. New Jersey: John Wiley & Sons LTD, p8-9

[94] Balci, M. (2005). Basic 1H- and 13C-NMR Spectroscopy. Amsterdam: Elsevier, p12-13

[95] Keeler, J. (2010). Understanding NMR Spectroscopy. 2nd ed. Cambridge: John Wiley & Sons LTD, p27-28

[96] Sharon, M. Sharon, M. Shinohara, H. Tiwari, A. Tiwari, A. . (2015). NMR Analysis of Graphene. In: Sharon, M. Sharon, M. Graphene : An Introduction to the Fundamentals and Industrial Applications. Beverly: John Wiley & Sons, Incorporated. p89-90

[97] Gao, W. (2015). Solid-State 13C Nuclear Magnetic Resonance (SSNMR) Spectroscopy. In: Gao, W. Graphene Oxide. Cambridge: Springer. p1-28

[98] Dimiev, A.M. Eigler, S. (2016). Characterisation Techniques. In: Dimiev, A.M. Eigler, S. Graphene : An Introduction to the Fundamentals and Industrial Applications. West Sussex: John Wiley & Sons, Incorporated. p85-86

[99] Hutter, J. VandeVondele, J. Schütt, O. (2015). CP2K Open Source Molecular Dynamics. Available: https://www.cp2k.org/about. Last accessed 04/02/2020

[100] Humphrey, W. Dalke, A. Schulten, K. (2006). VMD Visual Molecular Dynamics. Available: https://www.ks.uiuc.edu/Research/vmd/. Last accessed 04/02/2020

[101] Frisch, M.J. (2015). Expanding the limits of computational chemistry. Available: https://gaussian.com/gaussview6/. Last accessed 04/02/2020

[102] Tatham,S. (1997). PuTTYFAQ. Available: https://www.chiark.greenend.org.uk/~sgtatham/putty/faq.html#faq-what. Last accessed 04/02/2020

[103] © 2020 VMware, Inc. (2020). Workstation Player. Available: https://www.vmware.com/uk/products/workstation-player.html. Last accessed 04/02/2020

[104] opentext^TM. (2020). OpenText Exceed 3D – Remote Access for 3D OpenGL Applications. Available: https://www.opentext.co.uk/products-andsolutions/products/specialtyTechnologies/connectivity/exceed-3d. Last accessed 04/02/2020

[105] Thomas, H.R. Day, S.P. Woodruff, W.E. Valles, C. Young, R.J. Kinloch, I.A. Morley, G.V. Hanna, J.V. Wilson, N.R. Rourke, J.P. (2013). Deoxygenation of Graphene Oxide: Reduction or Cleaning? Chemistry of Materials, 25, p3580-3588

[106] Cai, W. Piner, R.D. Stadermann, F.J. Park, S. Shaibat, M.A. Ishii, Y. Yang, D. Velamakanni, A. An, S.J. Stoller, M. An, J. Chen, D. Rodney S. (2008). Synthesis and Solid-State NMR Structural Characterization of ^{13}c-Labeled Graphite Oxide. Science. 321 (5897), p1815-1817

[107] Park, S. Hu, Y. Hwang, J. et al. (2012) Chemical structures of hydrazine-treated graphene oxide and generation of aromatic nitrogen doping. Nature Communications. 3, (638) p638-638

[108] Johra, F, T. Lee, JW. Jung, WG. (2014). Facile and safe graphene preparation on solution-based platform. Journal of Industrial and Engineering Chemistry. 20, p2883-2887

[109] Hasan, M.U. (1980). 13C NMR spectra of some amides and imides. Effect of inductive and mesomeric interactions, cyclization, and hydrogen bonding on 13C NMR chemical shifts. Magnetic Resonance in Chemistry. 14 (6), p447-450

[110] Aguilar-Boladosa, H. Contreras-Cid, A. Yazdani-Pedram, M. Acosta-Villavicencio, G. Flores, M. Fuenteal, P. Neira-Carrillo, A. Verde, R. López-Manchadoe, M.A. (2018). Synthesis of fluorinated graphene oxide by using an easy one-pot deoxyfluorination reaction. Journal of Colloid and Interface Science. 524, p219-226.

[111] Peng, X, Li, Y. Zhang, G. Zhang, F. Fan, X. (2013). Functionalization of Graphene with Nitrile Groups by Cycloaddition of Tetracyanoethylene Oxide. Low-Dimensional Carbon Nanomaterials. 2013 (5), Article ID 841789.

[112] Wei, M-P. Chai, H. Cao, Y-L. Jia, D-Z. (2018). Sulfonated graphene oxide as an adsorbent for removal of Pb2+ and methylene blue. Journal of Colloid and Interface Science. 524, p297-305

[113] Jensen, F. (2017). Introduction to computational chemistry. West Sussex: John Wiley & Sons, Incorporated. p404-405

[114] Sun, L. (2019). Structure and synthesis of graphene oxide. Chinese Journal of Chemical Engineering. 27 (10), p2251-2260

[115] Martin-Gullona, I. Péreza, J.M Domenea D. Salgado-Casanova A.J.A. Radovicb. L.R. (2020). New insights into oxygen surface coverage and the resulting two-component structure of graphene oxide. Carbon. 158, p406-417

[116] Pereraa, D. Abeywickrama, A. Zen, F. Colavita, P.E. Jayasundara, D.R. (2018). Evolution of oxygen functionalities in graphene oxide and its impact on structure and exfoliation: An oxidation time-based study. Materials Chemistry and Physics. 220, p417-425

[117] Aliyev, E. Filiz, V. Khan, M.M. Lee, Y.J. Abetz, C. Abetz, V. (2019). Structural Characterization of Graphene Oxide: Surface Functional Groups and Fractionated Oxidative Debris. Nanomaterials. 9 (8), p1180

[118] Bagri, A. Grantab, R. Medhekar, N.V. Shenoy. V.B (2010). Stability and Formation Mechanisms of Carbonyl- and Hydroxyl-Decorated Holes in Graphene Oxide. The Journal of Physical Chemistry. 114 (28), p12053-1206

[119] Liu, S.F. Schmidt-Rohr, K. (2001). High-Resolution Solid-State 13C NMR of Fluoropolymers. Macromolecules. 34, p8416-8418

Appendix

A – HGO EDS Spectra (Table 3.1)

Spectrum 5

	Wt%	σ
S	45.9	0.3
C	28.7	0.4
O	15.4	0.2
Mn	5.9	0.3
Si	2.9	0.1
K	0.9	0.1
Al	0.2	0.0
Mg	0.1	0.0

Spectrum 6

	Wt%	σ
C	48.3	0.2
O	29.6	0.2
S	18.0	0.1
Mn	2.9	0.1
K	0.7	0.0
Si	0.3	0.0
Al	0.1	0.0
Mg	0.1	0.0

B – RGO EDS Spectra (Table 3.2)

Spectrum 1

	Wt%	σ
C	74.6	0.2
O	11.1	0.1
S	8.9	0.1
Mn	3.7	0.2
K	1.3	0.0
Si	0.2	0.0
Ca	0.2	0.0
N	0.0	0.0

Spectrum 2

	Wt%	σ
C	70.0	0.3
O	14.9	0.1
S	10.2	0.1
Mn	2.1	0.1
K	1.5	0.0
N	1.1	0.3
Si	0.2	0.0
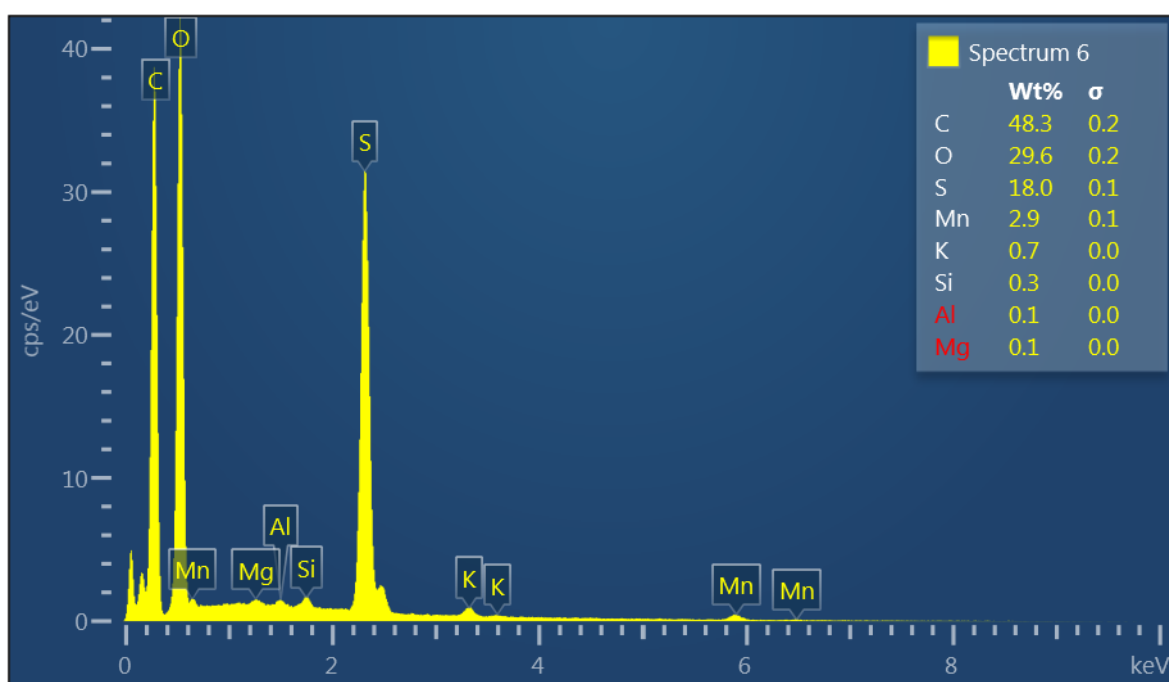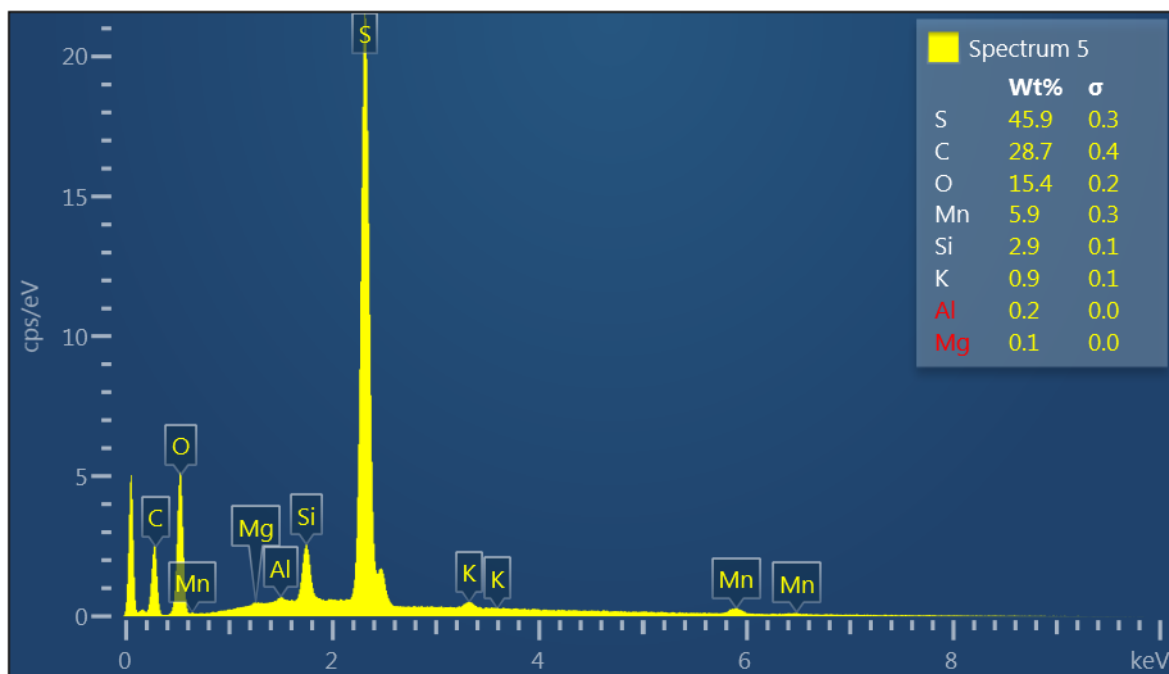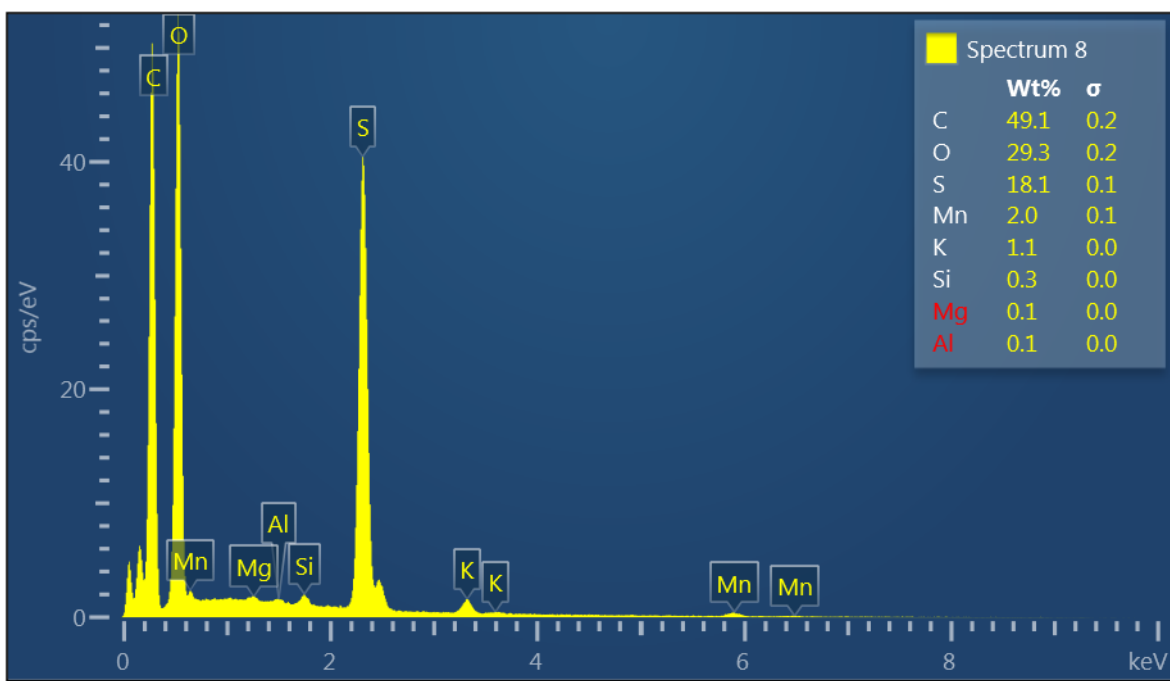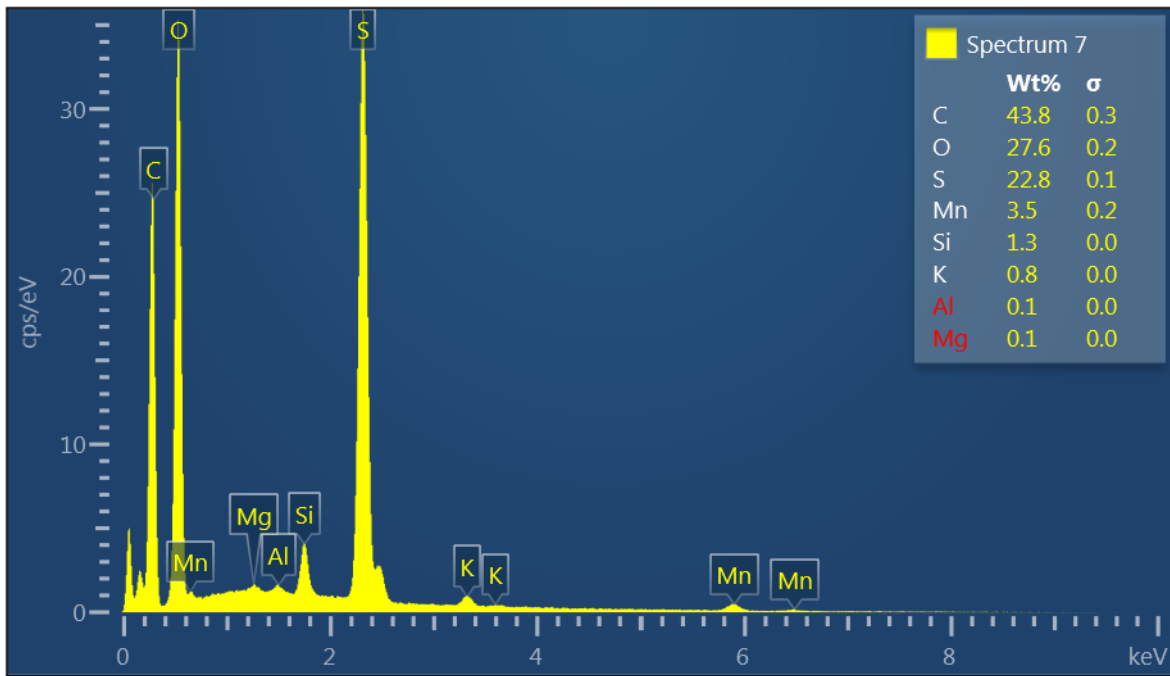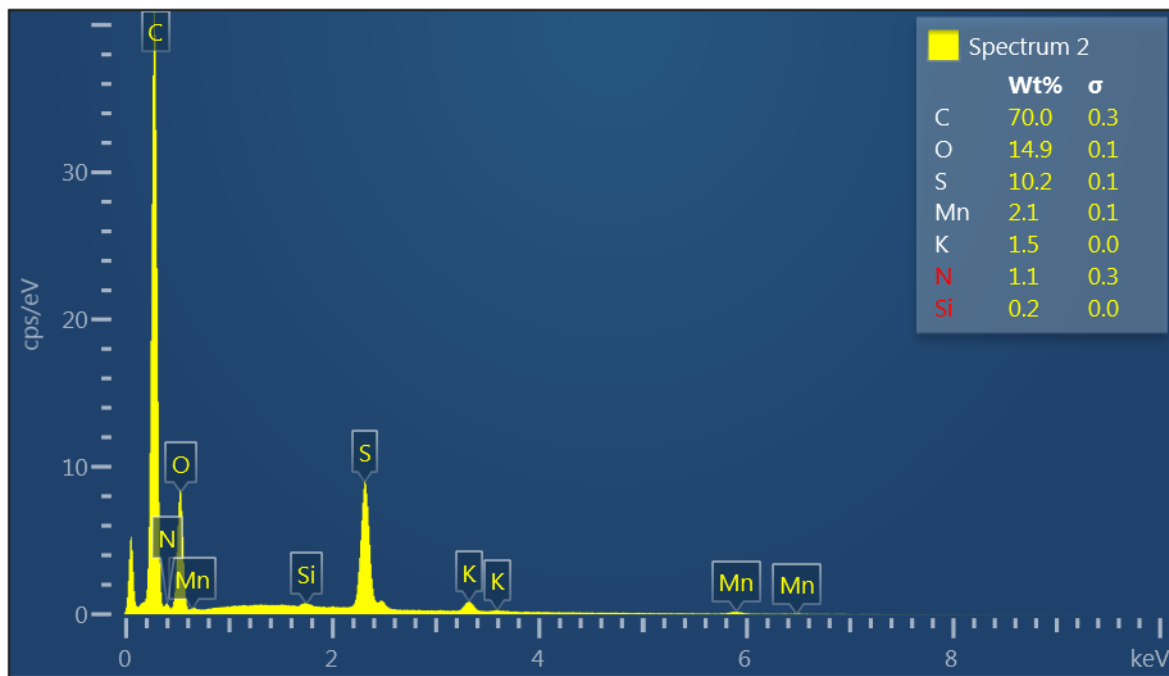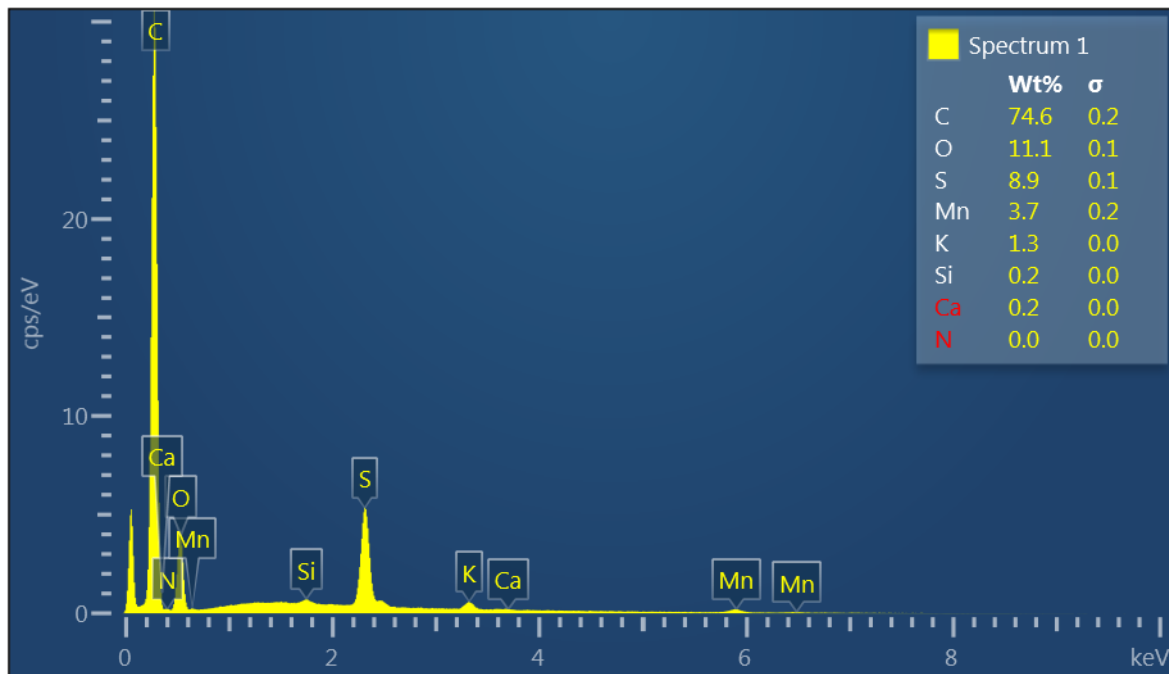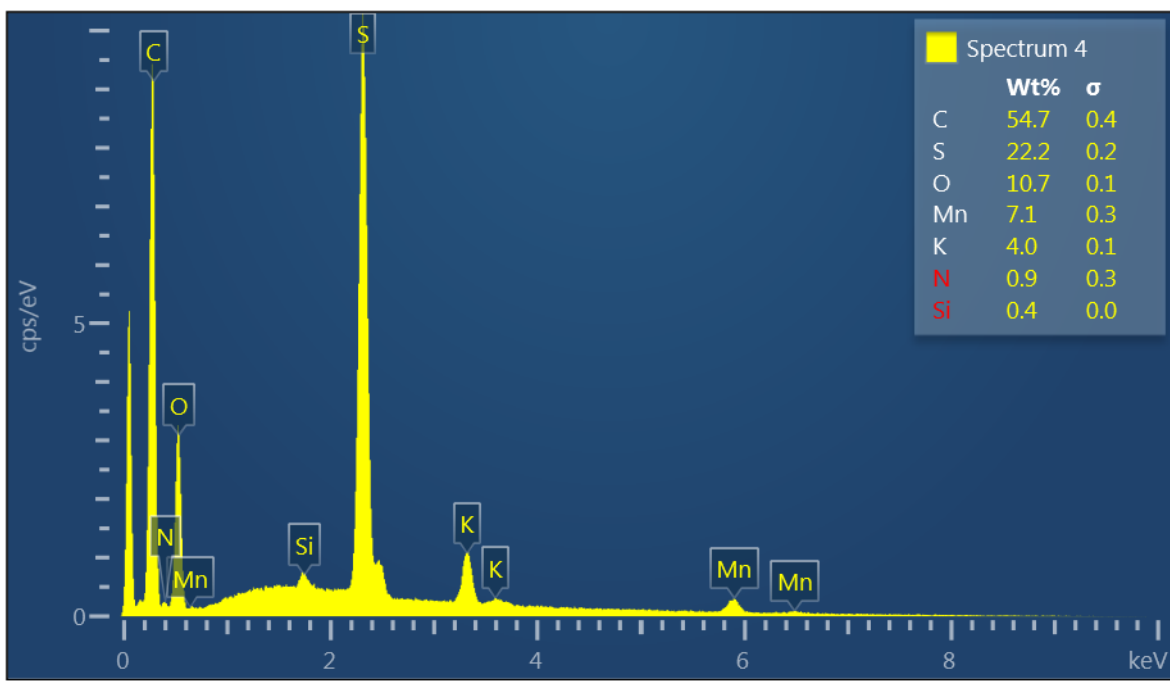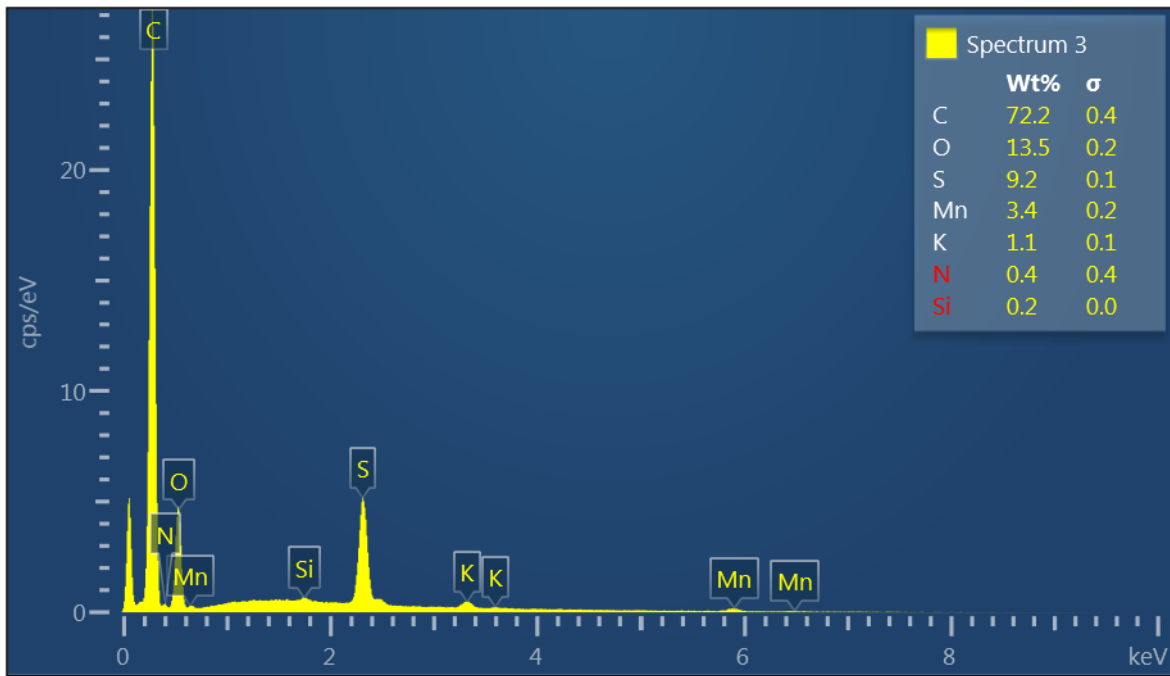
C – Graphite EDS Spectra (Table 3.3)

	Spectrum 10	
	Wt%	**σ**
C	97.4	0.1
O	2.6	0.1

	Spectrum 11	
	Wt%	**σ**
C	97.6	0.1
O	2.4	0.1
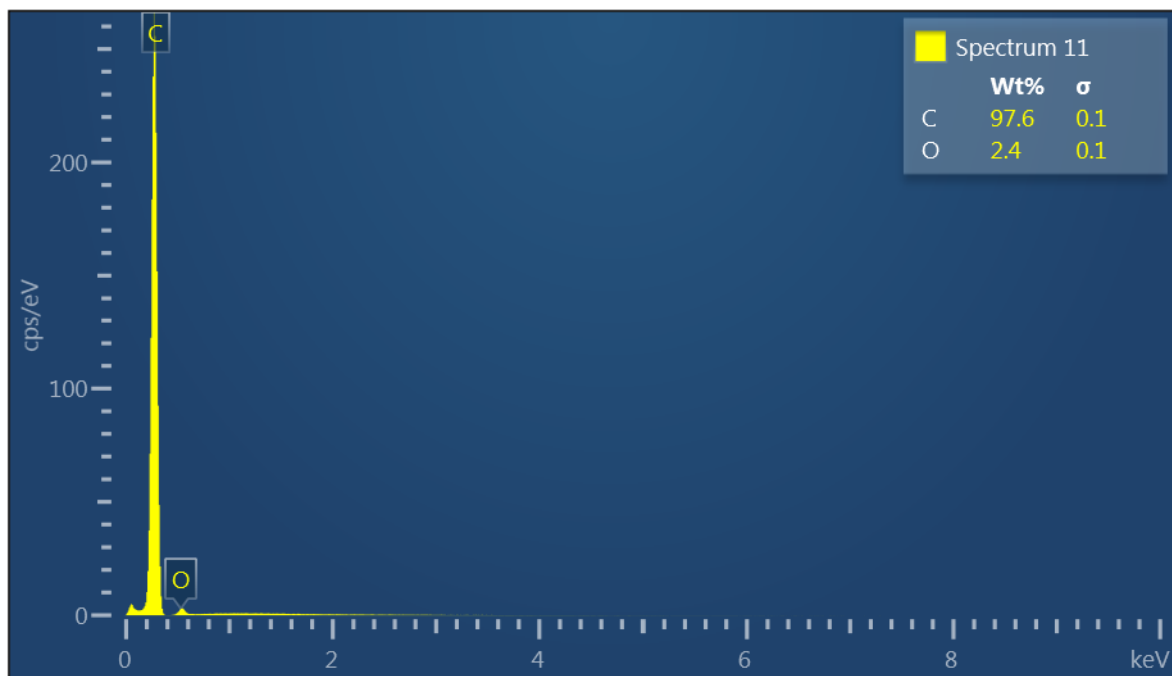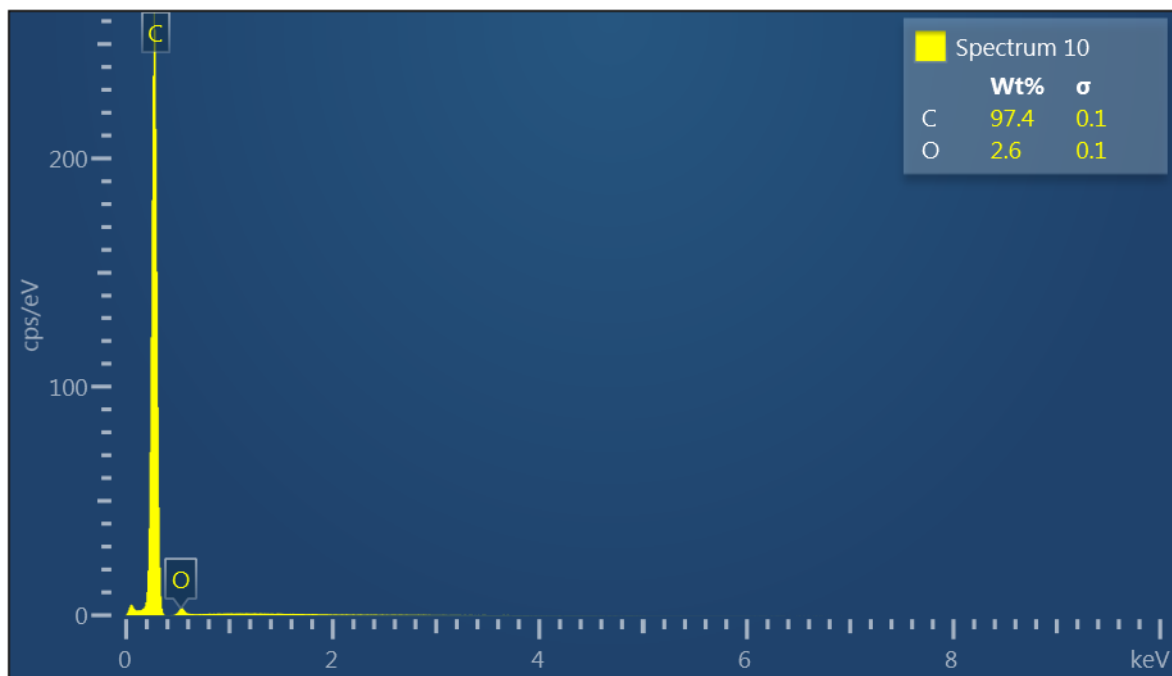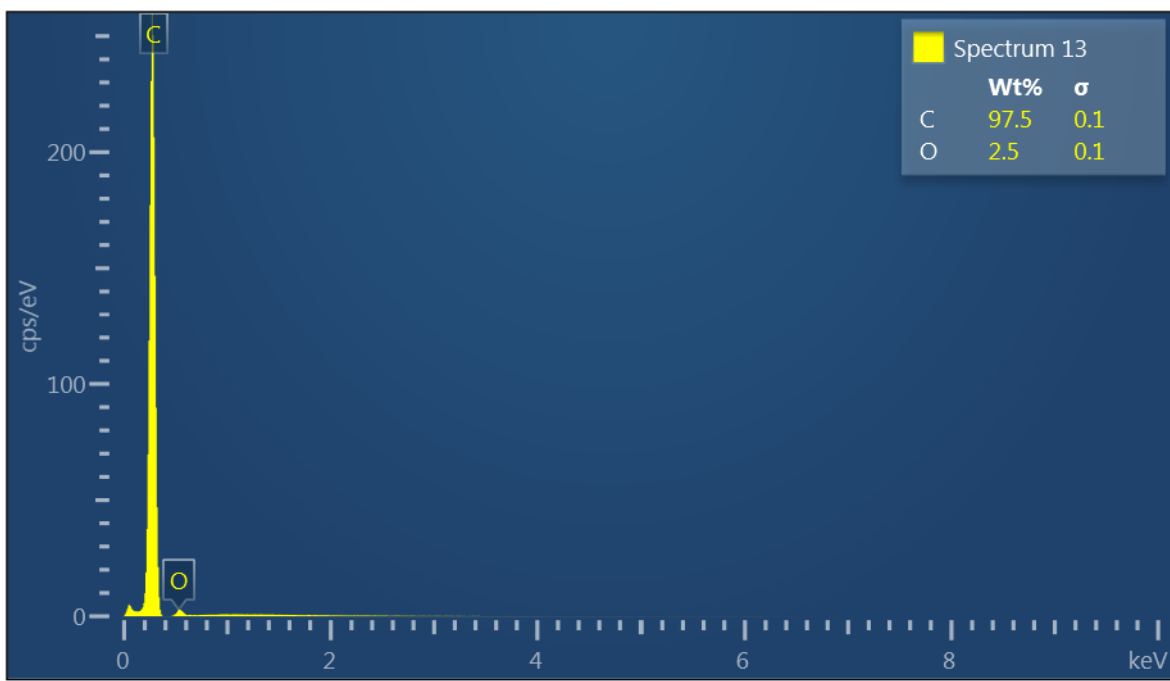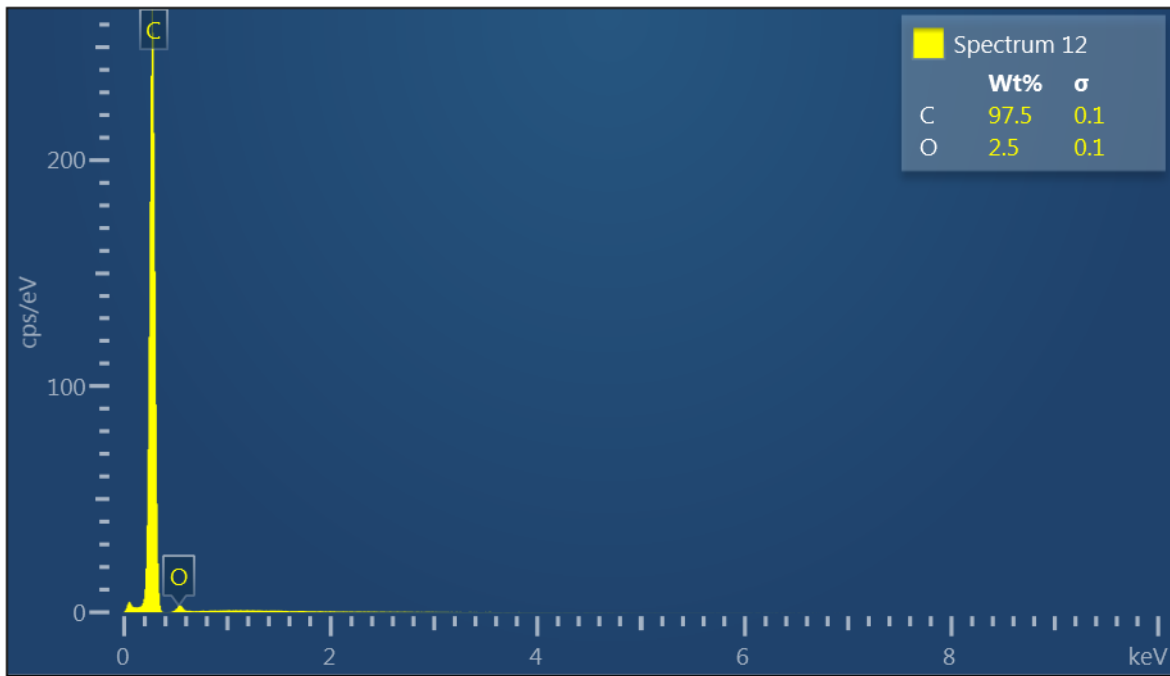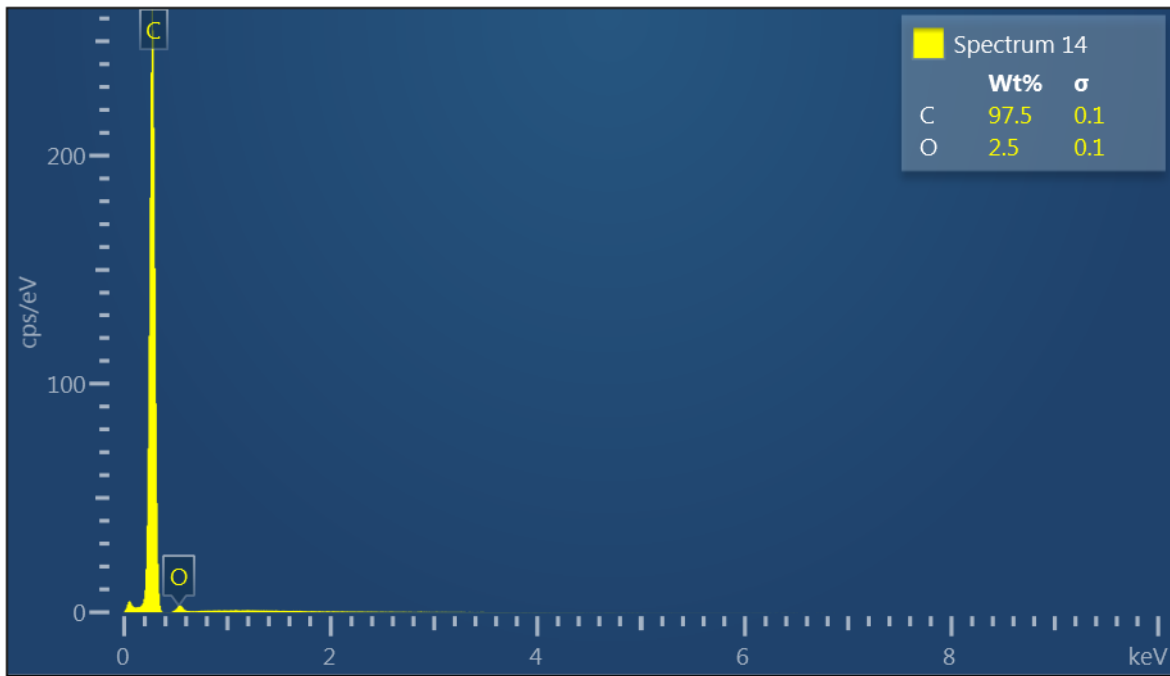
D – Optimisation input code for CP2K (Cs RGO template)

Notations in bold and bracketed are comments relating to code and are not present in the file:

```
&GLOBAL
PROJECT (Project name based on structure)
RUN_TYPE CELL_OPT
PRINT_LEVEL LOW
&END GLOBAL
&FORCE_EVAL
METHOD QS
STRESS_TENSOR ANALYTICAL
&SUBSYS
&CELL
ABC 12.351 12.351 26.000 (C value amended based on trial and error)
ALPHA_BETA_GAMMA 90.000 90.000 60.000
PERIODIC XYZ
&END CELL
&COORD
@INCLUDE 'in.coord' (xyz coordinate file taken from Guassview structure)
&END COORD
&KIND O (Basis sets and Pseudopotentials for each atom in model, adapted as required)
BASIS_SET DZVP-MOLOPT-SR-GTH-q6
POTENTIAL GTH-PBE-q6
&END KIND
&KIND C
BASIS_SET DZVP-MOLOPT-SR-GTH-q4
POTENTIAL GTH-PBE-q4
&END KIND
&KIND H
BASIS_SET DZVP-MOLOPT-SR-GTH-q1
POTENTIAL GTH-PBE-q1
&END KIND
&KIND Cs
BASIS_SET DZVP-MOLOPT-SR-GTH-q9
POTENTIAL GTH-PBE-q9
&END KIND
&END SUBSYS
&DFT
BASIS_SET_FILE_NAME ./BASIS_MOLOPT
POTENTIAL_FILE_NAME ./GTH_POTENTIALS
CHARGE 0
&QS
EPS_DEFAULT 1.0E-10
&END QS
&MGRID
CUTOFF 600
NGRIDS 5
REL_CUTOFF 80
&END MGRID
&SCF
```

```
MAX_SCF  1000
EPS_SCF  1.000E-6
SCF_GUESS  ATOMIC
&OT
PRECONDITIONER FULL_ALL
MINIMIZER DIIS
&END OT
&OUTER_SCF
MAX_SCF 1000
EPS_SCF 1.0E-6
&END
&PRINT
&RESTART OFF
&END RESTART
&END PRINT
&END SCF
&XC
&XC_FUNCTIONAL PBE
&END XC_FUNCTIONAL
&vdW_POTENTIAL
DISPERSION_FUNCTIONAL PAIR_POTENTIAL
&PAIR_POTENTIAL
TYPE DFTD3
REFERENCE_FUNCTIONAL PBE
PARAMETER_FILE_NAME /usr/shared_apps/packages/cp2k-full/data/dftd3.dat
&END PAIR_POTENTIAL
&END vdW_POTENTIAL
&END XC
&END DFT
&PRINT
&STRESS_TENSOR
&END
&FORCES ON
&END FORCES
&END PRINT
&END FORCE_EVAL
&MOTION
&GEO_OPT
TYPE MINIMIZATION
MAX_DR 1.0E-03
MAX_FORCE 1.0E-03
RMS_DR 1.0E-03
RMS_FORCE 1.0E-03
MAX_ITER 3000
OPTIMIZER CG
&END GEO_OPT
&CELL_OPT
TYPE DIRECT_CELL_OPT
KEEP_SYMMETRY
MAX_DR 1.0E-03
MAX_FORCE 1.0E-03
```

```
RMS_DR 1.0E-03
RMS_FORCE 1.0E-03
MAX_ITER 3000
OPTIMIZER CG
&END CELL_OPT
#  &CONSTRAINT
#   &FIXED_ATOMS
#    COMPONENTS_TO_FIX XYZ
#    LIST 1
#   &END FIXED_ATOMS
#  &END CONSTRAINT
&END MOTION
```

E – AIMD input code for CP2K (Cs RGO template)

Notations in bold and bracketed are comments relating to code and are not present in the file:

```
&GLOBAL
PROJECT (Project name based on structure)
RUN_TYPE MD
IOLEVEL  LOW
&END GLOBAL
&FORCE_EVAL
STRESS_TENSOR ANALYTICAL
&PRINT
&STRESS_TENSOR LOW
&END
&FORCES ON
&END FORCES
&END PRINT
METHOD Quickstep
&DFT
BASIS_SET_FILE_NAME ./BASIS_MOLOPT
POTENTIAL_FILE_NAME ./GTH_POTENTIALS
CHARGE 0
&MGRID
CUTOFF 600
NGRIDS 5
REL_CUTOFF 80
&END MGRID
&QS
METHOD GAPW
ALPHA0_HARD 10
EPS_GVG 1.0E-6
EPS_PGF_ORB 1.0E-6
EPSFIT 1.E-4
EPSISO 1.0E-12
EPSRHO0 1.E-8
EPS_DEFAULT 1.0E-12
EXTRAPOLATION ASPC
FORCE_PAW
LMAXN0 2
LMAXN1 6
QUADRATURE GC_LOG
&END
&POISSON
PERIODIC XYZ
&END
&SCF
SCF_GUESS ATOMIC
MAX_SCF 200
EPS_SCF 1.0E-6
&OT
PRECONDITIONER FULL_ALL
```

```
MINIMIZER DIIS
&END OT
&OUTER_SCF
MAX_SCF 20
EPS_SCF 1.0E-6
&END
&PRINT
&RESTART OFF
&END
&END
&END SCF
&XC
&XC_FUNCTIONAL
&PBE
&END
&END XC_FUNCTIONAL
&vdW_POTENTIAL
DISPERSION_FUNCTIONAL PAIR_POTENTIAL
&PAIR_POTENTIAL
TYPE DFTD3
REFERENCE_FUNCTIONAL PBE
PARAMETER_FILE_NAME /usr/shared_apps/packages/cp2k-full/data/dftd3.dat
&END PAIR_POTENTIAL
&END vdW_POTENTIAL
&END XC
#   &PRINT
#     &MULLIKEN ON
#      FILENAME charges.dat
#      PRINT_GOP
#     &END
#   &END
&END DFT
! description of the system
&SUBSYS
&CELL
ABC 12.351 12.351 25.000 (Values taken from successful optimisation)
ALPHA_BETA_GAMMA 90.000 90.000 60.000
PERIODIC XYZ
&END CELL
&COORD
@INCLUDE 'in.coord'
&END COORD
&KIND O (Basis sets and Pseudopotentials for each atom in model, adapted as required)
BASIS_SET DZVP-MOLOPT-SR-GTH-q6
POTENTIAL GTH-PBE-q6
&END KIND
&KIND C
BASIS_SET DZVP-MOLOPT-SR-GTH-q4
POTENTIAL GTH-PBE-q4
&END KIND
&KIND H
```

```
BASIS_SET DZVP-MOLOPT-SR-GTH-q1
POTENTIAL GTH-PBE-q1
&END KIND
&KIND Cs
BASIS_SET DZVP-MOLOPT-SR-GTH-q9
POTENTIAL GTH-PBE-q9
&END KIND
&END SUBSYS
&END FORCE_EVAL
&MOTION
&GEO_OPT
TYPE MINIMIZATION
MAX_DR 1.0E-03
MAX_FORCE 1.0E-03
RMS_DR 1.0E-03
RMS_FORCE 1.0E-03
MAX_ITER 1000
OPTIMIZER CG
&END GEO_OPT
&MD
ENSEMBLE NPT_I
TEMPERATURE [K] 400 (adapted as discussed in 5.1)
TIMESTEP [fs] 0.5
STEPS 40000 (adapted as discussed in 5.1)
&THERMOSTAT
TYPE NOSE
&NOSE
&END NOSE
&END THERMOSTAT
&BAROSTAT
PRESSURE 1
VIRIAL XYZ
&PRINT
&END PRINT
&END BAROSTAT
&END
# &CONSTRAINT
#  &FIXED_ATOMS
#   COMPONENTS_TO_FIX XYZ
#   LIST 1
#  &END FIXED_ATOMS
# &END CONSTRAINT
&END MOTION
&END
```

F – Sr ICP-OES calibration graphs and typical peak shapes

Sr (215.283 nm) Calibration

Intensity = 38227.45325847 * Concentration + 241.67632790
Correlation coefficient: 0.99939

Sr (215.283 nm), Sr3, Rack 1 Tube 4

Sr (232.236 nm) Calibration

Intensity = 2680.67191700 * Concentration + 8.20630066
Correlation coefficient: 0.99993

Sr (232.236 nm), Sr3, Rack 1 Tube 4

Sr (346.445 nm) Calibration

Intensity = 28972.10935088 * Concentration + 26.45263800
Correlation coefficient: 0.99966

Sr (346.445 nm), Sr3, Rack 1 Tube 4

Sr (416.179 nm) Calibration

Intensity = 55245.15974353 * Concentration + 36.82326423
Correlation coefficient: 0.99992

Sr (416.179 nm), Sr3, Rack 1 Tube 4

G – Cs ICP-OES calibration graphs and typical peak shapes

Cs (455.522 nm) Calibration

Intensity = 138.02686427 * Concentration + 86.35004125
Correlation coefficient: 0.99752

Cs (455.522 nm), Standard 4, Rack S1 Tube 5

Cs (672.328 nm) Calibration

Intensity = 130.12056612 * Concentration + 5208.60266584
Correlation coefficient: 0.99874

Cs (672.328 nm), Standard 4, Rack S1 Tube 5

Cs (697.327 nm) Calibration

Intensity = 289.74273336 * Concentration + 19.79298590
Correlation coefficient: 0.99819

Cs (697.327 nm), Standard 4, Rack S1 Tube 5